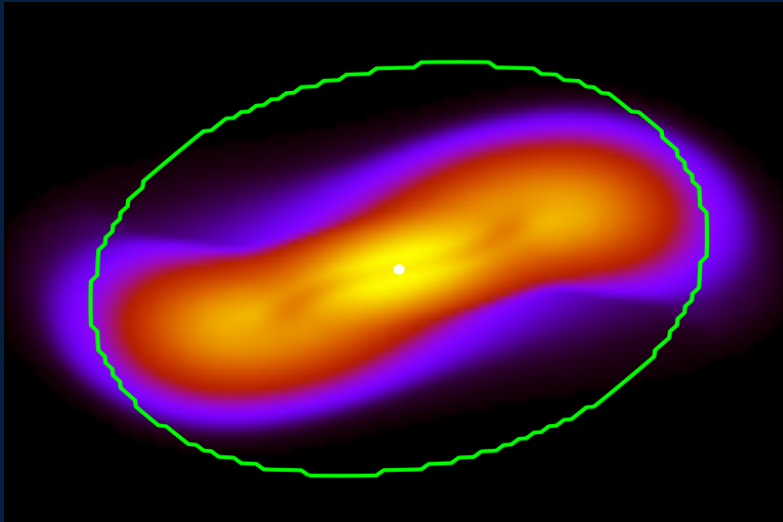




Dynamics of boson stars and fermion-boson stars: a numerical-relativity panorama



Fabrizio Di Giovanni

Directors:

José Antonio Font Roda

Pablo Cerdá Durán

Nicolás Sanchis-Gual

Doctorat en Física

Departament d'Astronomia i Astrofísica

Universitat de València

TESIS DOCTORAL

Septiembre 2022



VNIVERSITAT E VALÈNCIA

**Dynamics of boson stars and
fermion-boson stars: a
numerical-relativity panorama**

Fabrizio Di Giovanni

Doctorat en Física
Departament d'Astronomia i Astrofísica
Universitat de València

TESIS DOCTORAL

Directors:

José Antonio Font Roda
Pablo Cerdá Durán
Nicolás Sanchis-Gual

Septiembre 2022

To my parents, Lucio and Simonetta, and my siblings Giusy, Ale, Angelo and
Marta.

Acknowledgements

This thesis could have not carried out without the support of many people.

First of all, I want to thank my advisors. Prof. Toni Font for being always supportive and a source of good ideas and advices; without his guidance and help, from the master thesis to the PhD studies, I would have not reached this achievement; I thank you also for the dinner invitations and for the paella at the beach house. Prof. Pablo Cerdá-Durán for the help in solving technical problems in the numerical codes, and for the useful discussions about physics; I always knew during the thesis I could have counted on your help. Finally, Dr. Nicolas Sanchis-Gual, for introducing me into the world of boson stars, and for being always available for useful discussions and for helping me with my work in so many occasions I cannot even count them; also for the beers, the pizzas and montaditos, the pool and futbolin games and the visits in Portugal. The three of you guided me until this point and I am very grateful that I chose to join the Valencia group.

I thank all my collaborators. Prof. Juan Carlos Degollado, Prof. Carlos Herdeiro, Prof Eugen Radu, who have been involved in many of the works I have carried out during this thesis, and helped me with useful discussions and ideas. I thank them also for hosting me in Aveiro, Lisbon and in Cuernavaca, all these experiences have been very valuable for me. I also thank Miguel Zilhão, Saeed Fakhry, Davide Guerra, Miquel Miravét-Tenes, Simone Albanesi, and Dimitra Tseneklidou.

I want to thank also the reviewers of this thesis for dedicating time to read and comment my work: Helvi Witek, Carlos Herdeiro, Isabel Cordero-Carrión, Carlos Palenzuela, Juan Carlos Degollado, Katy Clough.

Ringrazio i miei genitori, Lucio e Simonetta, perchè nonostante le difficoltà e i momenti di incertezza mi hanno sempre supportato e sono fonte di ispirazione. Ringrazio le mie sorelle Marta, Ale e Giusy perchè so che anche se non ci vediamo spesso ci siete sempre; ringrazio mio fratello Angelo, uno dei miei modelli da seguire, anche se poi non sempre lo faccio! Un grazie anche ai miei nipoti Alessia,

Lucio, Sofia e Viola perchè è sempre un piacere rivedervi e passare il tempo con voi. Vi voglio bene. Ringrazio i miei nonni Maria, Antonio e Geppina, mi avete guidato e amato per buona parte della mia vita. Ringrazio tutta la famiglia allargata, zii e cugini e parenti tutti (inizia a sembrare un necrologio ora), compresi zia Mariliva e Pino, gli "zii" Grazia e Ennio, Elisanna e Pino, Carmine, e Mario ed Edda. Siete e sarete nel mio cuore tutti. Un ringraziamento speciale a Titti per mantenere sempre uniti noi cugini!

To all the members of the Department of Astronomy and Astrophysics, especially the secretaries Manel and Arancha for their attentive support with the documents and with the organization of my visits to other Universities, and Feli for her kindness and the xocolatada that she was always organizing.

A mis compañeros y amigos del departamento, pasados y presentes, Alex, Nico, Isa, Adri, Tomek, Joan, Jens, Pancho, Jose Adsuara, Rebecca, Davide, Michele, Bea, Sergio, Miquel bueno, Miquelito, David, Jose, Raquel, Alejandro, Alejandro Cruz, Raimon, Samuel, Marco and Carina. Os agradezco todas las risas, las pizzas, el billard y las salidas en general!

Quiero agradecer la Fasermi Maki Coalition, mis amigos Sergio and Miquel, por todas las risas, los chistes malos, las pizzas, los sushis y las visitas a Gandia y al salón del japon. Mi estancia en el departamento no hubiera sido tan divertida sin vosotros dos, y os quiero mucho. Una dedicatoria también a Paloma!

To my friends met in Los Angeles, Marina, Joana, Simone, Dimitra, Lorena, Peter, and YanYan for all the nice time spent together at IPAM, all the trips and the reunions we are organizing. I am really happy to have met such a nice group of people and that we are able to keep in touch and meet.

To Angela, the first friend I met in Valencia, for being part of my life in these past 5 years and for all the good and bad times, for all the white wines, all the IPAs, all the Kimmy's episodes, all the parties, all the smiles. To Manu for all the bad jokes and all your repetitive sentences and for being a true metal-head. To Lea for all the fun and parties, for being a good friend and listener. To Giovanni and Ashuni for being the best couple ever and being always so friendly and ready to help. To Mitch, my american Randy Marsh, just for being you, I wish you the best in your life. To Jesse for for all the cakes and leftover sushi. To Bea for always being so nice. To Stefano "commissaario" and Sabri. To all the other friends in Valencia randomly sorted in this list: Saidie, Joy, Filippo, Laura, Martin, Kat, Coni, Claire, Romina, Pavlina, Alessandra, Arnau, Luis, Frida, Idar, Kosta, Stebe, Emir, Monica, Pipo, Marco, Kyle, Fran, Manny, Luca, Bryson, Moritz, Jorge, Challos and all the Fiasco C.F. To all the Forevers, Mariana, Sarah, Perdo, Ana, Lukas, Jonathan, Lou, Lucy, Thomas, Andres,

Andy, Eric, Rachel and I add here B.J. To my old czech-slovak friends Andrej, Karolinka, Kristyna, Richard, Zuzka, Alzbeta, and Filip, I wish you people the best!

Voglio ringraziare Davide e Vito Daniele. Davide sei arrivato a Valencia solo da un paio d'anni ma mi sembra di conoscerti da na vita, grazie per le risate e le serate insieme, pe i viaggetti che ci siamo fatti e per avermi sposato a Las Vegas. Daniè, io e te ci inseguiamo dalle scuole superiori senza saperlo e ci siamo scoperti bene qua a Valencia. Grazie per le cenette e le chiacchiere che ci siamo fatti in questi anni. Un grazie pure a Federico Cocò, ci siamo conosciuti da poco ma ho subito capito che sei uno fregno pure se non ti fai vede mai.

Ai miei amici di Silvi. Ringrazio Donmazzone anche se ormai quasi non ci vediamo più ti voglio bene, Criasso per essere sempre un amico presente, Bolt per le grigliate e le visite al bagno della macelleria, Panfilo per i king e le lezioni di calciotennis, il Bomber per i sushi criminali a Milano, Tomo Antico per tutte le volte che rompi per andare al sushi, Astrolabio perchè sei un gigante buono, e tutti gli altri amici del Venere Stefanini per i ferragosto organizzati, Florio perchè si nu matt, Francescone e Fabietto per esse la coppia più bella, Serena per la tua dolcezza e simpatia, Irene e Giulia per le risate che mi fate fare, Maura per la tua solarità, Edo per i pugni che mi tiri sempre, Mario perché sei Jack Sparrow, Luca per la tua romanità, Giuseppe Mazzone, Marco, Pietro, Cate, Maria Elena, Eva, Giovanna, Carlo, Letizia, Francesca, Elena, Franceschino, Danielino, Muskit, Giuseppe, Zazá, nda cazz ni set... A Davidino per i 6 anni passati in Via Porpora insieme, i nabesix, i faburiziocouscous e le altre mattità che vai dicendo. Agli altri amici di Silvi/Abruzzo Alessio per ricomparire ogni tanto al mare, Cassandra per gli hot pot insieme, Guaglianone per i poker, Di Zio per gli anni da coinquilini, Ludo perchè anche se non ci vediamo quasi mai ti penso, Mr. Andrea per i pranzi spaziali a Teramo, Linaccia per le tue stories su instagram, Massi per esse esotico, Piercer e Pietropaolo per le partite a cod, Valentino per gli strilli in chat vocale, Bull per i tattoos, Simone per i tuoi balletti in Croazia, Matteo per i ricordi d'infanzia insieme, Jacopone per esse traveler, Lorenzo per gli abbracci, Alfonso e tutta la crew del Malibú, Robertino Ronca, FedeRonca, Elio, Vanni, Luciani, e tutti gli altri che non vi scrivo ma ci siete.

Agli amici di Pes. Ringrazio tutti gli Anacardi, Marta perché sei la amica di sempre e non smetterò mai di volerti bene, Ema perché i tuoi discorsi pazzi che fai ogni tanto mi fanno morire, Marco per tutti i pomeriggi passati insieme alle superiori, quelli virtuali su vulkania e giochi vari e quelli veri in giro, Roberta per le pizze e arrosticini che organizzi, pacmat perché sei un po' paxerello però

sei in gamba, Valerias perché i tuoi capelli profumano di frutta (ahaha), Daniele per i tuoi video e abbruzzesità che dici ogni tanto, Laura per la tua simpatia.. E wagliú qua io ho scritto veramente le prime cose che mi passavano per la mente così da non doverci pensare troppo, quindi prendete i miei messaggi per quello che sono!! Poi un saluto a Desa e Moris perchè ogni tanto ci becchiamo ancora.

Ai miei amici di Milano. Ad Anna per restare sempre in contatto con tutti e per essere super buona, tranne quando diventi dark Anna, a Marione il mio gemello segreto per le cene in famiglia con il padrino, a Tommy Roncio per l'invenzione della tua poltiglia e per i tuoi addominali scolpiti, a Tommy El per le gite al mulino e le tue sagge risposte alle mie domande di fisica, Ali mora semplicemente per essere come sei, Ali bionda per i tuoi discorsi complottistici e le tue tirate in mezzo, Ste ricco per le focacce e le chiacchierate, Marcone per le uscite al cinema e le chiacchierate sulle tipe, Costa per il capodanno dei mandarini ahaha, Iuri per i tuoi capelli bellissimi, Laura per le cene in Rombon e tutte le volte che mi ospiti, Ginny per i brownies e il salame al cioccolato , Martella per il salame della duja, Rota per le serate in sidreria e i racconti do brazil, Camo grazie per o birimbao, Gio e Ila grazie per le pizze e il belot, Jacopo per il belot e il banana bread, Bianca per tutte le volte che mi hai ascoltato ripetere, Pippo per avermi ospitato ormai non si sa quante volte, Eli per il viaggio in Albania, Betta per essere stata la mia coinquilina per qualche mese :) , Tommy romano per il tuo accento bellissimo, Sara per la tua solarità e simpatia, Giulio Fatti per le chiacchierate quando eri ancora a Milano, Xaxa per le proposte per serate o uscite che poi non rispettavamo mai, Bellandi per essere uno dei piú pazzi che conosca e per avermi installato Linux, Delo per i cuori che mi mandi, Nicoló per i bei discorsi di fisica teorica, Cape per i tuoi consigli, Eros per la sambuca ninja, e tutti gli altri di NZ che non ho citato ma mobbasta. Altre persone dell'uni (non finiró mai e a na certa scriveró "e tutti gli altri"): Bomba per essere uno scoppiato ma troppo carino, Chantal per essere una bad girl ma super dolce, Cate per la maratona dello svarione che dobbiamo ancora finire, Campa per le serate alcoliche e le cene a casa tua, tutti i Postumi (non cito tutti sorry ma cuori), Maria per essere sempre cosí gentile, Bruno per la tua calabresità, Shamil, Cinzia, Zunino per le partite a talisman, Daniele Bon per i nostri pettegolezzi e chiacchierate, Cicco e Jack per il tempo passato in laser insieme, Nigel per il weekend a casa tua con la piscina..Eccetera eccetera, chi non ho citato e leggerá fino a qui puó pretendere delle scuse. Ringrazio tutti quelli di via costa 31 Ara, Sid, Elenina, Sam per avermi accolto nella vostra fantastica casa, siete delle persone splendide e saró sempre in debito con voi per il tempo passato insieme e per l'ospitalitá che mi avete sempre dato. Ringrazio

la mia famiglia milanese Stefano, Marina e Robi per gli inviti a pranzo e le raccomandazioni del padrino!

Finally, as Snoop Dogg once said: last but not least, I wanna thank me. I wanna thank me for believing in me, I wanna thank me for doing all this hard work, I wanna thank me for having no days off, I wanna thank me for never quit, I wanna thank me for always being a giver and trying to give more than I receive, I wanna thank me for trying to do more right than wrong, I wanna thank me for just being me at all time.

Abstract

The dawn of gravitational-wave astronomy, currently lead by the LIGO-Virgo-KAGRA Collaboration, opens up a new channel to inspect the true nature of dark compact objects. The most compelling members of this category are black holes, which are widely believed to be well described by the Kerr metric near equilibrium. Several more exotic theoretical possibilities have been put forward, which are referred to as black hole mimickers, as their properties and dynamics resemble in certain ways those of black holes. Among those alternative dark compact objects, bosonic stars, either described by a scalar or vector field, are considered to be a robust, viable candidate, as, at least in spherical symmetry, they have been shown to be perturbatively stable and they have a sound dynamical formation mechanism. The results reported in this Thesis extend the study of the dynamical properties of such objects, analyzing for the first time the stability and dynamical formation of spinning bosonic stars and accounting for new families of solutions by considering multifield, multifrequency configurations. These investigations show that the parallelism between scalar boson stars and vector (Proca) stars is broken – scalar spinning mini-boson stars are all unstable due to the appearance of a non-axisymmetric instability while rotating Proca stars present a stable branch as happens in the spherically symmetric case. In a more recent study Siemonsen and collaborators found that a self-interaction term in the potential of the scalar field seems to quench this instability in a restricted area of the parameter space.

If ultralight bosonic fields exist, it is natural to speculate if objects which are a mixture of bosonic and fermionic particles might also exist in Nature. These macroscopic composites are known in the literature as fermion-boson stars. Most of my research has been devoted to the investigation of such objects, complementing and extending previous findings. I have constructed equilibrium configurations of fermion-boson stars with different scalar-field potentials, and have investigated their linear stability through the analysis of their critical points. I performed numerical-relativity evolutions to confirm the results from the linear

analysis and to characterize the dynamical formation of such objects through the accretion of a scalar field from a bosonic cloud onto an already-formed neutron star. Moreover, I have considered models with realistic equations of state for the baryonic matter and different bosonic contribution, and constructed curves in the mass-radius diagram to compare them with multi-messenger observational data from gravitational-wave events and the NICER and XMM-Newton experiments.

Finally, as a member of the Virgo Collaboration I have examined the gravitational waveforms produced in different scenarios involving exotic compact objects: *(i)* from the deformations of unstable spinning bosonic stars; *(ii)* from head-on collisions and mergers of Proca stars; and *(iii)* from bar-like deformations in neutron stars, focussing on how the presence of bosonic fields can impact their dynamics and the GW emission.

Resumen

Introducción

La composición de la materia oscura es todavía un problema abierto en astrofísica y cosmología. Los bosones libres y los axiones están entre los candidatos viables a materia oscura (conocida como *fuzzy dark matter*) que puede resolver una serie de cuestiones pendientes en cosmología. Se han propuesto como constituyentes de halos de materia oscura en galaxias [Hwang 1997, Matos, Guzman, and Urena-Lopez 2000, Matos and Urena-Lopez 2000, Matos and Urena-Lopez 2001, Marsh and Ferreira 2010, Hu, Barkana, and Gruzinov 2000], con masas de partículas en el rango $\hbar\mu \sim 10^{-22} - 10^{-24}$ eV, o con diferentes rangos de masa como candidatos a los inflatones [Freese, Frieman, and Olinto 1990], o incluso como modelos de energía oscura como *k-essence* [Armendariz-Picon, Mukhanov, and Steinhardt 2000]. Un resumen actual sobre la cosmología de los axiones puede encontrarse en Marsh [2016]. Si estas partículas existen, podrían condensar en objetos compactos autogravitantes conocidos como estrellas de bosones (en el caso de campos escalares) y estrellas de Proca (en el caso de campos vectoriales). Asimismo, parece natural suponer que podrían mezclarse con partículas fermiónicas, dando lugar a una nueva clase de objetos que se conocen en la literatura como estrellas mixtas de fermiones y bosones. Estos objetos pueden tener varios mecanismos de formación, ya sea como resultado final del colapso incompleto gravitacional a partir de un gas primordial compuesto tanto por bosones como por fermiones, o por la captura dinámica de partículas bosónicas (fermiónicas) por una estrella de neutrones (de bosones) ya formada en un sistema binario mixto.

Los sistemas físicos considerados en esta tesis involucran la gravedad en su régimen de campo fuerte, por lo que requieren para su descripción la Relatividad General [Einstein 1915, Einstein 1916, Einstein 1918], que es actualmente la teoría más fiable de la gravedad. Cabe señalar que se han propuesto diversas teorías alternativas de la gravedad, modificando el lado izquierdo de las ecuaciones

de Einstein (véase, por ejemplo Capozziello and de Laurentis [2011] para un resumen), pero este aspecto no fue explorado en mi investigación. Para resolver problemas teóricos de la Relatividad General que no son accesibles analíticamente, es fundamental el uso de ordenadores con los que realizar simulaciones numéricas de sistemas físicos: este campo de investigación se conoce como Relatividad Numérica. Aunque está bastante asentado después de unas seis décadas de desarrollo continuo, el campo de la Relatividad Numérica sigue expandiéndose, y las nuevas generaciones de relativistas numéricos emprenden nuevos retos para mejorar las simulaciones.

En esta tesis, como sugiere su título, he empleado ampliamente las herramientas de la Relatividad Numérica para estudiar varios sistemas físicos que involucran campos bosónicos, en concreto: *(i)* estrellas de bosones y de Proca en rotación; *(ii)* colisiones frontales y fusiones orbitales de estrellas de Proca; *(iii)* soluciones estacionarias y modelos dinámicos de estrellas mixtas de fermiones y bosones en simetría esférica; *(iv)* materia oscura ultraligera bosónica alrededor de estrellas de neutrones en rotación.

Objetivos

El objetivo principal del trabajo realizado en la presente tesis ha consistido en llevar a cabo evoluciones temporales utilizando la Relatividad Numérica para estudiar la dinámica de estrellas de bosones en diferentes escenarios de gravedad intensa, y analizar el efecto de campos bosónicos en estrellas fermiónicas como las estrellas de neutrones. Para conseguir dicho objetivo, en algunos de los proyectos de investigación desarrollados en esta tesis he trabajado en la construcción de datos iniciales que resuelven las ligaduras de Einstein y que describen sistemas que involucran campos bosónicos fundamentales.

En cuanto a las evoluciones numéricas realizadas, numerosas investigaciones en el régimen lineal y no lineal han analizado la estabilidad de las estrellas de bosones y de Proca en simetría esférica. Con estas simulaciones fue posible encontrar un mecanismo de formación dinámica para las estrellas de bosones escalares. Previamente, en mi Tesis de Máster, llevé a cabo simulaciones numéricas que me permitieron encontrar el mismo mecanismo de formación para las estrellas de Proca. Por lo tanto, era importante estudiar la estabilidad y la formación dinámica de los modelos de estrellas de bosones en rotación y ampliar la familia de soluciones considerando configuraciones formadas por más de un campo bosónico con iguales o diferentes frecuencias de oscilación, modelos que

van más allá de la simetría esférica. Estos proyectos fueron uno de los objetivos iniciales de esta tesis.

De igual modo, investigar el efecto de los campos bosónicos cuando están mezclados con materia fermiónica ha constituido una de las líneas de investigación principales que he seguido durante mi tesis doctoral. En este contexto, he ampliado trabajos anteriores en los cuales se analiza la estabilidad de modelos de estrellas mixtas: así, *(i)* he considerado nuevos tipos de potenciales para el campo escalar, como el potencial del axiÓN; *(ii)* he estudiado la formación dinámica de estos objetos, mediante la acreción de una nube bosónica sobre una estrella de neutrones ya formada; *(iii)* he construido modelos excitados con uno o más nodos radiales en el campo bosónico y examinado su dinámica y estabilidad; *(iv)* he analizado como modelos de estrellas mixtas con ecuaciones de estado realistas para la materia fermiónica podrían mitigar la tensión en medidas de masa y radios para las estrellas de neutrones; y *(v)* he construido modelos de estrellas de neutrones en rotación rodeadas por una nube de campo bosónico y analizado el efecto de la materia bosónica en las inestabilidades sufridas por estas estrellas.

Para estudiar la dinámica de los sistemas físicos descritos en los párrafos anteriores, es necesario construir configuraciones iniciales que describan sistemas físicos correctos (soluciones de las ecuaciones de ligadura de Einstein). Por un lado, para investigar la formación dinámica de diferentes modelos de estrellas de bosones en rotación y la acreción de una nube bosónica sobre una estrella de neutrones en rotación, he utilizado un código numérico para resolver las ligaduras de Einstein, desarrollado originalmente por mi co-director Pablo Cerdá-Durán, que he ampliado para considerar campos bosónicos. Con esta herramienta, he generado datos iniciales que describen una nube aislada de materia bosónica con rotación, considerando campos escalares y vectoriales. También, he construido datos numéricos que describen una nube de materia bosónica alrededor de una estrella de neutrones con alta rotación diferencial. Para realizar esta segunda tarea, he construido modelos de estrellas de neutrones con el código numérico *RNS* Stergioulas and Friedman [1995] y los he adaptado al caso de una métrica conformemente plana e introducido como métrica de fondo para así generar modelos rodeados de una nube bosónica. Por otro lado, para investigar la dinámica de estrellas mixtas en simetría esférica, he obtenido soluciones estáticas del sistema Einstein-Euler-Klein-Gordon que describe estos objetos compactos exóticos, desarrollando un código numérico que resuelve el conjunto de ecuaciones diferenciales. Usando este código he construido modelos de estrellas mixtas en

el estado fundamental, utilizando diferentes tipos de potenciales para el campo escalar y también modelos en el primer estado excitado.

Finalmente, en calidad de miembro de la Colaboración Virgo, uno de los objetivos de esta Tesis Doctoral ha sido generar patrones de ondas gravitatorias emitidas en diferentes sistemas físicos que involucran campos bosónicos. Así, he extraído y analizado las ondas gravitatorias producidas por estrellas de bosones en rotación, por sistemas binarios de estrellas de Proca, y por estrellas de neutrones con alta rotación diferencial rodeadas por campos bosónicos. También, he producido diagramas masa-radio para estrellas de neutrones con una componente bosónica y he utilizado estos modelos exóticos para comparar con los resultados de los eventos GW170817 y GW190814 observados por la colaboración LIGO-Virgo-KAGRA.

Metodología

Todos los artículos científicos presentados en esta tesis han sido posibles gracias a los resultados obtenidos mediante el desarrollo y uso de diferentes códigos numéricos. Por un lado, el enfoque de mi trabajo ha consistido en generar datos iniciales que satisfagan las ecuaciones de ligadura de Einstein, lo cual es necesario para poder realizar evoluciones temporales de sistemas físicos válidos, descritos por la Relatividad General. Por otro lado, he realizado dichas evoluciones temporales utilizando herramientas de la Relatividad Numérica.

En el marco de la construcción de datos iniciales, he desarrollado un código numérico en colaboración con Saeed Fakhry de la Universidad de Teherán para obtener soluciones de equilibrio que describen estrellas mixtas de fermiones y bosones. Este código ha sido actualizado y refinado en colaboración con los estudiantes de doctorado Simone Albanesi, Davide Guerra y Miquel Miravet-Tenés. Adicionalmente, con estos mismos colaboradores, hemos desarrollado otro código que identifica las curvas de nivel de una función numérica genérica y lo hemos empleado para encontrar curvas de igual masa en el dominio de existencia de las estrellas mixtas de fermiones y axiones. Esta nueva herramienta fue extremadamente útil para determinar las islas de estabilidad y se describe en el apéndice A de Di Giovanni et al. [2022]. El código es abierto y puede encontrarse en el repositorio público <https://github.com/SimoneA96/fermion-axion-pywrap>. Por otra parte, he examinado y utilizado un código numérico desarrollado por mi co-director Pablo Cerdá-Durán, que utiliza la *extended conformally flat approximation* (XCFC) para reescribir las restricciones de Einstein, y resuelve el conjunto de ecuaciones elípticas con diferentes métodos numéricos [Cordero-

Carrión et al. 2009]. He actualizado dicho código añadiendo subrutinas para construir datos iniciales de nubes aisladas de materia bosónica con rotación y nubes alrededor de estrellas de neutrones en rotación diferencial.

En cuanto a las evoluciones temporales de sistemas en simetría esférica, he ampliado y empleado extensamente el código numérico NADA1D [Montero and Cordero-Carrión 2012], que permite resolver las ecuaciones de evolución de Einstein, utilizando el formalismo 3+1 conocido como Baumgarte-Shapiro-Shibata-Nakamura (BSSN) con una métrica en coordenadas isotrópicas, y las ecuaciones de la hidrodinámica. La versión original de este código en 2D fue desarrollada por [Montero, Font, and Shibata 2008] y ha sido utilizada con éxito en simulaciones de evolución de agujeros negros, colapso gravitatorio, y en sistemas formados por agujeros negros rodeados por toros de acreción autogravitantes. En la versión en simetría esférica, se emplean los métodos PIRK (Partially-Implicit Runge-Kutta) [Cordero-Carrión, Cerdá-Durán, and Ibáñez 2012], especialmente diseñados para realizar simulaciones numéricas en coordenadas curvilíneas sin necesidad de regularización en el origen del sistema de coordenadas, donde las ecuaciones pueden presentar singularidades coordenadas. Estos métodos almacenan los operadores diferenciales que llevan términos problemáticos, como factores $1/r$ o $1/\sin(\theta)$, en operadores que son evaluados de manera implícita. De esta manera se consigue obtener evoluciones estables.

Durante mi tesis también he desarrollado diferentes subrutinas para transformar los datos iniciales de estrellas mixtas de fermiones y bosones construidos en coordenadas de Schwarzschild y adaptarlos a la métrica isotrópica y a la malla numérica del código NADA1D. Más allá de esto, he añadido al mismo código de evolución subrutinas para generar datos iniciales para estudiar la acreción de campos bosónicos sobre estrellas de neutrones y para evolucionar el campo bosónico con diferentes potenciales como el potencial cuártico de autointeracción o el potencial periódico del axión.

En cuanto a las evoluciones de sistemas en 3D he empleado la plataforma de software abierto de herramientas computacionales de Relatividad Numérica EINSTEINTOOLKIT [Babiuc-Hamilton et al. 2019, Loffler et al. 2012, Zilhão and Löffler 2013], la cual incluye diferentes componentes llamadas *thorns* y está basada en la infraestructura de los códigos Cactus y Carpet [Schnetter, Hawley, and Hawke 2004, Carpet] para poder emplear refinamiento de malla en las simulaciones. En los varios trabajos presentados en esta tesis, he utilizado la infraestructura MCLACHLAN [Reisswig et al. 2011, Brown et al. 2009] que implementa las ecuaciones de Einstein en la formulación BSSN, y en el caso de

sistemas que involucran la hidrodinámica he empleado las subrutinas GRHYDRO. Para la evolución de campos bosónicos he utilizado *thorns* privados basados en el código público CANUDA[Witek et al. 2021]. Además, he desarrollado diferentes subrutinas en estos *thorns* privados para implementar los datos iniciales que describen binarias de estrellas de Proca, nubes aisladas de campos bosónicos y nubes bosónicas alrededor de estrellas de neutrones en rotación.

Conclusiones

Dinámica no lineal de estrellas de bosones y de Proca en rotación

Las estrellas bosónicas son soluciones estacionarias, sin horizonte, similares a los solitones, no singulares en todo el espacio, del sistema Einstein-Klein-Gordon y Einstein-Proca para un campo escalar complejo o un campo vectorial complejo, respectivamente. Para ser consideradas verdaderas candidatas viables a constituir objetos astrofísicos, las estrellas bosónicas tienen que cumplir una serie de requisitos: *(i)* deben aparecer en teorías físicas bien motivadas y consistentes (como la Relatividad General); *(ii)* deben ser estables frente a perturbaciones suficientemente pequeñas; *(iii)* y deben tener un mecanismo de formación dinámico. Los dos últimos puntos de esta lista definen el concepto de robustez dinámica [Herdeiro 2022].

El destino dinámico de las estrellas de bosones escalares en simetría esférica se ha investigado en profundidad utilizando tanto teoría de perturbaciones lineales [Gleiser and Watkins 1989, Lee and Pang 1989] como simulaciones numéricas totalmente no lineales [Seidel and Suen 1990, Balakrishna, Seidel, and Suen 1998, Guzman 2004, Guzmán 2009]. Al igual que en el caso de las estrellas fermiónicas, las estrellas de bosones muestran una rama estable y otra inestable, que pueden identificarse mediante el análisis del punto crítico. Así, se puede generar una secuencia de soluciones que depende del valor central del campo escalar ϕ_c y buscar el valor crítico en el que la configuración de equilibrio muestra el valor máximo de la masa ADM, que para las “mini-estrellas de bosones” (las que tienen sólo un término cuadrático en el potencial) corresponde a $M_{\max} \approx 0.633 M_{\text{Planck}}^2 / \mu$, como se demostró en Seidel and Suen [1990]. Colpi, Shapiro, and Wasserman [1986] consideraron modelos con un término de autointeracción cuártica en el potencial y mostraron numéricamente que $M_{\max} \approx 0.22 \Lambda^{1/2} M_{\text{Planck}}^2 / \mu$, siendo Λ el parámetro de autointeracción. También se han propuesto otros potenciales, como el solitónico [Friedberg, Lee, and Pang

1987], el KKLS [Kleihaus, Kunz, and List 2005, Kleihaus et al. 2008], o el axiónico [Guerra, Macedo, and Pani 2019]. En el contexto no-lineal Seidel and Suen [1990] demostraron mediante simulaciones numéricas que el destino de una estrella de bosones inestable bajo pequeñas perturbaciones, producidas por el error de truncamiento asociado a la discretización numérica de las ecuaciones diferenciales, es el colapso a un agujero negro o la migración a la rama estable. Estudios posteriores [Seidel and Suen 1990, Balakrishna, Seidel, and Suen 1998, Guzman 2004, Guzmán 2009] establecieron que la evolución de estrellas de bosones inestables también puede dar lugar a la dispersión total del campo escalar, un destino que sólo ocurre para la materia bosónica y que no es posible para las estrellas fermiónicas. Además, Seidel and Suen [1994] propusieron un mecanismo de formación dinámica de estos objetos, que denominaron enfriamiento gravitacional, mediante el cual una nube de materia bosónica escalar se condensa y forma un objeto compacto que se aproxima a una configuración estacionaria irradiando el campo escalar excedente.

Por otro lado, más recientemente se han encontrado modelos de estrellas de bosones vectoriales, o *estrellas de Proca*, que corresponden a soluciones estacionarias del sistema Einstein-Proca [Brito et al. 2016b]. En simetría esférica estas nuevas soluciones se asemejan en muchos aspectos a sus “primas” escalares. En particular, las soluciones muestran también una rama estable y otra inestable, lo que fue confirmado mediante evoluciones numéricas no lineales por Sanchis-Gual et al. [2017], y tienen una masa máxima que es ligeramente mayor que la de las estrellas escalares, concretamente $M_{\max} \approx 1.058 M_{\text{Planck}}^2 / \mu$. Previamente a mi Tesis Doctoral, durante mi trabajo de Tesis de Máster, demostré que las estrellas de Proca también pueden formarse dinámicamente a partir de una nube de materia bosónica vectorial a través del mecanismo de enfriamiento gravitacional [Di Giovanni et al. 2018], como sucede para el caso escalar.

Más allá de la simetría esférica, se han obtenido soluciones de estrellas de bosones en rotación tanto para el caso escalar [Yoshida and Eriguchi 1997, Herdeiro and Radu 2014, Herdeiro and Radu 2015] como para un campo vectorial [Herdeiro, Radu, and Rúnarsson 2016]. Se podría esperar que las propiedades dinámicas de estas soluciones muestren similitudes con el caso esférico, donde siempre se puede identificar una rama estable. En Sanchis-Gual et al. [2019a], realizamos evoluciones numéricas no lineales de soluciones estacionarias de estrellas de bosones y estrellas de Proca en rotación y estudiamos su formación dinámica a partir de una nube de materia bosónica con momento angular no nulo. Nuestros resultados revelaron que las estrellas escalares en rotación son todas inestables debido al desarrollo de una inestabilidad dinámica no axisimétrica que causa la

pérdida de todo el momento angular, el decaimiento a la solución sin rotación, y el cambio de forma de la estrella de una morfología toroidal a una esferoidal. Las estrellas de Proca en rotación, que poseen una forma esferoidal, no sufren este tipo de inestabilidad y se ha podido encontrar una rama estable, al menos hasta la aparición de un *light ring* (anillo de luz) para las estrellas de Proca ultracompactas [Cunha et al. 2022]. Mi principal contribución a esta investigación fue la construcción de datos iniciales que satisfacen las ecuaciones de ligadura de Einstein para las nubes de materia bosónica en rotación y el estudio de la formación dinámica de las estrellas compactas resultantes, donde observamos el mismo destino para las estrellas escalares y vectoriales que en las evoluciones de las configuraciones de equilibrio. Los detalles sobre la construcción de los datos iniciales para los campos bosónicos pueden encontrarse en el apéndice de Sanchis-Gual et al. [2019a]. En Di Giovanni et al. [2020a] amplié estos resultados, añadiendo términos de autointeracción en el potencial del campo escalar y analizando de forma más cuantitativa la inestabilidad. Así, identifiqué el modo $m = 2$ como el modo dominante de la inestabilidad y comparé los resultados con ciertos modelos de estrellas de neutrones con rotación diferencial que también se caracterizan por sufrir una inestabilidad $m = 2$ de tipo barra. Por otra parte, he extraído la señal de ondas gravitatorias producida por la deformación no axisimétrica de las estrellas bosónicas, evaluando su *characteristic strain* h_{char} y la relación señal a ruido (SNR) promediada en todas las orientaciones angulares de la fuente a diferentes distancias y para detectores óptimamente orientados. Las curvas de sensibilidad empleadas corresponden a los detectores terrestres actuales y planeados (Advanced LIGO, Advanced Virgo, KAGRA, Einstein Telescope), el futuro detector espacial LISA y Pulsar Timing Arrays (PTAs). Cabe también señalar que, recientemente, Siemonsen and East [2021] han demostrado mediante evoluciones numéricas que considerar términos de autointeracción en el potencial de campo escalar puede impedir el desarrollo de la inestabilidad no axisimétrica en algunas regiones restringidas del espacio de parámetros de los modelos, delineando una isla de estabilidad también para las estrellas escalares en rotación.

En Sanchis-Gual et al. [2021] ampliamos la familia de soluciones de estrellas bosónicas en rotación considerando múltiples campos tanto con la misma frecuencia como con diferentes frecuencias. Estas nuevas soluciones las denominamos *estrellas bosónicas de múltiples campos y frecuencias*. Entre los miembros de esta familia extendida, hay configuraciones particulares conocidas como las estrellas de bosones ℓ , propuestas por Alcubierre et al. [2018]. Están compuestas por un número impar arbitrario ($2\ell + 1$, $\ell \in \mathbb{N}_0$) de campos escalares complejos de igual

frecuencia cuya dependencia angular viene dada por los armónicos esféricos $Y_{\ell,m}$, con la misma amplitud. Se puede demostrar que el tensor energía-momento total es esféricamente simétrico, aunque los campos individuales no lo sean. Los nuevos modelos investigados por Sanchis-Gual et al. [2021] amplían la familia al considerar diferentes amplitudes y frecuencias para los distintos campos, rompiendo así la simetría esférica. Además, también se consideran modelos con diferentes frecuencias propias individuales de los campos.

Colisiones frontales y fusiones orbitales de estrellas de Proca

Las primeras evoluciones numéricas de colisiones frontales y fusiones orbitales de mini-estrellas de bosones escalares fueron realizadas por [Palenzuela et al. 2007, Palenzuela, Lehner, and Liebling 2008]. Estos trabajos fueron posteriormente ampliados por [Bezares, Palenzuela, and Bona 2017, Palenzuela et al. 2017, Bezares and Palenzuela 2018] considerando modelos más compactos de estrellas de bosones con un potencial solitónico, y tomando pares de estrellas compuestas por dos campos escalares independientes que no interactúan directamente entre sí, únicamente a través de la gravedad. En todas estas investigaciones no fue posible obtener una estrella de bosones en rotación como remanente de las fusiones orbitales. Este resultado podría explicarse teniendo en cuenta nuestros hallazgos sobre las inestabilidades no axisimétricas que desarrollan las estrellas escalares con rotación. En Sanchis-Gual et al. [2019b] estudiamos las colisiones frontales y las fusiones orbitales de las estrellas de Proca. Al igual que en el caso de las estrellas escalares, consideramos datos iniciales que son una superposición de dos estrellas de Proca esféricamente simétricas situadas a una cierta distancia, a las cuales aplicamos un *boost* en una dirección ortogonal al segmento que conecta los dos objetos para imponer un movimiento orbital inicial. Nuestros resultados mostraron que el resultado de las fusiones orbitales es o una estrella de Proca o un agujero negro de Kerr rodeado por una nube de campo de Proca cuasi ligada. En el primer caso, a pesar de que la estrella de Proca tiene inicialmente momento angular, éste se pierde a medida que la estrella se acerca al equilibrio. Conviene señalar que las estrellas de Proca con rotación pueden ser estables, por lo que será necesario estudiar este resultado más en detalle. Además, investigamos las ondas gravitatorias emitidas tanto en las colisiones frontales como en las fusiones orbitales, comparándolas con las producidas en el caso de dos agujeros negros de Schwarzschild. Nuestros resultados mostraron que, en el caso de las estrellas de Proca, es posible en ocasiones distinguir la señal de la de los agujeros negros debido a la presencia de una fase intermedia durante la cual se forma una estrella

Proca “hipermasiva” antes de colapsar a un agujero negro. Por otro lado, los modos cuasi-normales del remanente pueden diferir de los de un agujero negro aislado si, en cambio, este está rodeado por una nube de Proca suficientemente extendida y de larga duración.

El trabajo anterior demuestra que uno de los posibles resultados de las fusiones de estrellas bosónicas es un agujero negro en rotación rodeado por una nube de campo bosónico. Los agujeros negros en rotación, que son descritos por la familia de soluciones de Kerr, tienen la característica de que parte de su energía puede ser extraída a través de su interacción con una onda bosónica entrante. Este proceso se conoce como *superradiancia* [Brito, Cardoso, and Pani 2015]. Para que este proceso ocurra se requiere que la onda cumpla la condición

$$\omega < m\Omega_{\text{BH}}, \quad (1)$$

donde ω es la frecuencia, m es el número azimutal de la onda, y Ω_{BH} es la velocidad angular del agujero negro. Cuando se cumple esta condición, la onda bosónica crece exponencialmente extrayendo energía del agujero negro, en forma de momento angular (o carga en el caso de los agujeros negros de Reissner-Nordström), hasta el punto en el que la velocidad angular del agujero negro en rotación se sincroniza con la frecuencia del campo, es decir, $\omega = m\Omega_{\text{BH}}$. En general, para campos bosónicos reales y complejos, los agujeros negros con nube bosónica que cumplen esta última condición se denominan átomos gravitatorios sincronizados. En el caso de campos complejos entran en la categoría de agujeros negros “con pelo”, como los encontrados por Herdeiro and Radu [2014] y Herdeiro, Radu, and Rúnarsson [2016].

En Sanchis-Gual et al. [2020] estudiamos más a fondo la dinámica de los sistemas binarios de estrellas de bosones y de Proca, centrándonos en el resultado de las fusiones orbitales, o de las colisiones frontales de estrellas de Proca en rotación, para investigar un posible canal alternativo al de la superradiancia para formar dinámicamente átomos gravitatorios sincronizados o agujeros negros con pelo. En el caso de la superradiancia, el campo bosónico hace disminuir la velocidad angular del agujero negro hasta su saturación. Se ha demostrado que un límite termodinámico universal impone que la nube bosónica no puede extraer más de 29% de la energía final del sistema agujero negro más nube (véase Brito, Cardoso, and Pani [2015]). Sin embargo, las simulaciones numéricas de East and Pretorius [2017] sólo pudieron alcanzar un máximo de 9% y el estudio analítico de Herdeiro, Radu, and Santos [2022] demostró que el límite real podría estar alrededor del 10%. En el nuevo canal investigado Sanchis-

Gual et al. [2020] el remanente de la fusión de las dos estrellas puede ser un agujero negro con una nube bosónica. Paulatinamente esta es acretada por el agujero negro, haciéndolo rotar más rápidamente, y acercándose a la condición de sincronización desde el otro lado. En este contexto, nuestro estudio demostró que pueden formarse átomos gravitatorios sincronizados en los que la nube almacena hasta alrededor de 18% de la energía, sin que exista, a priori, límite teórico. Sin embargo, para obtener este canal de formación de dos pasos, los datos iniciales deben ajustarse con precisión. Así, el escenario más común parece, en cambio, un mecanismo de formación de tres pasos en el que primero se forma un agujero negro, después aumenta su rotación debido a la acreción de la nube, y por último pierde rotación debido a la superradiancia, alcanzando finalmente la sincronización. Otro resultado interesante de este trabajo fue que pudimos formar nubes sincronizadas con modos azimutales más altos ($m = 5, 6$) que los encontrados con el mecanismo de superradiancia, donde sólo ha sido posible obtener el modo de crecimiento más rápido ($m = 1$) con las simulaciones numéricas realizadas hasta la fecha.

Soluciones estacionarias y dinámica de estrellas mixtas de fermiones y bosones

Las estrellas fermiónicas (por ejemplo, las estrellas de neutrones o las enanas blancas) podrían acumular partículas de materia oscura y dar lugar a lo que se conoce como estrellas de neutrones mezcladas con materia oscura (en inglés *dark-matter admixed neutron stars*). Las configuraciones de equilibrio de las estrellas compuestas por fermiones y bosones fueron encontradas por primera vez por Henriques, Liddle, and Moorhouse [1989] and Henriques, Liddle, and Moorhouse [1990]. Su estabilidad lineal fue investigada en Henriques, Liddle, and Moorhouse [1990] y en Jetzer [1990]. En los modelos más simples, la componente bosónica sólo interactúa con la fermiónica a través del campo gravitatorio y vice versa, lo que es consistente con la idea de que la materia oscura bosónica se acopla sólo gravitacionalmente con la visible. Más recientemente, ha crecido el interés por estas configuraciones, especialmente debido al nuevo canal de observación que ofrece la astronomía de ondas gravitatorias y a los nuevos experimentos que tratan de evaluar con más precisión la composición interna de las estrellas de neutrones, como NICER [Gendreau et al. 2016] y XMM-Newton [Barré, Nye, and Janin 1999]. Nuevos trabajos teóricos ampliaron los primeros resultados encontrados por Henriques y colaboradores: así Brito, Cardoso, and Okawa [2015] estudiaron la captura dinámica de materia oscura bosónica por parte de

estrellas de neutrones utilizando técnicas perturbativas y evoluciones no lineales, posteriormente ampliadas en Brito et al. [2016a]; Valdez-Alvarado et al. [2013] construyeron configuraciones de equilibrio de estrellas mixtas, formadas por una mezcla de fermiones y bosones, con el potencial simple de mini-estrellas de bosones y analizaron su estabilidad lineal mediante el método desarrollado por Henríquez y su estabilidad no lineal vía simulaciones de Relatividad Numérica. Este trabajo se extendió posteriormente al potencial de autointeracción en Valdez-Alvarado, Becerril, and López [2020].

Durante mi trabajo de doctorado, he contribuido a este campo de investigación con varias publicaciones. En Di Giovanni et al. [2020b] construimos configuraciones de equilibrio que pueblan el dominio de existencia para diferentes valores del parámetro de autointeracción Λ , y estudiamos la estabilidad lineal y evoluciones no lineales utilizando el código numérico NADA1D. Además, como se ha comentado antes, verificamos que las estrellas mixtas pueden formarse mediante la acreción dinámica de materia bosónica a través del mecanismo de enfriamiento gravitatorio.

En este primer trabajo, encontramos un resultado interesante. Uno de los modelos de formación dinámica mostró como resultado final una estrella mixta con el campo escalar oscilando alrededor de una configuración de equilibrio con un nodo radial. Existen soluciones de mini-estrellas de bosones en estado excitado que muestran uno o más nodos radiales, pero se ha demostrado que son inestables en el régimen no lineal [Lee and Pang 1989, Balakrishna, Seidel, and Suen 1998]. Recientemente se ha encontrado que un término de autointeracción cuártica en el potencial puede estabilizar los estados excitados [Sanchis-Gual et al. 2022]. Por otro lado, Bernal et al. [2010] encontraron que un campo escalar excitado puede ser estabilizado por otro campo bosónico co-existente en el estado fundamental, bajo la condición de que el número de ocupación N_B del campo en el estado fundamental sea mayor que el del excitado. Motivados por este resultado y por nuestro hallazgo anterior, exploramos en Di Giovanni et al. [2021] la estabilidad de las estrellas mixtas excitadas. Para ello poblamos el dominio de existencia con modelos con un nodo radial para tres valores diferentes de Λ y realizamos cientos de evoluciones numéricas para delinear empíricamente la supuesta región de estabilidad. Si existe una isla de estabilidad, debía estar en un entorno de la rama estable de las estrellas de neutrones. Nuestros resultados confirmaron esta hipótesis. Además, realizamos varias simulaciones nuevas de formación dinámica, encontrando configuraciones estables con más de un nodo radial y que además eran dinámicamente robustas. Observamos que tras la acreción del campo escalar, el objeto final perturbado oscila alrededor de

diferentes configuraciones de equilibrio con cero, uno o más nodos. Este hallazgo fue confirmado evaluando la transformada de Fourier del campo escalar en la parte final de la evolución, encontrando que se excitaban más frecuencias que corresponden a soluciones estáticas con diferente número de nodos y el mismo número de partículas bosónicas y fermiónicas. Más allá de la simetría esférica y de las soluciones sin rotación, demostramos que tener una estrella de bosones formada por múltiples campos con una componente estelar estable también puede estabilizar mini-estrellas de bosones en rotación inestables propensas a inestabilidades de modo de barra y estrellas de bosones dipolares.

Motivados por los resultados obtenidos sobre el mecanismo de estabilización de un campo escalar excitado y las estrellas de bosones en rotación, investigamos si un campo escalar o vectorial estable podría tener el mismo efecto e impedir las inestabilidades dinámicas que sufren ciertos modelos de estrellas de neutrones en rotación (para resúmenes sobre el tema, véase Glampedakis and Gualtieri [2018] and Paschalidis and Stergioulas [2017]). Se sabe que las configuraciones de las estrellas de neutrones con rotación diferencial y un valor elevado de $\beta \equiv T/W$, siendo T la energía cinética rotacional y W la energía potencial gravitatoria, sufren una inestabilidad de un modo $m = 2$ llamada inestabilidad de modo barra [Shibata and Uryū 2000, Baiotti et al. 2007]. En nuestro trabajo [Di Giovanni et al. 2022] consideramos datos iniciales que describen un modelo de estrella de neutrones con alta rotación diferencial, rodeada por una nube bosónica, compuesta por un campo escalar o vectorial que acreta rápidamente sobre la estrella fermiónica y se aproxima a una configuración mixta de equilibrio. Como la escala de tiempo dinámica de la acreción es menor que la del desarrollo de la inestabilidad de tipo barra, es posible observar los efectos del campo bosónico en la dinámica. Consideramos varios modelos de estrellas de neutrones en rotación y centramos nuestro estudio en el modelo con el mayor valor de β . Investigamos el efecto de las nubes de materia bosónica escalar con tres valores diferentes de la masa de las partículas μ y también nos centramos en un valor concreto de μ pero considerando ahora diferentes masas totales de la nube inicial. Este último enfoque reveló cómo la presencia de una mayor cantidad de materia bosónica provoca la amortiguación del modo $m = 2$ del contenido individual de materia fermiónica, pero no la supresión completa de la inestabilidad. Un modo $m = 2$ de la energía total (bosónica y fermiónica) es de hecho excitado, mostrando la aparición de lo que definimos como una barra “mixta”. Por último, estudiamos la emisión de ondas gravitatorias asociada a la inestabilidad de la estrella de neutrones aislada y la comparamos con la de los modelos con campo bosónico, lo que reveló la aparición de frecuencias más altas en la señal,

procedentes de sobretonos tanto de la inestabilidad de tipo barra como de las oscilaciones cuasi-radiales del objeto. También proporcionamos una estimación de la SNR de estas señales a una distancia de 10 kpc para una variedad de detectores terrestres y evaluamos la distancia del horizonte de observación, que es la distancia a la que $SNR = 8$, lo que proporciona una estimación de la distancia máxima a la que se espera detectar la señal.

Recientemente, se ha podido determinar con alta precisión tanto la masa como el radio de dos estrellas de neutrones, PSR J0030+0451 y PSR J0740+6620. La inferencia bayesiana sobre el modelado del perfil de los pulsos de las observaciones de NICER del púlsar de rayos X PSR J0030+0451, arrojó valores de $M \sim 1.5M_{\odot}$ y radio circunferencial $R \sim 13km$ [Miller et al. 2019, Riley et al. 2019]. A partir de los datos combinados de NICER y XMM-Newton de PSR J0740+6620 [Riley et al. 2021, Miller et al. 2021], el púlsar más masivo conocido, estos equipos infirieron valores de $M \sim 2.08M_{\odot}$ y $R \sim 13km$. Estos dos resultados desafían los modelos teóricos propuestos para describir la composición del interior de las estrellas de neutrones, que requieren una ecuación de estado muy rígida. Las observaciones de ondas gravitatorias de los sistemas binarios de estrellas de neutrones también han establecido restricciones sobre la masa y el radio de estos objetos, lo que añade más tensión a las medidas. Además, a partir de la estimación de los parámetros del evento GW190814, la colaboración LIGO-Virgo-KAGRA (LVK) dedujo un valor de la masa de la componente secundaria de $\sim 2.50 - 2.67M_{\odot}$. Este valor se encuentra en el denominado *lower mass gap*, lo que plantea dudas sobre la naturaleza de este objeto, ya sea el agujero negro más ligero jamás observado o la estrella de neutrones más pesada también jamás observada, o quizá un objeto compacto exótico. En Di Giovanni et al. [2022] investigamos cómo modelos de estrellas mixtas con ecuaciones de estado realistas podrían mitigar la tensión en estas medidas. Para llevar a cabo este estudio, consideramos para la componente fermiónica tres ecuaciones de estado diferentes que se ajustan (o se ajustan marginalmente) al menos a una parte de los resultados observacionales y construimos secuencias de soluciones con contribución bosónica constante. Además, consideramos dos valores diferentes del parámetro de masa μ del campo escalar, concretamente $\hbar\mu = \{1.34 \times 10^{-11}, 1.34 \times 10^{-10}\}$ eV. Nuestra investigación reveló que, en algunos casos, nuestros modelos presentan mayor compatibilidad con los datos observacionales multimensajero que los modelos de estrellas de neutrones aisladas.

Finalmente, en Di Giovanni et al. [2022] encontramos novedosas configuraciones de equilibrio de estrellas mixtas con el potencial axiónico y estudiamos sus propiedades de estabilidad. Este potencial periódico fue introducido por Guerra,

Macedo, and Pani [2019] y está inspirado en el potencial del axi3n de la cromodinámica cuántica introducido por Peccei and Quinn [1977] para resolver el problema CP fuerte en física fundamental. Su peculiaridad es que, dependiendo del valor del parámetro de decaimiento f_a , las estrellas de axiones muestran una o más ramas estables en su dominio de existencia. Como consecuencia, en el espacio de parámetros bidimensional de las estrellas mixtas podríamos identificar con un análisis de estabilidad lineal una o más islas de estabilidad. Centramos nuestro análisis en los modelos con el valor de $\log_{10}(f_a) = -1.7$ que muestra dos islas de estabilidad, y confirmamos los resultados del análisis lineal realizando evoluciones numéricas no lineales, mapeando el dominio de existencia y obteniendo los tres destinos diferentes habituales de los modelos inestables: una parte de ellos colapsa a un agujero negro de Schwarzschild, otros migran a una configuración estable, y en una pequeña región del espacio de parámetros las soluciones se enfrentan a la dispersión total del campo escalar.

Mi aportación a la Colaboración Virgo

La Colaboración Virgo se formó en 1993 con el objetivo de construir un detector europeo de ondas gravitatorias. En 2003 se construyó una primera versión de dicho detector, a la que siguieron importantes actualizaciones que culminaron en el detector Virgo avanzado. A partir de 2007, la Colaboración Virgo y la Colaboración Científica LIGO firmaron un memorando de entendimiento para analizar conjuntamente los datos y publicar los resultados. A día de hoy se han llevado a cabo tres periodos de observaciones (*Observing Runs*) con los detectores avanzados y se han identificado 90 eventos seguros de ondas gravitatorias. Al final del último *Observing Run*, el detector japonés KAGRA se unió a la colaboración, y en este momento se están realizando nuevas actualizaciones de los tres detectores, y se espera que el cuarto *Observing Run* comience en marzo de 2023. En julio de 2016 el Grupo Virgo de la Universitat de València se unió a la Colaboración Virgo, y desde el inicio de mis estudios de doctorado en 2018 he sido miembro de este grupo. Mi trabajo dentro de la colaboración implica sobre todo la modelización de ondas gravitatorias de objetos compactos exóticos y también he participado en varias actividades de servicio.

Como ya se ha mencionado en la memoria, he modelado la señal de ondas gravitatorias emitida en varios sistemas físicos. En Di Giovanni et al. [2020a] estudié la emisión de ondas gravitatorias generada por la inestabilidad no axisimétrica de tipo barra de estrellas bosónicas en rotación, evaluando la *characteristic strain* de la señal y la distancia del horizonte para varios detectores. Además,

dimos una estimación de la escala de tiempo de la onda gravitatoria emitida evaluando la escala de tiempo de amortiguación característica en la que se disipa la deformación, encontrando que este tipo de señal podría ser potencialmente una fuente continua de ondas gravitatorias. También realizamos un análisis similar en Di Giovanni et al. [2022] para modelos de estrellas de neutrones en rotación rodeadas de nubes bosónicas. En Sanchis-Gual et al. [2019b] caracterizamos por primera vez las señales de ondas gravitatorias procedentes de colisiones frontales y fusiones orbitales de estrellas de Proca, comparándolas con agujeros negros con las mismas masas. Finalmente, en Di Giovanni et al. [2022] presenté diagramas de masa-radio para estrellas de neutrones con una componente bosónica y utilicé estos modelos exóticos para ajustar mejor los resultados de la observación de la binaria de estrellas de neutrones GW170817 y también para dar una posible explicación teórica para el objeto secundario de $2.6M_{\odot}$ del evento GW190814. Todos estos resultados se han presentado en discusiones internas de la Colaboración LVK al resto de la colaboración.

Además del trabajo de investigación directamente relacionado con mi proyecto de tesis, he participado en actividades de *servicio* en la Colaboración LVK. En febrero de 2020 presté servicio durante una semana en un turno de caracterización del detector Virgo, lo que implica supervisar el estado del detector durante el día, y ayudar a personas expertas en el funcionamiento del detector a identificar y caracterizar posibles fuentes de ruido y anomalías en el interferómetro. También, en 2021 participé en el equipo de redacción de uno de los artículos de la Colaboración LVK sobre la búsqueda de señales de ondas gravitatorias procedentes de objetos compactos de masa subsolar durante la primera mitad de la tercera *Observing Run O3a* [Abbott et al. 2022].

Publications

The present doctoral thesis has been written as a compendium of publications, which are listed below:

- Sanchis-Gual, N., Herdeiro, C., Font, J. A., Radu, E., & **Di Giovanni, F.** (2019).
Head-on collisions and orbital mergers of Proca stars.
Physical Review D 99, 024017.
- Sanchis-Gual, N., **Di Giovanni, F.**, Zilhão, M., Herdeiro, C., Cerdá-Durán, P., Font, J. A., & Radu, E. (2019).
Nonlinear Dynamics of Spinning Bosonic Stars: Formation and Stability.
Physical Review Letters 123, 221101.
- **Di Giovanni, F.**, Fakhry, S., Sanchis-Gual, N., Degollado, J. C., & Font, J. A. (2020).
Dynamical formation and stability of fermion-boson stars.
Physical Review D 102, 084063.
- Sanchis-Gual, N, Zilhão, M., Herdeiro, C., **Di Giovanni, F.**, Font, J. A., & Radu E. (2020).
Synchronized gravitational atoms from mergers of bosonic stars.
Physical Review D 102, 101504.
- **Di Giovanni, F.**, Sanchis-Gual, N., Cerdá-Durán, P., Zilhão, M., Herdeiro, C., Font, J. A., & Radu E. (2019).
Dynamical bar-mode instability in spinning bosonic stars.
Physical Review D, 102, 124009.
- Sanchis-Gual, N., **Di Giovanni, F.**, Herdeiro, C., Radu, E. & Font J. A. (2021).
Multifield, Multifrequency Bosonic Stars and a Stabilization Mechanism.
Physical Review Letters 126, 241105.

- **Di Giovanni, F.**, Fakhry, S., Sanchis-Gual, N., Degollado, J. C., & Font, J. A. (2021).
A stabilization mechanism for excited fermion–boson stars.
Classical and Quantum Gravity, Volume 38, Number 19.
- **Di Giovanni, F.**, Sanchis-Gual, N., Cerdá-Durán, P., & Font, J. A. (2022).
Can fermion-boson stars reconcile multimessenger observations of compact stars?
Physical Review D 105, 063005
- **Di Giovanni, F.**, Sanchis-Gual, N., Guerra, D., Miravet-Tenés, M., Cerdá-Durán, P., & Font, J. A. (2022).
Impact of ultralight bosonic dark matter on the dynamical bar-mode instability of rotating neutron stars.
Physical Review D, 106, 044008.
- **Di Giovanni, F.**, Guerra, D., Albanesi, S., Miravet-Tenés, M., & Tseneklidou, D. (2022).
Fermion-axion stars: Static solutions and dynamical stability.
Accepted in Physical Review D.

Contents

I	Summary	1
1	Introduction	3
1.1	Motivation	3
1.2	Numerical Relativity	7
1.3	Nonlinear dynamics of Boson stars and Proca stars	10
1.3.1	Spinning bosonic stars	10
1.3.2	Head-on collisions and orbital mergers	12
1.4	Stationary solutions and dynamics of fermion-boson stars	14
1.5	The Virgo Collaboration	18
2	Discussion	21
2.1	Boson stars, Proca stars, and gravitational waves	21
2.2	Nonlinear interactions between bosonic fields and fermionic stars	23
3	Outlook	27
II	Appendices	29
A	Publications	31

Part I

Summary

Chapter 1

Introduction

1.1 Motivation

Free bosons and axions are considered as a viable dark matter (DM) candidate (known as fuzzy DM) which may address a number of outstanding issues in cosmology; they have been proposed as constituents of DM halos in galaxies [Hwang 1997, Matos, Guzman, and Urena-Lopez 2000, Matos and Urena-Lopez 2000, Matos and Urena-Lopez 2001, Marsh and Ferreira 2010, Hu, Barkana, and Gruzinov 2000], with particle mass in the range $\hbar\mu \sim 10^{-22} - 10^{-24}$ eV, or with different mass assumptions as candidates for the inflatons [Freese, Frieman, and Olinto 1990], or as dark energy models like *k-essence* [Armendariz-Picon, Mukhanov, and Steinhardt 2000]. A review on axion cosmology can be found in Marsh [2016].

If these particles exist, they might also have a relevant role in astrophysics. In the mid-1950s, John Wheeler conjectured the existence of what he called *geons*, a nonsingular electromagnetic or gravitational field which is held together in a localized region by its own self-gravity. These solutions are considered to be unstable at the classical level. Nonetheless, in the pioneering works of David J. Kaup [1968] and Ruffini and Bonazzola [1969], it was found that taking a complex scalar field with a harmonic time dependence given by

$$\phi(\vec{r}, t) \equiv \phi_{\text{Re}}(\vec{r}, t) + i\phi_{\text{Im}}(\vec{r}, t) = \phi_0 e^{i\omega t}, \quad (1.1)$$

lead to the existence of static solutions of the Einstein-Klein-Gordon (EKG) system, being a realization of static Klein-Gordon geons which are known as boson stars (BSs). The field having a harmonic time dependence is a fundamental piece to obtain stationarity, as it allows the field itself to oscillate in time while

keeping the stress-energy tensor, and thus the metric, time-independent. This is sufficient to evade Derrick’s theorem, which states that no regular, static, non-topological localized scalar field can be stable in three dimensional asymptotically flat spacetime.

Scalar BSs (with spin zero) and their vector “cousins” (with spin one), known as Proca stars, are compact objects which are stationary solutions of a complex bosonic field (scalar or vector) minimally coupled to gravity. Such fields possess energy due to their spatial gradients and time derivatives, thus BSs are held together and they self-gravitate. Less clear is what supports a bosonic star against gravitational collapse. Fermionic compact stars such as white dwarfs and neutron stars (NSs) are supported against gravity by the degeneracy pressure of electrons and neutrons, respectively, which arises from the Pauli exclusion principle: it is not possible for fermions to occupy the same quantum state. Applying this quantum-mechanical principle, Subrahmanyan Chandrasekhar obtained the maximum mass for a white dwarf [Chandrasekhar 1931, Chandrasekhar 1935]. As for fermion stars, another quantum-mechanical principle supports BSs against gravity. In fact, they are considered to be Bose-Einstein condensates, meaning that they are in a macroscopic quantum state modeled by a unique wave function, which obeys the Heisenberg uncertainty principle

$$\Delta x \Delta p \geq \hbar, \quad (1.2)$$

which is responsible for a repulsive force, a sort of wave pressure, which acts against gravity. Δx and Δp in this equation are the uncertainty on the position and momentum of a particle respectively. Following a simple reasoning proposed in Liebling and Palenzuela [2012], using the assumption that a BS is confined in a certain radius $\Delta x = R$ and that the maximum momentum is $\Delta p = \mu c$, and looking for the maximum mass which saturates the uncertainty bound and drive the radius to the limit of the Schwarzschild radius $R_S = 2GM/c^2$, one finds that

$$M_{\max} = \frac{\hbar c}{2G\mu} = 0.5M_{\text{Planck}}^2/\mu, \quad (1.3)$$

where M_{Planck} is the Planck mass. This simple estimation using the uncertainty principle is in good agreement with numerical results found for self-gravitating scalar BSs [Seidel and Suen 1990], which is

$$M_{\max} \approx 0.633M_{\text{Planck}}^2/\mu. \quad (1.4)$$

The inverse relation between the maximum mass of the object and the particle mass μ , reveals that in order to have astrophysically relevant objects (with a

mass comparable to or larger than that of the Sun) we require the bosonic particle to be ultralight with a mass $\mu \lesssim 10^{-11}$ eV. One of the main subjects of this Doctoral Thesis has been to investigate the dynamical features of scalar and vector BSs within the regime of astrophysical relevance, with a major focus on both spinning and multifield models.

If ultralight bosonic particles exist in Nature, it seems natural to assume that they might mix with fermionic particles, giving rise to a new class of objects which are known in the literature as fermion-boson stars. There might be various formation mechanisms for these objects, either considering the gravitational collapse from a primordial gas comprised of both bosons and fermions, or by the dynamical capture of bosonic or fermionic particles by an already formed NS or BS in a mixed binary system. Macroscopic composites of baryonic matter and DM have been widely studied over the last decades, considering different models of particle DM, such as mirror baryonic DM [Sandin and Ciarcelluti 2009, Ciarcelluti and Sandin 2011], asymmetric fermionic DM [Kaplan, Luty, and Zurek 2009, Goldman et al. 2013, Gresham and Zurek 2019], weakly interacting massive particles (WIMPs) [Goldman and Nussinov 1989], or bosonic DM [Henriques, Liddle, and Moorhouse 1990, Valdez-Alvarado et al. 2013, Brito, Cardoso, and Okawa 2015, Brito et al. 2016a, Valdez-Alvarado, Becerril, and López 2020]. The growing interest for DM admixed NSs resides in the possible observable implications associated with their dynamics and with gravitational wave (GW) emission, leading to the intriguing possibility that these models could help reconcile recent observational results on the masses and radii of NSs obtained by the Neutron Star Interior Composition Explorer (NICER) and X-ray Multi-mirror Mission-Newton (XMM-Newton) experiments and the LIGO-Virgo-KAGRA Collaboration. In this thesis results from several investigations are reported, where models of fermion-boson stars with different potentials are constructed and their dynamical features and observational implications are analysed.

The physical systems considered in this dissertation involve gravity in its strong-field regime, thus requiring for their description General Relativity (GR) [Einstein 1915, Einstein 1916, Einstein 1918], which is currently the most reliable theory of gravity. The set of partial differential equations governing the dynamics of relativistic astrophysics are the Einstein equations which in their compact (covariant) form read

$$G_{\mu\nu} = \frac{8\pi G}{c^4} T_{\mu\nu}, \quad (1.5)$$

where $G_{\mu\nu}$ is Einstein's tensor, which carries the partial differential operators acting on the spacetime metric, G is the gravitational constant, and $T_{\mu\nu}$ is the

stress-energy tensor which contains the information on the matter content of the system. Alternative theories of gravity have been proposed, modifying the left-hand side of the Einstein equations (see e.g. [Capozziello and de Laurentis 2011] for a review), but this subject has not been explored in my research.

In order to solve theoretical problems which are not accessible analytically, the use of computers to perform numerical simulations of physical systems has become fundamental. Solving the set of equations (1.5), particularly in situations involving black hole spacetimes characterized by the presence of curvature singularities, has required decades of work to obtain long-term stable numerical frameworks, which culminated with the breakthrough accomplished in 2005-2006 where three different groups [Pretorius 2005, Campanelli et al. 2006, Baker et al. 2006] performed the first accurate and stable time evolutions of binary black hole (BBH) systems, using tools of numerical relativity (NR). While fairly mature after about six decades of continuous development, the field of NR is still expanding, and new generations of numerical relativists are undertaking new challenges to improve the simulations. In this thesis, as hinted in its title, I have extensively employed NR tools to study the physical systems discussed in the previous paragraphs.

Some of the main objectives of NR are to provide accurate GW templates to aid detections and make predictions, to better understand strong gravity and to possibly infer properties of matter at high densities as in NSs. The dawn of GW astronomy opens up an observational window which, combined with theoretical models and NR simulations, have already significantly broaden our understanding of the Cosmos. The first GW signal ever observed (GW150914) from the merger of a BBH was detected on September 14 2015 by the two advanced Laser Interferometer Gravitational-Wave Observatories (LIGO) [Abbott et al. 2016]. As of today, the Virgo and KAGRA (Kamioka Gravitational Wave Detector) Collaborations have joined the search, and three observing runs have been carried out identifying a total of 90 confident GW events [The LIGO Scientific Collaboration, the Virgo Collaboration, and the KAGRA Collaboration 2021]. Most of these events have been classified as BBH systems, while only two of them are binary NSs (BNS) [The LIGO Scientific Collaboration and the Virgo Collaboration 2017, The LIGO Scientific Collaboration and the Virgo Collaboration 2020], and three events of the last run are considered to be mixed neutron star-black hole systems [The LIGO Scientific Collaboration, the Virgo Collaboration, and the KAGRA Collaboration 2021]. In particular the BNS event GW170817 is associated with a short gamma-ray burst, GRB 170817A, detected 1.7 seconds after the GW merger signal. This momentous detection

triggered the long-anticipated birth of the so-called Multi-Messenger Astronomy with gravitational waves¹, in which the coordinated action of the LIGO-Virgo-KAGRA (LVK) Collaboration and dozens of astronomical facilities worldwide and in space attempt to find evidence of electromagnetic counterparts to the GW signals. This coordinated effort provides an extraordinary framework to investigate the state of matter in its extreme conditions and shed light on the equation of state of NSs. The generation of GW templates has been a major undertaking of my work. During my doctoral studies I have considered different dynamical scenarios involving BSs or bosonic fields interacting with baryonic matter, in which GW signals were emitted and I extracted and characterised those waveforms in detail.

As mentioned before, bosonic fields have become of increasing interest in astrophysics in recent decades, as viable candidates for DM. Moreover, the new observational channel opened by GW astronomy, along with other exciting possibilities as the one offered by the ground-breaking images of BH shadows recently reported by the Event Horizon Telescope Collaboration [Event Horizon Telescope Collaboration et al. 2019, Wielgus et al. 2022] might help in the future to unveil the true nature of this hypothetical form of matter and tighten the current constraints on the different candidates proposed, as well as helping shed some light on the existence of exotic compact objects. Numerical studies, such as those reported in this Thesis, are fundamental to understand the dynamical properties of exotic compact objects as BSs, and to discard or validate the various models in the literature.

1.2 Numerical Relativity

Numerical relativity emerged as an independent field of GR between the mid 1960s and mid 1970s, when pioneering works by Hahn and Lindquist [1964], Smarr et al. [1976] and Eppley [Eppley 1975, Eppley 1977] foresaw the importance of numerical simulations as theoretical laboratories for GR. The field improved dramatically during the 1980s-1990s and has now reached a state of maturity. All improvements in this field ran in parallel with the developments of advanced interferometric GW detectors. Nowadays NR plays an important role in LVK pipeline developments for detecting GWs, providing precise templates of waveforms from various astrophysical sources, most notably from compact binary coalescences, the only source detected so far thanks to the availability of GR

¹The actual birth of Multi-Messenger Astronomy can be identified with the supernova SN1987A, whose neutrino emission was detected at the Kamiokande-II detector.

and NR templates to implement matched-filtering searches. Detailed reviews on NR can be found in [Alcubierre 2008, Baumgarte and Shapiro 2003]

In 1962 Arnowitt, Deser and Misner presented a formulation of the Einstein equations which plays an important role in NR, which is known as ADM formalism [Witten 1962, Arnowitt, Deser, and Misner 2008]. This formulation is based on the so called 3 + 1 decomposition of Einstein's equations, introduced in the seminal works of Lichnerowicz [1944] and Fourès-Bruhat [1952], according to which the 4-dimensional spacetime is foliated into spatial hypersurfaces and the dynamical fields are components of the spatial metric γ^{ij} and their conjugated momenta π_{ij} . This formalism was well-suited for NR because it allows us to write the equations as a Cauchy problem (initial value problem) which can be solved numerically with methods that were already known in the community. A further step forward was the rewriting of the ADM equations accomplished by York [1979], which is the one that is commonly used in NR. Key aspects of this approach are the introduction of the extrinsic curvature K_{ij} as a dynamical field (which is related to the conjugated momenta of the metric) and the incorporation of one of the constraint equations (the Hamiltonian constraint) into one of the dynamical equations.

One of the first big challenges in NR was evolving BBH systems in order to provide numerical GW templates of such events. Simulations using the ADM formalism were found to be in general not stable. During the 90s, different rewriting of Einstein's equations, as the Bona-Massó [Bona and Massó 1989, Bona and Massó 1992, Bona et al. 1995], the Baumgarte-Shapiro-Shibata-Nakamura (BSSN) [Nakamura, Oohara, and Kojima 1987, Shibata and Nakamura 1995, Baumgarte and Shapiro 1999] and the Z4 [Bona et al. 2003, Bona et al. 2004] formulations, were developed and showed more stability than the original ADM. The key point of these formulations is the realization that the ADM equations were ill-posed and that this was causing the lack of stability in numerical codes. Consider a set of partial differential equations (PDEs)

$$\partial_t \vec{u} = P(D)\vec{u}, \quad (1.6)$$

where \vec{u} is a n -dimensional vector of variables which are function of time and space, and $P(D)$ is an $n \times n$ matrix whose components depend smoothly on partial differential operators. The system is *well-posed* if we can define a norm $\|\cdot\|$ such that

$$\|u(t, x)\| \leq K e^{\alpha t} \|u(0, x)\|, \quad (1.7)$$

where K and α are independent of the choice of the initial data $u(0, x)$. In other words, the norm of the solution at any time has to be bounded by the same

exponential, regardless of the initial data. This condition is very difficult to meet in practice for a generic system of PDEs. However, it can be shown that if a system of PDEs is strongly hyperbolic, it is also well-posed. A set of PDEs of the form

$$\vec{U}_t + A(x, t)\vec{U}_x = \vec{F}(x, t), \quad (1.8)$$

where the subscripts indicate derivative with respect to time and space, is strongly hyperbolic if the matrix $A(x, t)$ has real eigenvalues and if it exists a complete set of eigenvectors. Correspondingly, it is only weakly hyperbolic if there does not exist a complete set of eigenvectors. Fortunately showing that a system is strongly hyperbolic is much simpler than showing that the systems satisfies condition (1.7). For a detailed explanation on strong hyperbolicity and proof that it implies well-posedness, the interested reader is addressed to Section 5.3 of the review by Alcubierre [2008].

In this thesis I extensively employed the BSSN formulation to numerically evolve Einstein’s equations. While in three dimensions the ADM equations are only weakly-hyperbolic, this new formalism shows strong hyperbolicity, proving to be particularly robust in numerical evolutions. A crucial point in BSSN is the introduction of three auxiliary variables called “conformal connection functions” and the use of the momentum constraints to substitute a problematic term in the evolution equations of these new variables. This modification ensures stability due to the fact that it modifies the principal part of the equations, guaranteeing strong hyperbolicity.

In some of the studies presented in this manuscript I considered three-dimensional Cartesian coordinates, for which I used the numerical framework `EINSTEINTOOLKIT` [Babiuc-Hamilton et al. 2019, Löffler et al. 2012, Zilhão and Löffler 2013], employing, in particular, the `MCLACHLAN` infrastructure [Reisswig et al. 2011, Brown et al. 2009] which implements the BSSN formulation of Einstein’s equations for evolving the spacetime variables. In our group we have extensively used private *thorns*, mainly developed by Nicolas Sanchis-Gual, that implement the Klein-Gordon and Proca evolution equations, in order to study the dynamics of BSs and fermion-boson stars, or scalar fields and vector fields in general. Our thorns are based on the ones available in the public repository `CANUDA` [Witek et al. 2021].

For those works on fermion-boson stars based on simulations in spherical symmetry, I employed `NADA1D`, a NR code which is available in our group and which was originally developed by Pedro Montero and Isabel Cordero-Carrión [Montero and Cordero-Carrión 2012]. This code was originally presented

in its two-dimensional version in [Montero, Font, and Shibata 2008]. They implemented Brown’s covariant formulation of the BSSN equations [Brown 2009] which is well-suited for curvilinear coordinate systems. Moreover they adopted a partially implicit Runge-Kutta (PIRK) method, proposed by Cordero-Carrión, Cerdá-Durán, and Ibáñez [2012] in the Fully Constrained formulation of Einstein equations, to treat problematic $1/r$ terms that appears in the evolution equations in spherical coordinates. This method allows to perform stable numerical simulations of both vacuum and non-vacuum spacetimes without the need of a regularization algorithm at the origin. This numerical code has been upgraded to evolve a real or complex scalar field by Sanchis-Gual et al. [2015]. In my Master thesis work, I instead upgraded the code implementing the Proca evolution equations to perform simulations of the dynamical formation of Proca stars [Di Giovanni et al. 2018].

1.3 Nonlinear dynamics of Boson stars and Proca stars

1.3.1 Spinning bosonic stars

In Section 1.1, the exotic compact objects known as BSs were introduced. BSs are horizonless, soliton-like, everywhere non-singular, stationary solutions of the EKG and Einstein-Proca system for a complex scalar field or vector field, respectively. In order to be considered true viable candidate for astrophysical objects, bosonic stars have to fulfill a number of requirements: *(i)* appear in well motivated and consistent physical theories (such as GR); *(ii)* be stable against sufficiently small disturbances; *(iii)* and have a dynamical formation mechanism. The last two points on this list define the concept of dynamical robustness [Herdeiro 2022].

The dynamical fate of scalar BSs in spherical symmetry has been deeply investigated using both linear perturbation theory [Gleiser and Watkins 1989, Lee and Pang 1989] and fully nonlinear numerical simulations [Seidel and Suen 1990, Balakrishna, Seidel, and Suen 1998, Guzman 2004, Guzmán 2009]. As for fermionic stars, BSs show a stable and an unstable branch, which can be identified through the critical point analysis. One can generate a sequence of solutions which depends on the central value of the scalar field ϕ_c and look at the critical value at which the equilibrium configuration shows the maximum value for the ADM mass, which for “mini-boson stars” (those having only quadratic term in the potential) correspond to $M_{\max} \approx 0.633 M_{\text{Planck}}^2 / \mu$, as reported in [Seidel

and Suen 1990]. Colpi, Shapiro, and Wasserman [1986] considered models with a quartic self-interaction term in the potential, and showed numerically that $M_{\max} \approx 0.22\Lambda^{1/2}M_{\text{Planck}}^2/\mu$, with Λ the self-interaction parameter. Other potentials have been proposed, such as the solitonic [Friedberg, Lee, and Pang 1987], the KKLS [Kleihaus, Kunz, and List 2005, Kleihaus et al. 2008], or the axionic [Guerra, Macedo, and Pani 2019] potentials. Seidel and Suen [1990] showed through nonlinear numerical simulations that the fate of an unstable BS under small perturbations produced by the numerical truncation error is either the collapse to a black hole, or the migration to the stable branch. Further studies [Seidel and Suen 1990, Balakrishna, Seidel, and Suen 1998, Guzman 2004, Guzmán 2009] established that unstable BSs can also face the total dispersion of the scalar field, a fate which only happens for bosonic matter and which is not possible for fermionic stars. Seidel and Suen [1994] also proposed a formation mechanism, which they called gravitational cooling, through which a cloud of scalar bosonic matter condensates and forms a compact object which approaches a stationary configuration by radiating away the exceeding scalar field.

Moreover, vector boson stars, or *Proca stars*, have been recently found as stationary solutions of the Einstein-Proca system by Brito et al. [2016b]. In spherical symmetry these new solutions resemble in many aspects their scalar cousins. They show a stable and unstable branch, which was confirmed by nonlinear numerical evolutions by Sanchis-Gual et al. [2017], at a maximum mass which is slightly larger than that of scalar BSs, specifically $M_{\max} \approx 1.058M_{\text{Planck}}^2/\mu$. During my master thesis work, I showed that Proca stars can also form dynamically from a cloud of vector bosonic matter through the mechanism of gravitational cooling [Di Giovanni et al. 2018], as happens for the scalar case.

Spinning BS solutions have been obtained both for the scalar case by Yoshida and Eriguchi [1997], Herdeiro and Radu [2014], and Herdeiro and Radu [2015] and for a vector field by Herdeiro, Radu, and Rúnarsson [2016]. One could expect that the dynamical properties of these solutions show similarities to the spherically symmetric case, where a stable branch can always be identified. In Sanchis-Gual et al. [2019a], we performed fully nonlinear numerical evolutions of stationary solutions of spinning BSs and Proca stars, and dynamical formation from a cloud of bosonic matter with non-zero angular momentum. Our results revealed that spinning scalar BSs are all unstable due to the development of a non-axisymmetric dynamical instability which causes the loss of all the angular momentum, the decay to the a non-spinning solution, and the reshape of the star from a toroidal to a spheroidal morphology. Spinning Proca stars, which

already have a spheroidal shape, do not suffer this type of instability and a stable branch could be pinpointed, at least up to the appearance of a light ring for ultra-compact Proca stars [Cunha et al. 2022]. My main contribution to this investigation was the construction of constraint-satisfying initial data for the clouds of rotating bosonic matter, and studying the dynamical formation of the resulting compact stars, where we observed the same fate for the scalar and vector stars as in the evolutions of equilibrium configurations. The initial data was obtained making use of a numerical code developed by Pablo Cerdá-Durán, which uses the extended conformally flat approximation (XCFC) to rewrite the Einstein constraints, and solves the set of elliptic equations with different numerical methods. Further details on the formalism can be found in Cordero-Carrión et al. [2009] and details on the construction of the initial data for bosonic fields can be found in the appendix of Sanchis-Gual et al. [2019a]. Furthermore, in Di Giovanni et al. [2020a] I extended these results, taking into account self-interaction terms in the potential of the scalar field, and studying in a more quantitative way the instability. I identified the $m = 2$ mode as the dominant mode of the instability and compared the results with certain models of differentially rotating NSs, which also suffer from the $m = 2$ bar-mode instability. Moreover I extracted the GW signal produced by the non-axisymmetric deformation of the stars, evaluated its characteristic strain h_{char} and the signal-to-noise ratio (SNR) averaged on all the angular orientations of the source and for optimally-oriented detectors at different distances. Those include ground-based detectors (Advanced LIGO, Advanced Virgo, KAGRA, Einstein Telescope), the future space-based detector LISA, and Pulsar Timing Arrays (PTAs). Recently, Siemonsen and East [2021] have shown through numerical evolutions that considering self-interaction terms in the scalar-field potential can quench the non-axisymmetric instability in some restricted regions of the parameter space, delineating an island of stability also for scalar BSs.

In Sanchis-Gual et al. [2021] we extended the landscape of spinning bosonic star solutions by considering multiple fields either with the same or possibly with different frequencies. We refer to these new solutions as *multifield*, *multifrequency bosonic stars*. Particular configurations, members of this extended family, are ℓ -boson stars, which are solutions introduced by Alcubierre et al. [2018]. These are a composite of an arbitrary odd number ($2\ell + 1, \ell \in \mathbb{N}_0$) of equal-frequency complex scalar fields whose angular dependence is given by the spherical harmonics $Y_{\ell,m}$, with the same amplitude. It can be shown that the total stress-energy momentum tensor is spherically symmetric, even if the individual fields are not. The new models investigated in [Sanchis-Gual et al.

2021] extend the family by considering different amplitudes and frequencies for the various fields, thus breaking spherical symmetry. Moreover, models with different individual eigenfrequencies of the fields are also considered.

1.3.2 Head-on collisions and orbital mergers

The first numerical evolutions of head-on collisions and orbital mergers of scalar mini-BSs were performed by Palenzuela et al. [2007] and Palenzuela, Lehner, and Liebling [2008]. These works were extended in [Bezares, Palenzuela, and Bona 2017, Palenzuela et al. 2017, Bezares and Palenzuela 2018] by considering more compact models of BSs with a solitonic potential, and by taking pair of stars composed by two independent scalar fields which do not interact directly with each other, only through gravity. Interestingly in all these works they could not obtain a spinning BS as the remnant of the orbital mergers. This result could be explained taking into account our findings on the non-axisymmetric instabilities scalar BSs develop. In Sanchis-Gual et al. [2019b] we studied head-on collisions and orbital mergers of Proca stars. As it was done for scalar stars, we considered initial data which is a superposition of two spherically symmetric Proca stars at a certain distance, which are then boosted in a direction orthogonal to the segment connecting the two objects to impose an initial orbital motion. Our results showed that the outcome of orbital mergers is either a Proca star or a Kerr black hole surrounded by a cloud of quasi-bound Proca field. In the former case, despite the Proca star has initially angular momentum, this is lost as the star approaches equilibrium. Spinning Proca stars can be stable, for which it would be necessary to study these results more in details. Furthermore, we investigated the GW signals emitted in both the head-on collisions and the orbital mergers, comparing them with those of two Schwarzschild black holes. Our results showed that in the case of Proca stars, one can sometimes distinguish the signal from that of black holes due to the presence of an intermediate phase during which a hypermassive Proca star forms before collapsing to a black hole. Moreover, the quasi-normal modes of the remnant can differ from those of an isolated black hole if it is instead surrounded by a sufficiently extended and long-lived Proca cloud.

One of the possible outcomes of bosonic stars mergers is a rotating black hole surrounded by a cloud of bosonic field. Rotating black holes, which are described by the Kerr family of solutions, have the feature that part of their energy can be extracted through its interaction with an incoming bosonic wave. This process is known as *superradiance* [Brito, Cardoso, and Pani 2015]. For

this process to occur it is required that the wave fulfills the condition

$$\omega < m\Omega_{\text{BH}}, \quad (1.9)$$

where ω is the frequency, m is the azimuthal number of the wave, and Ω_{BH} is the angular velocity of the black hole. When this condition is fulfilled, the bosonic wave grows exponentially extracting energy from the black hole, in the form of its angular momentum (or its charge in the case of Reissner-Nordström black holes), up to the point when the angular velocity of the spun-down black hole is synchronised with the frequency of the field, i.e. $\omega = m\Omega_{\text{BH}}$. In general, for real and complex bosonic fields, the black holes with bosonic cloud that fulfill this last condition are called synchronised gravitational atoms (SGAs). In the case of complex fields they fall into the category of “hairy” black holes, as the ones found by Herdeiro and Radu [2014] and Herdeiro, Radu, and Rúnarsson [2016].

In Sanchis-Gual et al. [2020] we further studied the binary BSs dynamics focussing on the outcome of orbital mergers, or head-on collisions of spinning Proca stars, to investigate a possible alternative channel to that of superradiance to form dynamically SGAs or hairy black holes. In the case of superradiance the bosonic field spins down the black hole until saturation. It has been shown that a universal thermodynamical limit imposes that the bosonic cloud cannot extract more than 29% of the final BH-cloud energy (see Brito, Cardoso, and Pani [2015]). However, numerical simulations by East and Pretorius [2017] were able to reach only a maximum of 9%, and the analytic analysis by Herdeiro, Radu, and Santos [2022] have shown that the actual limit might be around 10%. In this new channel the remnant of the merger can be a black hole with a bosonic cloud that accretes into it, spinning it up, and approaching the synchronisation condition from the other side. Moreover, we could form SGAs where the cloud stores up to around 18% of the energy, and there is no theoretical bound. In order to obtain this 2-step formation channel the initial data must be fine-tuned, and the most common scenario is instead a 3-step formation mechanism where a BH forms, spins-up due to accretion from the cloud, and then it spins-down due to superradiance, finally reaching the synchronisation. Another interesting result of this work was that we could form higher azimuthal modes for the synchronised cloud ($m = 5, 6$), while with superradiance one can only obtain the $m = 1$ faster-growing mode with numerical simulations so far.

1.4 Stationary solutions and dynamics of fermion-boson stars

As introduced in Section 1.1, fermionic stars such as NSs or white dwarfs can accrete particle DM and result in what is generally known as DM admixed NSs (or white dwarfs). Equilibrium configurations of stars made of fermions and bosons were found for the first time by Henriques, Liddle, and Moorhouse [1989] and Henriques, Liddle, and Moorhouse [1990]. Their linear stability was studied in Henriques, Liddle, and Moorhouse [1990] and in Jetzer [1990]. In the simplest models, the bosonic component only interacts with the fermionic one via the gravitational field, which is consistent with the idea of bosonic DM coupling only gravitationally with the visible one. More recently the interest in these configurations has grown, especially due to the new observational channel offered by GW astronomy and the new experiments which try to evaluate with more precision the NS internal composition such as NICER [Gendreau et al. 2016] and XMM-Newton [Barré, Nye, and Janin 1999]. New theoretical works extended the early results found by Henriques and collaborators: Brito, Cardoso, and Okawa [2015] studied the dynamical capture of bosonic DM by NSs using perturbative techniques and nonlinear NR simulations, subsequently extended in Brito et al. [2016a]; Valdez-Alvarado et al. [2013] constructed equilibrium configurations of fermion-boson stars with the simple mini-BSs potential and studied their linear stability through the method developed by Henriquez and the nonlinear stability via NR evolutions. This work was later extended to the self-interaction potential in Valdez-Alvarado, Becerril, and López [2020].

During my doctorate work, I have contributed to this field of research with several publications. This new line of my research work began in 2019, when I spent one month at the Universidad Autónoma de México (UNAM) in Cuernavaca, and I started a scientific collaboration with Professor Juan Carlos Degollado with the aim of studying the dynamical formation of fermion-boson stars via the accretion of a bosonic cloud onto an already-formed NS, using NR techniques. In the same period a visiting PhD student from the University of Teheran (Iran), Saeed Fakhry, spent a semester visiting our group to learn about NR and start a collaboration. We combined our efforts to write a numerical code to solve the set of ordinary differential equations whose static solutions describe fermion-boson stars with a bosonic potential which includes a self-interaction term. In [Di Giovanni et al. 2020b] we constructed equilibrium configurations populating the existence domain for different values of the self-interaction parameter Λ , and studied the linear stability and the fully nonlinear

evolutions using the numerical code NADA1D. Moreover, as commented, we verified that fermion-boson stars can form through dynamical accretion of bosonic matter via the mechanism of gravitational cooling.

In this first work, we found an interesting result. One of the dynamical formation models showed as a final outcome a fermion-boson star with the scalar field oscillating around an equilibrium configuration with one radial node. Mini-BSs excited-state solutions which show one or more radial nodes exist but they have been shown to be unstable in the nonlinear regime as reported in Lee and Pang [1989] and Balakrishna, Seidel, and Suen [1998]. It was recently shown that a quartic self-interaction term in the potential can stabilise excited states [Sanchis-Gual et al. 2022]. Bernal et al. [2010] found that an excited scalar field can be stabilised by another co-existing bosonic field in the ground state, under the condition that the occupation number N_B of the ground-state field is larger than that of the excited one. Motivated by this result and by our previous finding, we explored in Di Giovanni et al. [2021] the stability of excited fermion-boson stars. We populated the domain of existence with models with one radial node for three different values of Λ and performed hundreds of numerical evolutions to delineate empirically the supposed stability region. If a stability island exists it must have been in a neighbourhood of the stable NS branch. This expectation was confirmed by our results. Moreover, we performed several new simulations of dynamical formation, finding that even configurations with more than one radial node were dynamically robust. We observed that after the accretion of the scalar field, the perturbed final object was oscillating around different equilibrium configurations with zero, one, or more nodes. We confirmed this finding by evaluating the Fourier transform of the scalar field in the late-part of the evolution, finding that more frequencies were excited which correspond to static solutions with different number of nodes and same number of bosonic and fermionic particles. Moving beyond spherical symmetry and non-spinning solutions, we showed that having a multifield BSs with a stable star component could also stabilise unstable spinning scalar mini-BSs prone to bar-mode instabilities and dipolar BSs. I will further discuss these results in Sec. 2.1.

Motivated by the results on the stabilisation mechanism for an excited scalar field and spinning BSs, we investigated if a stable scalar or vector field could have the same effect and quench dynamical instabilities suffered by certain models of rotating NSs (for reviews, see Glampedakis and Gualtieri [2018] and Paschalidis and Stergioulas [2017]). Configurations of NSs with differential rotation and high value of $\beta \equiv T/W$, T being the kinetic energy and W the

gravitational potential energy, are known to suffer an $m = 2$ instability called the bar-mode instability [Shibata and Uryū 2000, Baiotti et al. 2007]. In our study [Di Giovanni et al. 2022] we considered initial data which described a model of highly differentially rotating NS, surrounded by a bosonic cloud, either comprised of a scalar or a vector field, which rapidly accretes onto the fermionic star and approaches an equilibrium mixed configuration. As the dynamical timescale of the accretion is lower than that of the development of the bar-mode instability, it is possible to observe the effects of the bosonic field in the dynamics. We considered various models of rotating NS, and showed the results of the one which had the highest value of β . We investigated the effect of clouds of scalar bosonic matter with three different values of the particle mass μ and also focused on one particular value of μ but considered different total mass stored in the initial cloud. This latter approach revealed how the presence of a larger amount of bosonic matter causes the damping of the $m = 2$ mode of the individual fermionic matter content, but not the complete suppression of the instability. An $m = 2$ mode of the total energy (bosonic and fermionic) is in fact excited, showing the appearance of what we defined as a “mixed” bar. Finally, we extracted the GW emission from the instability of the isolated NS and compared it with that from the models with bosonic field, unveiling the appearance of higher frequencies in the signal, coming from overtones of both the bar-mode instability and quasi-radial oscillations of the object. We also provided an estimation of the SNR from these signals at a distance of 10 kpc for a variety of ground-base detectors and we evaluated the horizon distance, which is the distance at which $SNR = 8$ and provides an estimation of the maximum distance at which the signal is expected to be detected.

Recently it has been possible to determine accurately both the mass and the radius of two NSs. Bayesian inference on pulse-profile modelling of observations from NICER of the X-ray millisecond pulsar PSR J0030+0451, yielded values of $M \sim 1.5M_{\odot}$ and circumferential radius $R \sim 13km$ [Miller et al. 2019, Riley et al. 2019]. From the combined data from NICER and XMM-Newton of PSR J0740+6620 [Riley et al. 2021, Miller et al. 2021], the most-massive known pulsar, these teams inferred values of $M \sim 2.08M_{\odot}$ and $R \sim 13km$. These two results together challenge theoretical models of the interior of NSs, requiring a very stiff equation of state (EoS). GW observations of NS binary systems have also set constraints on the NS mass and radius, adding more tension in the measurements. Moreover, from the parameter estimation of the event GW190814, the LVK collaboration inferred the value of the mass of the secondary component of $\sim 2.50 - 2.67M_{\odot}$, which raises doubts on the nature of this object, either being

the lightest black hole ever observed or the heaviest NS, or an exotic compact object. In Di Giovanni et al. [2022] we investigated how fermion-boson star models with realistic EoSs could mitigate the tension in these measurements. We considered for the NS component three different EoS which fit (or marginally fit) at least part of the observational results, and we constructed sequences of solutions with fixed bosonic contribution which in some cases were more compatible with the multi-messenger observational data than isolated NSs. Furthermore, we considered for this study two different values of the mass parameter μ of the scalar field, namely $\hbar\mu = \{1.34 \times 10^{-11}, 1.34 \times 10^{-10}\}$ eV.

Finally, in Di Giovanni et al. [2022] we found equilibrium configurations of novel solutions of fermion-boson stars with the axionic potential and studied their stability properties. This periodic potential was introduced by Guerra, Macedo, and Pani [2019] and it is inspired by that of the QCD axion introduced by Peccei and Quinn [1977] to solve the strong CP problem in fundamental physics. Its peculiarity is that, depending on the value of the decay parameter f_a , axion boson stars show one or more stable branches in their domain of existence. As a consequence, in the fermion-axion stars two-dimensional parameter space we could identify with the linear stability analysis one or more islands of stability. We focussed our study on the models with the value of $\log_{10}(f_a) = -1.7$ which shows two islands of stability, and confirmed the results of the linear analysis performing nonlinear numerical evolutions, mapping the domain of existence and obtaining the three different fates for the unstable models: part of them collapse to a Schwarzschild black hole, others migrate to a stable configuration, and in a small region of the parameter space the solutions face the total dispersion of the scalar field.

The numerical code I used during my thesis to find stationary solutions describing fermion-boson stars was originally developed by myself and Saeed Fakhry. This code have been upgraded and polished with the collaboration of Simone Albanesi, Davide Guerra and Miquel Miravet-Tenés. Furthermore, with these same collaborators, we wrote an additional code which identifies level curves of a generic numerical function and we used it to find equal-mass curves in the existence domain of fermion-axion stars. This new tool was extremely useful to determine the stability islands and it is described in appendix A of Di Giovanni et al. [2022]. The code can be found in the public git repository at <https://github.com/SimoneA96/fermion-axion-pywrap>.

1.5 The Virgo Collaboration

The Virgo Collaboration formed in 1993 with the aim of building an European GW detector. A first version of such detector was built in 2003, followed by major upgrades which culminated into the Advanced Virgo detector. From 2007 the Virgo Collaboration and the LIGO Scientific Collaboration signed an MoU to jointly analyse the data and jointly publish the results. As of today three Observing Runs have been carried out by the Advanced detectors, and 90 confident GW events have been identified. At the end of the last Observing Run, the Japanese KAGRA detector joined the collaboration, and at the moment new upgrades of the three detectors are ongoing, and a fourth Observing Run is expected to start in March 2023. In July 2016 the Valencia Virgo Group joined the Virgo Collaboration, and from the start of my doctorate studies in 2018 I have been member of this group. My work within the collaboration involves mostly GW modelling of exotic compact objects and I also participate in several *service work* activities.

I modelled the GW signal emitted in various physical systems. In Di Giovanni et al. [2020a] I studied the GW emission generated by the non-axisymmetric bar-mode instability of spinning bosonic stars, evaluating the characteristic strain of the signal and the horizon distance for several detectors. Moreover, we gave an estimation of the timescale of the emitted GW by evaluating the characteristic damping timescale in which the bar-like deformation is dissipated, finding that this type of signal could potentially be a continuous-wave source. We performed a similar analysis also in Di Giovanni et al. [2022] for rotating NS models surrounded by bosonic clouds. In Sanchis-Gual et al. [2019b] we instead characterised for the first time GW signals from head-on collisions and orbital mergers of Proca stars, comparing them with black holes of same component masses. Finally in Di Giovanni et al. [2022], I depicted mass-radius diagrams for NSs with a bosonic component, and used these exotic models to better fit the posterior distribution from the BNS event GW170817, and also to give a possible theoretical explanation for the $2.6M_{\odot}$ secondary object of the GW190814 event. All these results have been presented in internal calls of the LVK Collaboration to the rest of the collaboration.

Apart from the research work directly related to my thesis project, I participated to *service work* activities. In February 2020 I served for a week as a Detector Characterization shifter for the Virgo detector, which involves supervising the status of the detector during the day-time, and help expert people to characterise possible sources of noise and glitches in the interferometer. In

2021 I was involved in the paper writing team of one of the LVK Collaboration papers on searches of GW signals from sub-solar mass compact objects during the first half of the third observing run O3a [Abbott et al. 2022].

Chapter 2

Discussion

2.1 Boson stars, Proca stars, and gravitational waves

Around half of the research work presented in this Thesis deals with the numerical investigation of the dynamical features of scalar BSs and Proca stars. I considered physical systems that do not assume spherical symmetry or axisymmetry, in order to inspect the GW emission in different dynamical scenarios involving these exotic compact objects. Firstly, I have contributed to a series of works where we have studied the nonlinear stability of spinning bosonic stars and enlarged the family of solutions with configurations having more than one field with same or different frequencies. Secondly, I have inspected the GW emission from a number of physical systems involving such objects.

The linear and nonlinear stability of spherically symmetric BSs and Proca stars have been extensively investigated. Solutions of spinning axisymmetric bosonic stars have been found by Herdeiro and Radu [2014] and by Herdeiro, Radu, and Rúnarsson [2016] for the scalar and vector case respectively, but an investigation on their stability properties was missing. Naively we could expect that a stable branch exists for these objects, as it happens for the spherically symmetric case or for NSs. We performed for the first time NR evolutions of spinning bosonic stars in Sanchis-Gual et al. [2019a], aiming to answer two different questions about their dynamics: *(i)* are spinning bosonic stars stable under nonlinear perturbations? And *(ii)* can they form dynamically from a generic cloud of bosonic particles with non-zero angular momentum? As for the first question, we considered various initial configurations of already-formed stars

and evolved them under the weak perturbation generated by the discretization error of the numerical grid. For the formation scenario we instead studied constraint-solving initial data describing a dilute, axisymmetric cloud of bosonic matter with non-zero angular momentum, which collapses towards a spinning bosonic star, expelling exceeding energy and angular momentum through the gravitational cooling mechanism.

Interestingly, our findings showed that all considered models of spinning scalar mini-BSs suffer from a non-axisymmetric instability, which causes the reshaping of the object from a toroidal to a spheroidal morphology via a fragmentation phase, and the loss of all the angular momentum stored in the cloud. The final state of this process seems to be approaching a spherically-symmetric non-spinning BS. On the contrary, Proca stars are exempt from this fate, at least for the $m = 1$ family of solutions, and a stable branch could be identified. We tentatively attributed this contrast with the different morphology of the scalar and vector stars, supported by the analogy with instabilities found in differentially rotating NSs which show a quasi-toroidal shape [Paschalidis and Stergioulas 2017]. It is worth commenting that in a more recent study by Siemonsen and East [2021], the authors found that a self-interaction term in the potential seems to quench this instability in a restricted area of the parameter space, which means that some toroidal configurations could be nevertheless stable.

In a following paper [Di Giovanni et al. 2020a], we examined more deeply the instabilities of these exotic objects in the context of their dynamical formation. Firstly, I considered scalar field clouds with quartic self-interaction to assess if this different potential could affect the instability. Our findings showed that it was not possible to damp the instability with several values of the self-interaction potential. This result is still in agreement with what Siemonsen and East [2021] found, as we did not cover the part of the parameter space where they found stable models. Secondly, we investigated spinning Proca stars members of the $m = 2$ family of solutions, which show a toroidal shape, and we found that all the models undergo bar-mode instability, as we expected from our reasoning on the toroidal morphology of these objects. Finally, we showed that unstable bosonic stars exhibit a corotation point, which establish a parallelism with low $T/|W|$ differentially rotating NS models [Watts, Andersson, and Jones 2005, Cerdá-Durán, Quilis, and Font 2007]. This is the radius where the angular frequency of the unstable $m = 2$ mode matches the local angular velocity of the fluid, defined as $\Omega = j^\phi/\rho_e$, where j^ϕ is the ϕ -component of the bosonic matter current, and ρ_e is the bosonic energy density.

In Sanchis-Gual et al. [2021] we reported novel solutions of spinning bosonic stars, which are obtained by combining an odd number $N = (2\ell + 1)$ of complex fields with a single or different frequencies. A particular member of this family are ℓ -boson stars [Alcubierre et al. 2018]. Our results show that for the scalar case only ℓ -boson stars are stable. We then considered hybrid solutions where a stable $\ell = m = 0$ spherically-symmetric configuration with sufficient energy is combined with an unstable $\ell = 1, m = \pm 1, 0$ field, and we found through NR evolutions that a stabilisation mechanism was allowing the overall solution to be stable in the nonlinear regime.

Finally, I inspected the GW emission from a number of physical systems involving bosonic stars. Part of the research published in Di Giovanni et al. [2020a] dealt with the analysis of the GWs emitted by spinning BSs as a result of their non-axisymmetric deformations and the decay to non-spinning configurations. We compared the characteristic strain of the signal for some representative models with the sensitivity curves of current detectors (Advanced LIGO, Advanced Virgo and KAGRA), the 3rd-generation detector Einstein Telescope, and space missions such as LISA and PTAs. Our analysis revealed that GWs from stellar-size BSs in the $1 - 100M_{\odot}$ mass range might be detected by current detectors up to a few Mpc, while the range increases up to 10 Mpc for the Einstein Telescope. LISA could instead observe sources in the $10^4 - 10^6M_{\odot}$ range up to few Gpc, and PTAs in the range $10^9 - 10^{11}M_{\odot}$ up to a redshift ≈ 100 . Moreover, as the bar-like deformation is dissipated only through GW emission, the signal can last long. If spinning BSs existed in Nature, they could be a potentially interesting source of continuous GWs and the theoretical estimates we found could shed light on the existence of these exotic objects, or set constraints on the mass of the bosonic particle.

2.2 Nonlinear interactions between bosonic fields and fermionic stars

A relevant part of my research was devoted to investigate the gravitational interactions between bosonic fields, as DM candidates, and fermionic stars as NSs and white dwarfs. As I reported in the introduction, fermion-boson stars are hypothetical exotic objects which are composed by a mixture of fermionic and bosonic particles. Studying the nature of such configurations is of interest for their potential observational implications. My series of publications on the subject [Di Giovanni et al. 2020b, Di Giovanni et al. 2021, Di Giovanni et al.

2022, Di Giovanni et al. 2022] complement and extend previous studies. In my first work [Di Giovanni et al. 2020b], I extended the previous characterizations of spherically-symmetric fermion-boson stars by considering a quartic self-interaction term in the potential and studying the dynamical formation scenario through the accretion of bosonic field from a scalar cloud onto an already-formed NS. For one of the models considered the dynamical formation revealed the presence of a radial node in the scalar field. This is an intriguing result as configurations of scalar field with node(s) are considered to be unstable, and it hinted to the hypothesis that the fermionic star could stabilise an otherwise unstable bosonic field when considered in isolation. A natural continuation of this investigation was carried out in Di Giovanni et al. [2021] where we constructed equilibrium configurations of fermion-boson stars with the scalar field in an excited state with one radial node. The nonlinear stability analysis, performed by means of hundreds of numerical evolutions, showed evidence of the existence of a limited region in the parameter space where stable excited fermion-boson stars exist. This finding, together with several other dynamical formation simulations where we observed the presence of one or more nodes, supported the existence of a stabilisation mechanism. In Di Giovanni et al. [2022] I showed that the additional degrees of freedom provided by the presence of a bosonic component in NS could play a role in the determination of masses and radii of NSs with consequences in the interpretation of the measurements from the NICER and XMM-Newton experiments, and from the LVK GW observations. I also discussed two different astrophysical scenarios in which fermion-boson stars can form: *(i)* the bosonic field is captured during the formation of the stars from a primordial gas, mixture of bosons and fermions, which leads to an approximately universal bosonic-to-fermionic particle ratio; *(ii)* the bosonic matter is captured by already-formed compact objects like white dwarfs or NSs, which leads to a bosonic-to-fermionic ratio which depends on the age of the observed NS.

Finally, I made a first step in the study of fermion-boson stars with rotation, analysing the impact of bosonic DM which accretes onto highly differentially rotating NSs. The aim of this work was to check if it was possible to stabilise NS models which suffer from the bar-mode instability by adding bosonic matter into the system. This would have had major impact because the deformations induced by the instabilities in rotating NSs are considered to be valuable sources of gravitational waves. Our findings showed that the presence of even a high percentage of DM is not enough to quench completely the instabilities which affect differentially rotating NSs. Nonetheless we showed that the GW emission

is influenced by the presence of bosonic fields and that this could have potential consequences in the observations. In particular we found that the characteristic frequency peaks of the signal are influenced and excited modes are enhanced when a scalar or vector field is included in the system.

Chapter 3

Outlook

All the results presented in this Thesis and the publications that have resulted thereof have contributed to extend previous investigations on the role bosonic fields might play in astrophysics. There are several ways in which the lines of research I have carried out during my doctorate studies can be broaden. I am currently involved in a few projects which go in this direction, while some others could be pursued in the future.

First of all, I am currently involved in a collaboration with Dr. Miguel Bezares and Nicola Franchini in an extension of the results from my previous publication [Di Giovanni et al. 2022]. In this work we have compared curves in the mass-radius diagram for fermion-boson stars with tabulated EoS with the posterior distribution for the mass and radius of GW170817. While the estimation for the component masses of the binary only depend on the structure of the considered object at 5PN order in the waveform models, the estimation of the radius is indirect, as the actual parameter measured is the quadrupole tidal deformability, and it depends on assumptions on the nature of the component objects in the binary. To perform a proper analysis, we should have evaluated the tidal deformability Λ for fermion-boson stars and compared the results with the observed data in the mass- Λ plot. This new collaboration aims to use a numerical code developed by Nicola Franchini to evaluate the tidal deformability of my models of fermion-boson stars and obtain a more robust analysis.

In a second project I am collaborating with Davide Guerra and Nicolas Sanchis-Gual to perform head-on collisions of fermion-boson stars to analyse the dynamics of these events and the gravitational waves emitted.

During my doctorate studies I have also been involved in the project of generating constraint-satisfying initial data for binary systems of bosonic stars.

This would be an important achievement for our group as we are involved in several investigations, such as [Sanchis-Gual et al. 2022, Calderon Bustillo et al. 2022b, Calderon Bustillo et al. 2022a], related to head-on collisions and orbital mergers of Proca stars and we have a long-term aim to build a catalog of gravitational wave signals from this class of events. At the moment the construction of such initial data is still under development, even though I have made steps towards the accomplishment of this objective.

One interesting direction to continue the study of the gravitational interactions between bosonic DM and fermionic stars is to obtain equilibrium configurations for spinning fermion-boson stars. This would be an important step that would allow an extensive analysis of the dynamics of such objects and it would give insight on how NSs are affected when they live in a rich DM environment. I made a first step in the analysis of the effects of bosonic fields on the bar-mode instability of highly differentially rotating NSs but this study can be better analysed if initial data describing stationary solutions were available. Moreover, other models of fermionic stars which suffer dynamical instabilities, like the low $T/|W|$ differentially-rotating NSs, should be analysed, as the presence of DM could make the corotation point inside such stars disappear, thus killing the instability.

Finally, another possible future project would be to construct stationary solutions of fermion-Proca stars, a mixture of fermionic and a vector bosonic field. Even though Proca star solutions have been already constructed and their stability has been investigated, at the moment there are no studies related to fermion-Proca stars. Moreover, recently vector field have become of certain interest for various reasons: *(i)* the superradiance instability of massive vector fields around black holes cause significantly stronger GW emission, and the growth rate of the instability is faster than in the scalar case [East and Pretorius 2017, East 2017, Siemonsen and East 2020]; *(ii)* head-on collisions of Proca stars have been considered as a possible alternative to quasi-circular, precessing BBH mergers to explain the LVK event GW190521 [Bustillo et al. 2021].

Part II

Appendices


Appendix A

Publications

The format of the present doctoral thesis as a compendium of publications requires the permission from the corresponding publishers. Permission to re-use published material was obtained from all journals.

- Copyright credit to Physical Review D and Physical Review Letters, whose publisher is the ©American Physical Society.
- Copyright credit to Classical and Quantum Gravity, whose publisher is ©IOP Publishing.

The paper [Di Giovanni et al. 2021] was added in the Appendix of this Thesis in its Preprint version. The rights to upload in online repositories of the final published version belong to IOP Publishing. The paper [Di Giovanni et al. 2022] was added in its Preprint version, as the paper is not yet published but it is accepted by the Journal Physical Review D.

Head-on collisions and orbital mergers of Proca starsNicolas Sanchis-Gual,¹ Carlos Herdeiro,^{2,3} José A. Font,^{1,4} Eugen Radu,² and Fabrizio Di Giovanni¹¹*Departamento de Astronomía y Astrofísica, Universitat de València, Dr. Moliner 50, 46100, Burjassot (València), Spain*²*Departamento de Física da Universidade de Aveiro and Centre for Research and Development in Mathematics and Applications (CIDMA), Campus de Santiago, 3810-183 Aveiro, Portugal*³*Centro de Astrofísica e Gravitação—CENTRA, Departamento de Física, Instituto Superior Técnico—IST, Universidade de Lisboa—UL, Avenida Rovisco Pais 1, 1049-001, Portugal*⁴*Observatori Astronòmic, Universitat de València, C/ Catedrático José Beltrán 2, 46980, Paterna (València), Spain* (Received 25 June 2018; revised manuscript received 21 December 2018; published 11 January 2019)

Proca stars, *aka* vector boson stars, are self-gravitating Bose-Einstein condensates obtained as numerical stationary solutions of the Einstein-(complex)-Proca system. These solitonic objects can achieve a compactness comparable to that of black holes, thus yielding an example of a black hole mimicker, which, moreover, can be both stable and form dynamically from generic initial data by the mechanism of gravitational cooling. In this paper we further explore the dynamical properties of these solitonic objects by performing both head-on collisions and orbital mergers of equal mass Proca stars, using fully nonlinear numerical evolutions. For the head-on collisions, we show that the end point and the gravitational waveform from these collisions depends on the compactness of the Proca star. Proca stars with sufficiently small compactness collide emitting gravitational radiation and leaving a stable Proca star remnant. But more compact Proca stars collide to form a transient *hypermassive* Proca star, which ends up decaying into a black hole, albeit temporarily surrounded by Proca quasibound states. The unstable intermediate stage can leave an imprint in the waveform, making it distinct from that of a head-on collision of black holes. The final quasinormal ringing matches that of Schwarzschild black hole, even though small deviations may occur, as a signature of sufficiently nonlinear and long-lived Proca quasibound states. For the orbital mergers, we have considered eccentric orbits and the outcome also depends on the compactness of the stars. For the binaries with the most compact stars, the binary merger forms a Kerr black hole which retains part of the initial orbital angular momentum, being surrounded by a transient Proca field remnant; in cases with lower compactness, the binary merger forms a massive Proca star with angular momentum, but out of equilibrium. As in previous studies of (scalar) boson stars, the angular momentum of such objects appears to converge to zero as a final equilibrium state is approached.

DOI: [10.1103/PhysRevD.99.024017](https://doi.org/10.1103/PhysRevD.99.024017)**I. INTRODUCTION**

The recent spectacular detections of gravitational waves [1–6] opened up a new window into the strong-field regime of gravity [7]. Even though the data so far is well fitted by the expected physics—i.e., collision of Kerr black holes (BHs) or neutron stars—it is important to understand if alternative, nonconventional models of compact objects can also fit the data (i.e., the level of degeneracy) or how much these can be ruled out by current/future data—see [8] for such a discussion. In the best-case scenario, obtaining gravitational waveforms of such nonconventional objects could lead to their future discovery, and the exciting prospect of unveiling new surprising physics via the gravitational-wave window.

Amongst such exotic models, self-gravitating solitons composed of complex (boson stars [9]) or real (oscillatons

[10]) scalar fields are some of the most dynamically studied cases—see, e.g., [11]. Dynamical studies include the generation of waveforms for head-on collisions of boson stars [12,13] and oscillatons [14–16] as well as orbital mergers of boson stars [17–21]. Even if the orbital mergers describe the astrophysically more likely scenario [22,23], and constitute a possible mechanism to form spinning boson stars or Kerr BHs with scalar hair [24,25], the head-on collisions represent a first step to compute the gravitational waveforms produced by these objects, allowing a simpler comparison to those produced in head-on collisions of BHs or neutron stars.

It has been recently found that a complex Proca field can form *Proca stars* (PSs), vector analogues of the scalar boson stars. PSs were constructed as static or stationary solutions of the Einstein-(complex)Proca system [26]—see also [27–30] for generalizations. Similarly to their scalar

cousins, they can be regarded as single frequency, macroscopic, self-gravitating (vector) Bose-Einstein condensates. This frequency appears as a harmonic time dependence for the Proca potential and the domain of existence of PSs is very similar to that of scalar boson stars—see, e.g., Fig. 1 in [31]—except that the latter have a smaller maximal mass and a wider frequency range.

Several dynamical aspects of the gravitational interaction of Proca fields have been addressed in recent years, using numerical studies. Long-lived, quasibound states of Proca fields around Schwarzschild BHs have been considered in [32,33] (see also [34]). The superradiant instability of Kerr BHs was triggered by Proca fields in [35,36], leading, in particular, to the formation of Kerr BH with Proca hair [27,37]. In [38] fully nonlinear evolutions of PSs were performed, to assess their stability. The simulations showed the existence of a stable branch (connecting the vacuum with the solution with maximal ADM mass) and an unstable branch. Solutions belonging to the latter may have different fates, depending on the initial perturbation and the sign of their binding energy. As their scalar cousins, with and without a self-interacting term [39–42], unstable solutions with positive binding energy migrate to the stable branch, whereas unstable solutions with a negative binding energy (excess energy) undergo fission; i.e., they disperse entirely. Both cases can also collapse to form a Schwarzschild BH. More recently, additional numerical simulations [43] have shown that PS can also form dynamically from generic initial data describing a non-compact “cloud” of the Proca field, through the so-called gravitational cooling mechanism, first described in the 1990s in the context of scalar boson stars [44].

In this work we shall continue the exploration of the dynamics of PSs by performing numerical evolutions describing both head-on collisions and orbital mergers of PS binaries and computing the gravitational radiation emitted. In the case of head-on collisions, the results we obtain parallel qualitatively those for head-on collisions of scalar boson (or even oscillaton) stars. For sufficiently small compactness, or equivalently, low mass in units of the Proca field mass—see Fig. 1 below—the collisions form a more massive, but still stable, PS, not a BH. The final star is, however, perturbed and in the timescale of our simulations it only partially relaxes to equilibrium. Sufficiently compact PSs, on the other hand, form a horizon when colliding, but only after an intermediate phase that could be described as a *hypermassive* PS. This intermediate stage leaves an imprint in the waveform, making it distinct from that of a head-on collision of Schwarzschild BHs. After horizon formation the BH ringdown can be seen, which matches well that of a Schwarzschild BH. But in the cases where a larger Proca remnant remains outside the horizon, in the form of Proca quasibound states, we observe a difference with the BH ringdown. A similar observation was reported recently in the study of head-on collisions of oscillaton stars [16].

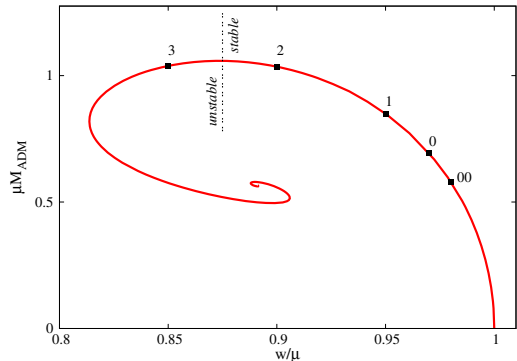


FIG. 1. Domain of existence of the spherical (fundamental) PS solutions (solid line) in an ADM mass vs vector field frequency diagram. We highlight the five solutions used in the head-on collisions and the orbital mergers in this work.

For the orbital mergers, similar results to the head-on case are also found. The mergers are eccentric and cover less than an orbit. They can lead to the formation of a Kerr BH wherein part of the initial orbital angular momentum of the configuration is deposited. In such cases, a Proca field remnant can be seen outside the horizon. This remnant is a quasi-bound state that decays exponentially. Thus, with the initial parameters chosen we do not see the formation of a Kerr BH with Proca hair. On the other hand, we obtain the formation of a massive PS with angular momentum for small compactness. The solitonic remnant is, however, out of equilibrium, and the angular momentum decreases significantly during and after the merger, approaching zero. In this process, the system emits gravitational waves continuously.

This paper is organized as follows. In Sec. II we present the equations of the Einstein-(complex)Proca model that will be used for the numerical evolutions. In Sec. III we present the initial data that will be used in our numerical evolutions. A brief description of the numerical techniques is given in Sec. IV and our results are presented in Sec. V. Final remarks are presented in Sec. VI. A brief assessment of the numerical code is given in Appendix.

II. BASIC EQUATIONS

We shall investigate the dynamics of a complex Proca field by solving numerically the Proca equations coupled to the Einstein equations. The system is described by the action $\mathcal{S} = \int d^4x \sqrt{-g} \mathcal{L}$, where the Lagrangian density depends on the Proca potential \mathcal{A} , and field strength $\mathcal{F} = d\mathcal{A}$; it is given by:

$$\mathcal{L} = \frac{R}{16\pi G} - \frac{1}{4} \mathcal{F}_{\alpha\beta} \bar{\mathcal{F}}^{\alpha\beta} - \frac{1}{2} \mu^2 \mathcal{A}_\alpha \bar{\mathcal{A}}^\alpha, \quad (1)$$

where the bar denotes complex conjugation, R is the Ricci scalar, G is Newton's constant, and μ is the Proca field mass. The stress-energy tensor of the Proca field reads

$$T_{ab} = -\mathcal{F}_{c(a}\bar{\mathcal{F}}_{b)}^c - \frac{1}{4}g_{ab}\mathcal{F}_{cd}\bar{\mathcal{F}}^{cd} + \mu^2 \left[\mathcal{A}_{(a}\bar{\mathcal{A}}_{b)} - \frac{1}{2}g_{ab}\mathcal{A}_c\bar{\mathcal{A}}^c \right]. \quad (2)$$

Using the standard 3 + 1 split (see, e.g., [38] for more details) the Proca field is split into 3 + 1 quantities:

$$\mathcal{A}_\mu = \mathcal{X}_\mu + n_\mu \mathcal{X}_\phi, \quad (3)$$

$$\mathcal{X}_i = \gamma_i^\mu \mathcal{A}_\mu, \quad (4)$$

$$\mathcal{X}_\phi = -n^\mu \mathcal{A}_\mu, \quad (5)$$

where \mathcal{X}_i is the vector potential and \mathcal{X}_ϕ is the scalar potential. The fully nonlinear Einstein-Proca system reads:

$$\partial_t \gamma_{ij} = -2\alpha K_{ij} + \mathcal{L}_\beta \gamma_{ij}, \quad (6)$$

$$\partial_t \mathcal{X}_i = -\alpha(E_i + D_i \mathcal{X}_\phi) - \mathcal{X}_\phi D_i \alpha + \mathcal{L}_\beta \mathcal{X}_i, \quad (7)$$

$$\partial_t E^i = \alpha(KE^i + D^i Z + \mu_\nu^2 \mathcal{X}^i + \epsilon^{ijk} D_j B_k) - \epsilon^{ijk} B_j D_k \alpha + \mathcal{L}_\beta E^i, \quad (8)$$

$$\begin{aligned} \partial_t K_{ij} = & -D_i D_j \alpha + \alpha(R_{ij} - 2K_{ik}K^k_j + KK_{ij}) \\ & + 2\alpha \left(E_i E_j - \frac{1}{2} \gamma_{ij} E^k E_k + B_i B_j \right. \\ & \left. - \frac{1}{2} \gamma_{ij} B^k B_k - \mu_\nu^2 \gamma_i \mathcal{X}_j \right) + \mathcal{L}_\beta K_{ij}, \end{aligned} \quad (9)$$

$$\partial_t \mathcal{X}_\phi = -\mathcal{X}^i D_i \alpha + \alpha(K\mathcal{X}_\phi - D_i \mathcal{X}^i - Z) + \mathcal{L}_\beta \mathcal{X}_\phi, \quad (10)$$

$$\partial_t Z = \alpha(D_i E^i + \mu_\nu^2 \mathcal{X}_\phi - \kappa Z) + \mathcal{L}_\beta Z, \quad (11)$$

where α is the lapse function, β is the shift vector, γ_{ij} is the spatial metric, K_{ij} is the extrinsic curvature (with $K = K^i_i$), D_i is the covariant 3-derivative, and \mathcal{L}_β is the Lie derivative. Moreover, the three-dimensional ‘‘electric’’ E^i and ‘‘magnetic’’ B^i fields are also introduced in the previous equations. The system is solved using the time-evolution numerical code from [33] (see Sec. IV).

III. INITIAL DATA

PSs were obtained in [26] as stationary solutions to the model described by the action (1). Five illustrative examples of spherically symmetric PSs will be taken as the initial data for our time evolutions. Their basic physical

TABLE I. Spherically symmetric Proca star models.

Model	w/μ	μM_{ADM}	$\mu^2 Q$	$\Phi_c(r=0)$
PS00	0.98	0.580	0.584	0.0046
PS0	0.97	0.693	0.702	0.0087
PS1	0.95	0.849	0.864	0.0214
PS2	0.90	1.036	1.063	0.0779
PS3	0.85	1.039	1.065	0.2121

properties, frequency, w , ADM mass, M_{ADM} , Noether charge Q and the Proca ‘‘electric’’ potential at the origin, Φ_c , all in units of the vector field mass, can be found in Table I and their distribution in an ADM mass vs. Proca field frequency diagram is shown in Fig. 1.

When computed as static solutions [26], spherically symmetric PSs are given by the line element

$$ds^2 = -e^{2F_0} dt^2 + e^{2F_1} [dr^2 + r^2(d\theta^2 + \sin^2\theta d\varphi^2)], \quad (12)$$

where F_0, F_1 are radial functions and r, θ, φ correspond to isotropic coordinates. The Proca field ansatz is given in terms of another two real functions (V, H_1) which depend also on r

$$\mathcal{A} = e^{-i\omega t} \left(iV dt + \frac{H_1}{r} dr \right), \quad (13)$$

where $w > 0$ is the frequency of the field. The translation between the four radial functions above, F_0, F_1, V, H_1 , and the initial value for the metric and the 3 + 1 Proca field variables described is given as follows:

$$\alpha = e^{F_0}, \quad (14)$$

$$\gamma_{rr} = e^{2F_1}, \quad \gamma_{\theta\theta} = e^{2F_1} r^2, \quad \gamma_{\phi\phi} = e^{2F_1} r^2 \sin^2\theta, \quad (15)$$

$$\mathcal{X}_\phi = -n^\mu \mathcal{A}_\mu, \quad (16)$$

$$\mathcal{X}_i = \gamma_i^\mu \mathcal{A}_\mu, \quad (17)$$

$$E^i = -i \frac{\gamma^{ij}}{\alpha} (D_j(\alpha \mathcal{X}_\phi) + \partial_t \mathcal{X}_j). \quad (18)$$

We follow [12] to construct appropriate initial data to study the head-on collision of these compact objects. We take a superposition of two PS solutions:

- (i) $\mathcal{A}(x_i) = \mathcal{A}^{(1)}(x_i - x_0) + \mathcal{A}^{(2)}(x_i + x_0)$,
- (ii) $\gamma_{ij}(x_i) = \gamma_{ij}^{(1)}(x_i - x_0) + \gamma_{ij}^{(2)}(x_i + x_0) - \gamma_{ij}^{\text{flat}}(x_i)$,
- (iii) $\alpha(x_i) = \alpha^{(1)}(x_i - x_0) + \alpha^{(2)}(x_i + x_0) - 1$,

where superindex (i) labels the stars and $\pm x_0$ indicates their initial positions. The stars are initially separated by $\Delta x = 39$, which corresponds to $x_0 = \pm 19.5$ (in $G = c = 1$ units). The solutions are not boosted. These initial data introduce constraint violations. However, they are small

and do not grow during the evolution, as we discuss in Appendix.

For the construction of initial data describing orbiting PS binary we extended the same method of the superposition of two isolated PSs solution, with the only difference that in this case the two stars are boosted along the y -axis which is perpendicular to the line segment linking them, with velocity $\pm v_y$, following [23,45]. In this case, the stars are initially separated by $\Delta x = 30$, which corresponds to $x_0 = \pm 15.0$. We call $\mathcal{B}_b^{(i)} = v_y^{(i)}/c$ and $\Gamma_b^{(i)} = (1 - \mathcal{B}_b^{(i)2})^{-1/2}$ the Lorentz factor, and the matrix associated with the transformation has the following form

$$\Lambda^{(i)} = \begin{pmatrix} \Gamma_b^{(i)} & -\Gamma_b^{(i)}\mathcal{B}_b^{(i)} & 0 & 0 \\ -\Gamma_b^{(i)}\mathcal{B}_b^{(i)} & \Gamma_b^{(i)} & 0 & 0 \\ 0 & 0 & 1 & 0 \\ 0 & 0 & 0 & 1 \end{pmatrix}, \quad (19)$$

with the features that $\Lambda^T = \Lambda$ and Λ^{-1} can be obtained using opposite velocity v_y . Note that $\Gamma_b^{(1)} = \Gamma_b^{(2)}$ and $\mathcal{B}_b^{(1)} = -\mathcal{B}_b^{(2)}$.

The line element of each star is in Cartesian coordinates given by

$$ds^2 = -\alpha_0^2 dt^2 + \psi_0^4 [dx_0^2 + dy_0^2 + dz_0^2], \quad (20)$$

with $r_0 = \sqrt{x_0^2 + y_0^2 + z_0^2}$. We perform a Lorentz transformation $t = \Gamma_b(t_0 + v_y y_0)$ and $y = \Gamma_b(y_0 + v_y t_0)$ and obtain from (20)

$$ds^2 = -\Gamma_b^2(\alpha_0^2 - \psi_0^4 v_y^2) dt^2 + 2\Gamma_b^2 v_y (\alpha_0^2 - \psi_0^4) dt dy + \psi_0^4 [dx^2 + B_0^2 dy^2 + dz^2], \quad (21)$$

then

$$\alpha = \frac{\alpha_0}{B_0}, \quad \beta^y = \left(\frac{\alpha_0^2 - \psi_0^4}{\psi_0^4 - \alpha_0^2 v_y^2} \right) v_y, \quad (22)$$

where $B_0 = \Gamma_b \sqrt{1 - \frac{v_y^2 \alpha_0^2}{\psi_0^4}}$.

The extrinsic curvature is computed from:

$$K_{ij} = \frac{1}{2\alpha} (\mathcal{L}_\beta \gamma_{ij} - \partial_t \gamma_{ij}) \quad (23)$$

where \mathcal{L}_β is the Lie derivative and $\partial_t \gamma_{ij} = -\Gamma_b v_y \partial_{y_0} \gamma_{ij}$.

We have to transform the Proca fields. The Lorentz transformation resembles the one for the common electromagnetic fields. We consider that in the rest frame the magnetic field is zero, due to the spherical symmetry. The boosted fields are obtained as follows:

$$E_x^{(i)(\text{boost})} = \Gamma_b^{(i)} E_x^{(i)}, \quad (24)$$

$$E_y^{(i)(\text{boost})} = E_y^{(i)}, \quad (25)$$

$$E_z^{(i)(\text{boost})} = \Gamma_b^{(i)} E_z^{(i)}, \quad (26)$$

$$\mathcal{X}_\phi^{(i)(\text{boost})} = \Gamma_b^{(i)} (\mathcal{X}_\phi^{(i)} + \mathcal{B}_b^{(i)} \mathcal{X}_y^{(i)}), \quad (27)$$

$$\mathcal{X}_x^{(i)(\text{boost})} = \mathcal{X}_x^{(i)}, \quad (28)$$

$$\mathcal{X}_y^{(i)(\text{boost})} = \Gamma_b^{(i)} (\mathcal{X}_y^{(i)} + \mathcal{B}_b^{(i)} \mathcal{X}_\phi^{(i)}), \quad (29)$$

$$\mathcal{X}_z^{(i)(\text{boost})} = \mathcal{X}_z^{(i)}. \quad (30)$$

The initial data for the PS binary is a superposition of the two boosted solution as in the head-on case.

IV. NUMERICS

To perform the numerical evolutions we use the freely available EINSTEIN TOOLKIT [46,47], which uses the CACTUS framework and mesh refinement. The method-of-lines is employed to integrate the time-dependent differential equations. In particular, we use a fourth-order Runge-Kutta scheme for this task. The left-hand-side of the Einstein equations is solved using the MACLACHLAN code [48,49], which is based on the 3 + 1 Baumgarte-Shapiro-Shibata-Nakamura (BSSN) formulation.

The Proca evolution equations, Eqs. (6)–(11), are solved using the code developed independently by M. Zilhão and H. Witek [33]. We have extended this code to take into account a complex field. All technical details, assessment of the code and convergence tests can be found in [33].

We use a numerical grid with 6 refinement levels for the head-on collisions, its structure being $\{(512, 64, 64, 32, 32, 8), (4, 2, 1, 0.5, 0.25, 0.125)\}$, where the first set of numbers indicates the spatial domain of each level and the second set indicates the resolution. Figure 2 shows the grid structure at $t = 0$. The outer boundary is located at $\Delta x = 392$ from the gravitational-wave extraction radii. This ensures that the total time of the simulations is shorter than twice the light-crossing time, which prevents numerical reflections at the boundary from affecting the extraction. Due to the geometry of head-on collisions, we consider equatorial-plane symmetry and reflection symmetry with respect to the x - z plane.

Correspondingly, Fig. 3 shows the grid structure we employ for the orbital mergers, which contains 7 refinement levels with spatial extent and resolution given by $\{(412, 64, 64, 32, 32, 8, 4), (4, 2, 1, 0.5, 0.25, 0.125, 0.0625)\}$. In this case there is a reflection symmetry along the equatorial-plane but no reflection symmetry with respect to the x - z plane.

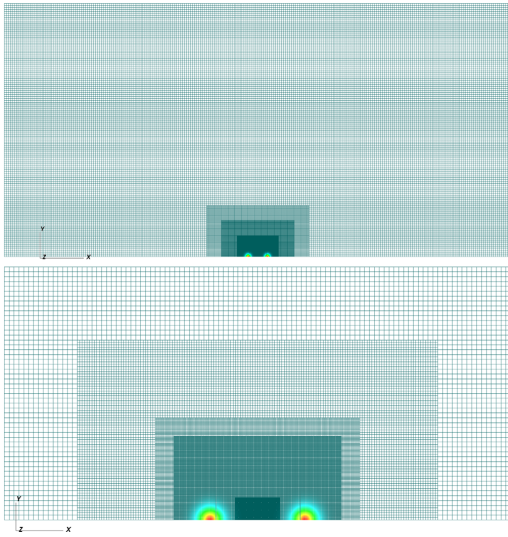


FIG. 2. Computational mesh-refined grid used for the evolutions of the head-on collisions. The top panel shows the entire domain while the bottom panel is a magnification of the inner region.

V. RESULTS

A. Head-on collisions

We evolve the initial data described in Sec. III for four equal-mass PS binaries, using the four types of PSs described in Table I and highlighted in Fig. 1. We label these four models as PS0-PS0, PS1-PS1, PS2-PS2, and PS3-PS3. We also evolve the latter including an initial perturbation which consists in multiplying by a number slightly larger than one the initial values of the Proca variables, as we did in [38], a model that we dub PS3b-PS3b. By including a perturbation the stars are forced to collapse before the collision, since the PS3 model is unstable against radial perturbations.

1. Visualisation of the collisions

Figure 4 shows equatorial-plane snapshots of the evolutions of the PS0-PS0, PS1-PS1, PS2-PS2, and PS3-PS3 binaries, from top to bottom. Our computational grid only extends from $y = 0$ to 512, therefore the data for negative values of y are mirrored by the corresponding positive y values, due to axisymmetry. Animations illustrating these collisions can be found in [50].

The collision of the two Proca stars happens at $t \sim 160$ for models PS0-PS0 and PS3-PS3, and at $t \sim 192$ for PS1-PS1 and PS2-PS2. The merged object oscillates in the x and y directions. For PS0-PS0, part of the field is ejected from the polar caps and approaches spherical symmetry.

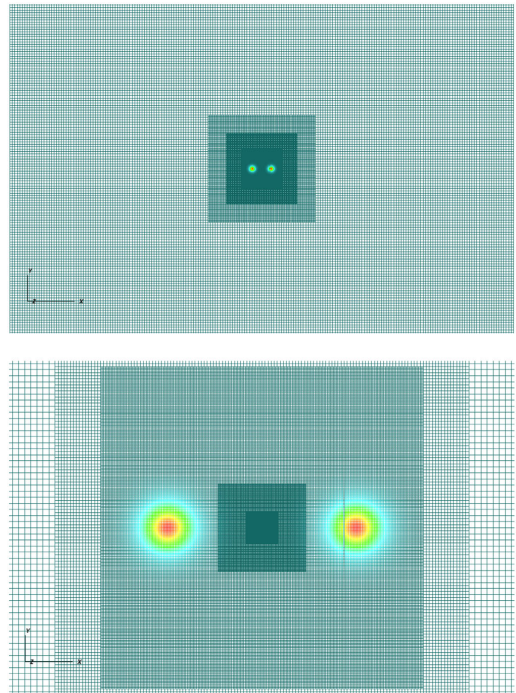


FIG. 3. Computational mesh-refined grid used for the evolutions of the orbital merger case. The top panel shows the entire domain while the bottom panel is a magnification of the inner region.

Model PS2-PS2 collapses quickly after the collision at $t_{\text{collapse}} \sim 245$, while models PS1-PS1 and PS3-PS3 oscillate during a short period of time before an apparent horizon (AH) appears at $t_{\text{collapse}} \sim 375$ and $t_{\text{collapse}} \sim 425$, respectively. Moreover, the PS1-PS1 collision forms a perturbed massive PS that oscillates and produces the first part of the gravitational-wave signal, as we show below. In the case of PS3-PS3, the stars migrate and expand before the collision. For all models, the morphology and amplitude of the gravitational waves are clearly influenced by the dynamics during the collision (cf. Sec. VA 3).

2. Proca energy and horizon formation

In Fig. 5 we plot the time evolution of the Proca field energy

$$E_{\text{PF}} = - \int_{\Sigma} dr d\theta d\varphi (2T_t^t - T_a^a) \alpha \sqrt{\gamma}, \quad (31)$$

and of the amplitude of the real and imaginary parts of the time component of the Proca 4-potential (hereafter the

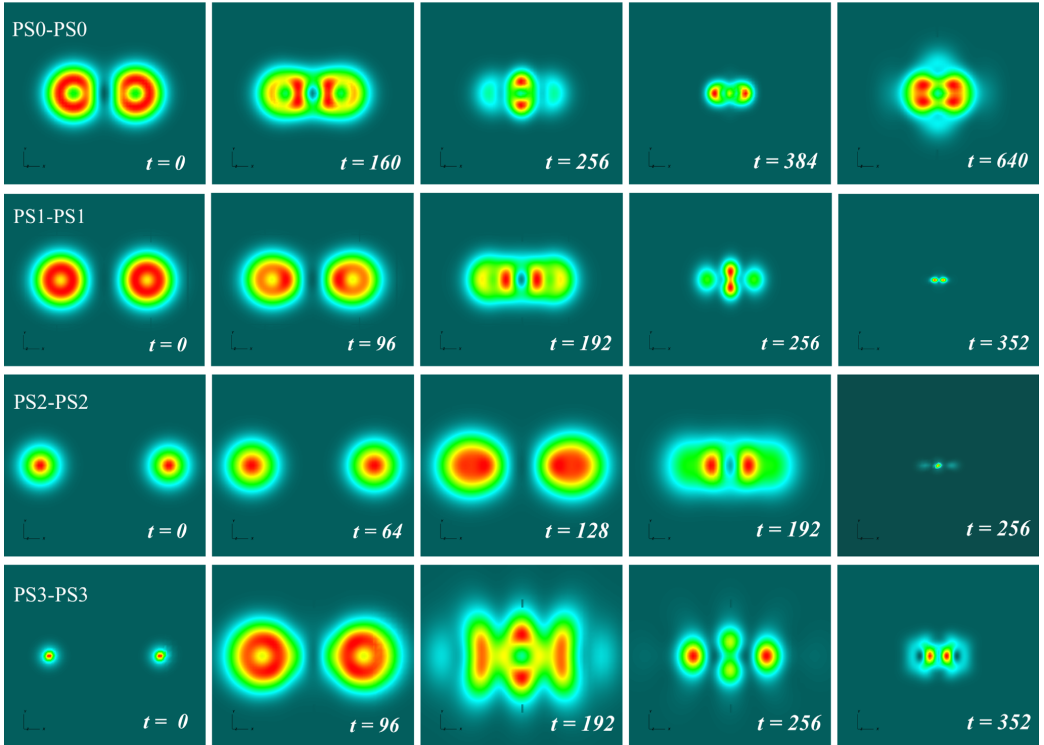


FIG. 4. Snapshots of the energy density for PS0-PS0, PS1-PS1, PS2-PS2 and PS3-PS3 in the equatorial plane. The vertical axis correspond to the y direction and the horizontal to the x direction.

“scalar” potential) for model PS0-PS0. In this case we see no horizon formation. The stars have sufficiently low mass so that the final state is still a star. The amplitude of the scalar potential stabilizes within the timescale of our

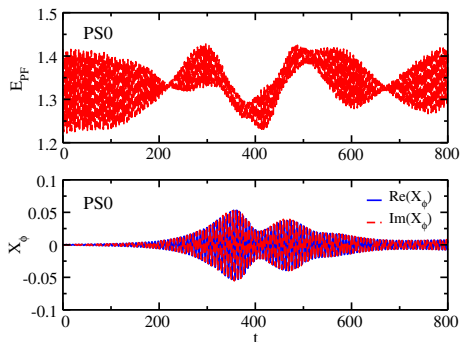


FIG. 5. Model PS0-PS0. Time evolution of the Proca field energy (top panel) and of the amplitude of the real and imaginary parts of the scalar potential extracted at $r = 0$ (bottom panel).

simulation. It has been reported in [14,16] that some collapsed oscillatons from head-on collisions can lose part of the field and form a stable, less compact oscillaton, not collapsing to a BH even if the total mass is larger than the maximum mass of the equilibrium configuration. This seems to be precisely what is occurring for model PS0-PS0. The mass of the PS0 Proca star is $\mu M_{\text{ADM}} = 0.693$, so that twice that mass is larger than the maximum mass for spherical PSs, which is $\mu M_{\text{ADM}}^{\text{max}} = 1.058$ [26]. Still, a PS forms, as a result of the inelasticity of the collision.

Figure 6 displays the time evolution of the Proca field energy and of the irreducible mass of the AH for models PS1-PS1, PS2-PS2 and PS3-PS3. For these three models, the collapse of the solutions is triggered after the collision and an AH forms. After the collapse there is still a Proca field remnant outside the horizon, as Fig. 7 shows. For PS1-PS1 and PS3-PS3 this remnant has a visible dynamics, reminiscent of a beating pattern, a signature of the presence of more than one quasibound state outside the AH. In the case of the PS3-PS3 model, the Proca remnant seems particularly long lived. We shall observe a possible impact of this feature in the gravitational waveform below.

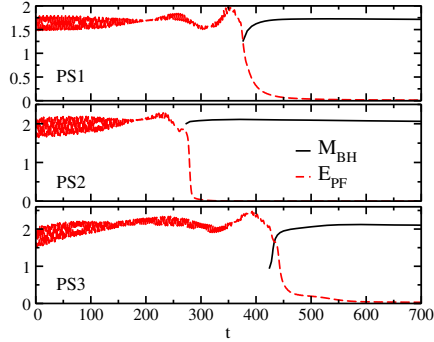


FIG. 6. Time evolution of the Proca field energy and BH mass for models PS1-PS1 (top panel), PS2-PS2 (middle panel) and PS3-PS3 (bottom panel).

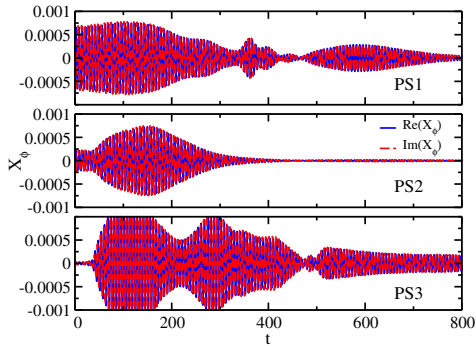


FIG. 7. Time evolutions of the amplitude of the real and imaginary parts of the scalar potential extracted at $r = 12$ for models PS1-PS1 (top panel), PS2-PS2 (middle panel), and PS3-PS3 (bottom panel).

3. Waveforms

In Figs. 8 and 9 we plot the resulting gravitational waveforms, showing the Newman-Penrose scalar $r\Psi_4^{l=2,m}$, for the modes $l = 2, m = \{0, +2\}$, extracted at radii $r_{\text{ext}} = \{100, 120\}$. The waves, conveniently shifted and rescaled, overlap, as expected in the wave zone. Nonaxisymmetric modes $l = 2, m = \pm 1$ are consistent with zero. In agreement with the results for head-on collisions of spherical boson stars in [12], we find that the coefficients $C_{2,m}$ of the different modes are related in the following way:

$$\text{Re}(C_{2,+2}) = \text{Re}(C_{2,-2}), \quad (32)$$

$$\text{Re}(C_{2,+2}) = -\sqrt{3/2}\text{Re}(C_{2,0}). \quad (33)$$

For our sample of models, the amplitude of the gravitational waves increases monotonically with decreasing

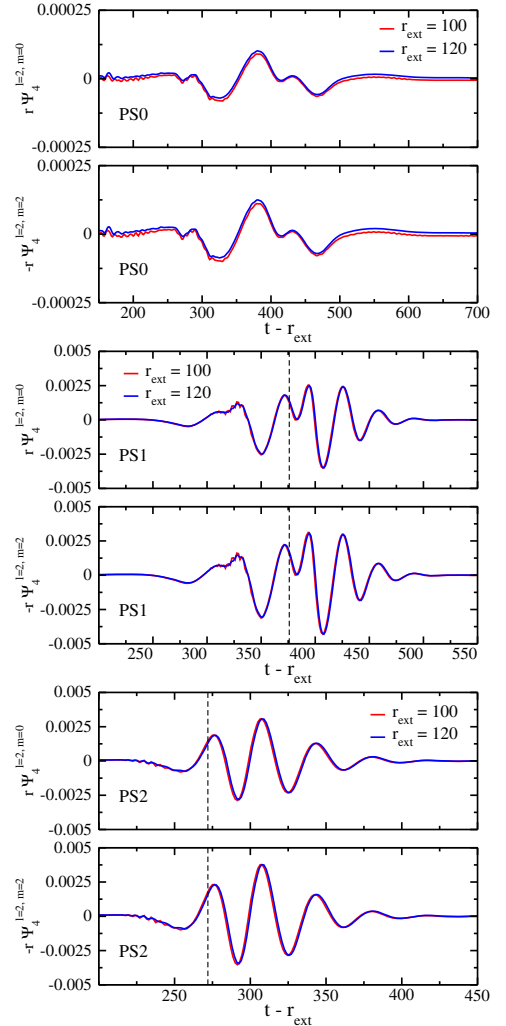


FIG. 8. Real part of $r\Psi_4^{l=2,m=0}$ and $r\Psi_4^{l=2,m=+2}$ for PS0-PS0 (top panels), PS1-PS1 (middle panels), and PS2-PS2 (bottom panels).

vector-field frequency. The largest amplitude is achieved for model PS3-PS3 which is more than an order of magnitude larger than for model PS0-PS0. All waveforms are of the burst-type, of which PS2-PS2 and PS3-PS3 are clear examples. Morphological differences are apparent in model PS0-PS0 and, in particular, in model PS1-PS1. For the latter, plotted in the middle panels of Fig. 8, there is a time delay $\Delta t \sim 100$ between the first negative peak of the waveform (at around $t \sim 275$) and the collapse (at around $t \sim 375$). The waveform can be regarded as composed by

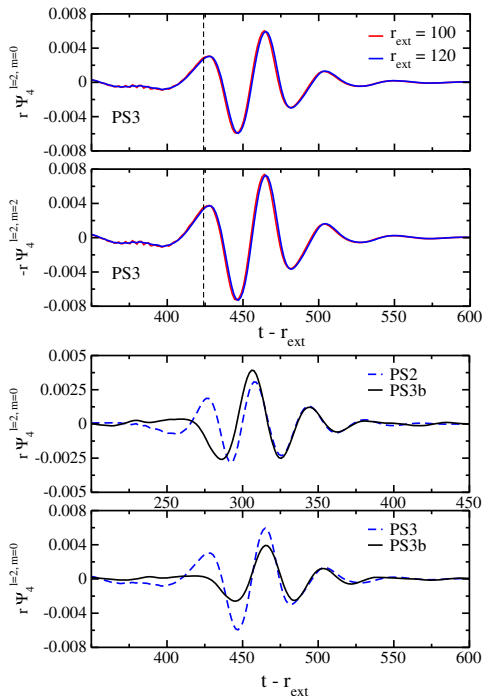


FIG. 9. Real part of $r\Psi_4^{l=2,m=0}$ and $r\Psi_4^{l=2,m=+2}$ for PS3-PS3 (top panels). Comparison of the real part of $r\Psi_4^{l=2,m=0}$ between PS2-PS2, PS3-PS3, and PS3b-PS3b computed at $r_{\text{ext}} = 120$. The latter is conveniently time shifted (bottom panels).

two contributions: the first part, from $t \sim 250$ to $t \sim 375$, would correspond to the collision of the stars, forming a “hypermassive” PS, a remnant that oscillates and eventually collapses to a BH at $t \sim 375$, triggering the second part of the wave. The collapse nearly coincides with a peak of the waveform and the corresponding time is highlighted by a vertical dashed line in the figure. For PS2-PS2 and PS3-PS3, these dynamics are absent, the AHs form promptly and their times of formation are very close to the first positive peak in the waveforms (vertical dashed lines).

The bottom panels of Fig. 9 show the gravitational waveform for the PS3b-PS3b model together with those of models PS2-PS2 and PS3-PS3. Recall that PS2 and PS3 have almost the same mass (less than 1% difference), therefore the BH formed will have a similar mass. Thus, we can compare the quasinormal modes (QNMs) of the three cases. For PS2-PS2, the QNMs are in good agreement in at least four of the peaks, while for PS3-PS3 there are some differences in the frequency. This comparison becomes more clear in the QNM ringdown plots shown in Fig. 10, where we plot the waveforms in logarithmic scale and we

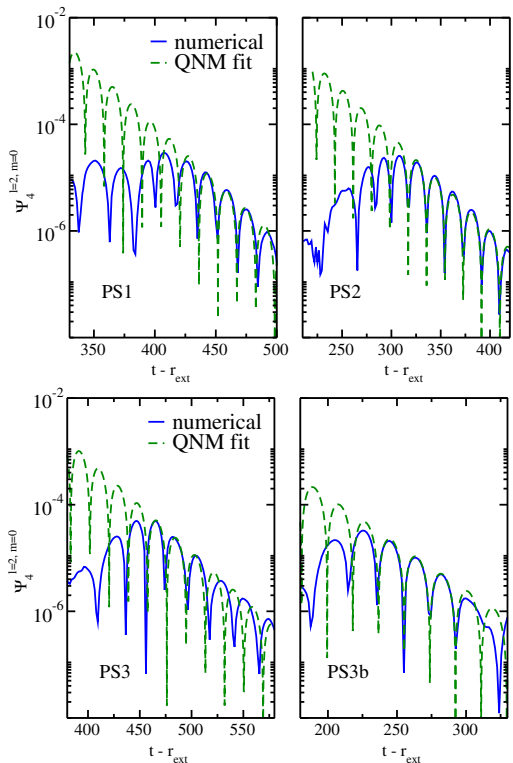


FIG. 10. Black hole ringing and quasinormal modes (QNMs) for models PS1-PS1 (top left panel), PS2-PS2 (top right panel), PS3-PS3 (bottom left panel), and PS3b-PS3b (bottom right panel). The QNM fit shown for PS2-PS2, PS3-PS3, and PS3b-PS3b corresponds to the same BH mass. All waveforms are computed at $r_{\text{ext}} = 120$.

fit them to the QNMs of a Schwarzschild BH, following the results of [51]. PS2-PS2, PS3-PS3, and PS3b-PS3b have almost the same total mass, therefore the fit is the same. The agreement for PS2-PS2 and PS3b-PS3b is very good. The masses that we obtain from the fits have an error of 7% for PS1-PS1 and 4% for PS2-PS2, PS3-PS3, and PS3b-PS3b, with respect to the masses computed with the AHFINDER algorithm of the EINSTEIN TOOLKIT. However, for the PS3-PS3 waveform the frequency does not match the PS3b-PS3b nor the QNM fit. A possible interpretation is that this is due to the fact that there is still a rich Proca field environment around the newly form BH, *cf.* Figures 6 and 7.

4. Comparison with BH collisions

We also perform head-on collisions of Schwarzschild BHs with the same mass as the PSs in each model. This

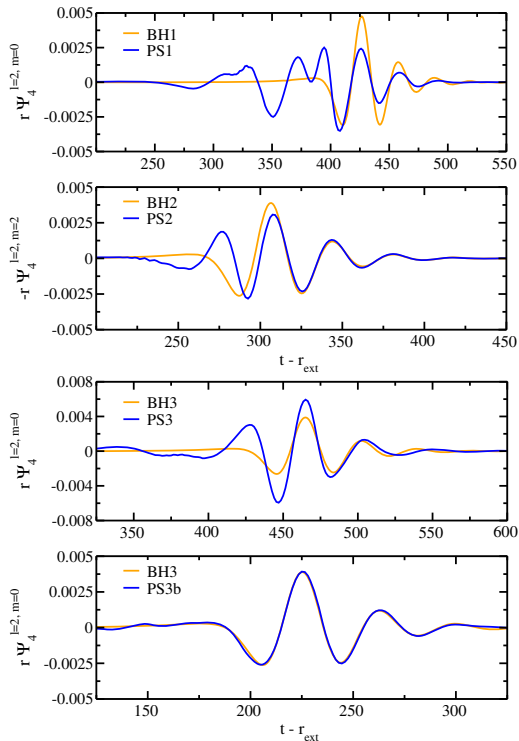


FIG. 11. Comparison of the real part of $r\Psi_4^{l=2,m=0}$ computed at $r_{\text{ext}} = 120$ from head-on collisions of PSs (blue lines) and Schwarzschild BHs of the same mass (orange lines).

allows to compare the resulting gravitational waveforms with those from the PS binaries. The real part of $r\Psi_4^{l=2,m=0}$ for both cases is shown in Fig. 11. Observe that for model PS3b-PS3b, we obtain essentially the same gravitational waveform. This is the expected result; in this case, the PSs collapse to BHs before the actual collision due to the initial perturbation we have imposed, thus leading to a head-on collision of BHs. In the case of PS2-PS2, the ringdown phase overlaps almost perfectly that same phase for the BH collision in agreement with the QNMs analysis in Fig. 10. The first part of the wave, however, is different: the frequency is higher but the amplitude is slightly smaller at the peak of the emission.

On the other hand, as already shown in the previous subsection, for PS1-PS1 and PS3-PS3, the comparison indicates that the waveforms depart from those of the Schwarzschild BH collisions. The amplitudes are different for both models. Some of the QNM oscillations can be fitted with the Schwarzschild BH-BH waveforms but not

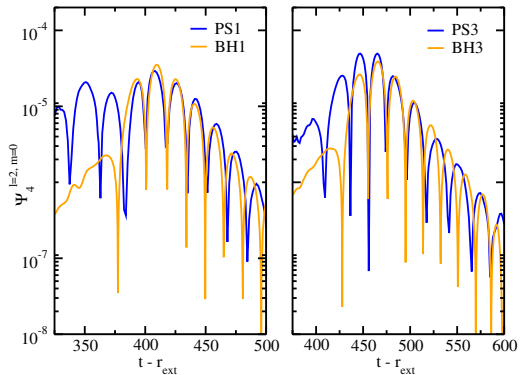


FIG. 12. Black hole ringing and quasinormal modes (QNMs) for models PS1-PS1 and the corresponding BH binary with the same mass (left panel). Same for PS3-PS3 (right panel).

all, as the frequency changes, see Fig. 12. The deviation in the frequency could be a signature of the presence of quasibound states around the BH and might be in particular related to the compactness of the remaining Proca field around the BH. The gravitational radiation induced by accreting shells of matter evolving in fixed BH backgrounds was first studied in [52] by numerically solving the linearized curvature perturbation equations (see also [53] for a dynamical spacetime study). It was found that the excitation of the BH QNM ringing strongly depends on the shell thickness, becoming increasingly clear with progressively more compact shells (see Fig. 10 in [52]). In the infinitesimally thin limit, the gravitational energy asymptotes to a finite value, about a third of the point particle upper limit. Those findings confirmed earlier ideas about the QNM excitation mechanism made by [54], namely that the *strong* excitation is induced by curvature profiles that have spatial wavelengths comparable to the width of the BH potential.

B. Orbital binary simulations

We turn now to describe the orbital binary merger simulations of models PS00-PS00, PS1-PS1, PS2-PS2, and PS3-PS3. The stars are boosted in the y direction. In this case, the objects are initially separated by $\Delta x = 30$.

1. Visualization of the binary mergers

The results are similar to the head-on collision case. The stars do not complete a full orbit since the mergers are eccentric; nonetheless, the final object has nonzero angular momentum. Figure 13 shows snapshots of the evolution of the energy density of models PS1-PS1, PS2-PS2, and PS3-PS3 in the equatorial plane for an initial velocity $v_y = 0.050$. The collision happens at $t \sim 128$ for models

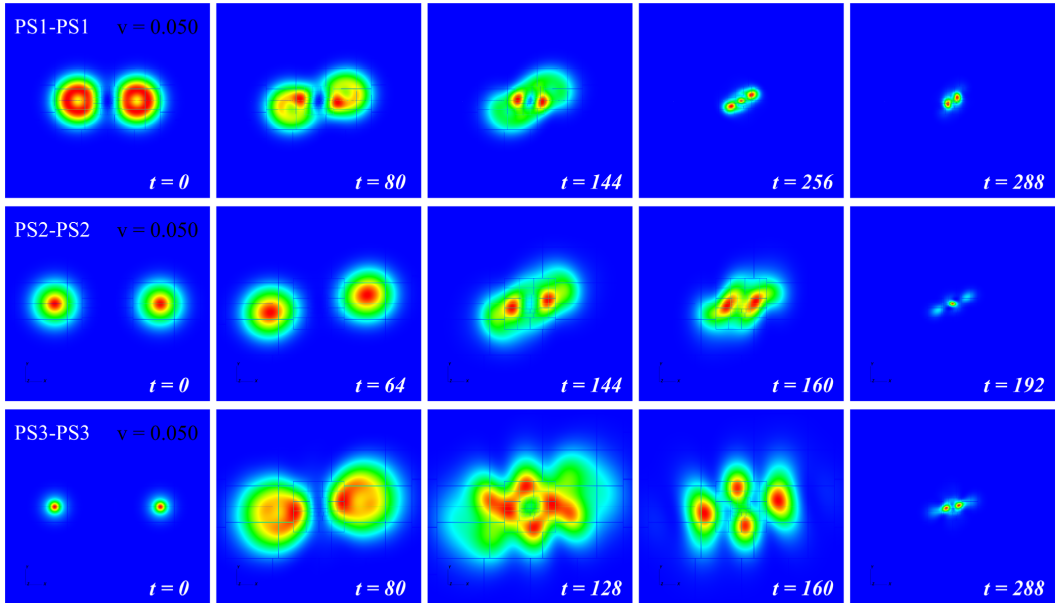


FIG. 13. Snapshots of the energy density for the orbital merger of PS1-PS1, PS2-PS2, and PS3-PS3 in the equatorial plane. The vertical axis correspond to the y direction and the horizontal to the x direction.

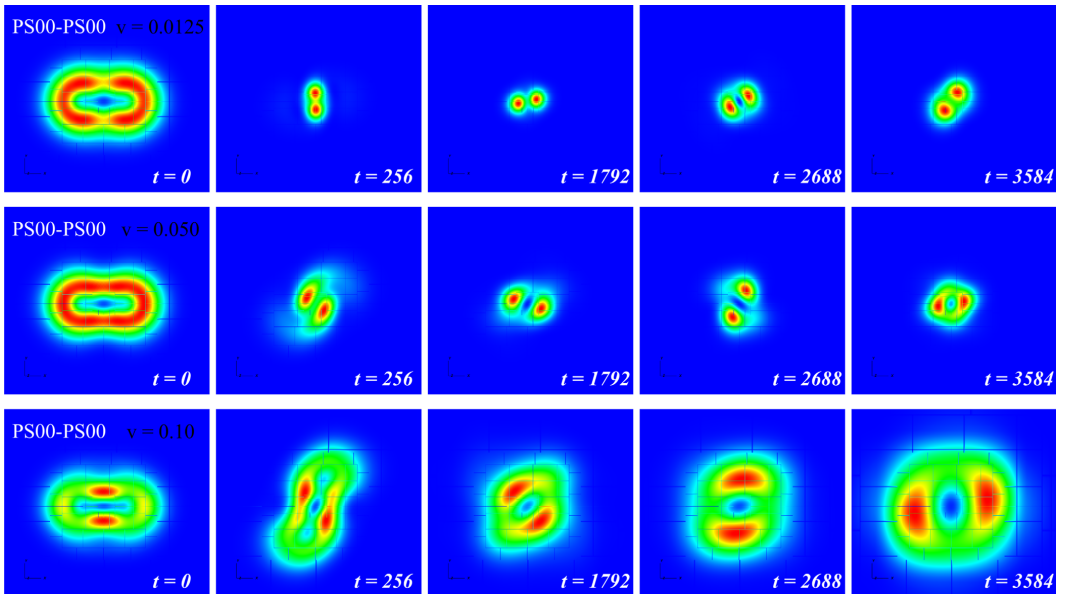


FIG. 14. Snapshots of the energy density for the orbital merger of PS00-PS00 with five initial velocities, namely $v_y = \{0.0125, 0.05, 0.10\}$ in the equatorial plane. The vertical axis correspond to the y direction and the horizontal to the x direction.

PS1-PS1 and PS3-PS3, and at $t \sim 144$ for PS2-PS2. The merged object has still some angular momentum left. An AH appears at $t \sim 350$ for model PS1-PS1, at $t \sim 200$ for model PS2-PS2 and at $t \sim 300$ for PS3-PS3.

In Fig. 14 we exhibit the evolution of the energy density for the model PS00-PS00, with three different initial velocities, $v_y = 0.0125$, $v_y = 0.050$ and $v_y = 0.10$. For PS00-PS00, the result of the merger does not lead to BH formation; instead the final object is a Proca star with angular momentum. The larger the initial velocity, the larger the fraction of the initial Proca mass and angular momentum that is ejected during and after the merger. With the largest initial velocity, $v_y = 0.10$, almost all the Proca field is dispersed away at the end of the simulation.

2. Proca energy and horizon formation

In Fig. 15 we plot the time evolution of the Proca field energy, Eq. (31), and the Proca field angular momentum

$$J_{\text{PF}} = \int_{\Sigma} drd\theta d\varphi T_{\varphi}^t \alpha \sqrt{\gamma}, \quad (34)$$

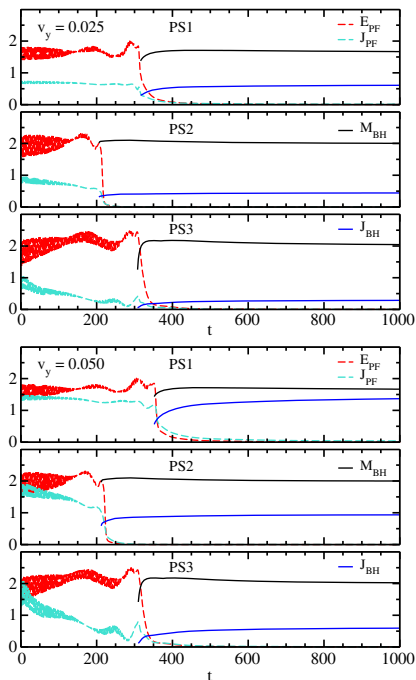


FIG. 15. Time evolution of the Proca field energy and angular momentum, together with the BH mass and spin for models PS1-PS1, PS2-PS2, and PS3-PS3, for two initial velocities $v_y = 0.025$ (top panel) and $v_y = 0.050$ (bottom panel).

together with the BH mass and the BH spin J for models PS1-PS1, PS2-PS2, and PS3-PS3 (bottom panels). In all these cases there is AH formation. These models collapse after the merger and form a Kerr BH with angular momentum. There is a remnant Proca field outside the rotating horizon, forming a quasibound state. We do not see evidence of infinitely long-lived Proca remnants (hair) forming around the BH.

The binary takes longer to collapse for a larger initial velocity v_y , but for the models PS2-PS2 and PS3-PS3 the difference is small for the velocities we have chosen. A large part of the total angular momentum is lost before the collapse for these models. On the other hand, for model PS1-PS1 the difference in collapse time is more noticeable: it takes about 50 times longer to collapse for the largest velocity and the final BH stores almost all of the initial angular momentum.

Figure 16 shows that a quasibound state appears outside the horizon after the collapse and formation of a BH. As in the head-on collision case, the final amount of Proca field remaining is smaller for model PS2-PS2 than for models PS1-PS1 and PS3-PS3.

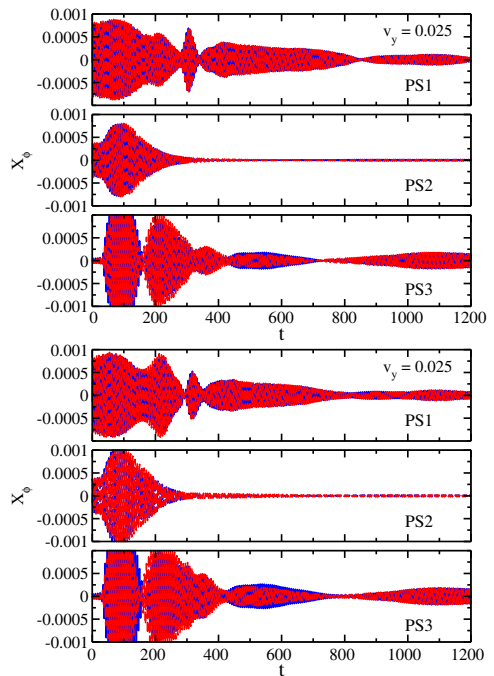


FIG. 16. Time evolution of the real and imaginary parts of the scalar potential amplitude for models PS1-PS1, PS2-PS2, and PS3-PS3 for two initial velocities $v_y = 0.025$ (top panel) and $v_y = 0.050$ (bottom panel).

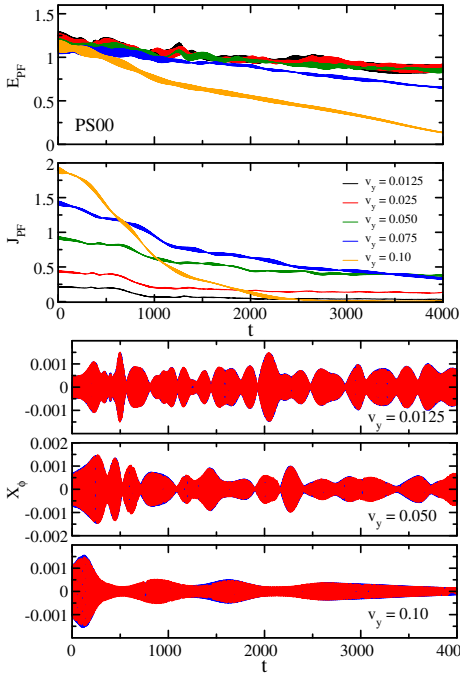


FIG. 17. Time evolution of the Proca field energy and angular momentum (top panels) and of the amplitude of the scalar potential for model PS00-PS00 (bottom panels).

For PS00-PS00 there is no BH formation. In Fig. 17, we show the time evolution of the energy and angular momentum of this model that we evolve with five different initial boost velocities, therefore increasing the initial angular momentum, namely $v_y = \{0.0125, 0.025, 0.050, 0.075, 0.10\}$. The PS formed after the collision has non-zero residual angular momentum. The total Proca energy is larger than the maximum mass of a rotating PS with $m = 1$ ($M \sim 1.124$, see Fig. 6 in [37]). To prevent the collapse, the star can lose energy through two mechanisms: gravitational cooling (ejecting Proca particles) and gravitational-wave emission (which also carries angular momentum). One may ask if there is formation of a rotating Proca star after the merger; we see that if we increase the initial velocity the angular momentum is rapidly lost and goes below the energy of the Proca field. This result could be due to the constraint-violating initial data we use; thus, it is interesting to revisit this problem once constraint-satisfying initial data becomes available, as it would provide a more reliable answer. For very large initial velocities, the final star can be completely dispersed away. For the largest velocity, we see that the amplitude of the scalar potential is decreasing with time.

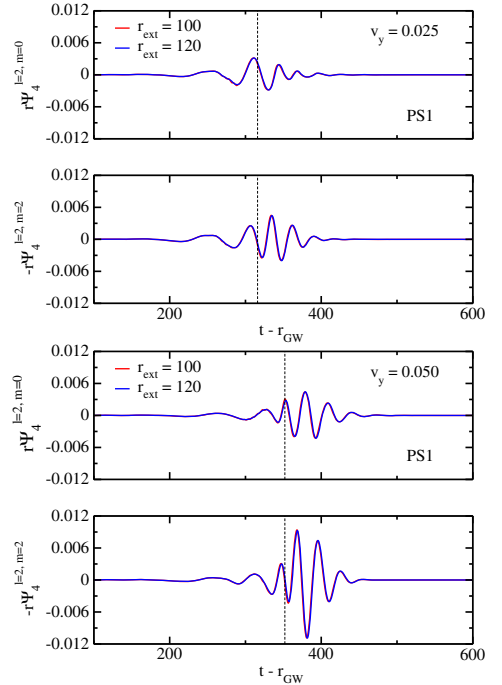


FIG. 18. Real part of $r\Psi_4^{l=2,m=0}$ and $r\Psi_4^{l=2,m=+2}$ for PS1-PS1 with initial boost velocity $v_y = 0.025$ (top panels) and $v_y = 0.050$ (bottom panels).

3. Waveforms

In Figs. 18–21 we exhibit the gravitational waveforms produced in the orbital mergers, showing again the $l = 2$, $m = \{0, +2\}$ modes, extracted at two radii, $r_{\text{ext}} = \{100, 120\}$. The waveforms, conveniently shifted and rescaled, overlap in the wave zone. For the PS1-PS1 merger one observes that, as one increases the initial velocity, the non-axisymmetric $m = 2$ mode grows visibly more than the axisymmetric $m = 0$ mode. In fact the same trend occurs for the PS2-PS2 and PS3-PS3 mergers, but it is less pronounced. Therefore, the rescaling presented in Eq. (33) is no longer true. Moreover, the two parts of the waveforms shown in Figs. 18–20 seem to indicate that for models PS1-PS1 and PS3-PS3 a transient hypermassive PS forms before it collapses to a BH. Finally, for model PS00-PS00 (cf. 21) the gravitational-wave emission does not decay as the result of this merger is a highly perturbed PS. The waveform is filled with high frequency noise, probably coming from reflections with the outer boundary. The gravitational waveforms for this case are markedly similar to previous results in the scalar case [17,18,21].

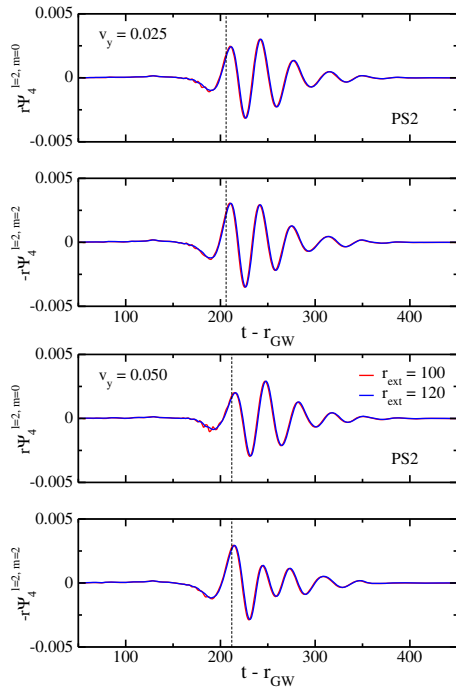


FIG. 19. Real part of $r\Psi_4^{l=2,m=0}$ and $r\Psi_4^{l=2,m=+2}$ for PS2-PS2 with initial boost velocity $v_y = 0.025$ (top panels) and $v_y = 0.050$ (bottom panels).

VI. CONCLUSIONS

In this paper we have used numerical-relativity techniques to study both head-on collisions and orbital binary mergers of Proca stars of equal ADM mass and vector field frequency and we have extracted the gravitational waves produced in those collisions. This work continues our numerical exploration of the dynamics of PSs initiated in [38,43]. PSs are macroscopic, self-gravitating, Bose-Einstein condensates built out of a massive, complex, vector field [26]. Since they can achieve a compactness comparable to that of BHs, they are a type of BH mimicker with appealing dynamical properties, namely they are stable against perturbations [26,38] and they can form dynamically through a gravitational cooling mechanism [43].

Our investigation shows that the head-on collision of these spherically symmetric solutions may lead either to the formation of a more massive PS, which we dub “hypermassive” PS or, if the initial PSs are sufficiently massive/compact, to the formation of a Schwarzschild BH. Horizon formation, however, only occurs after an intermediate phase, which leaves an imprint in the waveform, making it distinct from that of a head-on collision of

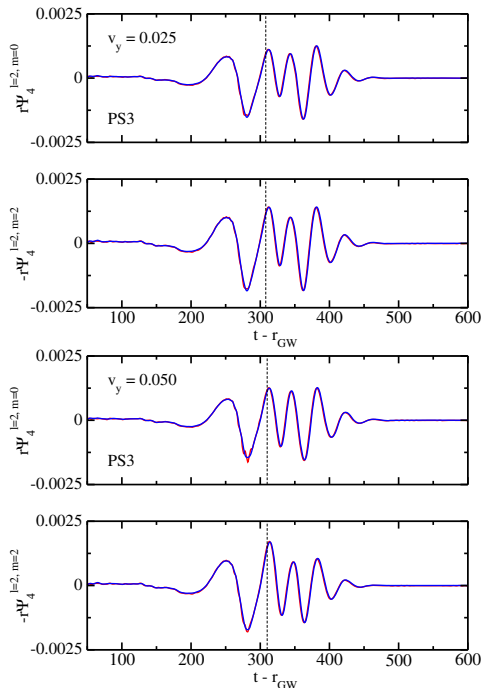


FIG. 20. Real part of $r\Psi_4^{l=2,m=0}$ and $r\Psi_4^{l=2,m=+2}$ for PS3-PS3 with initial boost velocity $v_y = 0.025$ (top panels) and $v_y = 0.050$ (bottom panels).

Schwarzschild BHs. After horizon formation the BH QNMs match those of a Schwarzschild BH. However, we have found that for those cases where the final BH is surrounded by a sufficiently extended and long-lived

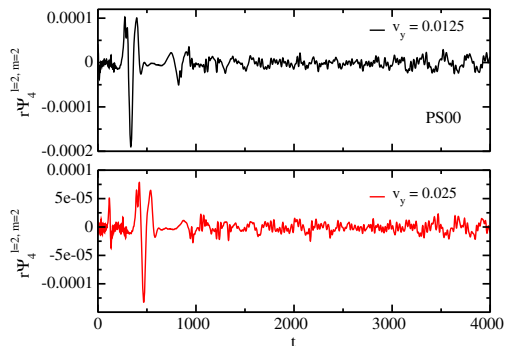


FIG. 21. Real part of $r\Psi_4^{l=2,m=0}$ and $r\Psi_4^{l=2,m=+2}$ for PS00-PS00 extracted at $r_{\text{ext}} = 120$ with initial boost velocity $v_y = 0.0125$ (top panel), and $v_y = 0.025$ (bottom panel).

quasistationary Proca cloud, differences with the BH ringdown are noticeable.

In the orbital binary case, we have also observed two fates: (i) the formation of a Proca star remnant, initially out of equilibrium and with angular momentum, but loosing such angular momentum as it approaches equilibrium; (ii) the formation of a Kerr BH, also initially surrounded by a cloud of quasi-bound states of the Proca field, which also tends to be absorbed/scattered during the evolution. We have not found evidence for the formation of either rotating Proca stars or infinitely long-lived Proca hair around a rotating horizon. In the case of the rotating Proca stars, since these are thought to be perturbatively stable in some region of parameter space (see [25] for a discussion in the analogue case of rotating boson stars), it may be that the island of initial conditions leading to their formation has not yet been scanned by our simulations. In the near future we plan to scan the space of initial data, in particular initial velocities. For larger velocities, obtaining reliable results requires constraint-preserving initial data. Obtaining such data and using it for performing further numerical evolutions is work underway.

ACKNOWLEDGMENTS

N. S. G. thanks Miguel Zilhão and Vassilios Mewes for useful discussions. This work has been supported by the Spanish MINECO (Grant No. AYA2015-66899-C2-1-P), by the Generalitat Valenciana (ACIF/2015/216), by the FCT (Portugal) IF programme, by the FCT Grant No. PTDC/FIS-OUT/28407/2017, by Centro de Investigação e Desenvolvimento em Matemática e Aplicações (FCT) strategic Project No. UID/MAT/04106/2013, by Centro Multidisciplinar de Astrofísica (FCT) strategic Project No. UID/FIS/00099/2013 and by the European Union's Horizon 2020 research and innovation (RISE) programmes H2020-MSCA-RISE-2015 Grants No. StronGrHEP-690904, No. H2020-MSCA-RISE-2017, and No. FunFiCO-777740. The authors would like to acknowledge networking support by the COST Action CA16104. Computations have been performed at the Servei d'Informàtica de la Universitat de València.

APPENDIX: CODE ASSESSMENT

We briefly comment here on the standard analyses we carried out to assess the quality of our simulations with the EINSTEIN TOOLKIT. In Fig. 22 we show the behavior of the L_2 -norm of the Hamiltonian constraint for the head-on case. The floor of the violation of this constraint is at $\sim 4 \times 10^{-4}$ during most of the simulation. A significant peak in the violations of the constraint appears when the BH forms, but the errors quickly decrease to the precollision values and remain stable during the rest of the simulation.

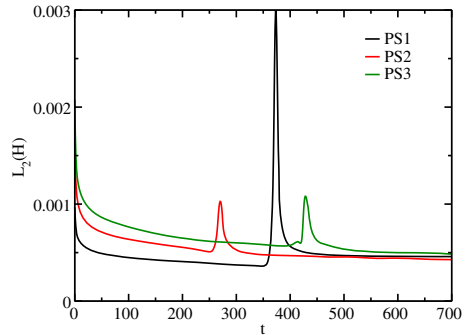


FIG. 22. L_2 -norm of the Hamiltonian constraint for PS1-PS1, PS2-PS2, and PS3-PS3.

In Fig. 23 we plot the gravitational wave from the head-on and orbital mergers of the PS2-PS2 and the PS3-PS3 cases for three different resolutions. The grid structure for the head-on collision is $\{(512,64,64,32,32,8), (8,4,2,1,0.5,0.25)\}$ and $\{(512,64,64,32,32,8),$

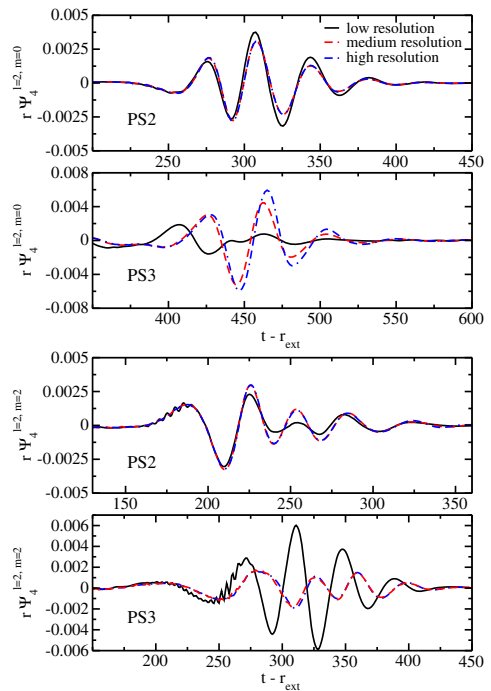


FIG. 23. Top panels: Resolution comparison for the gravitational wave extracted at $r_{\text{ext}} = 120$ for the head-on collisions of PS2-PS2 and PS3-PS3. Bottom panels: Resolution comparison for the gravitational wave extracted at $r_{\text{ext}} = 40$ for the orbital mergers of PS2-PS2 and PS3-PS3.

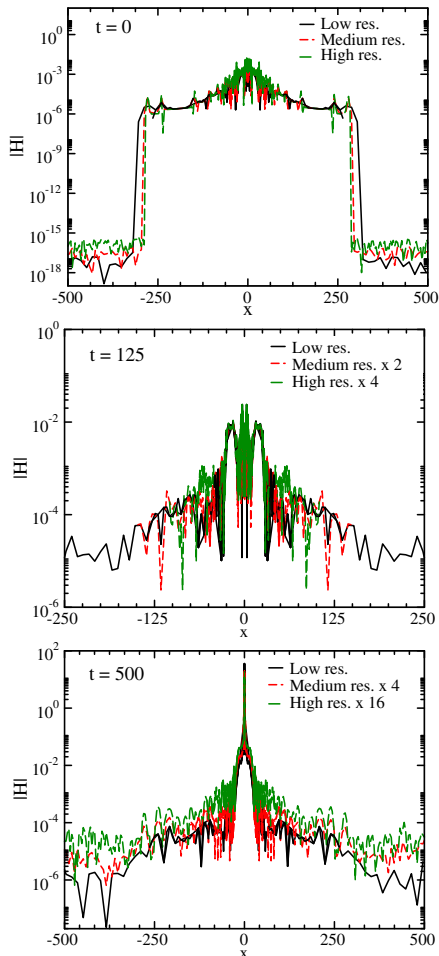


FIG. 24. Hamiltonian constraint for the head-on collision of PS2-PS2 at $t = 0$ (top panel), $t = 125$ (middle panel), and $t = 500$ (bottom panel).

$(16, 8, 4, 2, 1, 0.5)$ for medium and low resolution, respectively, and, correspondingly, for the orbital merger is $\{(416, 64, 64, 32, 32, 8, 4), (8, 4, 2, 1, 0.5, 0.25, 0.125)\}$ and $\{(416, 64, 64, 32, 32, 8, 4), (16, 8, 4, 2, 1, 0.5, 0.25)\}$. The high resolution is the one used in the simulations shown in this paper. For PS2-PS2, the results for the three resolutions converge in either type of collision. For the PS3-PS3 model the low resolution is not good enough to allow us to extract the gravitational waveform. The medium and high resolutions provide adequate results showing that they are in the convergence regime.

Finally, in Figs. 24 and 25 we plot the Hamiltonian constraint of the head-on collision of the PS2-PS2 model at

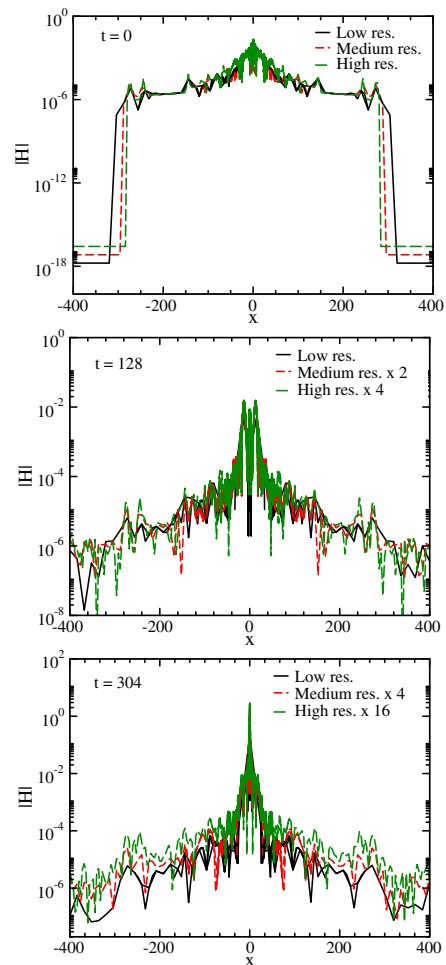


FIG. 25. Hamiltonian constraint for the orbital merger of PS2-PS2 at $t = 0$ (top panel), $t = 128$ (middle panel), and $t = 304$ (bottom panel).

$t = 0$, $t = 125$, and $t = 500$ and of the orbital merger at $t = 0$, $t = 128$, and $t = 304$. The analysis yields a similar result for both types of collisions. At $t = 0$ the constraint violations do not converge with resolution (our initial data do not satisfy the constraints). At intermediate times we obtain first-order convergence and, when the BH forms, a convergence of around second order is achieved. Therefore, we conclude that during the simulation we obtain between first- and second-order convergence. We note that the convergence order is greatly influenced by the linear second-order interpolation from the spherical grid of the Proca star solutions to the Cartesian grid we use to perform the evolutions with the EINSTEIN TOOLKIT.

- [1] B. P. Abbott, R. Abbott, T. D. Abbott, M. R. Abernathy, F. Acernese, K. Ackley, C. Adams, T. Adams, P. Addesso, R. X. Adhikari *et al.*, *Phys. Rev. Lett.* **116**, 061102 (2016).
- [2] B. P. Abbott *et al.* (Virgo and LIGO Scientific Collaborations), *Phys. Rev. Lett.* **116**, 241103 (2016).
- [3] B. P. Abbott *et al.* (Virgo and LIGO Scientific Collaborations), *Phys. Rev. Lett.* **118**, 221101 (2017).
- [4] B. P. Abbott *et al.* (Virgo and LIGO Scientific Collaborations), *Phys. Rev. Lett.* **119**, 141101 (2017).
- [5] B. P. Abbott *et al.* (Virgo and LIGO Scientific Collaborations), *Astrophys. J.* **851**, L35 (2017).
- [6] B. Abbott *et al.* (Virgo and LIGO Scientific Collaborations), *Phys. Rev. Lett.* **119**, 161101 (2017).
- [7] L. Barack *et al.*, [arXiv:1806.05195](https://arxiv.org/abs/1806.05195).
- [8] N. K. Johnson-McDaniel, A. Mukherjee, R. Kashyap, P. Ajith, W. Del Pozzo, and S. Vitale, [arXiv:1804.08026](https://arxiv.org/abs/1804.08026).
- [9] F. E. Schunck and E. W. Mielke, *Classical Quantum Gravity* **20**, R301 (2003).
- [10] E. Seidel and W. M. Suen, *Phys. Rev. Lett.* **66**, 1659 (1991).
- [11] S. L. Liebling and C. Palenzuela, *Living Rev. Relativity* **15**, 6 (2012).
- [12] C. Palenzuela, I. Olabarrieta, L. Lehner, and S. L. Liebling, *Phys. Rev. D* **75**, 064005 (2007).
- [13] V. Cardoso, S. Hopper, C. F. Macedo, C. Palenzuela, and P. Pani, *Phys. Rev. D* **94**, 084031 (2016).
- [14] R. Brito, V. Cardoso, and H. Okawa, *Phys. Rev. Lett.* **115**, 111301 (2015).
- [15] R. Brito, V. Cardoso, C. F. Macedo, H. Okawa, and C. Palenzuela, *Phys. Rev. D* **93**, 044045 (2016).
- [16] T. Helfer, E. A. Lim, M. A. Garcia, and M. A. Amin, [arXiv:1802.06733](https://arxiv.org/abs/1802.06733) [*Phys. Rev. D* (to be published)].
- [17] M. Bezares, C. Palenzuela, and C. Bona, *Phys. Rev. D* **95**, 124005 (2017).
- [18] C. Palenzuela, P. Pani, M. Bezares, V. Cardoso, L. Lehner, and S. Liebling, *Phys. Rev. D* **96**, 104058 (2017).
- [19] T. Dietrich, S. Ossokine, and K. Clough, [arXiv:1807.06959](https://arxiv.org/abs/1807.06959).
- [20] K. Clough, T. Dietrich, and J. C. Niemeyer, *Phys. Rev. D* **98**, 083020 (2018).
- [21] M. Bezares and C. Palenzuela, *Classical Quantum Gravity* **35**, 234002 (2018).
- [22] C. Palenzuela, L. Lehner, and S. L. Liebling, *Phys. Rev. D* **77**, 044036 (2008).
- [23] M. Bezares, C. Palenzuela, and C. Bona, *Phys. Rev. D* **95**, 124005 (2017).
- [24] C. A. R. Herdeiro and E. Radu, *Phys. Rev. Lett.* **112**, 221101 (2014).
- [25] C. Herdeiro and E. Radu, *Classical Quantum Gravity* **32**, 144001 (2015).
- [26] R. Brito, V. Cardoso, C. A. R. Herdeiro, and E. Radu, *Phys. Lett. B* **752**, 291 (2016).
- [27] C. Herdeiro, E. Radu, and H. Runarsson, *Classical Quantum Gravity* **33**, 154001 (2016).
- [28] F. Garca and I. S. Landea, *Phys. Rev. D* **94**, 104006 (2016).
- [29] M. Duarte and R. Brito, *Phys. Rev. D* **94**, 064055 (2016).
- [30] M. Minamitsuji, *Phys. Rev. D* **97**, 104023 (2018).
- [31] P. V. P. Cunha, J. A. Font, C. Herdeiro, E. Radu, N. Sanchis-Gual, and M. Zilhó, *Phys. Rev. D* **96**, 104040 (2017).
- [32] H. Witek, V. Cardoso, A. Ishibashi, and U. Sperhake, *Phys. Rev. D* **87**, 043513 (2013).
- [33] M. Zilhó, H. Witek, and V. Cardoso, *Classical Quantum Gravity* **32**, 234003 (2015).
- [34] J. G. Rosa and S. R. Dolan, *Phys. Rev. D* **85**, 044043 (2012).
- [35] W. E. East and F. Pretorius, *Phys. Rev. Lett.* **119**, 041101 (2017).
- [36] W. E. East, *Phys. Rev. D* **96**, 024004 (2017).
- [37] C. A. R. Herdeiro and E. Radu, *Phys. Rev. Lett.* **119**, 261101 (2017).
- [38] N. Sanchis-Gual, C. Herdeiro, E. Radu, J. C. Degollado, and J. A. Font, *Phys. Rev. D* **95**, 104028 (2017).
- [39] E. Seidel and W.-M. Suen, *Phys. Rev. D* **42**, 384 (1990).
- [40] J. Balakrishna, E. Seidel, and W.-M. Suen, *Phys. Rev. D* **58**, 104004 (1998).
- [41] F. S. Guzman, *Phys. Rev. D* **70**, 044033 (2004).
- [42] A. Escorihuela-Tomás, N. Sanchis-Gual, J. C. Degollado, and J. A. Font, *Phys. Rev. D* **96**, 024015 (2017).
- [43] F. Di Giovanni, N. Sanchis-Gual, C. A. R. Herdeiro, and J. A. Font, *Phys. Rev. D* **98**, 064044 (2018).
- [44] E. Seidel and W.-M. Suen, *Phys. Rev. Lett.* **72**, 2516 (1994).
- [45] M. Shibata, H. Okawa, and T. Yamamoto, *Phys. Rev. D* **78**, 101501 (2008).
- [46] E. Toolkit, <http://einsteintoolkit.org>.
- [47] F. Löffler, *Classical Quantum Gravity* **29**, 115001 (2012).
- [48] D. Brown, P. Diener, O. Sarbach, E. Schnetter, and M. Tiglio, *Phys. Rev. D* **79**, 044023 (2009).
- [49] C. Reisswig, C. D. Ott, U. Sperhake, and E. Schnetter, *Phys. Rev. D* **83**, 064008 (2011).
- [50] Head on collisions videos, <http://gravitation.web.ua.pt/node/1522>.
- [51] E. Leaver, *Proc. R. Soc. A* **402**, 285 (1985).
- [52] P. Papadopoulos and J. A. Font, *Phys. Rev. D* **59**, 044014 (1999).
- [53] P. Papadopoulos and J. A. Font, *Phys. Rev. D* **63**, 044016 (2001).
- [54] Y. Sun and R. H. Price, *Phys. Rev. D* **41**, 2492 (1990).

Nonlinear Dynamics of Spinning Bosonic Stars: Formation and Stability

N. Sanchis-Gual¹, F. Di Giovanni², M. Zilhão¹, C. Herdeiro^{1,3}, P. Cerdá-Durán², J. A. Font^{2,4} and E. Radu³

¹*Centro de Astrofísica e Gravitação—CENTRA, Departamento de Física, Instituto Superior Técnico—IST, Universidade de Lisboa—UL, Avenida Rovisco Pais 1, 1049-001 Lisboa, Portugal*

²*Departamento de Astronomía y Astrofísica, Universitat de València, Dr. Moliner 50, 46100 Burjassot (València), Spain*

³*Departamento de Matemática da Universidade de Aveiro and Centre for Research and Development in Mathematics and Applications (CIDMA), Campus de Santiago, 3810-183 Aveiro, Portugal*

⁴*Observatori Astronòmic, Universitat de València, C/ Catedrático José Beltrán 2, 46980 Paterna (València), Spain*



(Received 4 August 2019; published 25 November 2019)

We perform numerical evolutions of the fully nonlinear Einstein (complex, massive) Klein-Gordon and Einstein (complex) Proca systems, to assess the formation and stability of spinning bosonic stars. In the scalar (vector) case these are known as boson (Proca) stars. Firstly, we consider the formation scenario. Starting with constraint-obeying initial data, describing a dilute, axisymmetric cloud of spinning scalar or Proca field, gravitational collapse toward a spinning star occurs, via gravitational cooling. In the scalar case the formation is transient, even for a nonperturbed initial cloud; a nonaxisymmetric instability always develops ejecting all the angular momentum from the scalar star. In the Proca case, by contrast, no instability is observed and the evolutions are compatible with the formation of a spinning Proca star. Secondly, we address the stability of an existing star, a stationary solution of the field equations. In the scalar case, a nonaxisymmetric perturbation develops, collapsing the star to a spinning black hole. No such instability is found in the Proca case, where the star survives large amplitude perturbations; moreover, some excited Proca stars decay to, and remain as, fundamental states. Our analysis suggests bosonic stars have different stability properties in the scalar (vector) case, which we tentatively relate to its toroidal (spheroidal) morphology. A parallelism with instabilities of spinning fluid stars is briefly discussed.

DOI: 10.1103/PhysRevLett.123.221101

Introduction.—Recent data from gravitational-wave astronomy [1], as well as from electromagnetic very large baseline interferometry observations near galactic centers [2,3], support the black hole (BH) hypothesis: BHs commonly populate the cosmos, with masses spanning a range of (at least) 10 orders of magnitude. Yet, the elusiveness of the event horizon, the defining property of a BH, rules out an observational “proof” of their existence. Considering, thus, models of BH mimickers is a valuable tool to understanding the uniqueness of BH phenomenology.

Within the landscape of BH mimickers, bosonic stars (BSs) are particularly well motivated. They arise in simple and physically sound field theoretical models: complex, massive, bosonic fields (scalar [4,5] or vector [6]) minimally coupled to Einstein’s gravity. Dynamically, moreover, static, spherical BSs are viable; for some range of parameters, the lowest energy stars—the fundamental family (FF)—have a formation mechanism [7,8] and are perturbatively stable [6,9–11]. The properties and phenomenology of such static BSs have been considered at length (see, e.g., the reviews [12,13]), including dynamical situations such as orbiting binaries, from which gravitational waveforms have been extracted [14–16]. These studies unveiled a close parallel in the phenomenology of spherical BSs, regardless of their scalar or vector nature.

Astrophysically, however, rotation is ubiquitous and should, thus, be included in more realistic models of BSs. Both scalar [17–19] and vector [6,20] axisymmetric, spinning BSs (SBSs) have been constructed and some of their phenomenology has been studied [21,22]. Yet, their dynamical and stability properties, a key aspect of their physical viability, have remained essentially unexplored; see the discussion in Ref. [23].

In this Letter we describe the dynamical properties of SBSs, obtained from fully nonlinear numerical simulations of the corresponding Einstein-matter system. We provide evidence that scalar SBSs in the FF are prone to a nonaxisymmetric instability. Thus, such stars are transient states, in a dynamical formation scenario. Assuming an already formed scalar SBS, on the other hand, it collapses into a BH after a nonaxially symmetric instability develops. Vector SBSs (also known as spinning Proca stars), by contrast, are dynamically robust. In the formation scenario we find no evidence of an instability. In agreement, for already formed vector SBSs we observe that (i) even large perturbations are dissipated away, and (ii) some stars in excited families decay to the FF where they remain. This suggests that scalar (vector) SBSs have different dynamical properties and viability, and their toroidal (spheroidal) morphology provides a suggestive interpretation.

SBSs as stationary solutions.—Scalar and vector BSs, with and without spin, arise as equilibrium states in models with Lagrangian density $\mathcal{L} = R/(16\pi G) + \mathcal{L}_m$, where R is the Ricci scalar, G is Newton’s constant, and

$$\mathcal{L}_m = -\partial^\alpha \phi \partial_\alpha \bar{\phi} - \mu^2 \phi \bar{\phi}, \quad \mathcal{L}_m = -\frac{\mathcal{F}_{\alpha\beta} \bar{\mathcal{F}}^{\alpha\beta}}{4} - \frac{\mu^2}{2} \mathcal{A}_\alpha \bar{\mathcal{A}}^\alpha \quad (1)$$

describe the scalar and vector cases, respectively. The scalar (ϕ) and vector (\mathcal{A}_α) fields are complex valued, with conjugation denoted by an over bar, both with mass μ . As usual, $\mathcal{F} = d\mathcal{A}$. Henceforth, units with $G = 1 = c = \mu$ are used.

Scalar SBSs were first constructed numerically in Refs. [17,18] as asymptotically flat, stationary, and axisymmetric solutions of the above Einstein-Klein-Gordon system. They are a “mass torus” in general relativity; see Fig. 1 (left-hand panel). Scalar SBSs form a discrete set of families of continuous solutions. Each family is labeled by two integers: m , the azimuthal winding number, and n , the node (or overtone) number; see, e.g., Refs. [12,13,19,24,25]. The FF, which has the lowest energy, has $(m, n) = (1, 0)$. Fixing the family, i.e., (m, n) , SBSs are characterized by their total mass M and angular momentum J . They form a one-dimensional set, often labeled by M , and oscillation frequency ω . The (dynamically) most interesting solutions occur in between the Newtonian limit, $\omega \rightarrow 1$ and $M \rightarrow 0$, and the maximal mass solution. The latter occurs for $\omega \rightarrow \omega_{M\max}$ ($\simeq 0.775$ for the FF) and the Anowitt-Deser-Misner mass becomes highest, $M \rightarrow M_{\max}$ ($\simeq 1.315$ for the FF). In Table I we list the properties of two illustrative scalar SBSs used in the simulations below.

Vector SBSs were first reported as excited states ($n = 1$) in Refs. [6,20]. The FF was considered in Refs. [26,27]. The aforementioned description for scalar SBSs applies, *mutatis mutandis*. An important distinction, however, is that the energy distribution is now spheroidal, rather than toroidal [27]; see Fig. 1 (right-hand panel). Moreover, for the FF, $\omega_{M\max} \simeq 0.562$ and $M_{\max} \simeq 1.125$ [27]. For the excited family with $(m, n) = (1, 1)$, $\omega_{M\max} \simeq 0.839$

and $M_{\max} \simeq 1.568$ [6]. In Table I we list the properties of two (three) representative vector SBSs, in the FF [$(m, n) = (1, 1)$ family].

Dynamical formation of SBSs.—In the spherical case, numerical simulations established that both scalar [7] and vector [8] BSs form dynamically from a spherical “cloud” of dilute scalar or vector field. The cloud collapses due to its self-gravity. The ejection of energetic scalar or vector “particles”, dubbed gravitational cooling, allows the formation of a compact object.

For studying the formation of SBSs, with $m = 1$, the Hamiltonian, momentum, and (in the vector case) Gauss constraint are solved by appropriately choosing a Gaussian radial dependence for the key variables, together with a nonspherical profile; see Supplemental Material (SM, Sec. I [28], which includes additional Refs. [29,30]). For the scalar case, the “matter” initial data are

$$\phi(t, r, \theta, \varphi) = A r e^{-r^2/\sigma^2} \sin \theta e^{i(\varphi - \omega t)}, \quad (2)$$

where A, σ are constants and $e^{-i\omega t}$ is the harmonic dependence. Besides this unperturbed initial data, we also evolve perturbed initial data of two types: replacing in Eq. (2) $e^{i\varphi} \rightarrow e^{i\varphi}[1 + A_1 \cos(2\varphi)]$, or, alternatively, replacing $e^{i\varphi} \rightarrow e^{i\varphi} + A_2 e^{2i\varphi}$. A_1, A_2 are the amplitudes of the perturbations.

Fully nonlinear numerical evolutions of the Einstein-matter system using this initial data were carried out with the EINSTEIN TOOLKIT [40,41]; see SM, Sec. II [28], which includes additional Refs. [31–39]. Two choices of A were considered, both of which yield global data for the scalar cloud (M_{sc}, J_{sc}) close to that of equilibrium scalar SBS solutions. The first and second choices give $M_{sc}^{(1)} \sim 0.46 \sim J_{sc}^{(1)}$ and $M_{sc}^{(2)} \sim 0.89 \sim J_{sc}^{(2)}$, respectively. We have run simulations with both perturbed and unperturbed initial data, with $A_1 = 0, 0.001, 0.01, 0.05$ and $A_2 = 0, 0.05$. Typically, $\sigma = 40$. The evolutions are typically thousands of times longer than the dynamical timescale defined by μ .

All evolutions show the emergence of a nonaxisymmetric instability. The time at which the instability kicks in depends on the type and amplitude of the perturbation, but even the lowest mass unperturbed model ($M_{sc}^{(1)}$) exhibits

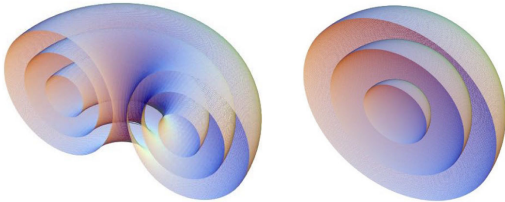


FIG. 1. Surfaces of constant energy density for illustrative SBSs. Left: Scalar configuration 2_S . Right: Vector configuration 1_P . The toroidal vs spheroidal nature is clear.

TABLE I. Physical properties of some illustrative SBSs. The second row identifies if they are scalar (S) or vector or Proca (P). All solutions have $m = 1$ and none have an ergo region.

Configuration	1_S	2_S	1_P	2_P	3_P	4_P	5_P
Type (S or P)	S	S	P	P	P	P	P
n	0	0	0	0	1	1	1
ω	0.90	0.83	0.95	0.90	0.95	0.90	0.85
M	1.119	1.281	0.534	0.726	1.149	1.456	1.564
J	1.153	1.338	0.543	0.750	1.171	1.500	1.622

nonaxisymmetric features at a sufficiently long timescale [$t \sim \mathcal{O}(10^4)$]. The instability generically triggers a larger ejection of angular momentum than mass, reshaping the toroidal energy distribution into a spherical one. This suggests that the asymptotic end state of the cloud evolution is either a spherical (nonspinning) scalar BS or even, merely, ejected debris carrying all angular momentum and energy.

As an illustration, Fig. 2 exhibits snapshots of the equatorial plane evolution of the energy density ρ_E (left-hand panels) and angular momentum density ρ_J (middle left-hand panels) for the unperturbed scalar initial data with mass $M_{\text{sc}}^{(2)}$ [42]. Initially, the collapse preserves axial symmetry. Around $t \sim 4000$, however, the nonaxisymmetric instability is visible, producing a fragmentation event: the star splits into a roughly symmetric orbiting binary. The binary is, nonetheless, bound and recollapses to a deformed spinning star, around $t \sim 6500$. This star breaks into two

asymmetric pieces, which again recollapse into a spheroidal star with angular momentum. Around $t \sim 10000$, this residual, still evolving, star has $(M, J) = (0.49, 0.16)$, evaluated up to $r = 30$, and an oscillation frequency $\omega \sim 0.96$. For this ω , the FF static scalar BS has $(M, J) = (0.45, 0)$. Thus, this (or a neighbor) static scalar BS appears to be asymptotically approached, after the remaining J is shed away.

Now consider the formation of a vector SBS. The construction of initial data is more complex due to the Gauss constraint [8,44]. After a 3 + 1 splitting of \mathcal{A}_μ , the key variables are the scalar and three-vector potentials together with the electric field. The first of these admits a solution almost identical to Eq. (2), but the others are more involved; see SM, Sec. I [28]. These initial data can again be perturbed. We have considered a perturbation analogous to the first type considered in the scalar case; the perturbation amplitudes studied were $A_1 = A_2 = 0, 0.05$. Initial data describing a Proca cloud with three different values of global data were used: $M_{\text{Pc}}^{(1)} \sim 0.46 \sim J_{\text{Pc}}^{(1)}$, $M_{\text{Pc}}^{(2)} \sim 0.56 \sim J_{\text{Pc}}^{(2)}$, and $M_{\text{Pc}}^{(3)} \sim 0.77 \sim J_{\text{Pc}}^{(3)}$.

The unperturbed models' evolutions are instability-free during the simulations, lasting up to $t \sim 10^4$. This is illustrated by the third and fourth columns in Fig. 2, which show snapshots of the time evolution of the unperturbed Proca cloud $M_{\text{Pc}}^{(2)}$. The gravitational collapse ejects part of the mass and angular momentum, which shows the gravitational cooling mechanism at play. At $t \sim 10^4$ the star has $(M, J) \sim (0.25, 0.30)$, evaluated up to $r = 30$, and $\omega \sim 0.99$. For this ω , the FF vector SBS has $(M, J) = (0.247, 0.249)$; see SM, Sec. III [28]. Thus, this (or a neighbor) vector SBS appears to be asymptotically approached. For the perturbed initial Proca clouds, on the other hand, the energy density oscillates strongly. Nonetheless, no sudden loss of angular momentum is observed, which suggests the end point is still a vector SBS.

Evolution of equilibrium SBSs.—The dichotomy observed in the formation scenario can be further assessed by considering the dynamics of SBSs obtained as equilibrium solutions of the corresponding Einstein-matter system. A perturbative stability analysis of these SBSs, such as the ones in Refs. [6,9,10] for the spherical case, seems challenging. Thus, we resort to nonlinear numerical evolutions of the Einstein-matter system, analogous to the ones in the formation scenario, but now starting with the equilibrium solutions as initial data. This generalizes the evolutions in Ref. [43] for nonspinning BSs.

We first consider the scalar SBSs. Figure 3 shows the time evolution of model 2_S . Up to $t \sim 1000$ the star remains essentially undisturbed; then, following the development of a nonaxisymmetric perturbation, see upper panels, the star pinches off into two fragments. The resulting binary is gravitationally bound and collapses into a BH at $t \sim 1200$. This is diagnosed by both the appearance of an apparent

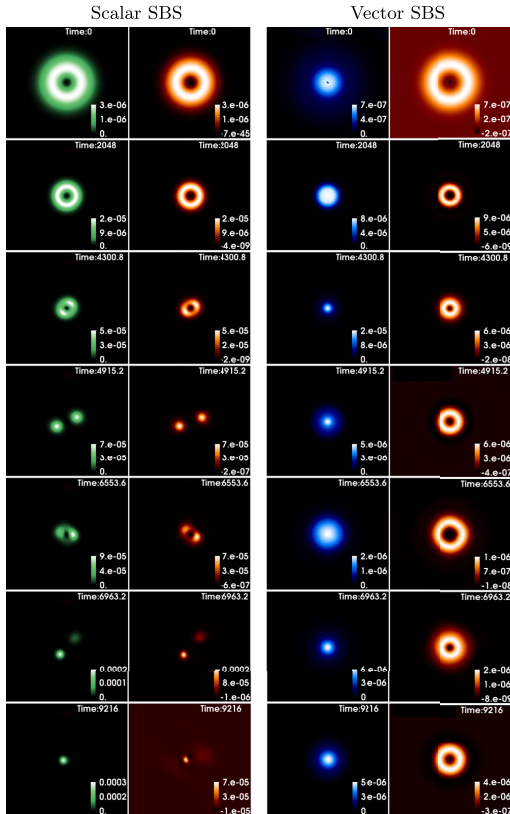


FIG. 2. Time evolution of an equatorial cut of ρ_E (blue or green) and ρ_J (orange) in the formation scenario of a scalar (left-hand side) or a vector (right-hand side) SBS.

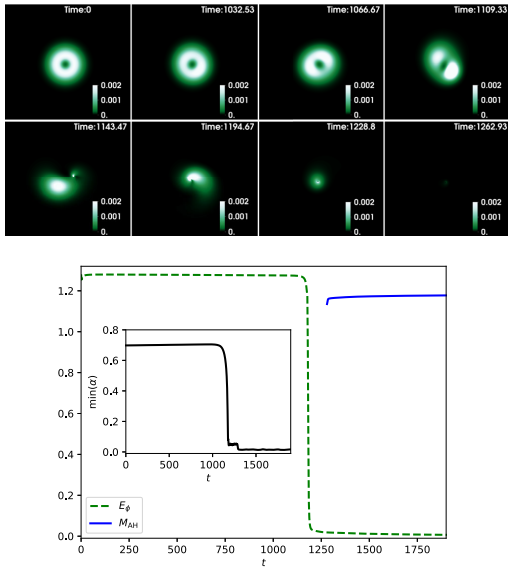


FIG. 3. Time evolution of a scalar SBS, model 2_s . Six sequential snapshots of ρ_E (top panels). Time runs left to right, first to second row. Total scalar field energy and apparent horizon mass (main panel) and lapse function (inset).

horizon, whose mass is shown in the main panel, and the vanishing of the lapse function α , as seen in the inset of Fig. 3. A similar evolution is observed for model 1_s . This confirms that scalar SBSs, even in the FF, are prone to a nonaxisymmetric instability. Unlike the formation scenario, here the instability leads to a complete gravitational collapse, likely due to the more compact initial data.

The behavior of the vector SBSs is distinct. FF solutions, such as models 1_p and 2_p , show no sign of instability, in the absence of large perturbations. They neither disperse away nor collapse to a BH up to $t \sim 4000$, the time at which the drift in the Proca field energy and angular momentum for model 1_p is 2.0% and 2.2%, respectively, whereas for model 2_p , the drift is less than 1%. We further tested the dynamical robustness of vector SBSs by perturbing models 1_p and 2_p and by considering some excited states, such as model $3_p - 5_p$. Figure 4 exhibits the time evolution of two examples: (i) model 1_p with a perturbation of the sort considered in the formation scenario for the vector case, and with a sufficiently large amplitude to visibly distort the star (see first panel), and (ii) the excited model 3_p . In the first case, the perturbation, albeit large enough to deform the morphology of the star away from its spheroidal shape, is dissipated away, and the star recovers its shape. In the second case, the excited state structure of the star is manifest in the composite, Saturn-like, structure of its energy distribution [20]. After $t \sim 1000$, the star abruptly

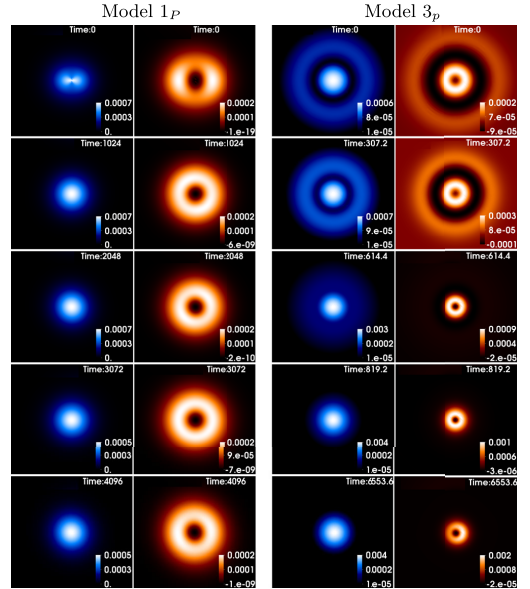


FIG. 4. Time evolution of vector SBSs. Equatorial cut of ρ_E (blue) and ρ_I (orange) for the FF model 1_p with a perturbation (left-hand side) and the excited model 3_p (right-hand side).

loses energy and angular momentum, until $t \sim 3000$ when it asymptotically tends to a new equilibrium configuration; see SM, Sec. IV [28]. This new configuration has no nodes and it is close to model 2_p . Thus, the star migrates from the excited family to the FF, where it settles, advocating the stability of the latter. Excited models 4_p and 5_p , on the other hand, collapse to a BH.

Interpretation and further remarks.—The contrasting dynamical properties of the scalar or vector SBSs break the phenomenological (qualitative) degeneracy observed between these two types of BSs in the spherical case. It is tempting to attribute this contrast to the different morphology of these stars, as exhibited in Fig. 1. This interpretation is partly supported by the analogy with dynamical instabilities in differentially rotating relativistic (neutron) stars [45]. In that case the existence of a toroidal shape has been suggested to be a necessary condition for the development of nonaxisymmetric corotational instabilities [46,47]. In fact, the pinching instabilities and fragmentation exhibited in the scalar models above are reminiscent of evolutions of unstable toroidal fluid stars [48,49], but also of other corotational instabilities observed in toroidal systems such as the Papaloizou-Pringle instability in accretion disks [50]. Preliminary results, moreover, indicate that vector SBSs with $m = 2$ (which are toroidal) are also unstable. The analogy with corotational instabilities in relativistic fluid stars will be further explored elsewhere.

The instability of scalar SBSs may explain the inability to find them as end points in the evolution of orbiting binaries of (nonspinning) BSs [51,52]. By the same token, however, vector SBSs should form in the equivalent vector scenarios. This suggests revisiting the work in Ref. [16] using constraint-abiding initial data. A related question pertains to the impact of matter self-interactions in the dynamics reported herein.

We thank Carlos Palenzuela, Darío Núñez, Juan Carlos Degollado, and Sergio Gimeno-Soler for useful discussions and valuable comments. This work has been supported by the Spanish Agencia Estatal de Investigación (Grants No. AYA2015-66899-C2-1-P and No. PGC2018-095984-B-I00), by the Generalitat Valenciana (ACIF/2015/216, GRISOLIAP/2019/029, PROMETEO/2019/071), by the Fundação para a Ciência e a Tecnologia (FCT) Projects No. PTDC/FIS-OUT/28407/2017, No. UID/MAT/04106/2019 (CIDMA), and No. UID/FIS/00099/2013 (CENTRA), by national funds (OE), through FCT, I. P., in the scope of the framework contract foreseen in the numbers 4, 5, and 6 of the article 23, of the Decree-Law 57/2016, changed by Law 57/2017. This work has further been supported by the European Union's Horizon 2020 research and innovation (RISE) programmes H2020-MSCA-RISE-2015 Grants No. StronGrHEP-690904 and No. H2020-MSCA-RISE-2017, Grant No. FunFiCO-777740. We would like to acknowledge networking support by the COST Action GWverse CA16104. M. Z. acknowledges financial support provided by FCT/Portugal through the IF programme, Grant No. IF/00729/2015. P. C. acknowledges the Ramon y Cajal funding (RYC-2015-19074) supporting his research. Computations have been performed at the Servei d'Informàtica de la Universitat de València, on the "Baltasar Sete-Sois" cluster at IST, and at MareNostrum (via PRACE Tier-0 Grant No. 2016163948).

[1] B. P. Abbott *et al.* (LIGO Scientific Collaboration and Virgo Collaborations), *Phys. Rev. X* **9**, 031040 (2019).
 [2] R. Abuter, A. Amorim, M. Bauböck, J. P. Berger, H. Bonnet, W. Brandner, Y. Clénet, V. Coudé Du Foresto, and P. T. de Zeeuw (Gravity Collaboration), *Astron. Astrophys.* **618**, L10 (2018).
 [3] K. Akiyama *et al.* (Event Horizon Telescope), *Astrophys. J.* **875**, L1 (2019).
 [4] D. J. Kaup, *Phys. Rev.* **172**, 1331 (1968).
 [5] R. Ruffini and S. Bonazzola, *Phys. Rev.* **187**, 1767 (1969).
 [6] R. Brito, V. Cardoso, C. A. R. Herdeiro, and E. Radu, *Phys. Lett. B* **752**, 291 (2016).
 [7] E. Seidel and W.-M. Suen, *Phys. Rev. Lett.* **72**, 2516 (1994).
 [8] F. Di Giovanni, N. Sanchis-Gual, C. A. R. Herdeiro, and J. A. Font, *Phys. Rev. D* **98**, 064044 (2018).
 [9] M. Gleiser and R. Watkins, *Nucl. Phys.* **B319**, 733 (1989).
 [10] T. D. Lee and Y. Pang, *Nucl. Phys.* **B315**, 477 (1989).
 [11] N. Sanchis-Gual, C. Herdeiro, E. Radu, J. C. Degollado, and J. A. Font, *Phys. Rev. D* **95**, 104028 (2017).

[12] F. E. Schunck and E. W. Mielke, *Classical Quantum Gravity* **20**, R301 (2003).
 [13] S. L. Liebling and C. Palenzuela, *Living Rev. Relativity* **15**, 6 (2012); **20**, 5 (2017).
 [14] C. Palenzuela, I. Olabarrieta, L. Lehner, and S. L. Liebling, *Phys. Rev. D* **75**, 064005 (2007).
 [15] C. Palenzuela, L. Lehner, and S. L. Liebling, *Phys. Rev. D* **77**, 044036 (2008).
 [16] N. Sanchis-Gual, C. Herdeiro, J. A. Font, E. Radu, and F. Di Giovanni, *Phys. Rev. D* **99**, 024017 (2019).
 [17] F. E. Schunck and E. W. Mielke, *Phys. Lett. A* **249**, 389 (1998).
 [18] S. Yoshida and Y. Eriguchi, *Phys. Rev. D* **56**, 762 (1997).
 [19] B. Kleihaus, J. Kunz, M. List, and I. Schaffer, *Phys. Rev. D* **77**, 064025 (2008).
 [20] C. Herdeiro, E. Radu, and H. Runarsson, *Classical Quantum Gravity* **33**, 154001 (2016).
 [21] F. H. Vincent, Z. Meliani, P. Grandclément, E.ourgoulhon, and O. Straub, *Classical Quantum Gravity* **33**, 105015 (2016).
 [22] Z. Meliani, F. H. Vincent, P. Grandclément, E.ourgoulhon, R. Monceau-Baroux, and O. Straub, *Classical Quantum Gravity* **32**, 235022 (2015).
 [23] C. A. R. Herdeiro and E. Radu, *Phys. Rev. Lett.* **112**, 221101 (2014).
 [24] P. Grandclément, C. Somé, and E.ourgoulhon, *Phys. Rev. D* **90**, 024068 (2014).
 [25] C. Herdeiro and E. Radu, *Classical Quantum Gravity* **32**, 144001 (2015).
 [26] C. A. R. Herdeiro and E. Radu, *Phys. Rev. Lett.* **119**, 261101 (2017).
 [27] C. Herdeiro, I. Perapechka, E. Radu, and Ya. Shnir, *Phys. Lett. B* **797**, 134845 (2019).
 [28] See Supplemental Material at <http://link.aps.org/supplemental/10.1103/PhysRevLett.123.221101> for further details on the initial data, code assessment and profiles and evolutions of physical quantities, which includes Refs. [29–39].
 [29] I. Cordero-Carrion, P. Cerda-Duran, H. Dimmelmeier, J. L. Jaramillo, J. Novak, and E.ourgoulhon, *Phys. Rev. D* **79**, 024017 (2009).
 [30] H. Okawa, H. Witek, and V. Cardoso, *Phys. Rev. D* **89**, 104032 (2014).
 [31] F. Löffler, J. Faber, E. Bentivegna, T. Bode, P. Diener *et al.*, *Classical Quantum Gravity* **29**, 115001 (2012).
 [32] M. Zilhão and F. Löffler, *Int. J. Mod. Phys. A* **28**, 1340014 (2013).
 [33] E. Schnetter, S. H. Hawley, and I. Hawke, *Classical Quantum Gravity* **21**, 1465 (2004).
 [34] Carpet: Adaptive mesh refinement for the cactus framework, <http://www.carpetcode.org/>.
 [35] J. Thornburg, *Classical Quantum Gravity* **21**, 743 (2004).
 [36] J. Thornburg, *Phys. Rev. D* **54**, 4899 (1996).
 [37] H. Witek and M. Zilhão, CANUDA, <https://bitbucket.org/canuda/>.
 [38] U. Sperhake, *Phys. Rev. D* **76**, 104015 (2007).
 [39] D. Brown, P. Diener, O. Sarbach, E. Schnetter, and M. Tiglio, *Phys. Rev. D* **79**, 044023 (2009).
 [40] EinsteinToolkit, Einstein Toolkit: Open Software for Relativistic Astrophysics, <http://einstein toolkit.org/>.
 [41] F. Löffler, *Classical Quantum Gravity* **29**, 115001 (2012).
 [42] The energy and angular momentum densities are the ones defined from the Komar integrals, as in Refs. [16,43].

-
- [43] P. V. P. Cunha, J. A. Font, C. Herdeiro, E. Radu, N. Sanchis-Gual, and M. Zilhão, *Phys. Rev. D* **96**, 104040 (2017).
- [44] M. Zilhão, H. Witek, and V. Cardoso, *Classical Quantum Gravity* **32**, 234003 (2015).
- [45] V. Paschalidis and N. Stergioulas, *Living Rev. Relativity* **20**, 7 (2017).
- [46] M. Saijo, T. W. Baumgarte, and S. L. Shapiro, *Astrophys. J.* **595**, 352 (2003).
- [47] A. L. Watts, N. Andersson, and D. I. Jones, *Astrophys. J.* **618**, L37 (2005).
- [48] B. Zink, N. Stergioulas, I. Hawke, C. D. Ott, E. Schnetter, and E. Mueller, *Phys. Rev. Lett.* **96**, 161101 (2006).
- [49] B. Zink, N. Stergioulas, I. Hawke, C. D. Ott, E. Schnetter, and E. Mueller, *Phys. Rev. D* **76**, 024019 (2007).
- [50] K. Kiuchi, M. Shibata, P. J. Montero, and J. A. Font, *Phys. Rev. Lett.* **106**, 251102 (2011).
- [51] M. Bezares, C. Palenzuela, and C. Bona, *Phys. Rev. D* **95**, 124005 (2017).
- [52] C. Palenzuela, P. Pani, M. Bezares, V. Cardoso, L. Lehner, and S. Liebling, *Phys. Rev. D* **96**, 104058 (2017).

Dynamical formation and stability of fermion-boson starsFabrizio Di Giovanni¹, Saeed Fakhry^{2,1}, Nicolas Sanchis-Gual³, Juan Carlos Degollado⁴, and José A. Font^{1,5}¹*Departament de Astronomia y Astrofísica, Universitat de València, Dr. Moliner 50, 46100 Burjassot (València), Spain*²*Department of Physics, Shahid Beheshti University, G. C., Evin, Tehran 19839, Iran*³*Centro de Astrofísica e Gravitação—CENTRA, Departamento de Física, Instituto Superior Técnico—IST, Universidade de Lisboa—UL, Avenida Rovisco Pais 1, Lisbon 1049-001, Portugal*⁴*Instituto de Ciencias Físicas, Universidad Nacional Autónoma de México, Apdo. Postal 48-3, 62251 Cuernavaca, Morelos, México*⁵*Observatori Astronòmic, Universitat de València, C/ Catedrático José Beltrán 2, 46980 Paterna (València), Spain*

(Received 22 June 2020; accepted 30 September 2020; published 27 October 2020)

Gravitationally bound structures composed by fermions and scalar particles known as fermion-boson stars are regular and static configurations obtained by solving the coupled Einstein-Klein-Gordon-Euler system. In this work, we discuss one possible scenario through which these fermion-boson stars may form by solving numerically the Einstein-Klein-Gordon-Euler system under the simplifying assumption of spherical symmetry. Our initial configurations assume an already existing neutron star surrounded by an accreting cloud of a massive and complex scalar field. The results of our simulations show that once part of the initial scalar field is expelled via gravitational cooling the system gradually oscillates around an equilibrium configuration that is asymptotically consistent with a static solution of the system. The formation of fermion-boson stars for large positive values of the coupling constant in the self-interaction term of the scalar-field potential reveal the presence of a node in the scalar field. This suggests that a fermionic core may help stabilize configurations with nodes in the bosonic sector, as happens for purely boson stars in which the ground state and the first excited state coexist.

DOI: [10.1103/PhysRevD.102.084063](https://doi.org/10.1103/PhysRevD.102.084063)**I. INTRODUCTION**

Identifying the relevance scalar fields may have for astrophysics and cosmology, in particular as potential components of the dark-matter content of the Universe, has long received considerable attention [1–4]. Different scalar fields have been considered, namely, the dilaton in string theories [5,6], the Higgs boson in the standard model of particle physics [7,8], the inflaton in studies of the early Universe [9,10], or the axion as a possible component of cold dark matter [11–14].

It has been argued that ultralight bosons form localized and coherently oscillating configurations very similar to Bose-Einstein condensates [15,16]. When the mass of the bosonic particle is around 10^{-22} eV [17,18], these condensates provide an alternative to the standard approach to explain large-scale structure formation through dark-matter seeds. For heavier bosons, the bound configurations are smaller and may have the typical size and mass of a stellar compact object such as a neutron star. These objects are generically known as boson stars [19].

Boson stars are gravitationally bound configurations of scalar particles. Since the seminal works of Kaup [20] and Ruffini and Bonnazola [21], their description has been

generalized in several ways including self-interaction [22], charge [23], rotation [24,25], oscillating soliton stars [26], stars with more than a single scalar field [27,28], and even vector fields (in which case the bosonic star is known as a Proca star [29]). Reviews on the subject can be found in Refs. [30,31].

If such bosonic configurations could form from some primordial gas, it is natural to assume that other particles, such as fermions, could also be present during the condensation. Therefore, it would seem theoretically possible that objects made out of a mixture of both bosons and fermions might also form. Even if the original configurations were mainly composed by either bosons or fermions, they could be susceptible to further capture fermions and bosons through accretion giving rise to mixed configurations. It is thus a theoretically interesting question to investigate the properties of these macroscopic composites of fermions and bosons, referred in the literature as fermion-boson stars [32–36] and to discuss possible means by which they might form. This is the focus of this paper. Here we propose a dynamical scenario in which a fermionic star (FS) (modeled as a polytropic star for simplicity) accretes part of the scalar field, while part of it is radiated to infinity, and a mixed fermion-boson star forms.

The gravitational condensation of a primordial gas and the subsequent radiation of part of the bosonic field has been dubbed gravitational cooling and has been addressed in [37] for purely scalar fields and in [38] for vector fields. Using numerical-relativity simulations, those studies have shown the dynamical formation of boson stars and Proca stars, respectively, under the assumption of spherical symmetry. In order to be astrophysically relevant, a gravitationally bound system that forms dynamically must be stable for times much longer than its characteristic dynamical time scale. The stability properties of boson stars have been considered in [39–46]. In Ref. [47], Seidel and Suen discussed the dynamical evolution of perturbed boson stars finding, in particular, that unstable stars migrate to the stability region of static configurations which suggests the formation of boson stars under generic initial conditions. Further studies on the formation of boson stars were performed in [37] in general relativity and in [48,49] in the Newtonian regime. These studies concluded that self-gravitating, scalar-field stellar systems settle down into equilibrium configurations. We note that this conclusion does not only apply to the scalar case, but it is also valid for the vector counterparts of boson stars, i.e., Proca stars, as has recently been reported in [38].

The purpose of this work is twofold: on the one hand, we aim to describe the dynamical formation of fermion-boson stars; on the other hand, we will analyze the stability properties of those configurations considering a strong self-interaction term in the Klein-Gordon potential of the bosonic part. For this study, and for the sake of simplicity, we shall focus on fermion-boson stars assuming spherical symmetry. The starting point of our analysis assumes a preexisting neutron star (described with a polytropic equation of state) surrounded by a cloud of scalar field. Different initial configurations have evolved in time using numerical-relativity simulations. We find that the fermionic star is able to capture part of the scalar field and the new system evolves toward an almost static configuration giving rise to a stable fermion-boson star. In addition to show that the dynamical formation of mixed stars is possible, we also obtain the corresponding equilibrium configurations for fermion-boson stars with different values of the self-interaction potential and we study their stability properties under spherical perturbations.

This paper is organized as follows: in Sec. II, we introduce the matter model we employ to describe fermion-boson stars and set up the basic equations. Section III addresses the initial data for the dynamical formation of the mixed stars and the initial static configurations considering a self-interaction term in the bosonic sector. The numerical framework for our simulations is described in Sec. IV, while in Sec. V the results of the evolutions are presented. Finally, our conclusions and final remarks are reported in Sec. VI. Our units are such that the relevant fundamental constants are equal to one ($G = c = \hbar = 1$).

II. SETUP

In this study, we consider that bosonic and fermionic matter only interact through gravity. Therefore, our model is described by a total stress-energy tensor which is the sum of two contributions, one from a perfect fluid and one from a complex scalar field,

$$T_{\mu\nu} = T_{\mu\nu}^{\text{fluid}} + T_{\mu\nu}^{\phi}, \quad (1)$$

where

$$T_{\mu\nu}^{\text{fluid}} = [\rho(1 + \epsilon) + P]u_{\mu}u_{\nu} + Pg_{\mu\nu}, \quad (2)$$

$$T_{\mu\nu}^{\phi} = -\frac{1}{2}g_{\mu\nu}\partial_{\alpha}\bar{\phi}\partial^{\alpha}\phi - V(\phi) + \frac{1}{2}(\partial_{\mu}\bar{\phi}\partial_{\nu}\phi + \partial_{\mu}\phi\partial_{\nu}\bar{\phi}). \quad (3)$$

The perfect fluid is described by its pressure P , its rest-mass density ρ , and its internal energy ϵ , while u^{μ} is the fluid four-velocity. We consider a quartic self-interaction potential for the scalar field ϕ ,

$$V(\phi) = \frac{1}{2}\mu^2\bar{\phi}\phi + \frac{1}{4}\lambda(\bar{\phi}\phi)^2, \quad (4)$$

where μ is the mass of the bosonic particle and λ is the self-interaction parameter; the bar symbol in the last two equations denotes complex conjugation. The equations of motion are given by the conservation laws of the stress-energy tensor and the baryonic particles

$$\nabla_{\mu}T_{\text{fluid}}^{\mu\nu} = 0, \quad (5)$$

$$\nabla_{\mu}(\rho u^{\mu}) = 0 \quad (6)$$

for the fermionic matter, and by the Klein-Gordon equation

$$\nabla_{\mu}\nabla^{\mu}\phi = \mu^2\phi + \lambda|\phi|^2\phi \quad (7)$$

for the complex scalar field, together with the Einstein equation $G_{\mu\nu} = 8\pi T_{\mu\nu}$ governing the spacetime dynamics. Differential operator ∇_{μ} is the covariant derivative with respect to the four-metric $g_{\mu\nu}$. The set of equations (5) and (6) is closed by an equation of state (EOS) for the fluid. We consider both the polytropic EOS and the ideal-gas EOS,

$$P = K\rho^{\Gamma} = (\Gamma - 1)\rho\epsilon. \quad (8)$$

The polytropic EOS is employed to build the equilibrium initial data while the Γ -law is used for the evolutions as it would allow to take into account eventual shock-heating (thermal) effects. All equilibrium models we consider are constructed using $K = 100$ and $\Gamma = 2$. In the next subsections, we specify our choice for the metric and the

relevant equations for both the construction of the static models and the evolution.

A. Basic equations for the equilibrium configurations

Our formalism for the construction of equilibrium configurations of fermion-boson stars relies on the choice of a spherically symmetric metric in Schwarzschild coordinates,

$$ds^2 = -\alpha(r)^2 dt^2 + \tilde{a}(r)^2 dr^2 + r^2(d\theta^2 + \sin^2\theta d\varphi^2), \quad (9)$$

written in terms of two geometrical functions $\tilde{a}(r)$ and $\alpha(r)$. We set a harmonic time dependence ansatz for the complex scalar field $\phi(t, r) = \phi(r)e^{-i\omega t}$ where ω is its eigenfrequency, and we consider the quartic self-interaction potential for the field given by Eq. (4). We replace the self-interaction parameter λ by the dimensionless variable Λ , defined as

$$\Lambda = \frac{M_{\text{Pl}}^2 \lambda}{4\pi\mu^2}, \quad (10)$$

in which $M_{\text{Pl}} = \sqrt{\frac{\hbar c}{G}}$ indicates the Planck mass (which is one in our units). In the following, we consider a scaled radial coordinate $r \rightarrow r\mu$ (together with $M \rightarrow M\mu$, $t \rightarrow t\mu$, $\omega \rightarrow \omega/\mu$). Some comments about this scaling are in order. It is well known (see, e.g., [31]) that the maximum mass of the system for an isolated boson star in general relativity depends solely on the mass of the boson particle,

$$M_{\text{max}} = 0.633 \frac{M_{\text{Planck}}^2}{\mu} \sim 0.633 M_{\odot} \frac{1.34 \times 10^{-10} \text{ eV}}{\mu[\text{eV}]}. \quad (11)$$

Therefore, depending on the value of μ , this maximum mass can range (in solar mass units) from very small masses to masses comparable to that of dark matter halos in galaxies. In order to have objects with astrophysical relevance (from stars to dark matter halos), ultralight fields must be considered, with a boson mass in the range $\mu = \{10^{-10}, 10^{-24}\}$ eV [24]. In this work, we also consider fermionic stars without restricting to neutron stars, but our analysis can nonetheless be applied directly to them. In the neutron star case, there is another mass involved (the neutron star mass) that determines the mass of the boson particle μ . If one assumes that the maximum mass of a neutron star is around $2M_{\odot}$, the boson star will have a maximum mass of order $1M_{\odot}$ and, therefore, μ would be of the order of 10^{-10} eV.

It is also worth commenting on the relationship between the units used in our numerical code and physical units. From the previous discussion, it follows that if the mass of the particle is given in eV, all masses reported in this paper are expressed in M_{\odot} . To obtain the distances in meters and the time in seconds, the following conversion must be applied:

$$r(m) = \frac{G}{c^2} M_{\text{ADM}} r (\text{c.u.}), \quad (12)$$

$$t(s) = \frac{G}{c^3} M_{\text{ADM}} t (\text{c.u.}), \quad (13)$$

where c.u. stands for code units and M_{ADM} is the so-called Anowitt-Desser-Misner (ADM) mass [see Eq. (42) below] expressed in kg. For example, if $\mu = 1.34 \times 10^{-10}$ eV, model MS9 in Table III below has $M_{\text{ADM}} = 1.202 M_{\odot}$, its total radius is $R_T = 12.56 \times 10^3$ m, and the frequency of the scalar field is $\omega = 1.79 \times 10^5$ Hz.

Assuming a static fluid, $u^\mu = (-1/\alpha, 0, 0, 0)$, Einstein's equations lead to the following ordinary differential equations (ODEs):

$$\frac{d\tilde{a}}{dr} = \frac{\tilde{a}}{2} \left(\frac{1 - \tilde{a}^2}{r} + 4\pi r \left[\left(\frac{\omega^2}{\alpha^2} + \mu^2 + \frac{\lambda}{2} \phi^2 \right) \tilde{a}^2 \phi^2 + \Psi^2 + 2\tilde{a}^2 \rho(1 + \epsilon) \right] \right), \quad (14)$$

$$\frac{d\alpha}{dr} = \frac{\alpha}{2} \left(\frac{\tilde{a}^2 - 1}{r} + 4\pi r \left[\left(\frac{\omega^2}{\alpha^2} - \mu^2 - \frac{\lambda}{2} \phi^2 \right) \tilde{a}^2 \phi^2 + \Psi^2 + 2\tilde{a}^2 P \right] \right), \quad (15)$$

$$\frac{d\phi}{dr} = \Psi, \quad (16)$$

$$\frac{d\Psi}{dr} = - \left(1 + \tilde{a}^2 - 4\pi r^2 \tilde{a}^2 (\mu^2 \phi^2 + \frac{\lambda}{2} \phi^4 + \rho(1 + \epsilon) - P) \right) \frac{\Psi}{r} - \left(\frac{\omega^2}{\alpha^2} - \mu^2 - \lambda \phi^2 \right) \tilde{a}^2 \phi^2, \quad (17)$$

$$\frac{dP}{dr} = -[\rho(1 + \epsilon) + P] \frac{\alpha'}{\alpha}, \quad (18)$$

where the prime indicates the derivative with respect to r . The system is closed by the EOS (8). To solve these equations, it is necessary to apply certain initial and boundary conditions that are consistent with the geometry and physical behavior of the mixed stars. In Sec. III B, we will introduce these conditions.

B. Basic equations for the evolution

For the numerical evolutions, we consider a spherically symmetric metric in isotropic coordinates,

$$ds^2 = -\alpha(\hat{r})^2 dt^2 + \psi(\hat{r})^4 \gamma_{ij} (dx^i + \beta^i dt)(dx^j + \beta^j dt), \quad (19)$$

where α is the lapse function and β^i is the shift vector. The spatial three-dimensional metric components are

$$\gamma_{ij}dx^i dx^j = a(\hat{r})d\hat{r}^2 + b(\hat{r})\hat{r}^2(d\theta^2 + \sin^2\theta d\varphi^2). \quad (20)$$

We note that a and \tilde{a} should not be confused as they are different functions; $a(\hat{r})$ and $b(\hat{r})$ are the metric functions for the isotropic metric, \hat{r} denotes the isotropic radial coordinate (see Sec. VB for details), and $\psi^4 \equiv e^{4\chi}$ is the conformal factor. To simplify the notation, we will substitute $\hat{r} \rightarrow r$ in the following, keeping in mind that all equations and definitions refer nonetheless to the isotropic radial coordinate.

Our choice of evolution equations for the spacetime variables follows Brown's covariant form [50,51] of the Baumgarte-Shapiro-Shibata-Nakamura (BSSN) formulation of Einstein's equations [52–54]. The evolved quantities used in this work are the spatial metric γ_{ij} , the conformal factor χ , the trace of the extrinsic curvature K , its traceless part $A_a = A'_r$, $A_b = A_\theta^\theta = A_\varphi^\varphi$, and the radial component of the so-called conformal connection functions Δ^r (see [53,54] for definitions).

We will not report here explicitly the full system of evolution equations as it can be found, e.g., in Ref. [55]. We remind the reader that the equations involve matter source terms arising from suitable projections of the total stress-energy tensor $T_{\mu\nu}$, namely, the energy density \mathcal{E} , the momentum density j_i measured by a normal observer n^μ , and the spatial projection of the energy-momentum tensor S_{ij} . These quantities read as

$$\mathcal{E} = n^\mu n^\nu T_{\mu\nu}, \quad (21)$$

$$j_i = -\gamma_i^\mu n^\nu T_{\mu\nu}, \quad (22)$$

$$S_{ij} = \gamma_i^\mu \gamma_j^\nu T_{\mu\nu}. \quad (23)$$

In our setup, these quantities are obtained by adding up the contributions of both the fluid and the scalar field. The explicit expressions we use are listed at the end of this section.

The gauge conditions we employ in our simulations are the so-called “nonadvective 1 + log” gauge condition for the lapse function α and a variation of the gamma-driver condition for the shift vector β^r . Further details regarding the BSSN evolution equations, gauge conditions, and the formalism for the hydrodynamic equations can be found in [55].

Following our previous work [56], we use two auxiliary variables

$$\Pi = \frac{1}{\alpha}(\partial_t - \beta^r \partial_r)\phi, \quad (24)$$

$$\Psi = \partial_r \phi \quad (25)$$

to cast the Klein-Gordon equation (7) as a first-order system of evolution equations,

$$\partial_t \phi = \beta^r \partial_r \phi + \alpha \Pi, \quad (26)$$

$$\begin{aligned} \partial_t \Pi = & \beta^r \partial_r \Pi + \frac{\alpha}{ae^{4\chi}} \left[\partial_r \Psi + \Psi \left(\frac{2}{r} - \frac{\partial_r a}{2a} + \frac{\partial_r b}{b} + 2\partial_r \chi \right) \right] \\ & + \frac{\Psi}{ae^{4\chi}} + \alpha K \Pi - \alpha(\mu^2 + \lambda \phi \bar{\phi}), \end{aligned} \quad (27)$$

$$\partial_t \Psi = \beta^r \partial_r \Psi + \Psi \partial_r \beta^r + \partial_r(\alpha \Pi). \quad (28)$$

Finally, the system of equations is closed by two constraint equations, namely, the Hamiltonian constraint and the momentum constraint, which read as

$$\mathcal{H} = R - (A_a^2 + 2A_b^2) + \frac{2}{3}K^2 - 16\pi\mathcal{E} = 0, \quad (29)$$

$$\begin{aligned} \mathcal{M}_r = & \partial_r A_a - \frac{2}{3}\partial_r K + 6A_a \partial_r \chi + (A_a - A_b) \left(\frac{2}{r} + \frac{\partial_r b}{b} \right) \\ & - 8\pi j_r = 0, \end{aligned} \quad (30)$$

where R is the Ricci scalar.

The bosonic contribution to the matter source terms is

$$\mathcal{E}^\phi = \frac{1}{2} \left(\bar{\Pi} \Pi + \frac{\bar{\Psi} \Psi}{e^{4\chi} a} \right) + \frac{1}{2} \mu^2 \bar{\phi} \phi + \frac{1}{4} \lambda (\bar{\phi} \phi)^2, \quad (31)$$

$$j_r^\phi = -\frac{1}{2} (\bar{\Pi} \Psi + \bar{\Psi} \Pi), \quad (32)$$

$$S_a^\phi = \frac{1}{2} \left(\bar{\Pi} \Pi + \frac{\bar{\Psi} \Psi}{e^{4\chi} a} \right) - \frac{1}{2} \mu^2 \bar{\phi} \phi - \frac{1}{4} \lambda (\bar{\phi} \phi)^2, \quad (33)$$

$$S_b^\phi = \frac{1}{2} \left(\bar{\Pi} \Pi - \frac{\bar{\Psi} \Psi}{e^{4\chi} a} \right) - \frac{1}{2} \mu^2 \bar{\phi} \phi - \frac{1}{4} \lambda (\bar{\phi} \phi)^2, \quad (34)$$

where $S_a = S_r^r$ and $S_b = S_\theta^\theta = S_\varphi^\varphi$. Correspondingly, the fermionic contribution to those source terms read

$$\mathcal{E}^{\text{fluid}} = [\rho(1 + \epsilon) + P]W^2 - P, \quad (35)$$

$$j_r^{\text{fluid}} = e^{4\chi} a [\rho(1 + \epsilon) + P]W^2 v^r, \quad (36)$$

$$S_a^{\text{fluid}} = e^{4\chi} a [\rho(1 + \epsilon) + P]W^2 v^r + P, \quad (37)$$

$$S_b^{\text{fluid}} = P, \quad (38)$$

where $W = \alpha u^t$ is the Lorentz factor and v^r is the radial component of the fluid three-velocity.

III. INITIAL DATA

As mentioned in the Introduction, we consider two different physical situations in this paper, namely, the dynamical formation of a fermion-boson star and the stability properties of different equilibrium models of such stars. In the following, we discuss the corresponding initial data for either situation.

A. Dynamical formation

To study the dynamical formation of a mixed star, we begin with a stable FS model surrounded by a dilute cloud of bosonic particles. This cloud accretes on to the FS under the gravitational pull of the latter. Suitable initial data describing this system are secured after solving the Hamiltonian constraint (29) and the momentum constraint (30). To do so, we assume a harmonic time dependence for the scalar field and choose a Gaussian radial distribution for the cloud, yielding

$$\phi(r, t) = A_0 e^{-\frac{r^2}{\sigma^2}} e^{-i\omega t}, \quad (39)$$

where parameters A_0 and σ are the amplitude and the width of the Gaussian profile, respectively, and ω is the initial frequency of the field.

To solve the constraints, we initially consider the spacetime of an isolated spherically symmetric FS by solving the Tolman-Oppenheimer-Volkoff equation. Next, we add to this solution the dilute cloud of bosonic matter described by (39). The time symmetry condition, $K_{ij} = 0$, and the conformally flat condition, $a = b = 1$, yield the following initial values for a set of spacetime variables:

$$\begin{aligned} \beta^r &= 0, \\ K &= 0, \\ A_a &= A_b = 0, \\ \Delta^r &= 0, \end{aligned} \quad (40)$$

while the values of the conformal factor ψ and of the lapse function α are inferred directly from the FS spacetime. Starting with these initial conditions, we solve numerically the Hamiltonian constraint (29) using the procedure described in [56]. This yields an updated value of the conformal factor ψ and of the γ_{rr} metric component.

Due to the harmonic time dependence of the scalar field, it follows that \int_r^ϕ defined by (32) is zero. This means that the scalar field does not contribute to the momentum constraint equation (30). Therefore, considering (40), the momentum constraint is analytically solved.

B. Equilibrium configurations

In Sec. II A, we introduced the basic equations to construct the static models of mixed stars. To solve the

set of equations, namely, Eqs. (14)–(18) and the EOS (8), we need to construct suitable initial data which are compatible with the physical and geometrical conditions of the stellar configurations. The system of ODEs becomes an eigenvalue problem for the frequency ω , which is a function of two parameters, the central value of the scalar field, ϕ_c , and of the fermionic density, ρ_c . We make use of the two-parameter shooting method to find the solution for ω . Once this is found and the central values of all variables are available, we use a fourth-order Runge-Kutta method to solve the ODEs and reconstruct the radial profiles of the solution.

We require the condition of regularity at the origin to be satisfied for the metric functions. At the outer boundary, we employ the values provided by the Schwarzschild solution at the outer radius, which do not depart much from the values of a flat metric, together with a vanishing scalar-field value. Hence, the boundary conditions for solving the set of ODEs can be defined as follows:

$$\begin{aligned} \tilde{a}(0) &= 1, & \phi(0) &= \phi_c, \\ \alpha(0) &= 1, & \lim_{r \rightarrow \infty} \alpha(r) &= \lim_{r \rightarrow \infty} \frac{1}{\tilde{a}(r)}, \\ \Psi(0) &= 0, & \lim_{r \rightarrow \infty} \Psi(r) &= 0, \\ \rho(0) &= \rho_c, & P(0) &= K\rho_c^\Gamma, & \lim_{r \rightarrow \infty} P(r) &= 0. \end{aligned} \quad (41)$$

Once the solution is found, one can define the total gravitational mass based on the value of the metric coefficients at infinity,

$$M_T = \lim_{r \rightarrow \infty} \frac{r}{2} \left(1 - \frac{1}{\tilde{a}^2} \right), \quad (42)$$

which coincides with the ADM mass at infinity. As the Klein-Gordon Lagrangian for a complex scalar field exhibits invariance under global U(1) transformations $\phi \rightarrow \phi e^{i\theta}$, Noether's theorem predicts the existence of a conserved charge which can be associated with the number of bosonic particles N_B ; moreover, the conservation of the baryonic number provides a definition of the number of fermionic particles N_F . These two quantities can be evaluated by integrating their volume density as follows:

$$N_B = 4\pi \int \frac{\tilde{a}\omega\phi^2 r^2}{\alpha} dr, \quad N_F = 4\pi \int \tilde{a}\rho r^2 dr. \quad (43)$$

These quantities will be used to determine the conservation of the number of particles, both bosons and fermions during the numerical evolutions. Finally, we evaluate the radius of the bosonic (fermionic) contribution to the mixed star, R_B (R_F), as the radius of the sphere containing 99% of the corresponding particles.

As mentioned before, the construction of the static solutions for the fermion-boson stars depends on two parameters, namely, the central fluid density ρ_c and the central value of the scalar field ϕ_c . We can therefore express the mass of the system (42) as a function of these two parameters $M_T(\rho_c, \phi_c)$ as we depict in Fig. 1 for three different values of Λ . In the case of nonrotating boson stars, the parameter space is one-dimensional and stability theorems [57] indicate that for each value of Λ , there exists a critical mass such that $dM_T/d\phi_c = 0$. These critical points indicate the transitions between the stability and the instability regions of the parameter space. Analogous transitions in stability occur in fermionic stars (see, e.g., [58,59]). In the case of fermion-boson stars, as the parameter space is two-dimensional, the analysis is more involved. Following [32], we define the critical points as the values of the pair (ρ_c, ϕ_c) such that the conditions

$$\begin{aligned} \left. \frac{\partial N_B}{\partial \rho_c} \right|_{M=\text{constant}} &= \left. \frac{\partial N_F}{\partial \rho_c} \right|_{M=\text{constant}} = 0, \\ \left. \frac{\partial N_B}{\partial \phi_c} \right|_{M=\text{constant}} &= \left. \frac{\partial N_F}{\partial \phi_c} \right|_{M=\text{constant}} = 0 \end{aligned} \quad (44)$$

are satisfied. In Fig. 1, we show several curves of constant mass in the parameter space (dashed colored lines). For each point of the curves, we evaluate the number of bosons N_B and fermions N_F . If we start from a purely FS configuration (a point on the horizontal axis in Fig. 1) and we move along a curve of fixed mass changing the values of ϕ_c and ρ_c , the number of bosons increases and the number of fermions decreases up to a critical point in the parameter space where a maximum is found for N_B and a minimum for N_F . If we start from a pure boson star (a point on the vertical axis), the behavior is the opposite, with N_B decreasing up to a minimum and N_F increasing up to a maximum. For each value of the mass, these critical points signal the boundary between the stability and instability regions. The black solid line in Fig. 1 represents these boundaries in the parameter space for the values of $\Lambda = \{-30, 0, 30\}$. This construction follows the same approach laid out in [33,36].

As FS does not depend on Λ , their threshold mass is constant for all values of Λ and equal to $M_c = 1.637$. On the contrary, for boson stars, the threshold mass changes with Λ . In particular, the threshold masses for our pure boson star models are $M_c = 0.248, 0.633$, and 1.336 , for $\Lambda = -30, 0$, and 30 , respectively. For fermion-boson stars, one can observe that for the same point in the parameter space with fixed values of ϕ_c and ρ_c , the total mass decreases (increases) for positive (negative) values of Λ , with respect to the $\Lambda = 0$ case.

We point out that considering negative values of λ raises the issue that the scalar potential $V(|\phi|) = \frac{1}{2}\mu^2|\phi|^2 + \frac{1}{4}\lambda(|\phi|^2)^2$ is not bounded from below and can become

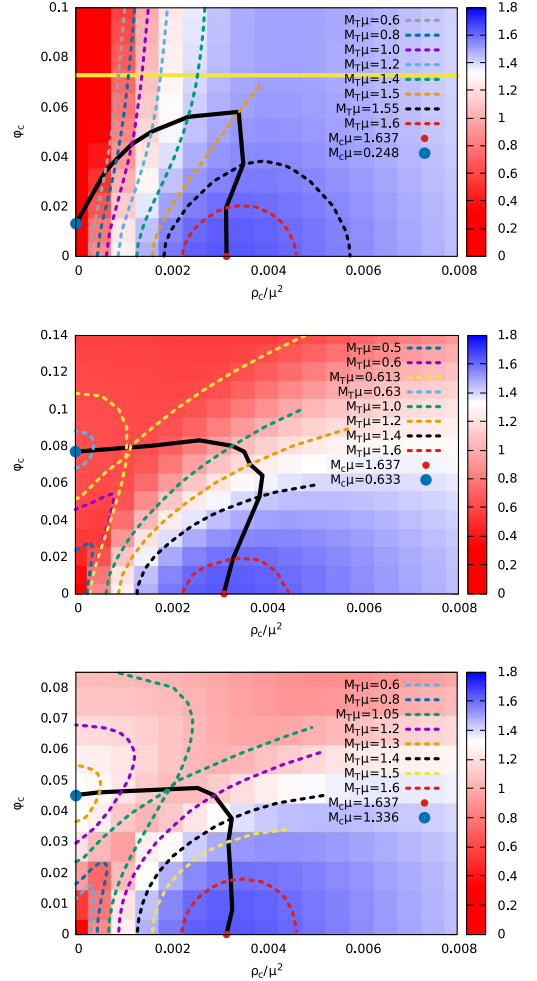


FIG. 1. Equilibrium configurations of fermion-boson stars for $\Lambda = -30$ (top), $\Lambda = 0$ (middle), and $\Lambda = 30$ (bottom). Dashed lines correspond to models with the same total mass M_T . The black solid line depicts the boundary between stable and unstable models, and the solid yellow line for the case $\Lambda = -30$ indicates the maximum value of ϕ_c that assures the non-negativity of the scalar-field potential $V(\phi)$ in the entire spatial domain.

negative, breaking the weak-energy condition (see, e.g., the discussion in [60]). For $\Lambda = -30$, we evaluate the maximum central value of ϕ that ensures the non-negativity of the scalar-field potential, yielding $\phi_c = 0.0728$. We depict in the top plot of Fig. 1 a horizontal yellow line at this value. We disregard all stellar models above this line as they may give rise to naked singularities.

IV. NUMERICAL FRAMEWORK

The numerical evolutions of the Einstein-Klein-Gordon-Euler system are performed with the numerical-relativity code originally developed by [55] and upgraded to take into account the complex scalar-field equations in [61]. This computational infrastructure has been extensively used by our group in studies of fundamental bosonic fields in strong-gravity spacetimes (see, e.g., [38,45,56,62,63]).

The time update of the evolution equations is evaluated using a partially implicit Runge-Kutta method developed by [64,65]. In this scheme, the operators on the right-hand side of the BSSN evolution equations are divided into operators which are evaluated explicitly and operators carrying geometrical singularities which are evolved implicitly using the updated values of the first ones. This allows to handle potential numerical instabilities arising from $1/r$ terms in the equations. While the construction of the equilibrium configurations employs Schwarzschild coordinates and an equally spaced linear grid, the dynamical evolutions make use of isotropic coordinates and a logarithmic grid. More precisely, the computational domain of the simulations is covered with an isotropic grid which is composed by two different patches, a geometrical progression up to a certain radius and an hyperbolic cosine in the exterior part. This allows to place the outer boundary sufficiently far from the origin and prevent the effects of reflections. Further details about the computational grid can be found in [62]. The minimum resolution we employ in our simulations is $\Delta r = 0.0125$. The inner boundary is then set at $r_{\min} = \Delta r/2$ and the outer boundary is at $r_{\max} = 6000$. The time step is given by $\Delta t = 0.3\Delta r$ in order to obtain long-term stable simulations. We add fourth-order Kreiss-Oliger numerical dissipation terms to the evolution equations to damp out spurious, high-frequency numerical noise. All advection terms (such as $\beta^i \partial_{r_i} f$) are treated with an upwind scheme. At the outer boundary, we impose radiative boundary conditions.

V. RESULTS

A. Dynamical formation of fermion-boson stars

As described in Sec. III A, we start with an initial configuration describing a bosonic cloud of matter surrounding an already formed FS, and we study the accretion of the bosonic matter on to the FS. The bosonic cloud loses part of its energy through gravitational cooling and plunges toward the center of the FS. Intuitively, this process can lead to two possible outcomes: either to the formation of a fermion-boson star or, if the mass of the entire system is above a certain threshold, to the formation of a Schwarzschild black hole.

During the evolutions, we compute useful physical quantities in order to keep track of the formation process and to evaluate the features of the final object. Those will be used below to compare with some of our static models.

We define the bosonic and fermionic energy contained in spheres of different radii r^* as

$$E_r^{\text{fluid}} = 4\pi \int_0^{r^*} \mathcal{E}^{\text{fluid}} \sqrt{\gamma} dr, \quad (45)$$

$$E_r^\phi = 4\pi \int_0^{r^*} \mathcal{E}^\phi \sqrt{\gamma} dr, \quad (46)$$

where $\sqrt{\gamma} = \psi^6 \sqrt{\alpha} br^2$ is the spatial volume element for the metric (19). Note that we will refer to $E_{r_{\max}}^{\text{fluid}/\phi}$ when referring to the total energy in the computational grid. Other useful quantities we evaluate along the numerical evolution are the number of bosonic and fermionic particles within spheres of radii r^* , computed by means of the following integrals:

$$N_{r^*}^B = 4\pi \int_0^{r^*} g^{0\nu} J_\nu \alpha \sqrt{\gamma} dr, \quad (47)$$

$$N_{r^*}^F = 4\pi \int_0^{r^*} \rho \sqrt{\gamma} dr, \quad (48)$$

where $J_\nu = \frac{i}{2}(\bar{\phi} \partial_\nu \phi - \phi \partial_\nu \bar{\phi})$ is the conserved current associated with the transformation of the U(1) group. We also extract the scalar-field frequency ω by performing a fast Fourier transform (FFT) of the real/imaginary part of the scalar field ϕ . The time window for the FFT is chosen at a sufficiently late time of the evolutions, once the bosonic cloud has already accreted on to the FS and the final object oscillates around an equilibrium configuration.

For our study, we use two different FS models, both described by the polytropic EoS, $P = K\rho^\Gamma$, with different central value of the rest-mass density ρ_c . We consider the same scalar-field mass parameter, $\mu = 1$, frequency, $\omega = 0.8$, and three different values for the self-interaction parameter $\Lambda = \{-30, 0, +30\}$. Our model for the bosonic cloud, Eq. (39), has a couple of free parameters we can vary, namely, the amplitude A_0 and the width of the Gaussian profile σ . For all our models, we consider $\sigma = 90$ which corresponds to a bosonic cloud much larger than the FS radii. We summarize some of the properties of our initial models in Tables I and II.

In Fig. 2, we show the evolution of the scalar-field energy contained in spheres of different radii r^* calculated with Eq. (46), for models MS3, MS4, and MS5 described in Table I. The growth of the lines E_{50}^ϕ , E_{30}^ϕ , E_{20}^ϕ , and E_{10}^ϕ shows that during the evolution the energy of the scalar cloud, which at the initial time is spread over a large spatial volume, gradually concentrates in a smaller volume, as it is being accreted by the FS. Part of the cloud energy does not fall on to the FS but it is radiated away through the gravitational cooling mechanism. For all three models, from time $t \simeq 750$ the curves start to converge slowly to each other, indicating that the scalar field is contained

TABLE I. Initial models leading to stable fermion-boson stars. The vertical lines divide the initial parameters (left), from the physical quantities evaluated at the end of the time evolution (center) and from the physical quantities of the corresponding equilibrium configuration (right). Note that as model MS5 forms an excited state, we cannot compare it with a nodeless static solution. Columns on the left indicate the central rest-mass density ρ_c , the self-interaction parameter Λ , and the amplitude of the scalar-field profile A_0 . Columns at the center indicate the scalar-field frequencies ω_n , the fermionic energy E_{30}^{fluid} contained in a sphere of radius $r = 30$, the bosonic energy E_{30}^ϕ , and the ratio between number of bosons and fermions N_{30}^B/N_{30}^F . Columns on the right side indicate the frequency ω , the fermionic energy E^{fluid} , the bosonic energy E^ϕ , and the ratio between number of bosons and fermions N^B/N^F of the corresponding equilibrium configuration.

Model	ρ_c/μ^2	Λ	A_0	ω_1/μ	ω_2/μ	$E_{30}^{\text{fluid}}/\mu$	E_{30}^ϕ/μ	N_{30}^B/N_{30}^F	ω/μ	E^{fluid}/μ	E^ϕ/μ	N^B/N^F
MS1	1.28×10^{-3}	0	4.5×10^{-4}	0.705	0.725	1.5330	0.1305	0.0775	0.695	1.5166	0.1223	0.0805
MS2	1.28×10^{-3}	30	4.5×10^{-4}	0.696	0.720	1.5380	0.1290	0.0813	0.715	1.531	0.1289	0.0839
MS3	1.28×10^{-3}	-30	4.0×10^{-4}	0.703	0.729	1.5751	0.0719	0.0423	0.696	1.569	0.0696	0.0444
MS4	1.28×10^{-3}	0	4.0×10^{-4}	0.720	0.745	1.5548	0.0956	0.0496	0.715	1.556	0.0795	0.0511
MS5	1.28×10^{-3}	30	4.0×10^{-4}	0.731	0.752	1.5679	0.1053	0.0568

TABLE II. Initial models leading to Schwarzschild black hole formation. As no fermion-boson star forms for these models, we only report the initial parameters of the bosonic cloud. Columns indicate the central rest-mass density ρ_c , the self-interaction parameter Λ , and the amplitude of the scalar-field profile A_0 .

Model	ρ_c/μ^2	Λ	A_0
MS6	3.15×10^{-3}	-30	3.5×10^{-4}
MS7	3.15×10^{-3}	0	3.5×10^{-4}
MS8	3.15×10^{-3}	30	3.5×10^{-4}

within small radii, radiating the excess energy to infinity. The remnant energy is confined into a volume delimited by $r \simeq 6$ and is, hence, entirely contained inside the FS. The total scalar-field energy of the three models is $E^\phi \simeq 0.065$ for MS3, $E^\phi \simeq 0.09$ for MS4, and $E^\phi \simeq 0.11$ for MS5.

Figure 2 shows some differences between models with and without self-interaction, and also depending on the sign of the self-interaction term. In the case with $\Lambda = -30$ (top panel), the lines E_{50}^ϕ , E_{30}^ϕ , E_{20}^ϕ , and E_{10}^ϕ slowly converge to each other and, at around $t \simeq 4700$, the energy within larger volumes radiates away and all the lines converge to the red one (E_{10}^ϕ) with a final energy around $E^\phi \simeq 0.065$. For the case with positive Λ (bottom panel), again there is an initial phase during which the lines slowly converge to each other, but then the red line, corresponding to E_{10}^ϕ , grows reaching the green one, E_{50}^ϕ . This indicates that all the scalar matter around the forming compact object is accreting onto it. The case with $\Lambda = 0$ (central panel) is an intermediate case, with the lines slowly converging to each other for the entire evolution. This result can be understood as follows: a $\Lambda > 0$ term in the Lagrangian is an attractive term, helping gravity letting the cloud collapse on to the FS and acting against the gravitational cooling mechanism that radiates away scalar particles. This means that the formation process is accelerated and the final object will also have higher number of bosonic particles and mass. On the other

hand, $\Lambda < 0$ is a repulsive term, which increases the amount of bosonic particles expelled to infinity. Nonetheless, the formation process seems to be accelerated but it is due to the fact that the scalar particles around the formed compact object escape faster to infinity. We point out that, as $|\phi| < 1$, the self-interaction term, which is proportional to $\lambda|\phi|^4$, gives a lower order contribution than the mass term $\mu^2|\phi|^2$. They are only comparable when the object is compact enough to reach high values of ϕ . This is the reason why the first part of the evolution before the object forms is basically the same for the three models.

In Fig. 3, we depict the late-time radial profiles of the scalar-field module $|\phi|$ for models MS3 (top panel) and MS5 (bottom panel). For model MS3, we compare three different snapshots during the evolution with an equilibrium configuration of a mixed star with comparable mass and number of bosons and fermions. The comparison shows that the radial profile of $|\phi|$ obtained through the dynamical formation process resembles that of the static solution.

The bottom panel of Fig. 3 shows that for model MS5 there are two maxima of the scalar field and there is a node at around $r \simeq 3$ which oscillates radially with the rest of the profile. At first sight, this result seems surprising because, at least for boson stars, all models with nodes are in excited states, which are intrinsically unstable and collapse to a black hole or decay to the nodeless fundamental configuration [43,57]. We note that in [66] configurations of two coexisting states of the scalar field, the ground state and one excited state, were investigated. Their results showed that it is possible to combine an intrinsically unstable first excited state (with a node) and the ground nodeless configuration, and obtain a stable configuration. In the fermion-boson case analyzed here, our results seem to indicate that an excited state of the scalar field in the presence of fermionic matter may form a stable configuration as well.

To provide further grounds for this result, Fig. 4 depicts a three-dimensional plot of the late-time evolution of the scalar field for models MS3 and MS5. The presence of the

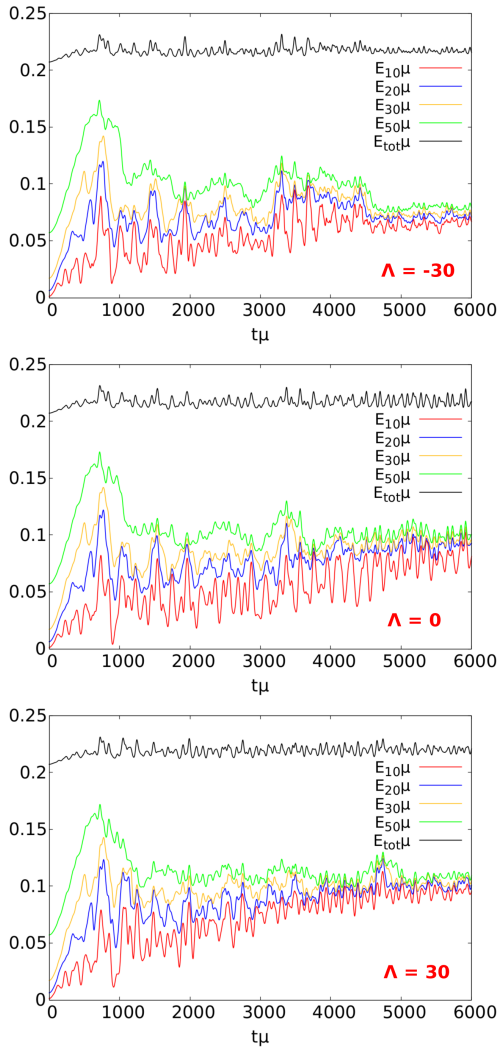


FIG. 2. Scalar-field energy in spheres of different radii, for model MS3 (top), MS4 (center), and MS5 (bottom). The red, blue, gold, and green lines correspond to $r^* = 10, 20, 30, 50$, respectively. The black line represents the total energy.

node for model MS5 (bottom plot) is clearly visible. This figure shows that this is not just a transient state as the evolution is characterized by radial oscillations around an equilibrium configuration. This is in contrast with model MS3 where we can only see transient nodes in the scalar profile which are due to the bosonic particles radiated away through gravitational cooling. This and previous results [66] would indicate that mixed states that

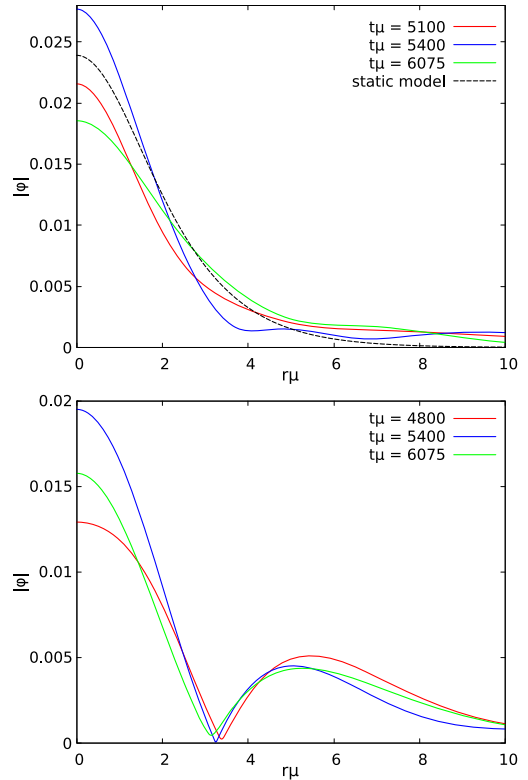


FIG. 3. Late-time radial profiles of the scalar-field module $|\phi|$ for model MS3 with $\Lambda = -30$ (upper panel) and model MS5 with $\Lambda = 30$ (bottom panel). The three snapshots of model MS3 are compared with the radial profile of a static mixed star model of similar ρ_c , ϕ_c , and bosonic and fermionic energy and number (dashed black line in the plot). Model MS5 presents a node at $r \simeq 3$ that radially oscillates together with the rest of the profile.

only interact through gravity and in which one of the components is intrinsically unstable can cooperate so they become globally stable.

B. Evolutions of the equilibrium configurations

In Sec. II A, we discussed how we identify the region of the parameter space where stable configurations are found. In this section, we intend to verify the results obtained by performing numerical evolutions of stable and unstable models. We expect stable mixed stars to show a combination of the typical behavior of isolated stable boson stars and fermion stars. This means that we expect the scalar field to oscillate with its characteristic eigenfrequency ω while the fermionic density ρ is expected to oscillate slightly around its initial state due to the numerical

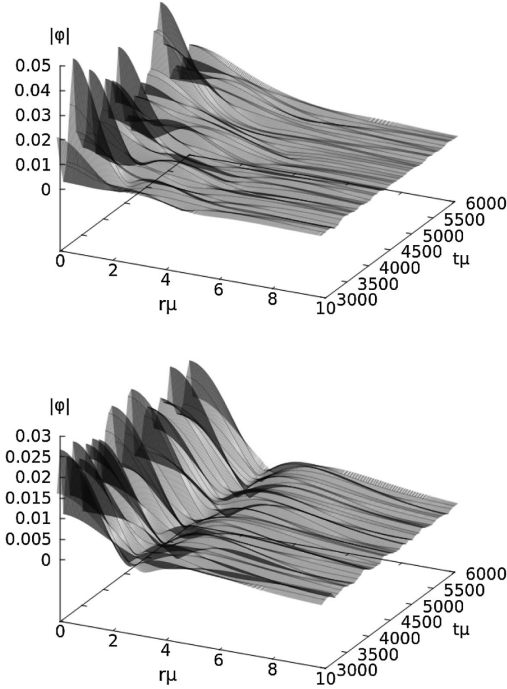


FIG. 4. Evolution of the radial profile of the scalar-field module $|\phi|$ for model MS3 with $\Lambda = -30$ (upper panel) and model MS5 with $\Lambda = 30$ (bottom panel) in the time window $t \in [3000, 6000]$. The difference between configuration MS3, which does not show a node in the last part of the evolution, and the excited state MS5 is apparent.

truncation errors introduced by the discretization of the differential equations of the continuum model. All physical quantities of the stable models such as mass, boson number density, or fermion number density are expected to be constant in time. Even under the introduction of a small perturbation, stable models are expected to oscillate around their static solutions.

For a model in the unstable region, however, we expect the small-amplitude perturbations induced by the numerical errors to grow due to the nonlinearity of the system. The growth of the perturbations can lead to three different outcomes: the migration to the stable region, the gravitational collapse, and formation a Schwarzschild black hole, or the dispersion of the bosonic particles.

As our evolution code is based on isotropic coordinates (19) and the mixed-star models are constructed using Schwarzschild coordinates (9), we must apply a coordinate transformation to be able to evolve the initial configurations. We follow the procedure proposed in [67] which can be divided in two steps. First, we perform the change of

coordinates noting that from the comparison between the two metrics we have that

$$\frac{d\hat{r}}{dr} = \tilde{a}(r) \frac{\hat{r}}{r}. \quad (49)$$

To obtain the coordinate transformation, we introduce the function β ,

$$\beta = \frac{\hat{r}}{r}. \quad (50)$$

Rewriting Eq. (49) in terms of $\ln \beta$, we obtain

$$\frac{d \ln \beta}{dr} = \frac{1}{r} (\tilde{a}(r) - 1), \quad (51)$$

which leads to

$$\beta(r) = \exp \left[- \int_r^{r_{\max}} \frac{1}{r'} (\tilde{a}(r') - 1) dr' \right]. \quad (52)$$

As initial condition to solve this integral, we impose that at the outer boundary the spacetime resembles the Schwarzschild solution which yields

$$\hat{r}_{\max} = \left(\frac{1 + \sqrt{\tilde{a}(r_{\max})}}{2} \right)^2 \frac{r_{\max}}{\tilde{a}(r_{\max})}. \quad (53)$$

Once we obtain β , we can finally obtain the conformal factor which is defined as

$$\psi = \sqrt{\frac{r}{\hat{r}}} = \sqrt{\frac{1}{\beta}}. \quad (54)$$

We point out that the introduction of the new variable β is necessary to make the integral (52) behave well at the origin and to be able to reconstruct the solution in the entire radial domain. The interested reader is addressed to [67] for further details.

We perform evolutions of several models for values of the self-interaction parameter $\Lambda = \{-30, 0, 30\}$, both in the stable and unstable regions of the existence surface. These numerical evolutions confirm our analysis about the stability of the models. We summarize their relevant physical properties in Table III.

Figure 5 shows the time evolution of the results obtained for the case $\Lambda = 30$, in particular models MS11 and MS12 of Table III. In the left panels, we display the evolution of the central value of the fluid density ρ_c and of the scalar field ϕ_c (top row) and the evolution of the number of fermions and bosons (bottom row) for the stable model MS11. As expected, all these physical quantities remain constant in time confirming that the model is stable. The middle panels show the time evolution of the same physical

TABLE III. Static fermion-boson star models. From left to right the columns indicate the model name, its stability, the value of the self-interaction parameter Λ , the central value of the fluid density ρ_c and of the scalar field ϕ_c , the field frequency obtained with the shooting method ω_{shoot} , the normalized frequency ω/μ , the total mass $M_T\mu$, the number of bosons to fermions ratio $N_{B\mu}/N_F$, the number of bosons N_B , the radius containing 99% of bosons, fermions, and total particles, R_B , R_F , R_T , respectively. All radii are evaluated using Schwarzschild coordinates.

Model	Branch	Λ	ρ_c/μ^2	ϕ_c	$\omega_{\text{shoot}}/\mu$	ω/μ	$M_T\mu$	$N_{B\mu}/N_F$	$N_{B\mu}^2$	$R_{B\mu}$	$R_{F\mu}$	$R_{T\mu}$
MS9	Stable	0	1.88×10^{-3}	4.04×10^{-2}	1.199	0.732	1.202	0.191	0.208	5.51	7.22	7.08
MS10	Unstable	0	4.55×10^{-3}	8.03×10^{-2}	1.436	0.602	1.200	0.251	0.261	3.66	5.81	5.63
MS11	Stable	30	1.50×10^{-3}	3.00×10^{-2}	1.238	0.807	1.126	0.344	0.308	7.06	7.08	7.04
MS12	Unstable	30	1.50×10^{-3}	6.00×10^{-2}	1.629	0.815	1.135	13.03	1.134	6.93	3.06	6.81
MS13	Stable	-30	1.83×10^{-3}	3.02×10^{-2}	1.129	0.681	1.401	0.055	0.079	5.18	7.73	7.64
MS14	Unstable	-30	2.41×10^{-3}	6.06×10^{-2}	1.099	0.604	1.401	0.068	0.097	3.99	7.34	7.24

quantities for model MS12, which is in the unstable region. We can observe that the central values of the scalar field and the fluid density very rapidly depart from their initial values, with a large variation which is damped in a few cycles. The system settles on a new configuration in the stable branch, oscillating around the new central values $\rho_c \simeq 0.0007$ and $\phi_c \simeq 0.038$. The number of bosons and fermions oscillate around a value very close to the initial one. These results indicate that this unstable model is migrating to a new configuration in the stable branch.

Finally, in the right panels of Fig. 5, we show the evolution of the same model MS12 under the effects of a

perturbation. To do so, we replace the initial profile of the scalar field with

$$\phi(r) \rightarrow \phi(r) \left(1 + \frac{A_1}{100} \right), \quad (55)$$

where $A_1 = 2$, which corresponds to a 2% level perturbation. Despite fairly small, this artificial perturbation is stronger than that introduced by the discretization errors alone which triggered the evolution shown in the middle panels of Fig. 5. We now observe that due to the stronger perturbation the model does not migrate to the stable region

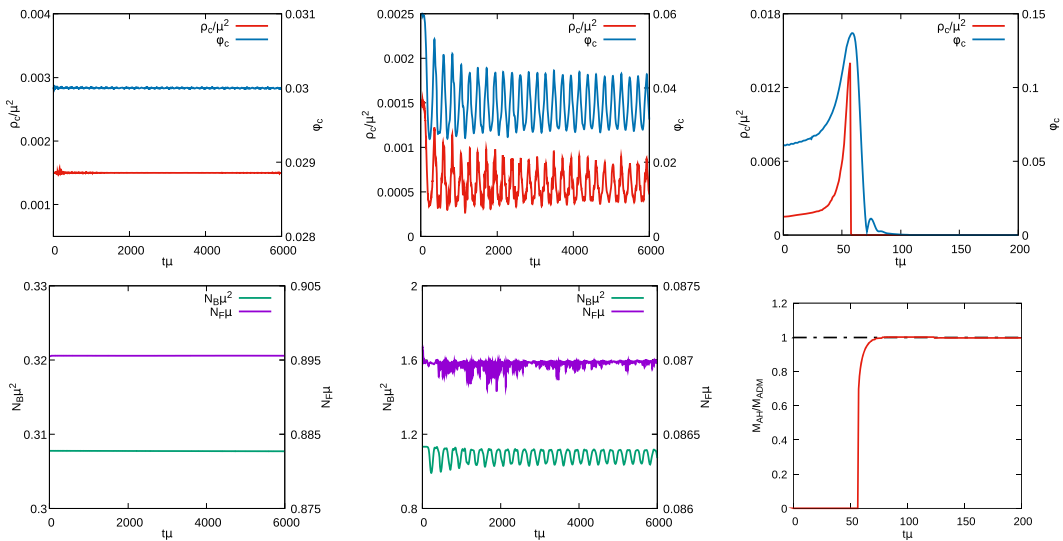


FIG. 5. Time evolution of static models with self-interaction parameter $\Lambda = 30$. Left panels depict the central value of the fluid density ρ_c and of the scalar field ϕ_c (top row) and number of bosons N_B and fermions N_F (bottom row) for the stable model MS11. Middle panels show the same physical quantities for the unstable model MS12 without the addition of an artificial perturbation. The right panels show the collapse to a Schwarzschild black hole of model MS12 when a 2% perturbation is induced in the scalar field. The right bottom plot displays the apparent horizon mass in units of the ADM mass (red solid line) and the time evolution of the ADM mass normalized by its initial value (black dashed line).

but rather collapses to a Schwarzschild black hole, as signaled by the formation of an apparent horizon (AH). In the top row, we show the time evolution of the central values of the fluid density and of the scalar field, while in the bottom row, we show the time evolution of the mass of the black hole evaluated on the AH in units of the ADM mass of the system (which we depict with a dashed black curve). We could not find any model for which the bosonic part dispersed, leaving behind a purely FS. The binding energy of the whole configuration is never positive and therefore, unstable models can only either migrate or collapse.

VI. CONCLUSIONS

Fermion-boson stars are gravitationally bound structures composed by fermions and scalar particles. They are regular and static macroscopic configurations obtained by solving the coupled Einstein-Klein-Gordon-Euler system. In this paper, we have discussed a possible scenario through which fermion-boson stars may form assuming an initial configuration in which an already existing FS (i.e., a neutron star) is surrounded by an accreting dilute cloud (a Gaussian pulse) of a massive, complex scalar field. Our setup has considered positive and negative values of a quartic self-interaction term in the Klein-Gordon potential. We have built constraint-satisfying initial data, and we have modeled the astrophysical situation by considering different bosonic cloud amplitudes and widths and two different fermion star models. The results of our spherically symmetric, numerical-relativity simulations have shown that once part of the initial scalar field is expelled via gravitational cooling the system oscillates around an equilibrium configuration that is asymptotically consistent with the static solutions of the system.

Existence diagrams of such equilibrium solutions in the central-field-amplitude versus central-fermionic-density plane have been constructed to draw such comparisons. Our results are in agreement, in the corresponding limits, with the work of [33,36]. The nonlinear stability of static models residing in both the stable and unstable regions of the existence diagrams has been assessed through simulations with a quartic self-interaction potential in the bosonic sector, not attempted in previous works. Those

have shown that, for stable configurations, all physical quantities describing the star, such as energy and number of particles, remain constant during the evolution, while unstable models either migrate to the stable region or collapse to a Schwarzschild black hole.

The dynamical formation of fermion-boson stars for large positive values of the coupling constant in the quartic self-interaction term (namely, $\Lambda = 30$) has revealed the presence of a node in the scalar field. This is an intriguing result as purely boson stars with nodes correspond to excited states and are known to be intrinsically unstable [43,57]. However, fermion-boson stars with nodes in the bosonic sector can dynamically form and appear long-term stable. This indicates that an excited state of the scalar field in the presence of fermionic matter may form a stable configuration. This result is akin to the findings of [66] who found that boson star configurations in which the ground state and the first excited state of the scalar field coexist are stable. In upcoming investigations, we plan to build equilibrium fermion-boson configurations with an excited state of the scalar field and study their stability properties to confirm the result reported here. Likewise, we will analyze the dynamical formation of rotating mixed stars as it might as well be possible that the presence of fermionic matter stabilized otherwise unstable spinning boson stars [46].

ACKNOWLEDGMENTS

We thank Eugen Radu and Carlos Herdeiro for useful suggestions. This work was supported by the Spanish Agencia Estatal de Investigación (Grant No. PGC2018-095984-B-I00), by the Generalitat Valenciana (PROMETEO/2019/071 and GRISOLIAP/2019/029), by the European Union's Horizon 2020 RISE programme H2020-MSCA-RISE-2017 Grant No. FunFiCO-777740, by DGAPA-UNAM through Grants No. IN110218, No. IA103616, and No. IN105920, by the Fundação para a Ciência e a Tecnologia projects PTDC/FIS-OUT/28407/2017 and UID/FIS/00099/2020 (CENTRA), and CERN/FIS-PAR/0027/2019. S. F. gratefully acknowledges support by the Erasmus+International Credit Mobility Program KA-107 for an academic stay at the University of Valencia.

-
- [1] S. Weinberg, *Phys. Rev. Lett.* **40**, 223 (1978).
 [2] J. Preskill, M. B. Wise, and F. Wilczek, *Phys. Lett.* **120B**, 127 (1983).
 [3] T. Matos and L. A. Urena-Lopez, *Phys. Rev. D* **63**, 063506 (2001).

- [4] T. Matos and L. A. Urena-Lopez, *Classical Quantum Gravity* **17**, L75 (2000).
 [5] M. Gasperini and G. Veneziano, *Phys. Rev. D* **50**, 2519 (1994).
 [6] P. Svrcek and E. Witten, *J. High Energy Phys.* **06** (2006) 051.

- [7] P. W. Higgs, *Phys. Lett.* **12**, 132 (1964).
- [8] G. Aad *et al.* (ATLAS Collaboration), *Science* **338**, 1576 (2012).
- [9] A. H. Guth, *Adv. Ser. Astrophys. Cosmol.* **3**, 139 (1987).
- [10] D. Langlois, in *Cargese School of Particle Physics and Cosmology: The Interface* (Springer, Netherlands, 2005), pp. 235–278.
- [11] M. Kawasaki and K. Nakayama, *Annu. Rev. Nucl. Part. Sci.* **63**, 69 (2013).
- [12] A. Arvanitaki, S. Dimopoulos, S. Dubovsky, N. Kaloper, and J. March-Russell, *Phys. Rev. D* **81**, 123530 (2010).
- [13] L. Hui, J. P. Ostriker, S. Tremaine, and E. Witten, *Phys. Rev. D* **95**, 043541 (2017).
- [14] V. B. Klaer and G. D. Moore, *J. Cosmol. Astropart. Phys.* **11** (2017) 049.
- [15] S.-J. Sin, *Phys. Rev. D* **50**, 3650 (1994).
- [16] P.-H. Chavanis and T. Harko, *Phys. Rev. D* **86**, 064011 (2012).
- [17] T. Matos, F. S. Guzman, and L. A. Urena-Lopez, *Classical Quantum Gravity* **17**, 1707 (2000).
- [18] W. Hu, R. Barkana, and A. Gruzinov, *Phys. Rev. Lett.* **85**, 1158 (2000).
- [19] P. Jetzer, *Phys. Rep.* **220**, 163 (1992).
- [20] D. J. Kaup, *Phys. Rev.* **172**, 1331 (1968).
- [21] R. Ruffini and S. Bonazzola, *Phys. Rev.* **187**, 1767 (1969).
- [22] M. Colpi, S. L. Shapiro, and I. Wasserman, *Phys. Rev. Lett.* **57**, 2485 (1986).
- [23] P. Jetzer and J. van der Bij, *Phys. Lett. B* **227**, 341 (1989).
- [24] S. Yoshida and Y. Eriguchi, *Phys. Rev. D* **56**, 762 (1997).
- [25] F. E. Schunck and E. W. Mielke, *Phys. Lett. A* **249**, 389 (1998).
- [26] E. Seidel and W.-M. Suen, *Phys. Rev. Lett.* **66**, 1659 (1991).
- [27] M. Alcubierre, J. Barranco, A. Bernal, J. C. Degollado, A. Diez-Tejedor, M. Megevand, D. Nunez, and O. Sarbach, *Classical Quantum Gravity* **35**, 19LT01 (2018).
- [28] V. Jaramillo, N. Sanchis-Gual, J. Barranco, A. Bernal, J. C. Degollado, C. Herdeiro, and D. Nez, *Phys. Rev. D* **101**, 124020 (2020).
- [29] R. Brito, V. Cardoso, C. A. Herdeiro, and E. Radu, *Phys. Lett. B* **752**, 291 (2016).
- [30] F. E. Schunck and E. W. Mielke, *Classical Quantum Gravity* **20**, R301 (2003).
- [31] S. L. Liebling and C. Palenzuela, *Living Rev. Relativity* **20**, 5 (2017).
- [32] A. Henriques, A. R. Liddle, and R. Moorhouse, *Phys. Lett. B* **251**, 511 (1990).
- [33] S. Valdez-Alvarado, C. Palenzuela, D. Alic, and L. A. Ureña-López, *Phys. Rev. D* **87**, 084040 (2013).
- [34] R. Brito, V. Cardoso, and H. Okawa, *Phys. Rev. Lett.* **115**, 111301 (2015).
- [35] R. Brito, V. Cardoso, C. F. B. Macedo, H. Okawa, and C. Palenzuela, *Phys. Rev. D* **93**, 044045 (2016).
- [36] S. Valdez-Alvarado, R. Becerril, and L. A. Ureña-López, *Phys. Rev. D* **102**, 064038 (2020).
- [37] E. Seidel and W.-M. Suen, *Phys. Rev. Lett.* **72**, 2516 (1994).
- [38] F. Di Giovanni, N. Sanchis-Gual, C. A. R. Herdeiro, and J. A. Font, *Phys. Rev. D* **98**, 064044 (2018).
- [39] T. D. Lee and Y. Pang, *Nucl. Phys.* **B315**, 477 (1989).
- [40] S. H. Hawley and M. W. Choptuik, *Phys. Rev. D* **62**, 104024 (2000).
- [41] M. Gleiser, *Phys. Rev. D* **38**, 2376 (1988); **39**, 1257(E) (1989).
- [42] M. Gleiser and R. Watkins, *Nucl. Phys.* **B319**, 733 (1989).
- [43] J. Balakrishna, E. Seidel, and W.-M. Suen, *Phys. Rev. D* **58**, 104004 (1998).
- [44] F. Guzman, *Rev. Mex. Fis.* **55**, 321 (2009), <https://rmf.smf.mx/ojs/rmf/article/view/3695>.
- [45] N. Sanchis-Gual, C. Herdeiro, E. Radu, J. C. Degollado, and J. A. Font, *Phys. Rev. D* **95**, 104028 (2017).
- [46] N. Sanchis-Gual, F. Di Giovanni, M. Zilhão, C. Herdeiro, P. Cerdá-Durán, J. A. Font, and E. Radu, *Phys. Rev. Lett.* **123**, 221101 (2019).
- [47] E. Seidel and W. Suen, *Phys. Rev. D* **42**, 384 (1990).
- [48] F. S. Guzman and L. A. Urena-Lopez, *Phys. Rev. D* **69**, 124033 (2004).
- [49] F. Guzman and L. Urena-Lopez, *Astrophys. J.* **645**, 814 (2006).
- [50] J. D. Brown, *Phys. Rev. D* **79**, 104029 (2009).
- [51] M. Alcubierre and M. D. Mendez, *Gen. Relativ. Gravit.* **43**, 2769 (2011).
- [52] T. Nakamura, K. Oohara, and Y. Kojima, *Prog. Theor. Phys. Suppl.* **90**, 1 (1987).
- [53] M. Shibata and T. Nakamura, *Phys. Rev. D* **52**, 5428 (1995).
- [54] T. W. Baumgarte and S. L. Shapiro, *Phys. Rev. D* **59**, 024007 (1998).
- [55] P. J. Montero and I. Cordero-Carrion, *Phys. Rev. D* **85**, 124037 (2012).
- [56] N. Sanchis-Gual, J. C. Degollado, P. J. Montero, and J. A. Font, *Phys. Rev. D* **91**, 043005 (2015).
- [57] T. D. Lee and Y. Pang, *Nucl. Phys.* **B315**, 477 (1989).
- [58] G. B. Cook, S. L. Shapiro, and S. A. Teukolsky, *Astrophys. J.* **424**, 823 (1994).
- [59] J. L. Friedman, J. R. Ipser, and R. D. Sorkin, *Astrophys. J.* **325**, 722 (1988).
- [60] C. Barceló and M. Visser, *Classical Quantum Gravity* **17**, 3843 (2000).
- [61] A. Escorihuela-Tomás, N. Sanchis-Gual, J. C. Degollado, and J. A. Font, *Phys. Rev. D* **96**, 024015 (2017).
- [62] N. Sanchis-Gual, J. C. Degollado, P. J. Montero, J. A. Font, and V. Mewes, *Phys. Rev. D* **92**, 083001 (2015).
- [63] N. Sanchis-Gual, J. C. Degollado, P. J. Montero, J. A. Font, and C. Herdeiro, *Phys. Rev. Lett.* **116**, 141101 (2016).
- [64] I. Cordero-Carrión and P. Cerdá-Durán, arXiv:1211.5930.
- [65] I. Cordero-Carrión and P. Cerdá-Durán, *Advances in Differential Equations and Applications*, SEMA SIMAI Springer Series Vol. 4 (Springer International Publishing, Switzerland, 2014).
- [66] A. Bernal, J. Barranco, D. Alic, and C. Palenzuela, *Phys. Rev. D* **81**, 044031 (2010).
- [67] B. Kleihaus and J. Kunz, *Phys. Rev. D* **57**, 834 (1998).

Synchronized gravitational atoms from mergers of bosonic stars

Nicolas Sanchis-Gual¹, Miguel Zilhão¹, Carlos Herdeiro², Fabrizio Di Giovanni³,
José A. Font^{3,4} and Eugen Radu²

¹*Centro de Astrofísica e Gravitação—CENTRA, Departamento de Física, Instituto Superior Técnico—IST, Universidade de Lisboa—UL, Avenida Rovisco Pais 1, 1049-001 Lisbon, Portugal*

²*Departamento de Matemática da Universidade de Aveiro and Centre for Research and Development in Mathematics and Applications (CIDMA), Campus de Santiago, 3810-183 Aveiro, Portugal*

³*Departamento de Astronomía y Astrofísica, Universitat de València, Dr. Moliner 50, 46100 Burjassot (València), Spain*

⁴*Observatori Astronòmic, Universitat de València, C/ Catedrático José Beltrán 2, 46980 Paterna (València), Spain*

 (Received 27 July 2020; accepted 27 October 2020; published 16 November 2020)

If ultralight bosonic fields exist in nature as dark matter, superradiance spins down rotating black holes (BHs), dynamically endowing them with equilibrium bosonic clouds, here dubbed synchronized gravitational atoms (SGAs). The self-gravity of these same fields, on the other hand, can lump them into (scalar or vector) horizonless solitons known as bosonic stars (BSs). We show that the dynamics of BSs yield a new channel forming SGAs. We study BS binaries that merge to form spinning BHs. After horizon formation, the BH spins up by accreting the bosonic field, but a remnant lingers around the horizon. If just enough angular momentum is present, the BH spin up stalls precisely as the remnant becomes a SGA. Different initial data lead to SGAs with different quantum numbers. Thus, SGAs may form both from superradiance-driven BH spin *down* and accretion-driven BH spin *up*. The latter process, moreover, can result in heavier SGAs than those obtained from the former: in one example herein, $\sim 18\%$ of the final system's energy and $\sim 50\%$ of its angular momentum remain in the SGA. We suggest that even higher values may occur in systems wherein *both* accretion *and* superradiance contribute to the SGA formation.

DOI: 10.1103/PhysRevD.102.101504

I. INTRODUCTION

Dynamical synchronization occurs in many physical and biological systems. Communities of fireflies or crickets, sets of metronomes or pendulums are amongst the examples wherein individual cycles converge to the same phase, if appropriate interactions are present; see, e.g., [1–3].

In Newtonian gravity, dynamical synchronization occurs in close binary systems [4]. Tidal interactions tend to synchronize orbital and rotational periods, locking them. In the Earth-Moon system, the latter has reached this equilibrium stage, whereas the Earth is spinning down to meet the longer orbital period. In the Solar System, full synchronization has been achieved in the lower mass ratio Pluto-Charon system [5].

In relativistic gravity, synchronization has been observed to occur in the interaction between spinning black holes (BHs) and bosonic fields. Via superradiance [6], the BH is spun down until it locks with the phase dynamics of the bosonic field [7,8]. This paper presents a new synchronization channel, through the dynamics of bosonic star (BS) binaries that form a spinning BH. When just enough angular momentum is present in the binary, the final BH spins up by accreting the remnant bosonic field after

horizon formation, and the process stops when synchronization is achieved.

II. SELF-GRAVITATING ULTRALIGHT BOSONIC FIELDS (UBFs)

Yet unseen UBFs are plausible dark-matter candidates [9]. For masses in the range 10^{-10} – 10^{-20} eV, UBFs efficiently trigger superradiance of astrophysical spinning BHs [10]. The process transfers a fraction of the BH's mass and angular momentum into a bosonic cloud with a slower (phase) angular velocity than that of the spinning horizon. The process stalls when the horizon angular velocity of the spun down BH synchronizes with the cloud's angular velocity [7,8], creating a synchronized gravitational atom (SGA) [11]. For complex UBFs, the BH-SGA system is a stationary “hairy” BH within the families found in [12–14].

UBFs form also horizonless self-gravitating solitons, called BSs [15–17]. They can be labeled by their phase oscillation frequency, ω , and ADM mass, M ; see e.g., [18,19]. Some spherical, nonspinning BSs are stable, forming dynamically, for both scalar (S) and vector (V, also known as Proca) bosonic fields [20–23]. Such BSs can be evolved in binaries [24–27]. By contrast, spinning BSs

are only dynamically robust in the vector case; the scalar stars are transient and develop instabilities [28]. We will show that the evolution of binaries of stable BSs, both scalar and vector, form SGAs.

III. SETUP

Fully nonlinear evolutions of BSs were performed in the same Einstein-Klein-Gordon and Einstein-Proca models as in [28]. We studied binary mergers. Using the initial data described in [26,27], two (**S** or **V**) BSs are superimposed, separated along the x axis by a coordinate distance D and boosted in opposite directions along the y axis, with the velocity v_y . The mergers yield a spinning BH with a bosonic field remnant (also known as a cloud) outside the horizon. The latter stores part of the BSs' system initial mass, M_i and angular momentum J_i , and its properties depend on v_y . Most simulations were performed for non-spinning (**S** or **V**) BSs, but mergers of spinning vector BSs (with parallel spins along the z axis) were also studied. In this case, we have taken $v_y = 0$ (head-on collisions); the BSs acquire orbital angular momentum due to frame dragging and a spinning BH forms.

We have used the codes described in [27–30], within the EINSTEINTOOLKIT infrastructure [31–33] with CARPET [34] for mesh refinement, AHFINDERDIRECT [35] for finding apparent horizons, and QUASILocalMEASURES [36] for extracting BH mass and angular momentum. Fields are evolved in time using the codes available in the CANUDA library [37]. For details, see [27–29,37,38].

IV. MERGERS OF NONSPINNING BSs

Two equal-mass binaries of nonspinning BSs were chosen to analyze the remnants after the merger and spinning BH formation: (i) two vector BSs with $(\omega, M) = (0.93, 0.952)$ [39]; (ii) two scalar BSs with $(\omega, M) = (0.94, 0.51)$. The initial separation of the BSs is fixed as $D = 30$ (**V**) or $D = 16.4$ (**S**). In both cases, the individual BSs are perturbatively stable, and we have performed a number of simulations, varying v_y , whose results can be summarized as follows: 1) the BSs have an eccentric trajectory, merge and an apparent horizon forms. 2) The final BH retains the largest part of M_i, J_i , denoted as $M_{\text{BH}}, J_{\text{BH}}$, respectively. Thus, the final object is *approximately* a vacuum Kerr BH. Its dimensionless spin $j \equiv J_{\text{BH}}/M_{\text{BH}}^2$ grows with time after horizon formation due to accretion of the bosonic remnant, saturating at a maximum value; this final j grows with v_y —Fig. 1, top panel. 3) After saturation there is a bosonic cloud outside the horizon, retaining a small fraction of M_i, J_i —Fig. 1, bottom panel. Increasing v_y , these fractions increase. The energy and spin in the bosonic fields are denoted, respectively E_B, J_B . Initially, $M_i = M_B$ and $J_i = J_B$. These behaviors are illustrated for the vector case in Fig. 1. A similar behavior is found for the scalar case (and for J_B , in the case of the bottom panel).

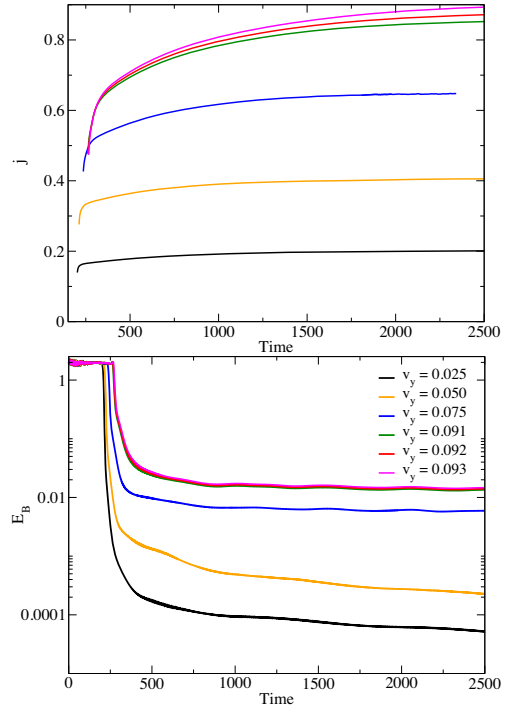


FIG. 1. Time evolution of the dimensionless spin of the final BH (top panel) and the energy in the Proca field (bottom panel) for different initial boost velocities, in the merger of two non-spinning vector BSs.

Let us address the nature of the remnant bosonic cloud. Synchronization in the BH-cloud system occurs when the latter is an oscillating field with phase $\sim e^{-i(\omega t - m\phi)}$ and the phase angular velocity locks with the BH horizon angular velocity Ω_H : $\omega/m = \Omega_H$ [12,40]. $m \in \mathbb{Z}$ is the azimuthal number of the bosonic remnant. Since the final BH in these simulations is approximately Kerr, we use the standard Kerr relation for $\Omega_H = \Omega_H(M_{\text{BH}}, J_{\text{BH}})$ [41]; thus,

$$\frac{\omega}{m} = \Omega_H \simeq \frac{J_{\text{BH}}}{2M_{\text{BH}}[M_{\text{BH}}^2 + \sqrt{M_{\text{BH}}^4 - J_{\text{BH}}^2}]} \quad (1)$$

The evolution of Ω_H is shown in Fig. 2 for the simulations with $v_y = 0.11$ (**S**) and $v_y = 0.092$ (**V**).

The panels exhibit the spin up of the formed BH, sourced by the accretion of (part) of the bosonic remnant. They also show the leading oscillation frequency of the remnant bosonic cloud, obtained as a Fourier transform, $\omega = 0.973$ (**S**) or $\omega = 0.948$ (**V**), divided by different values of m , corresponding to the different horizontal lines. One concludes that, for these initial data, the spin up stops when the

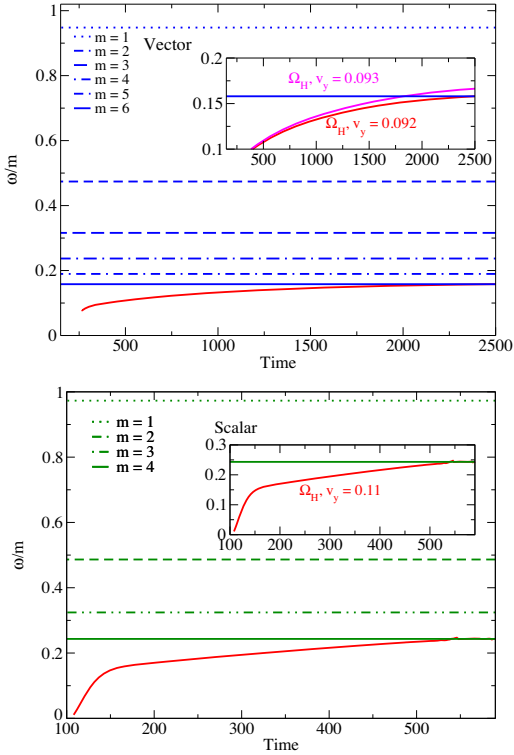


FIG. 2. Time evolution of the BH's Ω_H in the simulations with $v_y = 0.092$ (V, top panel) and $v_y = 0.11$ (S, bottom panel). The horizontal lines are the oscillation frequency of the bosonic cloud remnant divided by different m 's.

synchronization condition (1) becomes satisfied, for an $m = 6$ (V) or $m = 4$ (S) bosonic cloud remnant (see the insets in Fig. 2). Are these the correct m 's that describe the remnants obtained in the simulations?

An affirmative answer is provided in Fig. 3. Equatorial plane snapshots of the time evolution of both the vector and scalar amplitudes and energy densities are shown. Concerning the amplitudes, the left and middle right columns exhibit the real part of the scalar Proca potential, \mathcal{X}_ϕ [42] and of the scalar field, ϕ , respectively. The $m = 6$ and $m = 4$ azimuthal distributions are clearly seen, after the merger. This confirms the bosonic cloud remnant is a synchronized cloud (or SGA) with $m = 6$ (V) or $m = 4$ (S). Concerning the energy densities, one observes in the middle left (V) and right (S) columns the toroidal shape of the clouds's energy distribution, which is confirmed in Fig. 4. The inset of Fig. 2 (top panel) also shows a simulation with $v_y = 0.093$, whose implications will be discussed below.

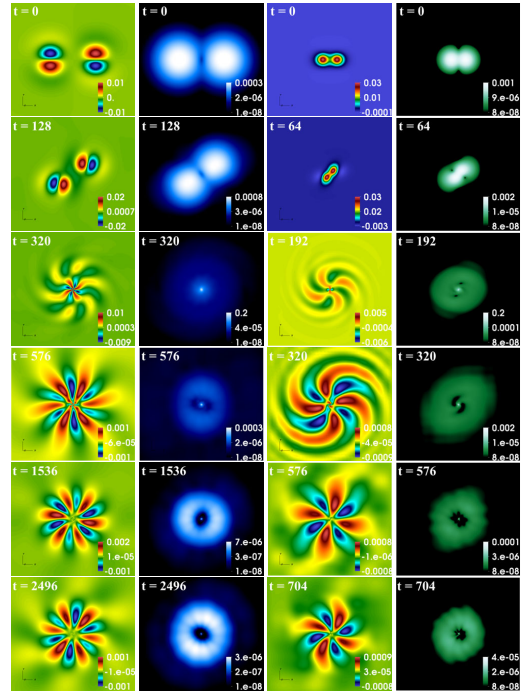


FIG. 3. Equatorial (xy) plane snapshots taken during the time evolution of the mergers of nonspinning BSs. Left column: real part of \mathcal{X}_ϕ ; (middle left column) Proca energy density; (middle right column) real part of ϕ ; (right column) scalar energy density.

If the remnant cloud were a pure synchronized mode it would be stationary. Only quasistationary clouds, however, are obtained from the BS mergers, due to subleading modes. This is corroborated by Fig. 5, wherein the time evolution of the amplitude of the real and imaginary parts of \mathcal{X}_ϕ , and ϕ are shown for the simulations with $v_y = 0.11$ (S) and $v_y = 0.092$ (V). In the vector case, the two leading modes have frequencies, $\omega_1 = 0.948$

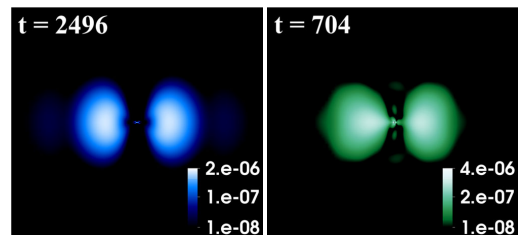


FIG. 4. xz -plane snapshots of the energy density taken during the time evolution of the mergers of nonspinning BSs for the vector (left panel) and scalar (right panel) cases.

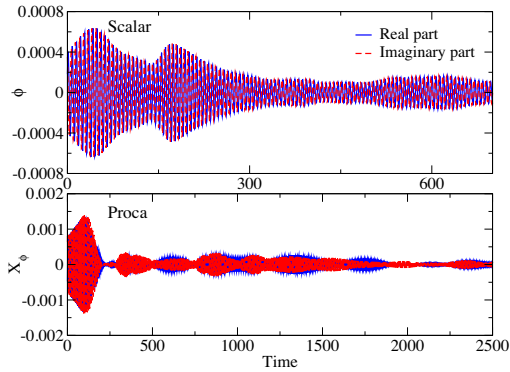


FIG. 5. Time evolution of the real and imaginary parts of ϕ (top panel) and \mathcal{X}_ϕ (bottom panel), extracted at radius $r = 20.78$.

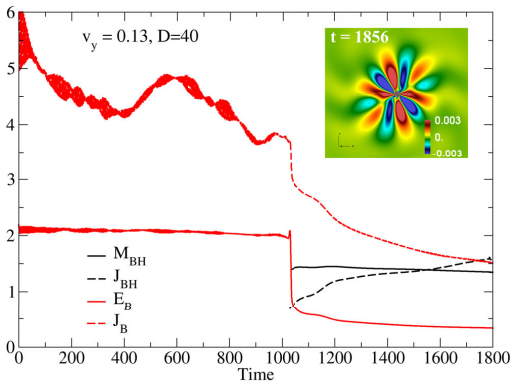


FIG. 6. Time evolution of E_B , J_B , M_{BH} , J_{BH} in a simulation with larger v_y , D . The inset confirms $m = 6$ for the final cloud.

(dominant) and $\omega_2 = 0.962$, which produce the beating pattern. In the scalar case, the leading modes have frequencies $\omega_1 = 0.973$ (dominant) and $\omega_2 = 0.993$.

So far, the remnant cloud contains only up to $\sim 0.01M_i$, *cf.* Figure 1 (bottom panel). Significantly higher energy fractions can be obtained by increasing v_y . As an illustration, consider a binary of (more compact) vector BSs $[(\omega, M) = (0.91, 1.015)]$, with $v_y = 0.13$ and $D = 40$ [43]. The system has $(M_i, J_i) = (2.08, 5.98)$, and the BSs perform almost one orbit before merging [44]. For this setup, the Proca remnant still has $m = 6$ but now stores $\sim 0.15M_i$ and $\sim 0.24J_i$ —Fig. 6; or, in terms of the final system, the cloud stores $\sim 18\%$ of the energy and $\sim 50\%$ of the angular momentum.

V. HEAD-ON COLLISIONS OF SPINNING BSs

A similar picture occurs for head-on collisions (i.e., with $v_y = 0$) of spinning vector BSs [45]. Spinning bosonic stars form a countable number of families, labeled by the azimuthal harmonic index $\bar{m} \in \mathbb{Z}$, which counts the number of (phase) azimuthal nodes. Here, we consider mergers of $\bar{m} = 1$ and $\bar{m} = 2$ spinning vector BSs (static BSs can be seen as the $\bar{m} = 0$ case). When the BSs are sufficiently massive, such mergers form a BH, which is spinning even for head-on collisions. However, the system must possess just enough angular momentum for the final BH to spin up the correct amount as to synchronize with the remnant. This can be achieved by considering sequences of mergers wherein the frequency of the two (equal mass and parallel spins) initial spinning vector BSs are varied. For this setup, one may envisage varying the frequency of the initial BSs as playing the same role as varying v_y in the nonspinning BSs mergers discussed before.

In Fig. 7, we exhibit snapshots of the time evolution of the vector amplitude for two head-on collisions of spinning vector BSs. Both collisions have $D = 40$, $v_y = 0$ and are

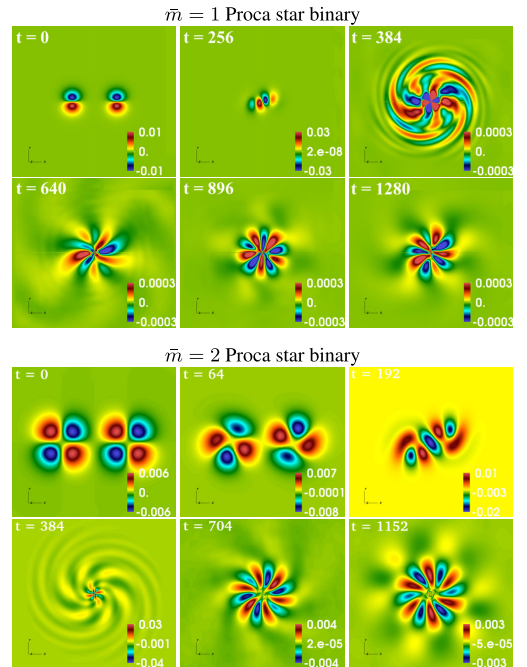


FIG. 7. Equatorial (xy) plane snapshots taken during the time evolution of the mergers of spinning BSs: the two top panels corresponds to a $\bar{m} = 1$ model, and the two bottom panels to a $\bar{m} = 2$ model. The real part of \mathcal{X}_ϕ is shown.

for systems where synchronization occurs. The first collision (top two rows) are for $\bar{m} = 1$ stars with $(\omega, M, J) = (0.92, 0.659, 0.677)$. The initial mass and angular momentum of the system are $(M_i, J_i) = (1.33, 1, 43)$. An $m = 5$ synchronized cloud remains at the end of the simulation, retaining 0.19% and 0.66% of M_i and J_i , respectively. The second collision (bottom two rows) are for $\bar{m} = 2$ stars with $(\omega, M, J) = (0.93, 1.071, 2.195)$. The initial mass and angular momentum of the system are now $(M_i, J_i) = (2.18, 4.62)$. An $m = 6$ synchronized cloud is now obtained at the end of the simulation, retaining 3.2% and 8.3% of M_i and J_i , respectively. We remark that the sort of collisions displayed in the top panels of Fig. 7 have been recently [46] argued to model the event GW190521 [47,48], with a slight statistical preference with respect to standard binary BH models.

VI. SGAs: THE BH, THE BSs AND THE MIXED CHANNEL

Superradiance of a Kerr BH forms a synchronized bosonic cloud-BH system by spinning down the Kerr BH [7,8]. Interestingly, we observe from Fig. 2 that in this new channel, mergers of BSs lead to a synchronized bosonic cloud-BH system by spinning up the BH that results from the merger. This confirms that the synchronized BH-cloud system can be approached from either side.

From the superradiance channel, a universal thermodynamical limit imposes that the bosonic cloud cannot store more than $\sim 29\%$ of the final BH-cloud system [6]. In practice, however, fully nonlinear numerical simulations in the Proca case were only able to reach about 9% [7]. Here, we have shown one example wherein the bosonic cloud stores $\sim 18\%$ of the energy and $\sim 50\%$ of the angular momentum of the final BH-cloud system. In fact, there appears to be no theoretical bound from the BSs channel, and we anticipate higher fractions of M_i, J_i can be stored in the bosonic cloud, in particular, via processes involving a mixed channel.

In order to get synchronization in a direct, two-step process from the BS channel [the two steps being 1) BH formation, 2) spin up by accretion up to synchronization], fine-tuning of the initial data is required. As illustrated in Fig. 2, a specific value of v_y is necessary. For smaller v_y , there is not enough angular momentum available for Ω_H to catch up with ω/m of the cloud; for larger v_y , Ω_H overshoots the synchronization value, as shown by the simulation with $v_y = 0.093$ in Fig. 2 (top panel). In the latter case, the cloud becomes dominated by a superradiant mode. Thus, energy and angular momentum extraction

from the BH ensue. This is what we call the mixed channel. We speculate that, in this case, synchronization is achieved by a three-step process: 1) BH formation, 2) spin up by accretion, 3) superradiant spin down, until synchronization. Moreover, the results herein indicate the trend that increasing v_y , the fractions of M_B/M_i and J_B/J_i increase. Thus, we anticipate that there will be open sets of initial data leading to synchronization via the three step process. Subsets of these initial data set may well lead to even higher fractions of energy and angular momentum in the final synchronized cloud. Checking this conjecture, however, is challenging. Whereas the two step process occurs in a much shorter time scale than the superradiance evolutions in [7], the three step process will be longer, in particular because high m modes are involved.

Finally, we remark that whereas generic initial data triggering superradiance of Kerr BHs always produce an $m = 1$ cloud, corresponding to the fastest growing superradiant mode, generic initial data in the mergers of BSs produce SGAs with different m 's, herein illustrated with $m = 4, 5, 6$.

ACKNOWLEDGMENTS

This work was supported by the Spanish Agencia Estatal de Investigación (Grant No. PGC2018-095984-B-I00), by the Generalitat Valenciana (Grants No. PROMETEO/2019/071 and No. GRISOLIAP/2019/029), by the Center for Research and Development in Mathematics and Applications (CIDMA) through the Portuguese Foundation for Science and Technology (FCT—Fundação para a Ciência e a Tecnologia), Reference Grants No. UIDB/04106/2020 and No. UIDP/04106/2020, by national funds (OE), through FCT, I. P., in the scope of the framework contract foreseen in the numbers 4, 5, and 6 of the article 23, of the Decree-Law 57/2016, of August 29, changed by Law 57/2017, of July 19 and by the Projects No. PTDC/FIS-OUT/28407/2017, No. CERN/FIS-PAR/0027/2019, and No. UID/FIS/00099/2020 (CENTRA). This work has further been supported by the European Union's Horizon 2020 research and innovation (RISE) programme No. H2020-MSCA-RISE-2017 Grant No. FunFiCO-777740 and by FCT through Project No. UIDB/00099/2020. We would like to acknowledge networking support by the COST Action GWverse CA16104. MZ also acknowledges financial support provided by FCT/Portugal through the IF programme, Grant No. IF/00729/2015. Computations have been performed at the Servei d'Informàtica de la Universitat de València, on the "Baltasar Sete-Sois" cluster at IST, and at MareNostrum.

- [1] R. E. Mirollo and S. H. Strogatz, *SIAM J. Appl. Math.* **50**, 1645 (1990).
- [2] J. Pantaleone, *Am. J. Phys.* **70**, 992 (2002).
- [3] S. Strogatz, *Sync: How Order Emerges from Chaos in the Universe, Nature, and Daily Life* (Hachette Books, New York, 2004).
- [4] P. Hut, *Astron. Astrophys.* **99**, 126 (1981).
- [5] W. H. Cheng, M. H. Lee, and S. J. Peale, *Icarus* **233**, 242 (2014).
- [6] R. Brito, V. Cardoso, and P. Pani, *Lect. Notes Phys.* **906**, pp. 1 (2015).
- [7] W. E. East and F. Pretorius, *Phys. Rev. Lett.* **119**, 041101 (2017).
- [8] C. A. R. Herdeiro and E. Radu, *Phys. Rev. Lett.* **119**, 261101 (2017).
- [9] L. Hui, J. P. Ostriker, S. Tremaine, and E. Witten, *Phys. Rev. D* **95**, 043541 (2017).
- [10] A. Arvanitaki and S. Dubovsky, *Phys. Rev. D* **83**, 044026 (2011).
- [11] D. Baumann, H. S. Chia, J. Stout, and L. ter Haar, *J. Cosmol. Astropart. Phys.* **12** (2019) 006.
- [12] C. A. R. Herdeiro and E. Radu, *Phys. Rev. Lett.* **112**, 221101 (2014).
- [13] C. Herdeiro, E. Radu, and H. Runarsson, *Classical Quantum Gravity* **33**, 154001 (2016).
- [14] N. M. Santos, C. L. Benone, L. C. Crispino, C. A. Herdeiro, and E. Radu, *J. High Energy Phys.* **07** (2020) 010.
- [15] F. E. Schunck and E. W. Mielke, *Classical Quantum Gravity* **20**, R301 (2003).
- [16] S. L. Liebling and C. Palenzuela, *Living Rev. Relativity* **15**, 6 (2012).
- [17] R. Brito, V. Cardoso, C. A. R. Herdeiro, and E. Radu, *Phys. Lett. B* **752**, 291 (2016).
- [18] C. A. R. Herdeiro, A. M. Pombo, and E. Radu, *Phys. Lett. B* **773**, 654 (2017).
- [19] C. Herdeiro, I. Perapechka, E. Radu, and Y. Shnir, *Phys. Lett. B* **797**, 134845 (2019).
- [20] E. Seidel and W.-M. Suen, *Phys. Rev. D* **42**, 384 (1990).
- [21] E. Seidel and W.-M. Suen, *Phys. Rev. Lett.* **72**, 2516 (1994).
- [22] N. Sanchis-Gual, C. Herdeiro, E. Radu, J. C. Degollado, and J. A. Font, *Phys. Rev. D* **95**, 104028 (2017).
- [23] F. Di Giovanni, N. Sanchis-Gual, C. A. R. Herdeiro, and J. A. Font, *Phys. Rev. D* **98**, 064044 (2018).
- [24] C. Palenzuela, L. Lehner, and S. L. Liebling, *Phys. Rev. D* **77**, 044036 (2008).
- [25] V. Cardoso, S. Hopper, C. F. Macedo, C. Palenzuela, and P. Pani, *Phys. Rev. D* **94**, 084031 (2016).
- [26] M. Bezares, C. Palenzuela, and C. Bona, *Phys. Rev. D* **95**, 124005 (2017).
- [27] N. Sanchis-Gual, C. Herdeiro, J. A. Font, E. Radu, and F. Di Giovanni, *Phys. Rev. D* **99**, 024017 (2019).
- [28] N. Sanchis-Gual, F. Di Giovanni, M. Zilhão, C. Herdeiro, P. Cerdá-Durán, J. Font, and E. Radu, *Phys. Rev. Lett.* **123**, 221101 (2019).
- [29] P. V. P. Cunha, J. A. Font, C. Herdeiro, E. Radu, N. Sanchis-Gual, and M. Zilhão, *Phys. Rev. D* **96**, 104040 (2017).
- [30] M. Zilhão, H. Witek, and V. Cardoso, *Classical Quantum Gravity* **32**, 234003 (2015).
- [31] F. Löffler, J. Faber, E. Bentivegna, T. Bode, P. Diener *et al.*, *Classical Quantum Gravity* **29**, 115001 (2012).
- [32] M. Zilhão and F. Löffler, *Int. J. Mod. Phys. A* **28**, 1340014 (2013).
- [33] M. Babiuç-Hamilton *et al.*, The Einstein Toolkit (2019), to find out more, visit <http://einstein toolkit.org>.
- [34] E. Schnetter, S. H. Hawley, and I. Hawke, *Classical Quantum Gravity* **21**, 1465 (2004).
- [35] J. Thornburg, *Classical Quantum Gravity* **21**, 743 (2004).
- [36] O. Dreyer, B. Krishnan, D. Shoemaker, and E. Schnetter, *Phys. Rev. D* **67**, 024018 (2003).
- [37] H. Witek, M. Zilhão, G. Ficarra, and M. Elley, Canuda: A public numerical relativity library to probe fundamental physics (2020).
- [38] EinsteinToolkit, Einstein Toolkit: Open software for relativistic astrophysics, <http://einstein toolkit.org/>.
- [39] Both the Einstein-Klein-Gordon and Einstein-Proca models introduce a single new parameter μ corresponding to the scalar or vector field mass. This scale is set to unity, so that masses, frequencies, etc, are given in units of μ . Also geometrized units $G = 1 = c$ are used.
- [40] S. Hod, *Phys. Rev. D* **86**, 104026 (2012).
- [41] P. Townsend, [arXiv:gr-qc/9707012](https://arxiv.org/abs/gr-qc/9707012).
- [42] See e.g., [27] for the definition of this potential.
- [43] The larger D guarantees a small constraints violation of the initial data.
- [44] The initial mass/energy is larger than the mass of the BSs due to the boosts.
- [45] As mentioned before spinning scalar boson stars are unstable [28].
- [46] J. Calderón Bustillo, N. Sanchis-Gual, A. Torres-Forné, J. A. Font, A. Vajpeyi, R. Smith, C. Herdeiro, E. Radu, and S. H. Leong, [arXiv:2009.05376](https://arxiv.org/abs/2009.05376).
- [47] R. Abbott *et al.* (LIGO Scientific and Virgo Collaborations), *Phys. Rev. Lett.* **125**, 101102 (2020).
- [48] R. Abbott, T. Abbott, S. Abraham, F. Acernese, K. Ackley, C. Adams, R. Adhikari, V. Adya, C. Affeldt, M. Agathos *et al.*, *Astrophys. J. Lett.* **900**, L13 (2020).

Dynamical bar-mode instability in spinning bosonic stars

Fabrizio Di Giovanni¹, Nicolas Sanchis-Gual², Pablo Cerdá-Durán¹, Miguel Zilhão²,
 Carlos Herdeiro³, José A. Font^{1,4}, and Eugen Radu³

¹*Departamento de Astronomía y Astrofísica, Universitat de València,
 Dr. Moliner 50, 46100 Burjassot (València), Spain*

²*Centro de Astrofísica e Gravitação—CENTRA, Departamento de Física, Instituto Superior Técnico—IST,
 Universidade de Lisboa—UL, Avenida Rovisco Pais 1, Lisbon 1049-001, Portugal*

³*Departamento de Matemática da Universidade de Aveiro and Centre for Research and Development in
 Mathematics and Applications (CIDMA), Campus de Santiago, 3810-183 Aveiro, Portugal*

⁴*Observatori Astronòmic, Universitat de València, C/ Catedrático José Beltrán 2,
 46980 Paterna (València), Spain*



(Received 16 October 2020; accepted 1 November 2020; published 1 December 2020)

Spinning bosonic stars (SBSs) can form from the gravitational collapse of a dilute cloud of scalar/Proca particles with nonzero angular momentum, via gravitational cooling. The scalar stars are, however, transient due to a nonaxisymmetric instability which triggers the loss of angular momentum. By contrast, no such instability was observed for the fundamental ($m = 1$) Proca stars. In [N. Sanchis-Gual *et al.*, *Phys. Rev. Lett.* **123**, 221101 (2019)] we tentatively related the different stability properties to the different toroidal/spheroidal morphology of the scalar/Proca models. Here, we continue this investigation, using three-dimensional numerical-relativity simulations of the Einstein-(massive, complex)Klein-Gordon system and of the Einstein-(complex)Proca system. First, we incorporate a quartic self-interaction potential in the scalar case to gauge its effect on the instability. Second, we investigate toroidal ($m = 2$) Proca stars to assess their stability. Third, we attempt to relate the instability of SBSs to the growth rate of azimuthal density modes and the existence of a corotation point in the unstable models. Our results indicate that: (a) the self-interaction potential can only delay the instability in scalar SBSs but cannot quench it completely; (b) $m = 2$ Proca stars always migrate to the stable $m = 1$ spheroidal family; (c) unstable $m = 2$ Proca stars and $m = 1$ scalar boson stars exhibit a pattern of frequencies for the azimuthal density modes which crosses the angular velocity profile of the stars in the corotation point. This establishes a parallelism with rotating neutron stars affected by dynamical bar-mode instabilities. Finally, we compute the gravitational waves emitted by SBSs due to the nonaxisymmetric instability. We investigate the detectability of the waveforms comparing the characteristic strain of the signal with the sensitivity curves of a variety of detectors, computing the signal-to-noise ratio for different ranges of masses and for different source distances. Moreover, by assuming that the characteristic damping timescale of the bar-like deformation in SBSs is only set by gravitational-wave emission and not by viscosity (unlike in neutron stars), we find that the postcollapse emission could be orders of magnitude more energetic than that of the bar-mode instability itself. Our results indicate that gravitational-wave observations of SBSs might be within the reach of future experiments, offering a potential means to establish the existence of such stars and to place tight constraints on the mass of the bosonic particle.

DOI: 10.1103/PhysRevD.102.124009

I. INTRODUCTION

The brand new field of gravitational-wave (GW) astronomy [1–6] is allowing for new explorations of the Universe from an astrophysical scale to a cosmological scale. The recent LIGO-Virgo detections of GW signals from coalescing compact binaries along with the Event Horizon Telescope observations of the center of the galaxy M87 [7] provide firm evidence to the black hole (BH) hypothesis. A picture is emerging that BHs seem to populate the cosmos in large numbers and they are widely

regarded as the main type of dark compact object, i.e., an object that barely interacts with baryonic matter except through gravity. Notwithstanding the prominent place that BHs currently occupy in our standard model, a good many varieties of *exotic* dark compact objects have been proposed in the past (see e.g., [8] and references therein). The study of these so-called BH “mimickers” is interesting from a number of perspectives, chiefly to test general relativity in the strong-field regime, possibly through the detection of GWs, but also to assess their potential

relevance as alternative candidates to explain the nature of dark matter (DM).

In particular, the introduction of new fields not included in the Standard Model of fundamental interactions is necessary in cosmology to explain the mounting evidence supporting the existence of DM. The simplest possible theory which minimally couples a massive bosonic field, either scalar [9,10] or vector [11], to Einstein's gravity, gives rise to self-gravitating compact objects. These are known as bosonic stars (BSs) or oscillatons [12], depending on whether the field is complex or real, respectively.¹ They are dark as far as their interaction with the Standard Model particles is considered to be weak. The dynamical features of BSs have been deeply studied (see e.g., [14,15] and references therein) in the static, spherically symmetric case. For some range of the model parameters, the fundamental family (FF) can form dynamically through the so-called gravitational cooling mechanism [16,17] and are stable under perturbations [11,18–21]. Spherical BS models have moreover been considered to build orbiting binaries, from which GWs have been extracted and compared to BHs signals [22–24]. All existing studies within spherical symmetry have shown a remarkable parallelism between the dynamics of scalar and vector BS models.

Models of axisymmetric, spinning bosonic stars (SBSs) have also been constructed for a scalar field [25–27], a vector field [11,28,29] (see also [30]), and some of their phenomenology has been studied, including geodesic motion [31–35], lensing [36,37] and properties of the x-ray spectrum due to an accretion disk [38,39]. Recently [40] we studied the dynamical properties of SBSs by performing fully nonlinear numerical-relativity simulations. The goal of that study was to answer two fundamental questions: (i) are SBSs stable? and (ii) may they form dynamically from the gravitational collapse of a bosonic cloud? Our study revealed that the parallelism between scalar and vector fields in the spherically symmetric case breaks down when we consider spinning models. We found that scalar SBSs in the FF always develop a nonaxisymmetric instability. Moreover, in the formation scenario, the collapse of the cloud leads only to a transient SBS, which then splits into an orbiting binary which eventually recollapses into a nonspinning scalar boson star, ejecting all the angular momentum. The evolution of an already formed stationary SBS triggers the same type of non-axisymmetric instability and the collapse to a BH, even considering models which were thought to be stable to linear axisymmetric perturbations—see the discussion in Sec. 6.2 in [32]. By contrast, the vector SBS models we considered, also known as spinning Proca stars, did not show any instability. As a result, in [40] we put forward the hypothesis that the different dynamical

properties of these two families of SBSs were related to their different morphology (the energy density profile of scalar SBSs has a toroidal shape while vector SBSs exhibit a spheroidal one) and possibly to the existence of a corotational instability in the scalar case.

In this work we further investigate this issue, extending our previous investigation along different directions. First, we carry out a deeper exploration of the two families of SBSs by taking into account the dynamics of a larger set of new models; second, we provide a qualitative description of the growth of the non-axisymmetric instability of scalar (and vector) SBSs and compare our findings with well-known results for differentially rotating neutron stars [41–43]. Our dynamical study is focused only on the formation scenario. Comparing with our previous work, we construct here new models of scalar bosonic clouds with a quartic self-interaction potential and study if the instability found in the scalar case is affected by increasing the contribution from the self-interaction term. For the vector field case, we consider Proca clouds belonging to the $m = 2$ family of solutions which, unlike the $m = 1$ case discussed in [40], show a toroidal morphology and may be subject of the same type of instability that affects the scalar case, which would support our conjecture.

We furthermore study the GWs emitted by unstable SBSs, computing the mode decomposition of the Newman-Penrose scalar Ψ_4 . We evaluate the characteristic GW strain h_{char} for some of our models and we compare it with the sensitivity curves of current and future ground-based and space interferometric detectors, as well as from future observational projects based on pulsar timing arrays. For each detector and for different ranges of masses of the SBS, we compute the horizon distance, defined as the distance between the observer and the source at which the signal-to-noise ratio (SNR) is equal to a certain threshold value. Our results show that the GW signals produced by the bar-mode instability in SBSs are within reach of future detectors which offers the intriguing possibility of an eventual detection of such exotic objects and might help place constraints on the mass of the bosonic particle. In this context it is worth pointing out our recent proposal to estimate such a mass by considering collisions of Proca stars to explain GW signal GW190521 [44–46].

This paper is organized as follows: in Sec. II we briefly present the basic set of equations we solve, for both the scalar field and the vector field. In Sec. III we construct the initial data for the bosonic cloud. Section IV presents our numerical framework and in Sec. V we discuss the main results of our work. Finally, our findings are summarized in Sec. VI. We use geometrized units, $G = c = \hbar = 1$, G being Newton's constant and c the speed of light. This choice makes the Planck mass equal to one, effectively disappearing from all equations. Latin (Greek) indices run from 1 (0) to 3.

¹See also [13] for multiscalar stars that may interpolate between oscillatons and boson stars.

II. FORMALISM

In this paper we study the dynamics of a scalar/Proca field minimally coupled to gravity by solving numerically the Einstein-Klein-Gordon and Einstein-Proca systems respectively. In both cases, the bosonic field is assumed to be complex and massive. The systems are described by the action

$$S = \int d^4x \sqrt{-g} \left(\frac{R}{16G\pi} + \mathcal{L}_{(S)} \right), \quad (1)$$

where the subscript (S) for the Lagrangian densities refers to the spin of the particles, i.e., 0 for the scalar field and 1 for the Proca field. The spacetime line element reads

$$ds^2 = g_{\mu\nu} dx^\mu dx^\nu = -(\alpha^2 - \beta_i \beta^i) dt^2 + 2\gamma_{ij} \beta^i dt dx^j + \gamma_{ij} dx^i dx^j, \quad (2)$$

where α is the lapse function, β^i is the shift vector, and γ_{ij} is the spatial metric. We cast the field equations into a 3 + 1 form, introducing the extrinsic curvature (conjugated momentum of the 3-metric) K_{ij} , defined as

$$K_{ij} = -\frac{1}{2\alpha} (\partial_t - \mathcal{L}_\beta) \gamma_{ij}, \quad (3)$$

where \mathcal{L}_β is the Lie derivative along β^i . We use the Baumgarte-Shapiro-Shibata-Nakamura (BSSN) formulation of Einstein's equations [47–49]. The matter source terms appearing in the BSSN equations depend on the energy density ρ_e , the momentum density j_i measured by an observer n^μ normal to the spatial hypersurfaces defining the spacetime foliation, and the spatial projection of the energy-momentum tensor S_{ij} , namely

$$\rho_e = n^\mu n^\nu T_{\mu\nu}, \quad (4)$$

$$j_i = -\gamma_i^\mu n^\nu T_{\mu\nu}, \quad (5)$$

$$S_{ij} = \gamma_i^\mu \gamma_j^\nu T_{\mu\nu}, \quad (6)$$

where the unit normal vector is $n^\mu = \frac{1}{\alpha}(1, -\beta^i)$ and γ_i^μ is the spatial projection operator.

A. Einstein-Klein-Gordon system

The Lagrangian density for a scalar field ϕ with a quartic self-interaction potential is given by

$$\mathcal{L}_{(0)} = -\frac{1}{2} \partial^\alpha \phi \partial_\alpha \bar{\phi} - \frac{1}{2} \mu_0^2 \phi \bar{\phi} - \frac{1}{4} \lambda (\phi \bar{\phi})^2, \quad (7)$$

where the bar denotes complex conjugation, μ_0 is the mass parameter of the scalar field, and λ is the coupling constant

of the self-interaction term. The energy-momentum tensor associated with this field is

$$T_{\mu\nu} = \frac{1}{2} g_{\mu\nu} \left(\partial_\lambda \bar{\phi} \partial^\lambda \phi + \mu_0^2 \bar{\phi} \phi + \frac{1}{2} \lambda (\bar{\phi} \phi)^2 \right) + \frac{1}{2} (\partial_\mu \bar{\phi} \partial_\nu \phi + \partial_\mu \phi \partial_\nu \bar{\phi}). \quad (8)$$

After introducing the conjugated momentum of the scalar field, Π , defined as

$$\Pi = -\frac{1}{\alpha} (\partial_t - \mathcal{L}_\beta) \phi, \quad (9)$$

it can be shown that in this case

$$\rho_e = \frac{1}{2} \left(\bar{\Pi} \Pi + \mu_0^2 \bar{\phi} \phi + \frac{1}{2} \lambda (\bar{\phi} \phi)^2 + D^i \bar{\phi} D_i \phi \right), \quad (10)$$

$$j_i = \frac{1}{2} (\bar{\Pi} D_i \phi + \Pi D_i \bar{\phi}), \quad (11)$$

$$S_{ij} = \frac{1}{2} (D_i \bar{\phi} D_j \phi + D_j \bar{\phi} D_i \phi) + \frac{1}{2} \gamma_{ij} (\bar{\Pi} \Pi - \mu_0^2 \bar{\phi} \phi - \frac{1}{2} \lambda (\bar{\phi} \phi)^2 - D^k \bar{\phi} D_k \phi), \quad (12)$$

where D_i stands for the covariant derivative associated with γ_{ij} .

B. Einstein-Proca system

Correspondingly, the Lagrangian density for a Proca field \mathcal{A}^α reads as

$$\mathcal{L}_{(1)} = -\frac{1}{4} \mathcal{F}_{\alpha\beta} \bar{\mathcal{F}}^{\alpha\beta} - \frac{1}{2} \mu_1^2 \mathcal{A}_\alpha \bar{\mathcal{A}}^\alpha, \quad (13)$$

where the bar denotes complex conjugation, $\mathcal{F} = d\mathcal{A}$ is the Proca field strength, and μ_1 is the Proca mass parameter. From the variation of this Lagrangian we can build the energy-momentum tensor of the Proca field,

$$T_{\mu\nu} = -\mathcal{F}_{\lambda(\mu} \bar{\mathcal{F}}_{\nu)}^\lambda - \frac{1}{4} g_{\mu\nu} \mathcal{F}_{\lambda\alpha} \bar{\mathcal{F}}^{\lambda\alpha} + \mu_1^2 \left[\mathcal{A}_{(\mu} \bar{\mathcal{A}}_{\nu)} - \frac{1}{2} g_{\mu\nu} \mathcal{A}_\lambda \bar{\mathcal{A}}^\lambda \right]. \quad (14)$$

The index notation (μ, ν) indicates, as usual, index symmetrization. The Proca 1-form \mathcal{A}_μ can be split into its scalar potential \mathcal{X}_ϕ , its 3-vector potential \mathcal{X}_i , and the 3-dimensional electric E_i and magnetic B_i field, defined by

$$\mathcal{X}_\phi = -n^\mu \mathcal{A}_\mu, \quad (15)$$

$$\mathcal{X}_i = \gamma_i^\mu \mathcal{A}_\mu, \quad (16)$$

$$E^i = -i \frac{\gamma^{ij}}{\alpha} (D_j(\alpha \mathcal{X}_\phi) + \partial_t \mathcal{X}_j), \quad (17)$$

$$B^i = \epsilon^{ijk} D_j \mathcal{X}_k, \quad (18)$$

where ϵ^{ijk} is the Levi-Civita tensor.

Finally, in this case

$$\rho_e = \frac{1}{2} \gamma_{ij} (\bar{E}^i E^j + \bar{B}^i B^j) + \frac{1}{2} \mu_1^2 (\bar{\mathcal{X}}_\phi \mathcal{X}_\phi + \gamma^{ij} \bar{\mathcal{X}}_i \mathcal{X}_j), \quad (19)$$

$$j_i = \frac{1}{2} \mu_1^2 (\bar{\mathcal{X}}_\phi \mathcal{X}_i + \mathcal{X}_\phi \bar{\mathcal{X}}_i), \quad (20)$$

$$S_{ij} = -\gamma_{ik} \gamma_{jl} (\bar{E}^k E^l + \bar{B}^k B^l) + \frac{1}{2} \gamma_{ij} (\bar{E}^k E_k + \bar{B}^k B_k) + \mu_1^2 \bar{\mathcal{X}}_\phi \mathcal{X}_\phi - \mu_1^2 \bar{\mathcal{X}}^k \mathcal{X}_k + \mu_1^2 \bar{\mathcal{X}}_i \mathcal{X}_j, \quad (21)$$

III. INITIAL DATA

To study the dynamical formation of SBSs we must first construct the initial configurations of the fields, both for the spacetime and the matter. As in [40] our choice of initial data is a cloud of bosonic matter with nonzero angular momentum. The initial data must satisfy the constraint equations of the system, namely the Hamiltonian constraint, the momentum constraint (see Eqs. (15)–(17) of [50]), and, for the Proca case, the Gauss constraint which reads as

$$D_i E^i = \mu_1^2 \mathcal{X}_\phi. \quad (22)$$

To build our initial configuration we assume an ansatz for the scalar/Proca field and we then build the spacetime fields by solving the Einstein constraint equations using the extended conformally flatness condition approximation [50]. We refer the interested reader to the Supplementary Material of [40] for the procedure we follow to construct the initial data.

For completeness, we report here the ansatz for the scalar and the Proca fields. For the scalar field case we specify the “shape” of the scalar cloud as in [40]

$$\phi(t, r, \theta, \varphi) = R(r) Y_{11}(\theta, \varphi) e^{-i\omega t}, \quad (23)$$

where $Y_{11}(\theta, \varphi) = \sin \theta e^{i\varphi}$ is the $\ell = m = 1$ spherical harmonic and $R(r) = A_0 r e^{-\frac{r^2}{\sigma^2}}$. The width of the Gaussian cloud σ is a free parameter of the initial data. At $t = 0$

$$\Pi = -\frac{i}{\alpha} (\omega + \beta^\varphi) \phi, \quad (24)$$

where we use that β^φ is the only nonzero component of the shift vector, a consequence of the axisymmetry invariance of the energy-momentum tensor.

For the components of the Proca field, we must also solve the Gauss constraint. In [40] we only considered the $m = 1$ Proca field. Here, we make a new ansatz for the scalar potential, to describe the $m = 2$ Proca field, namely

$$\mathcal{X}_\phi(t, r, \theta, \varphi) = R(r) Y_{22}(\theta, \varphi) e^{-i\omega t}, \quad (25)$$

where $R(r) = A_1 r e^{-\frac{r^2}{\sigma^2}}$ and $Y_{22}(\theta, \varphi) = \sin^2 \theta e^{2i\varphi}$ is the $\ell = m = 2$ spherical harmonic. We assume the electric field E^i is conservative, thus it can be written as the gradient of a potential. In this way the Gauss constraint can be solved analytically and yields

$$E^r(t, r, \theta, \varphi) = \frac{A_1 \sigma}{10 r^4} \left(-2\sqrt{\pi} r^5 + 6\sigma^5 - 3\sigma e^{-\frac{r^2}{\sigma^2}} r^4 + 2r^2 \sigma^2 + 2\sigma^4 \right) + 2\sqrt{\pi} r^5 \text{Erf} \left(\frac{r}{\sigma} \right) \times \sin^2 \theta e^{i(\omega t + 2\varphi)}, \quad (26)$$

$$E^\theta(t, r, \theta, \varphi) = \frac{A_1 \sigma}{5 r^5} \left(-\sqrt{\pi} r^5 - 2\sigma^5 + \sigma e^{-\frac{r^2}{\sigma^2}} r^4 + 2r^2 \sigma^2 + 2\sigma^4 \right) + \sqrt{\pi} r^5 \text{Erf} \left(\frac{r}{\sigma} \right) \times \sin \theta \cos \theta e^{i(\omega t + 2\varphi)}, \quad (27)$$

$$E^\varphi(t, r, \theta, \varphi) = \frac{A_1 \sigma}{5 r^5} \left(-\sqrt{\pi} r^5 - 2\sigma^5 + \sigma e^{-\frac{r^2}{\sigma^2}} r^4 + 2r^2 \sigma^2 + 2\sigma^4 \right) + \sqrt{\pi} r^5 \text{Erf} \left(\frac{r}{\sigma} \right) \times e^{i(\omega t + 2\varphi)}. \quad (28)$$

The vector potential can be obtained following the same reasoning we used in the Supplementary Material of [40], that gives us this relation

$$\mathcal{X}_i = \frac{i}{\alpha} (\omega + 2\beta^\varphi) \gamma_{ij} E^j. \quad (29)$$

IV. NUMERICAL CONSIDERATIONS

The numerical evolutions of the initial data are performed using the community-driven software platform EinsteinToolkit [51–53] which is based on the Cactus framework with Carpet [54,55] for mesh-refinement capabilities. The spacetime variables in the BSSN formulation are solved using the MCLACHLAN infrastructure [56,57]. The numerical code used in this work was originally assessed in [58] and is currently publicly available in [59] and distributed within each new release of the EinsteinToolkit; as in [24] we specifically employ a version of this code which was extended to take into account a complex Proca field.

Our numerical grid uses four refinement levels, each spanning a different spatial domain and each discretized with a different resolution. From the outermost grid to the innermost one, the spatial domains of the grids are $\{512, 256, 128, 32\}$ and the corresponding grid resolutions of each level are $\{6.4, 3.2, 1.6, 0.8\}$. We consider a larger numerical grid for the computation of the GWs; the spatial domains are $\{1024, 512, 256, 32\}$, and the corresponding grid resolutions of each level are $\{6.4, 3.2, 1.6, 0.8\}$. The time step is set as $\Delta_t = 0.125\Delta_x = 0.1$, where Δ_x is the grid spacing of the innermost grid along the x direction. All grids are equally spaced in all three spatial directions. Due to the geometry of the systems we investigate we assume reflection symmetry with respect to the equatorial plane. We use radiative (Sommerfeld) outer boundary condition implemented in the EinsteinToolkit thorn `NewRad` for the evolutions. We checked the convergence of our evolution code for the scalar field, evolving the model BS2 with $\lambda = 120$ with 4 different resolutions, namely $\Delta_x = \{6.4, 5.12, 4.096, 3.2\}$ for the outermost grid. We show in Fig. 1 the L_2 -norm of the Hamiltonian constraint at an arbitrary time $t = 1000$, for the different values of Δ_x , together with a numerical fit. We can observe that the convergence of our code follow a power-law of order 3.2, which is consistent with the expected 4th order convergence of our method. The convergence of the evolution code for the Proca field was already discussed in Appendix B of our previous work [40].

We set the value of the mass of the particle to $\mu_0 = \mu_1 = 1$ for all simulations. This sets the scale of the total mass of the systems under consideration at $M_0 \sim 1$. However, the simulations can be rescaled to obtain the results corresponding to different choices of $\mu_{0|1}$ by

making the transformation $r \rightarrow r \times \mu_{0|1}$, $M_0 \rightarrow M_0 \times \mu_{0|1}$, $t \rightarrow t \times \mu_{0|1}$ and $\omega \rightarrow \omega/\mu_{0|1}$.

V. RESULTS

The numerical simulations start with a Gaussian cloud of bosonic matter, built as described in Sec. III, which then collapses due to its own gravity. If enough energy is radiated away during this highly dynamical process through the mechanism of gravitational cooling [16], a compact bosonic star will form. As we already showed in [40] the presence of rotation may trigger the appearance of instabilities in the newly formed spinning compact object. More precisely, we found that scalar boson stars are affected by a nonaxisymmetric instability which triggers the loss of angular momentum and the reshaping of the energy density profile from a toroidal shape into a spheroidal one. This behavior was not observed for $m = 1$ spinning Proca stars, which have a spheroidal shape. As a consequence, we conjectured that this morphological difference was related to the dissimilar stability properties of these objects.

Here, we investigate if a self-interaction potential in the Klein-Gordon equation can quench the instability found in the scalar case and if our hypothesis that relates the instability to the toroidal shape of the energy density still holds when considering $m = 2$ spinning Proca stars, which have a toroidal shape. Table I summarizes the different models we consider to describe the initial cloud of bosonic matter. We use the same initial model BS2 in the scalar case as in our previous paper, building initial data for five different values of the self-interaction parameter, namely $\lambda = \{60, 120, 180, 240, 300\}$.

A. Boson stars with self-interaction

Figure 2 shows snapshots of the energy density distribution at the equatorial plane for model BS2 for evolutions with the five different values of λ . In all cases we observe that the final compact object is always affected by a nonaxisymmetric instability whose time of appearance depends on the value of the self-interaction parameter. The instability makes the energy density distribution to break into two pieces which subsequently recombine into a spheroidal, smaller piece, while the angular momentum is ejected from the region where the compact object forms.

TABLE I. Parameters of the initial models used in this study: S and P refer to scalar or Proca stars, respectively; σ is the width of the cloud; M_0 and J_0 indicate the initial mass and angular momentum of the cloud. All cases are for $\mu_0 = \mu_1 = 1$.

Model	Type	Mode	$A_{0 1}$	σ	M_0	J_0
BS2	S	1	16×10^{-5}	40	0.88	0.89
PS5	P	2	42×10^{-7}	70	1.48	2.93
PS6	P	2	51×10^{-7}	70	2.27	4.48

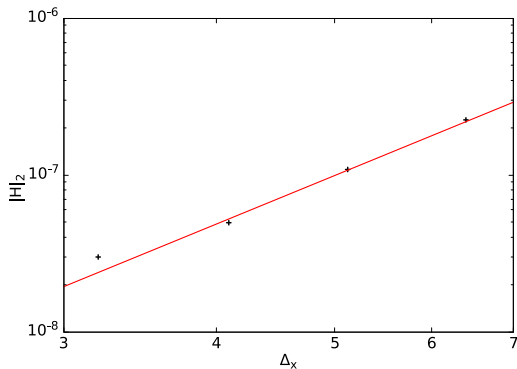


FIG. 1. L_2 -norm of the Hamiltonian constraint at time $t = 1000$ for model BS2 with $\lambda = 120$ and for 4 different resolutions. The black crosses correspond to the numerical data, and the red line is a numerical fit with the function $f(x) = a * \Delta_x^b$. The result of the fit gives the value $b = 3.2$.

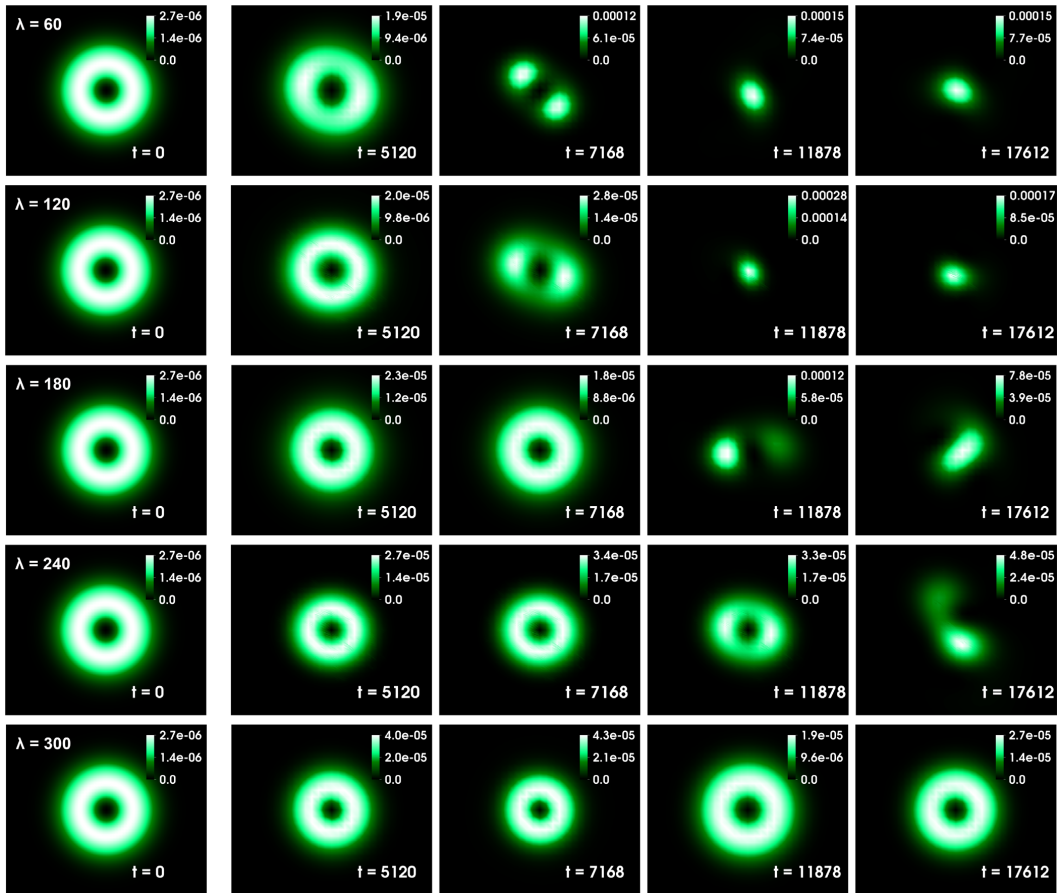


FIG. 2. Snapshots of the energy density at the equatorial plane for model BS2 with $\lambda = \{60, 120, 180, 240, 300\}$ (from top to bottom). The vertical axis corresponds to the y -direction and the horizontal to the x -direction. The spatial domain for the $t = 0$ snapshots is $[-80, 80] \times [-80, 80]$. The subsequent time snapshots are zoomed in the domain $[-40, 40] \times [-40, 40]$. The time of each snapshot is indicated in the panels.

By increasing the contribution of the self-interaction term it is possible to delay this occurrence. For the case $\lambda = 300$ (final row) the instability is not visible most probably because the evolution of the model is not sufficiently long.

Figure 3 depicts the evolution of the mass M_{30} and angular momentum J_{30} of the bosonic matter enclosed inside a sphere of radius $r = 30$ for the model with $\lambda = 60$. These two quantities are evaluated by means of the following integrals

$$M_{r^*} = -2 \int_0^{r^*} dr \int_0^{\frac{\pi}{2}} d\theta \int_0^{2\pi} d\varphi (2T_t^t - T_\alpha^\alpha) \sqrt{-g}, \quad (30)$$

$$J_{r^*} = 2 \int_0^{r^*} dr \int_0^{\frac{\pi}{2}} d\theta \int_0^{2\pi} d\varphi T_t^\varphi \sqrt{-g}, \quad (31)$$

where we take into account the reflection symmetry with respect to the equatorial plane we enforce in our numerical simulations.

We will use the notation M and J to refer to the total mass and angular momentum, evaluated up to the outer boundary of our numerical grid. Figure 3 shows that when the instability is triggered and the morphology of the object is reshaped into a spheroidal form, there is an abrupt loss of angular momentum which subsequently approaches

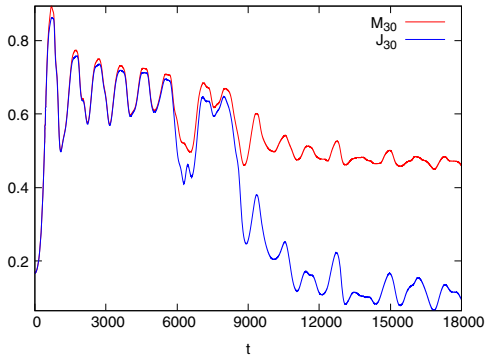


FIG. 3. Evolution of the mass and angular momentum contained in a sphere of radius 30 for the model BS2 with $\lambda = 60$.

zero. These two features—spheroidal shape and angular momentum loss—suggest that the final object approaches a non-spinning $l = m = 0$ boson star. While the model depicted in Fig. 3 corresponds to the case $\lambda = 60$, the results obtained for the other values of λ are remarkably similar. We note that it is possible to construct a countable number of families of boson stars and Proca stars labeled by the azimuthal number m . The ADM mass and angular momentum for these stars obey the simple rule $J = mQ$, where Q is their Noether charge, which means that there are

no solutions with a single bosonic field with intermediate values of the angular momentum between 0 and Q .

B. $m = 2$ spinning Proca stars

The initial data for the Proca field are described by Eqs. (25)–(28). Besides evolving the unperturbed case we also consider perturbed initial data. The latter are obtained by replacing in the field equations $e^{2i\varphi} \rightarrow e^{2i\varphi} + A \sum_{m=1}^4 e^{im\varphi}$, which explicitly breaks the axisymmetry of the energy density distribution. In Fig. 4 we display time snapshots of the energy density at the equatorial plane for model PS6 in the unperturbed case ($A = 0$; top row) and for two different values of the perturbation factor, namely $A = 0.01$ (middle row) and $A = 0.05$ (bottom row). We can observe that these stars undergo the same fragmentation process that happens for scalar boson stars. The larger the initial perturbation the sooner the instability that breaks the energy distribution into two pieces occurs. For our most extreme case ($A = 0.05$) this phenomenon happens during the gravitational collapse of the initial cloud and before the final compact object is formed. Nonetheless, in all three cases the two pieces remain bounded for a while during the evolution and the timescale at which they rejoin into a spheroidal Proca star is almost the same ($t \approx 4900$ for the unperturbed case, $t \approx 5500$ for both the perturbed cases) regardless of the initial perturbation. We speculate that the

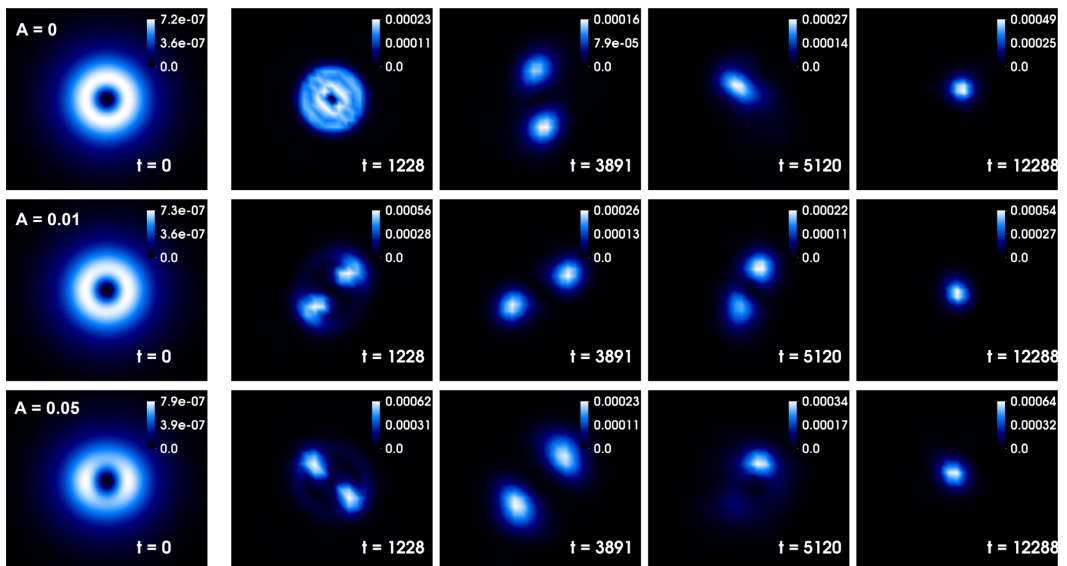


FIG. 4. Snapshots of the energy density in the equatorial plane for model PS6 and for three different perturbation parameters, $A = 0$, 0.01 and 0.05 (from top to bottom). The vertical axis correspond to the y direction and the horizontal to the x direction. Times are indicated in the legends. The spatial domain for the $t = 0$ snapshots is $[-160, 160] \times [-160, 160]$. The subsequent time snapshots are zoomed in the domain $[-30, 30] \times [-30, 30]$. The time of each snapshot is indicated in the panels.

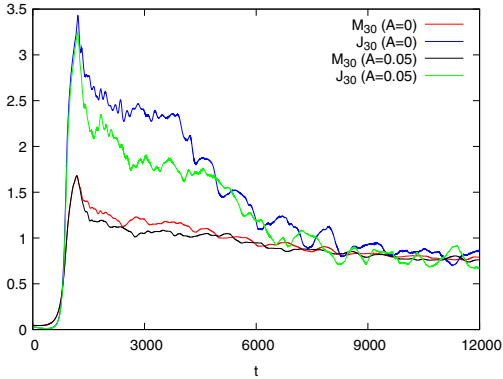


FIG. 5. Evolution of the mass and angular momentum enclosed in a sphere of radius 30 for model PS6, for the cases $A = 0$ (unperturbed) and $A = 0.05$. The different curves are indicated in the legend.

initial perturbation amplitude plays a role in the timescale on which the instability grows, but is not relevant for the timescale of the recombination (energy radiation timescale) because the latter is much longer than the first one.

Figure 5 depicts the mass M_{30} and angular momentum J_{30} enclosed inside a volume of radius $r = 30$ for model PS6 with $A = 0$ and $A = 0.05$. We observe that if we perturb the object, it loses smoothly angular momentum from $t \approx 1800$. In the unperturbed case we have a metastable phase from $t \approx 2000$ to $t \approx 3900$ during which the relation $J = mM$ is fulfilled and no loss of angular momentum is found. At $t \approx 3900$, this phase is lost and the angular momentum drops and rapidly reaches the same values as the perturbed case. Comparing this figure with Fig. 3 the different outcomes of spinning scalar and vector clouds become manifest. In the case of $m = 2$ Proca stars we observe that, for the two models, at the end of the evolution the angular momentum J_{30} is converging to a value similar to that of the mass M_{30} . This observation, together with the final spheroidal shape typical of $l = m = 1$ Proca solutions, suggest that the models dynamically approach a spinning $m = 1$ Proca star. Those stars are stable, as shown in [40].

C. Growth of nonaxisymmetric modes

We turn now to assess the nature of the nonaxisymmetry instability found for $m = 1$ scalar boson stars and for $m = 2$ Proca stars. In particular, we further elaborate on the analogy we first put forward in [40] between this dynamical phenomenon in rotating boson stars and differentially rotating neutron stars. It is well known that differentially rotating neutron stars can be subject to various nonaxisymmetric instabilities depending on the amount and degree of differential rotation (for a review see [43] and references

therein). For highly differentially rotating stars, an $m = 2$ dynamical bar-mode instability sets in, driven by hydrodynamics and gravity, m being the order of the azimuthal nonaxisymmetric fluid mode $e^{\pm im\varphi}$. While we follow the standard notation of using the letter m to indicate the azimuthal number of the perturbation, we warn the reader not to confuse it with the notation we also follow to denote the different families of bosonic stars in the manuscript. The distinction should be clear from the context. Moreover, highly differentially rotating neutron stars can also become unstable to a dynamical one-arm ($m = 1$) “spiral” instability. At lower rotation rates gravitational radiation and viscosity can drive a neutron star *secularly* unstable against bar-mode deformation. The occurrence of either kind of bar-mode instability depends on the particular value of the ratio $\beta = T/|W|$ of rotational kinetic energy T to gravitational potential energy W (see [43] for details).

As customary when studying the appearance of non-axisymmetric instabilities in differentially rotating fluids [42,60–63] we monitor the growth of the amplitude of the first few nonaxisymmetric modes. To this aim we define the volume-integrated azimuthal density (Fourier) mode decomposition as

$$C_m = \int dx^3 \rho_e(\mathbf{x}) e^{im\varphi}, \quad (32)$$

and the corresponding normalized quantity $\tilde{C}_m = \frac{C_m}{C_0}$. Note that C_0 is a measure of the total energy of the system. For our study we consider the first four modes $m = \{1, 2, 3, 4\}$. While we focus our discussion on model BS2 with $\lambda = 120$ as an illustrative case, the results are qualitatively similar for all values of λ considered.

In Fig. 6 we depict the time evolution of $|\tilde{C}_m|$ for the modes considered, in a logarithmic scale. As the initial data we construct have an axisymmetric energy-momentum tensor, the values of the mode amplitudes are initially

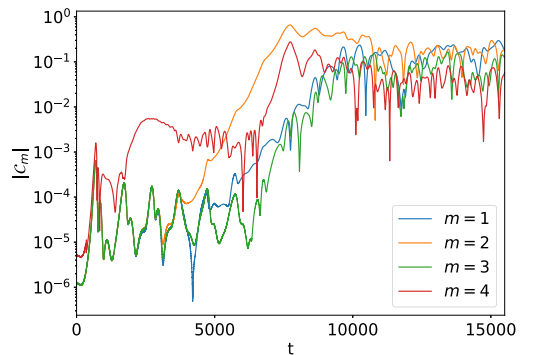


FIG. 6. Time evolution of the first four azimuthal modes $|\tilde{C}_m|$ ($m = \{1, 2, 3, 4\}$) for model BS2 with $\lambda = 120$.

close to zero. We first observe the growth of the $m = 4$ mode whose rapid excitation we attribute to the perturbation triggered by the Cartesian numerical grid employed in our code. Around time $t \approx 3000$ the other three modes start to be excited too, and around $t \approx 4000$ the $m = 2$ mode starts growing exponentially and soon become the dominant mode. At mode growth saturation the amplitude of the $m = 4$ mode is about one order of magnitude smaller than that of the other modes.

As the $m = 1$ mode starts to increase the boson star acquires a nonzero linear momentum. As a result, it undergoes a kick which displaces its center of mass from the origin of the numerical grid. This displacement has to be taken into account in order to properly estimate C_m with respect to the center of mass of the star [42]. To this end we redefine the azimuthal coordinate

$$\varphi = \arctan\left(\frac{y}{x}\right) \rightarrow \varphi = \arctan\left(\frac{y - y_{\text{CM}}}{x - x_{\text{CM}}}\right), \quad (33)$$

where $(x_{\text{CM}}, y_{\text{CM}})$ are the coordinates of the center of mass evaluated as

$$x_{\text{CM}} = \frac{1}{M} \int d\mathbf{x}^3 \rho_e(\mathbf{x}) x, \quad (34)$$

$$y_{\text{CM}} = \frac{1}{M} \int d\mathbf{x}^3 \rho_e(\mathbf{x}) y. \quad (35)$$

The coefficients shown in Fig. 6, including this correction, show that the $m = 2$ mode dominates over all the other modes. At late times in the numerical evolution the mode growth saturates and all modes have attained high amplitudes. Therefore, the newly formed nonspinning $l = m = 0$ boson star is still highly perturbed and far from a stationary solution. We note that the time evolution of azimuthal modes we observe for unstable SBSs is formally identical to what is observed in rotating neutron stars (see, e.g., Fig. 8 of [60] or Fig. 7 of [63]).

As discussed in [41,42] (see also [43]) the low $T/|W|$ dynamical bar-mode instability of differentially rotating neutron stars develops near the so-called corotation radius. This is the radius where the angular frequency of the unstable mode matches the local angular velocity of the fluid. We proceed next to search for the corotational radius in the case of BSs.

We consider that the azimuthal Fourier modes present in the evolution of C_m have the form

$$C_m \approx e^{(\sigma_m + i\omega_m)t}, \quad (36)$$

where σ_m is the growth rate of the mode and ω_m the mode frequency. The mode frequencies can be extracted by Fourier-transforming the time evolution of C_m .

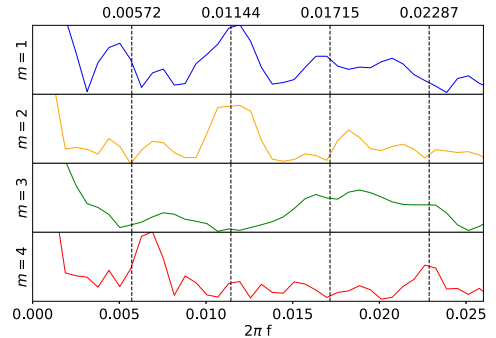


FIG. 7. Absolute value of the Fourier transform of C_m for model BS2 with $\lambda = 120$. The dashed vertical lines (and the values on top of them) are integer multiples of the pattern frequency estimated using the $m = 2$ mode frequency ($\omega_p = 0.0057$). The amplitude of the Fourier transform is normalized to fit all curves within the plot.

Figure 7 shows the Fourier transform of C_m for model BS2 with $\lambda = 120$. For the Fourier transform we consider only the late-time evolution of the modes (from $t \approx 5000$ to the end of the simulation). The main peaks in the spectrum correspond to the frequencies ω_m of the unstable modes. For the analysis it is interesting to compute the pattern frequency, $\omega_p = \omega_m/m$. This frequency corresponds to the rotational frequency of the perturbation pattern. For example, for $m = 2$ the time it takes for the bar to make a full rotation would be $2\pi/\omega_p$. In principle one could define a different pattern frequency for each of the modes. In practice, however, for instabilities associated with the existence of a corotation radius, the pattern frequency for all modes is very close [42]. To check this behavior we compute the pattern frequency from the main peak in the Fourier transform of the dominant $m = 2$ mode as $\omega_p = \omega_2/2$, which results in $\omega_p = 0.0057$ and overplot the value of $m\omega_p$ on top of the Fourier transform. The black dashed vertical lines in Fig. 7 represent $m\omega_p$, their values indicated on the top of the figure. We observe that there are peaks in the spectrum of the $m = \{1, 2, 3, 4\}$ modes approximately at $\omega_m = m\omega_p$, indicating that they are likely harmonics of the $\ell = m = 2$ mode. We point out that as the formation of bosonic stars is a very dynamical scenario, the spectrum of the modes appears to be noisy, especially for the lower amplitude modes. It is certainly not as clean as that obtained from a linear perturbation of an equilibrium solution, as shown in [42] for stationary models of neutron stars.

The corotation radius corresponds to the radius at which the pattern frequency is equal to the angular velocity Ω inside the star, which we define as

$$\Omega = \frac{j\dot{\phi}}{\rho_e}, \quad (37)$$

by analogy with the definition in relativistic hydrodynamics for a rotating fluid. We warn the reader that this definition of the angular velocity is not a gauge-invariant quantity. The mode pattern speed would be better compared to the angular velocity measured by an observer at infinity, u^ϕ/u^t , rather than to a local gauge-dependent quantity. The reason why we cannot use the latter definition involving a fluid velocity is because we do not have a fluid and, therefore, the only work-around is to compute the angular velocity from the angular momentum of the field.

The top panel of Fig. 8 shows the radial profile at the equatorial plane of the angular velocity Ω for model BS2 at different times. Due to the loss of axisymmetry, the radial profile is not the same when evaluated along different directions on the equatorial plane. To obtain clean profiles we consider time snapshots when the energy density profile is approximately axisymmetric and we evaluate the average from several directions. For each profile we estimate R_{95} ,

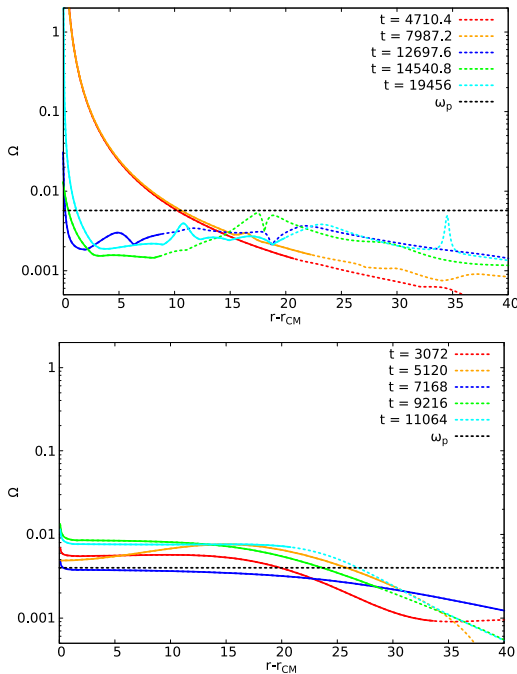


FIG. 8. Radial profiles of the angular velocity Ω for model BS2 with $\lambda = 120$ (upper panel) and for an $m = 1$ spinning Proca star (lower panel) evaluated at different times. The profiles are shown at the equatorial plane and along the x axis. The horizontal dashed lines indicate the pattern frequency, ω_p , computed using the $m = 2$ mode frequency in each case. Solid lines represent the region of the star inside R_{95} (interior of the star) and dashed lines outside this radius (exterior). Model BS2 shows a clear corotation radius at $r \approx 10$ at the beginning of the simulation.

defined as the radius of a sphere containing 95% of the energy, and highlight this radius in the figure by changing from solid to dashed lines. As the newly formed object suffers radial oscillations and radiates away energy through the gravitational cooling mechanism, this radius is only a rough estimation. The horizontal dashed line corresponds to the pattern frequency, ω_p , estimated above. The red line corresponds to a time when the compact object is already formed but the instability has not yet developed while the orange line shows the profile for a time when the fragmentation process has already started. The remaining lines correspond to times when the object is already spheroidal. We can observe that for the first two times shown a corotation point exists at radius $r \approx 10$ which is well inside the energy density profile of the star. At later times the angular velocity profile lays entirely below the pattern frequency except at the center. This is an indication that the origin of the observed instabilities is the presence of a corotation point. The instability drives the transport of angular momentum outwards until the corotation point disappears and the instability stops. We point out that the evaluation of the angular velocity Ω is subject to numerical errors when r approaches r_{CM} due to the fact that $j^\phi = j_\phi / (r - r_{\text{CM}})^2$ on the equatorial plane.

We repeat the same study for an $m = 1$ spinning Proca star model that we perturb by hand. In [40] we showed that this model does not develop a nonaxisymmetric instability, so one would expect not to observe a corotation point. The bottom panel of Fig. 8 shows the radial profile of the angular velocity Ω for this model extracted at different times, after the formation of the compact object. In this case the measured pattern frequency (horizontal line) is $\omega_p = 0.004$. For this model the profile of Ω is much flatter than in the case of the scalar SBS (BS2), and with values close to the pattern frequency. As the density profile radially oscillates, we observe 3 different phases. When the object is at its maximal extension, the angular velocity Ω is entirely below the pattern frequency (see $t = 7168$, blue line) meaning there is no corotational point. Note that, as mentioned above, the value of Ω close to the center should be disregarded due to the large numerical uncertainties in its calculation. When the object is at its maximal contraction (see $t = 11064$, cyan line) Ω is above the pattern frequency and only crosses it in regions outside R_{95} , meaning that there is no corotational point inside the star. For intermediate cases (the other 3 lines in the figure) we can find a corotational point which lies inside the star. This behavior is an indication of the presence of nonlinear oscillations because linear oscillations would have had an amplitude sufficiently small not to modify the background of Ω . The nonlinearity is caused by the high amplitude of the oscillations triggered by the collapse of the cloud that leads to the formation of the Proca star in our simulations and is hence unavoidable in our setup. Therefore, we suspect that the reason for the apparent equilibrium of

the system is either that it has no corotational point, and thus is stable to corotational instabilities, or that it has one but the profile of Ω is sufficiently shallow not to allow for the grow of instabilities in dynamical timescales.

D. Gravitational waveforms

The prospects of formation of rapidly-rotating neutron stars following the gravitational collapse of the core of massive stars or through the accretion-induced collapse of a white dwarf, highly motivates the investigation of the GWs produced by nonaxisymmetric instabilities (namely, the f -mode—or bar-mode—and the r -mode) that may affect them. Provided that neutron stars do not reach magnetarlike, magnetic-field values (i.e., for saturation values of the field $B \leq 10^{14}$ G) the GWs from the f -mode (i.e., bar-mode) instability should be well within the detection capabilities of third-generation interferometers such as the Einstein Telescope, yet they are only marginal for the current LIGO-Virgo detector network [64]. Notwithstanding the simplicity of our setup for the dynamical formation of SBSs, it is worth computing the corresponding gravitational waveforms for such bosonic objects and compare our estimates with those for neutron stars, an exercise we attempt in this section.

1. Gravitational wave extraction

The GW emission is computed through the mode decomposition of the Newman-Penrose scalar Ψ_4 in spin-weighted spherical harmonics with spin -2 . The coefficients $\Psi_4^{l,m}$ for $l = 2$ and $m = 1, 2$ are extracted at radii $r = \{200, 300, 500, 600, 1000\}$. The GW strain $h = h_+ - ih_\times$, where h_+ and h_\times are the two polarizations, is related to the second time-derivative of the Newman-Penrose scalar, as $\Psi_4 = -\ddot{h}$. We evaluate $r\Psi_4^{2,m}$ by interpolating with a third-order polynomial fit the values from three different extraction radii, namely $r = \{300, 600, 1000\}$. Figure 9 displays the real part of $r\Psi_4^{2,m}$ for $m = 0, 1, 2$, for model BS2 with $\lambda = 120$. During the formation process we observe a dominant $m = 0$ (axisymmetric) mode in the GW emission. The signal is periodic and it is due to energy emission triggered by the quasiradial oscillations of the newly formed object. When the nonaxisymmetric instability kicks in we observe, as expected, that the $m = 2$ quadrupolar mode becomes the dominant GW emitter while the $m = 1$ mode reaches maximum amplitudes about two orders of magnitude smaller. Correspondingly, the $m = 0$ mode is of comparable amplitude or one order of magnitude smaller.

The evolution of the waveform we have just described closely follows the dynamics of this model, displayed in the preceding figures. We observe that the GW emission from nonaxisymmetric modes starts around $t \approx 6000$ which, for model BS2 (see e.g., Fig. 6), corresponds to the time when the exponential growth of the $m = 2$ mode is about to reach its saturation amplitude. Around that time the object

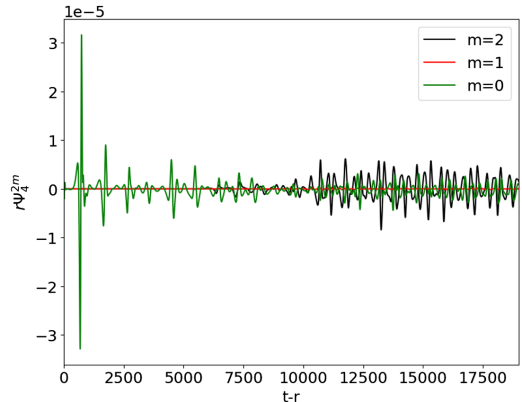


FIG. 9. Real part of $r\Psi_4^{2,m}$ for $m = 1, 2$ for model BS2 with $\lambda = 120$.

undergoes fragmentation (see second row of Fig. 2) and starts losing angular momentum (see Fig. 3). Therefore, we find a direct correspondence between the loss of angular momentum and the emission of GWs.

2. Detectability

For burstlike sources the characteristic GW amplitude is (see e.g., [65])

$$h_{\text{char}}(f) = \frac{1+z}{\pi D(z)} \sqrt{2 \frac{dE}{df} [(1+z)f]}, \quad (38)$$

where D is the distance to the source, z is the redshift, and dE/df is the energy spectrum of the waves. We use the cosmology calculator described in [66] to compute $D(z)$, with values of $H_0 = 70$ km/s/Mpc and $\Omega_m = 0.3$ for the Hubble constant and the fraction of energy density of matter, respectively.

For an optimally oriented detector the matched-filtering SNR squared, averaged over all possible source orientations is [65]

$$\rho_{\text{optimal}}^2 = \int_0^\infty d(\ln f) \frac{h_{\text{char}}(f)^2}{f S_n(f)}, \quad (39)$$

where $S_n(f)$ is the power spectral density (PSD) of the detector noise. Therefore, when plotting h_{char} of the signal with $\sqrt{f S_n(f)}$ in log-log scale, the area of the former quantity over the latter is directly related to the optimal SNR. The average SNR square over all possible detector orientations and sky locations is simply $\langle \rho^2 \rangle = \rho_{\text{optimal}}^2 / 5$.

The energy spectrum can be computed from the local energy flux

$$\frac{1}{r^2} \frac{dE}{d\Omega df} = \frac{\pi f^2}{2} |\tilde{h}(f)|^2 = \frac{1}{8\pi} \frac{|\tilde{\Psi}_4|^2}{(2\pi f)^2}, \quad (40)$$

where we use tilde for the Fourier transform. The energy spectrum can be obtained by integrating in angles

$$\frac{dE}{df} = \int d\Omega \frac{dE}{d\Omega df} = \frac{1}{8\pi(2\pi f)^2} \sum_{lm} |r\tilde{\Psi}_4^{lm}|^2, \quad (41)$$

where we have used the spherical decomposition of Ψ_4 and the orthonormality relations of the spin-weighted spherical harmonics. This expression allows us to compute the energy spectrum directly from the Ψ_4^{lm} extracted in the numerical simulations at the extraction radius r .

Since our system scales with the mass parameter μ_{01} , which sets the mass of the system, the typical frequency of the waveform may lie in the frequency band of different GW observatories. We have considered three cases: (i) ground-based laser interferometers, including the ongoing experiments Advanced LIGO (aLIGO) [67], Advanced Virgo (AdV) [68] and KAGRA [69], and the future observatory Einstein Telescope (ET) [70]; (ii) the space-based laser interferometer LISA [71]; and (iii) pulsar timing arrays (PTA), employing the canonical values used in [72] as a proxy to current observational limits, namely the future International Pulsar Timing Array (IPTA) [73] for 15 yr of observation and the Square Kilometre Array (SKA) [74] for 20 yr of observation (details can be found in [75]). In all cases we use the design sensitivity curves. For PTA we use as sensitivity curves the detection limits for a monochromatic source with a (sky averaged) SNR detection threshold of $\rho_{\text{thr}} = 3$.

Figure 10 shows the characteristic GW strain for model BS2 with $\lambda = 120$ (darker colors) and for model PS6

without perturbation (lighter colors). We consider three different values for the mass of the system, namely $\{5, 5 \times 10^5, 5 \times 10^{10}\} M_\odot$ for model BS2 and twice as much for model PS6. See, for instance Refs. [36,76,77] for discussions of boson stars as supermassive BH mimickers. For these ranges of masses the characteristic frequencies of the signals lie within the sensitivity ranges of ground-based detectors, space detectors, and PTA, respectively. For ground-based detectors we show the characteristic strain of a signal from a source at a distance $D = 1$ Mpc. For such a distance the signal is only marginally detectable by aLIGO, AdV, and KAGRA but it is within the detection capability of ET. For LISA and PTA we consider a distance to the source of $D = 1$ Gpc. Even at such large distance the signal could be detected. We next discuss quantitatively the detectability of these signals for each detector, defining and evaluating the horizon distance.

For the range of masses in the sensitivity range of ground-based and space-based GW observatories, the (scaled) duration of the event is ~ 1 s and ~ 1 day, respectively. The waveform can therefore be regarded as a burst, with limited time duration, and we can compute the SNR using Eq. (39). In these cases we define the horizon as the distance at which the average SNR is $\langle \rho \rangle = \rho_{\text{thr}} = 8$. For PTA the typical duration of the event is 300 y, much longer than the duration of the experiment. Here, the waveform can be regarded as a quasimonochromatic, continuous signal with frequency and characteristic strain corresponding to the peak h_{char} and frequency. In those cases we compute the horizon as the distance at which the peak amplitude is equal to the detection threshold (corresponding to $\text{SNR} \geq 3$) at the peak frequency.

Figure 11 shows the horizon for model BS2 with $\lambda = 120$ for a variety of detectors, as a function of the mass of

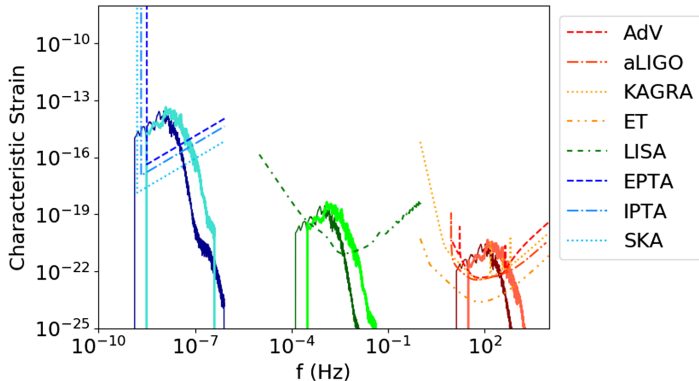


FIG. 10. Characteristic GW strain against frequency for model BS2 with $\lambda = 120$ (darker colors) and for model PS6 without a perturbation (lighter colors) compared with the sensitivity curves $\sqrt{fS_n(f)}$ of a variety of GW detectors. Three different masses are employed, namely $\{5, 5 \times 10^5, 5 \times 10^{10}\} M_\odot$ for model BS2 and twice those values for model PS6. A source distance $D = 1$ Mpc is assumed for ground-based detectors while for LISA and PTA we assume $D = 1$ Gpc.

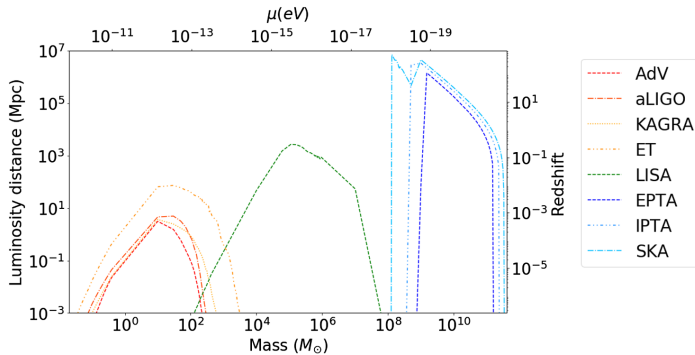


FIG. 11. Horizon distances as a function of mass for model BS2 with $\lambda = 120$ evaluated for a variety of GW detectors. The top x axis shows the corresponding particle mass μ and the right y axis the corresponding redshift. We again show the results for ground-based detectors (red colors), LISA (green color), and PTA (blue colors).

the source. In the right y axis we show the redshift value corresponding to the luminosity distances reported in the left y axis. One must recall that the mass of each SBS model is expressed in dimensionless units and that we can assign a physical mass $M(M_\odot)$ only after specifying a physical value for the particle mass μ_0 . The upper x axis indicates the particle mass μ_0 (eV) corresponding to the values of mass $M(M_\odot)$ shown in the lower x axis, evaluated as

$$\mu_0(\text{eV}) = \frac{\mathcal{M}_{\text{BS2}} M_{\text{Pl}}^2}{M_{\text{BS2}}(M_\odot) M_\odot}, \quad (42)$$

where $M_{\text{BS2}}(M_\odot)$ is the mass in physical units and $\mathcal{M}_{\text{BS2}} = 0.889$ is the mass of model BS2 in dimensionless units.

A GW signal from a stellar-size SBS with mass in the range $1\text{--}100 M_\odot$ might be detected by current 2nd-generation detectors at distances of a few Mpc. 3rd-generation detectors would increase the range of masses and the horizon to a few 10 Mpc. LISA sources would be in the $10^4\text{--}10^6 M_\odot$ range and detectable up to a few Gpc, while PTA sources would be in the $10^9\text{--}10^{11} M_\odot$ range and detectable up to redshifts of ~ 100 .

The nondetection of this kind of sources by the current GW detectors (aLIGO, AdV, and PTA) allows us to set upper limits on the expected rates of such events. A detailed calculation of these rates is out of the scope of this work but we can compute an order-of-magnitude estimate. Given the nonobservation, the rate of events per unit volume R cannot be much larger than $1/(V_{\text{obs}} T_{\text{obs}})$, where V_{obs} is the observing volume, which can be computed from the horizon estimation, D_{obs} , and T_{obs} is the duration of the observation. Using typical values for ground-based detectors and PTA yields rate estimates in two mass ranges:

$$R \lesssim 0.2 \left(\frac{D_{\text{obs}}}{1 \text{ Mpc}} \right)^{-3} \left(\frac{T_{\text{obs}}}{1 \text{ yr}} \right)^{-1} \text{ yr}^{-1} \text{ Mpc}^{-3}, \quad (43)$$

for $M \sim 10 M_\odot$, and

$$R \lesssim 2 \times 10^{-11} \left(\frac{D_{\text{obs}}}{1 \text{ Gpc}} \right)^{-3} \left(\frac{T_{\text{obs}}}{10 \text{ yr}} \right)^{-1} \text{ yr}^{-1} \text{ Mpc}^{-3}, \quad (44)$$

for $M \sim 10^{10} M_\odot$.

Future experiments (LISA, ET, SKA) will put even tighter constraints in the rate of these events and may have implication on the formation rate of bosonic stars or even on their existence. On the other hand, given the relation between the mass of the object and the particle mass μ_0 (or μ_1), observations of such events would help place tight constraints on the mass of the boson.

As a final remark we note that by the end of our simulations the barlike deformation ($m = 2$ mode) that was developed during the instability is still present. Even if the condition for the corotational instability is not fulfilled anymore, this deformation may last for a long time emitting GWs. Unlike neutron star matter, bosonic fields do not have efficient dissipation mechanisms such as viscosity to remove the deformation. Therefore, the characteristic damping timescale in which the deformation is erased is set by GW emission. We can estimate the GW damping timescale τ_m of a nonaxisymmetric mode ($m > 0$) as the ratio of the energy in each mode (approximately C_m) to the GW luminosity of the mode L_m ,

$$\tau_m = \frac{|C_m|}{L_m}, \quad (45)$$

where the GW luminosity can be computed integrating Eq. (41) for the relevant values of m ,

$$L_m = \frac{1}{8\pi} \int_0^\infty df \frac{1}{2\pi f} \sum_l |r\tilde{\Psi}_4^{lm}|^2. \quad (46)$$

Figure 12 shows the evolution of τ_m for $m = 1, 2$ in one of our simulations. After a transient phase associated with the gravitational collapse of the initial cloud and the development of the instability, τ_m settles to a mean value $\tau_m \approx 2 \times 10^7$. This value is about 1000 times longer than that of the signal connected with the instability. During this time, the emission is expected to be essentially monochromatic for each of the emitting modes. Therefore, the post-collapse GW emission is anticipated to be orders of magnitude more energetic than the emission due to the bar-mode instability itself, turning bar-mode-unstable SBSs into hypothetical potentially interesting sources of continuous GWs. For ground-based and space-based interferometers the typical duration of those events would be ~ 1000 s and 1000 days, respectively. Using the appropriate detection methods for monochromatic waveforms, whose sensitivity scales with $1/\sqrt{T_{\text{obs}}}$, and sufficiently long observation times (T_{obs} of the order of the event duration) the detector horizon for this kind of detectors (Fig. 11) could be enlarged by a factor $\sim \sqrt{1000}$.

We emphasize that the previous estimates should be taken as upper limits as Eq. (45) is overestimating the damping timescale. If it were possible to make a spherical-harmonic decomposition of the background, then C_m would include the energy of all the modes with $l \geq m$. Since GWs are emitted predominantly due to the $l = 2$ mode, the numerator of Eq. (45) includes the energy of all $l \geq 2$ while the denominator only includes, essentially, the $l = 2$ contribution. The most accurate computation of the damping timescale would involve the extraction of

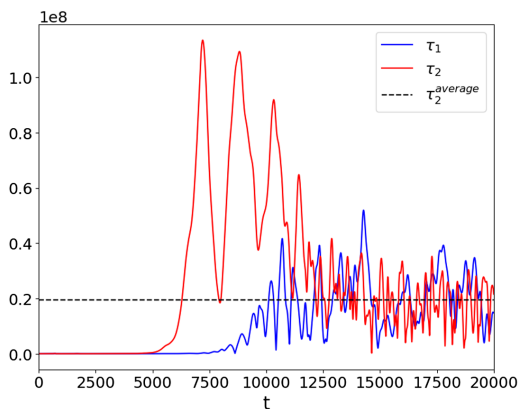


FIG. 12. Time evolution of the gravitational wave damping time τ_m for model BS2 with $\lambda = 120$. The dashed black horizontal line is the average value of τ_2 evaluated in the time window $t \in [12500, 20000]$.

the mode eigenfunctions of the background. While extracting the eigenfunctions from the numerical simulations is possible it would require additional simulations and a complicated analysis which is beyond the scope of the present investigation.

VI. CONCLUSIONS

The interest in studying exotic, horizonless compact objects [8] as BH mimickers has increased in recent years thanks, in part, to the detection of gravitational waves. Among the simplest, and dynamically more robust, proposals are self-gravitating compact objects made of bosonic particles, either scalar or vector, commonly referred to as boson stars and Proca stars, respectively [9–11]. In this paper we have studied these systems through three-dimensional numerical-relativity simulations of the Einstein-Klein-Gordon system and of the Einstein-Proca system, employing complex and massive fields. Using constraint-satisfying initial data representing clouds of scalar/Proca particles with nonzero angular momentum our time evolutions have shown the gravitational collapse of the clouds and the formation of SBSs via gravitational cooling. This paper is a significant extension of our previous work [40] where the transient nature of the newly formed SBS in the scalar case was established. The scalar star is always affected by the growth of a nonaxisymmetric instability which triggers the loss of angular momentum and its migration to a nonspinning boson star. The situation is different for $m = 1$ Proca stars, which do not suffer from such instability. In [40] we related the different stability properties to the different toroidal/spheroidal topology of the scalar/Proca models.

The results of the new numerical-relativity simulations reported in the present work have allowed us to draw a more complete picture of the dynamical formation scenario of SBS and of their stability properties in the nonlinear regime. Not only have we incorporated additional aspects for the physical description of the system (e.g., accounting for a quartic self-interaction potential in the scalar case to gauge its effect on the instability or investigating toroidal ($m = 2$) Proca stars to confirm our conjecture that they are indeed unstable) but we have also carried out a deeper analysis of the development of the bar-mode instability in SBS and associated GW emission. This analysis has made use of the study of the growth rate of azimuthal density modes in the stars and the search of a corotation point in unstable models. This is an approach commonly employed to study bar-mode unstable neutron stars. Interestingly, we have found that the dynamics of bar-mode unstable SBSs bears a close resemblance with that of their neutron star “relatives.” This parallelism has been discussed to some length in this paper.

Our main results regarding the stability properties of SBSs indicate that: (a) the self-interaction potential can only delay the instability in scalar SBSs but cannot quench

it completely; (b) $m = 2$ Proca stars always migrate to the stable $m = 1$ spheroidal family; and (c) unstable $m = 2$ Proca stars and $m = 1$ scalar boson stars exhibit a pattern of frequencies for the azimuthal density modes which crosses the angular velocity profile of the stars in the corotation point.

An important part of this research has dealt with the analysis of the GWs emitted by SBSs as a result of nonaxisymmetric deformations. We have extracted the gravitational waveforms of some representative models and we have investigated their detectability prospects. This has been done by comparing the characteristic strain of the signal with the sensitivity curves of a variety of detectors (current ground-based interferometers Advanced LIGO, Advanced Virgo and KAGRA, the 3rd-generation detector ET, and space missions such as LISA and Pulsar Timing Arrays) and by computing the signal-to-noise ratio for different ranges of masses and for different source distances. Our study has revealed that GWs from a stellar-size SBS in the $1\text{--}100 M_{\odot}$ mass range might be detected by 2nd-generation detectors up to a few Mpc while 3rd-generation detectors would increase the range of masses and the horizon to a few 10 Mpc. LISA could observe SBS sources in the $10^4\text{--}10^6 M_{\odot}$ mass range up to a few Gpc. For PTA the sources would be in the $10^9\text{--}10^{11} M_{\odot}$ mass range and could be detectable up to redshifts of ~ 100 . Moreover, by assuming that the characteristic damping timescale of the barlike deformation in SBSs is only set by GW emission and not by viscosity, unlike what happens for neutron stars where the two effects must be taken into account, we have found that the postcollapse emission could be orders of magnitude more energetic than that of the bar-mode instability itself. As a result, if SBS existed in Nature, the findings reported in this paper would turn them into potentially interesting sources of continuous gravitational waves. The theoretical

estimates reported in this work offer the intriguing possibility to probe (or constrain) the existence of bosonic stars and could in turn help place tight constraints on the mass of the constitutive bosonic particle.

ACKNOWLEDGMENTS

We thank Carlos Palenzuela, Darío Núñez, Juan Carlos Degollado, Sergio Gimeno-Soler, Jens Mahlmann and Christopher Moore for useful discussions and valuable comments, and Nikolaos Stergioulas for a careful reading of the manuscript. This work has been supported by the Spanish Agencia Estatal de Investigación (PGC2018-095984-B-I00), by the Generalitat Valenciana (grant No. PROMETEO/2019/071 and No. GRISOLIAP/2019/029), by the Fundação para a Ciência e a Tecnologia (FCT) projects No. PTDC/FIS-OUT/28407/2017, No. CERN/FIS-PAR/0027/2019, No. UIDB/04106/2020 and No. UIDP/04106/2020 (CIDMA) and No. UID/FIS/00099/2020 (CENTRA), by national funds (OE), through FCT, I. P., in the scope of the framework contract foreseen in the numbers 4, 5 and 6 of the article 23, of the Decree-Law 57/2016, of August 29, changed by Law 57/2017, of July 19. This work has further been supported by the European Union's Horizon 2020 research and innovation (RISE) programme H2020-MSCA-RISE-2017 Grant No. FunFiCO-777740. We would like to acknowledge networking support by the COST Action GWverse CA16104. M. Z. acknowledges financial support provided by FCT/Portugal through the IF programme, Grant No. IF/00729/2015. P. C. acknowledges the Ramon y Cajal funding (RYC-2015-19074) supporting his research. Computations have been performed at the Servei d'Informàtica de la Universitat de València, on the "Baltasar Sete-Sois" cluster at IST, and at MareNostrum (via PRACE Tier-0 Grant No. 2016163948).

-
- [1] B. P. Abbott *et al.* (Virgo and LIGO Scientific Collaborations), *Phys. Rev. Lett.* **116**, 061102 (2016).
 - [2] B. P. Abbott *et al.* (Virgo and LIGO Scientific Collaborations), *Phys. Rev. Lett.* **116**, 241103 (2016).
 - [3] B. P. Abbott *et al.* (Virgo and LIGO Scientific Collaborations), *Phys. Rev. Lett.* **118**, 221101 (2017).
 - [4] B. P. Abbott *et al.* (Virgo and LIGO Scientific Collaborations), *Astrophys. J.* **851**, L35 (2017).
 - [5] B. P. Abbott *et al.* (Virgo and LIGO Scientific Collaborations), *Phys. Rev. Lett.* **119**, 161101 (2017).
 - [6] B. P. Abbott *et al.* (Virgo and LIGO Scientific Collaborations), *Phys. Rev. Lett.* **119**, 141101 (2017).
 - [7] K. Akiyama *et al.* (Event Horizon Telescope Collaboration), *Astrophys. J.* **875**, L1 (2019).
 - [8] V. Cardoso and P. Pani, *Living Rev. Relativity* **22**, 4 (2019).
 - [9] D. J. Kaup, *Phys. Rev.* **172**, 1331 (1968).
 - [10] R. Ruffini and S. Bonazzola, *Phys. Rev.* **187**, 1767 (1969).
 - [11] R. Brito, V. Cardoso, C. A. R. Herdeiro, and E. Radu, *Phys. Lett. B* **752**, 291 (2016).
 - [12] D. N. Page, *Phys. Rev. D* **70**, 023002 (2004).
 - [13] S. H. Hawley and M. W. Choptuik, *Phys. Rev. D* **67**, 024010 (2003).
 - [14] F. E. Schunck and E. W. Mielke, *Classical Quantum Gravity* **20**, R301 (2003).
 - [15] S. L. Liebling and C. Palenzuela, *Living Rev. Relativity* **15**, 6 (2012).
 - [16] E. Seidel and W.-M. Suen, *Phys. Rev. Lett.* **72**, 2516 (1994).

- [17] F. Di Giovanni, N. Sanchis-Gual, C. A. R. Herdeiro, and J. A. Font, *Phys. Rev. D* **98**, 064044 (2018).
- [18] M. Gleiser and R. Watkins, *Nucl. Phys.* **B319**, 733 (1989).
- [19] T. D. Lee and Y. Pang, *Nucl. Phys.* **B315**, 477 (1989).
- [20] N. Sanchis-Gual, C. Herdeiro, E. Radu, J. C. Degollado, and J. A. Font, *Phys. Rev. D* **95**, 104028 (2017).
- [21] F. Guzmán, *Rev. Mex. Fis.* **55**, 321 (2009), <https://rmf.smf.mx/ojs/rmf/article/view/3695>.
- [22] C. Palenzuela, I. Olabarrieta, L. Lehner, and S. L. Liebling, *Phys. Rev. D* **75**, 064005 (2007).
- [23] C. Palenzuela, L. Lehner, and S. L. Liebling, *Phys. Rev. D* **77**, 044036 (2008).
- [24] N. Sanchis-Gual, C. Herdeiro, J. A. Font, E. Radu, and F. Di Giovanni, *Phys. Rev. D* **99**, 024017 (2019).
- [25] F. E. Schunck and E. W. Mielke, *Phys. Lett. A* **249**, 389 (1998).
- [26] S. Yoshida and Y. Eriguchi, *Phys. Rev. D* **56**, 762 (1997).
- [27] B. Kleihaus, J. Kunz, M. List, and I. Schaffer, *Phys. Rev. D* **77**, 064025 (2008).
- [28] C. Herdeiro, E. Radu, and H. Runarsson, *Classical Quantum Gravity* **33**, 154001 (2016).
- [29] N. M. Santos, C. L. Benone, L. C. Crispino, C. A. Herdeiro, and E. Radu, *J. High Energy Phys.* **07** (2020) 010.
- [30] C. Herdeiro, I. Perapechka, E. Radu, and Y. Shnir, *Phys. Lett. B* **797**, 134845 (2019).
- [31] Z. Meliani, F. H. Vincent, P. Grandclément, E.ourgoulhon, R. Monceau-Baroux, and O. Straub, *Classical Quantum Gravity* **32**, 235022 (2015).
- [32] C. Herdeiro and E. Radu, *Classical Quantum Gravity* **32**, 144001 (2015).
- [33] C. A. R. Herdeiro, E. Radu, and H. F. Runarsson, *Int. J. Mod. Phys. D* **25**, 1641014 (2016).
- [34] N. Franchini, P. Pani, A. Maselli, L. Gualtieri, C. A. R. Herdeiro, E. Radu, and V. Ferrari, *Phys. Rev. D* **95**, 124025 (2017).
- [35] J. F. Delgado, C. A. Herdeiro, and E. Radu, *J. Cosmol. Astropart. Phys.* **06** (2020) 037.
- [36] F. H. Vincent, Z. Meliani, P. Grandclément, E.ourgoulhon, and O. Straub, *Classical Quantum Gravity* **33**, 105015 (2016).
- [37] P. V. P. Cunha, C. A. R. Herdeiro, E. Radu, and H. F. Runarsson, *Phys. Rev. Lett.* **115**, 211102 (2015).
- [38] Z. Cao, A. Cardenas-Avendano, M. Zhou, C. Bambi, C. A. R. Herdeiro, and E. Radu, *J. Cosmol. Astropart. Phys.* **10** (2016) 003.
- [39] T. Shen, M. Zhou, C. Bambi, C. A. R. Herdeiro, and E. Radu, *J. Cosmol. Astropart. Phys.* **08** (2017) 014.
- [40] N. Sanchis-Gual, F. Di Giovanni, M. Zilhão, C. Herdeiro, P. Cerdá-Durán, J. A. Font, and E. Radu, *Phys. Rev. Lett.* **123**, 221101 (2019).
- [41] A. L. Watts, N. Andersson, and D. I. Jones, *Astrophys. J.* **618**, L37 (2005).
- [42] P. Cerd-Dum, V. Quilis, and J. A. Font, *Comput. Phys. Commun.* **177**, 288 (2007).
- [43] V. Paschalidis and N. Stergioulas, *Living Rev. Relativity* **20**, 7 (2017).
- [44] R. Abbott *et al.* (LIGO Scientific and Virgo Collaborations), *Phys. Rev. Lett.* **125**, 101102 (2020).
- [45] B. P. Abbott *et al.* (LIGO Scientific and Virgo Collaborations), *Astrophys. J. Lett.* **900**, L13 (2020).
- [46] J. C. Bustillo, N. Sanchis-Gual, A. Torres-Forné, J. A. Font, A. Vajpeyi, R. Smith, C. Herdeiro, E. Radu, and S. H. Leong, [arXiv:2009.05376](https://arxiv.org/abs/2009.05376).
- [47] T. Nakamura, K. Oohara, and Y. Kojima, *Prog. Theor. Phys. Suppl.* **90**, 1 (1987).
- [48] M. Shibata and T. Nakamura, *Phys. Rev. D* **52**, 5428 (1995).
- [49] T. W. Baumgarte and S. L. Shapiro, *Phys. Rev. D* **59**, 024007 (1998).
- [50] I. Cordero-Carrion, P. Cerda-Duran, H. Dimmelmeier, J. L. Jaramillo, J. Novak, and E.ourgoulhon, *Phys. Rev. D* **79**, 024017 (2009).
- [51] M. Babiuć-Hamilton *et al.*, The Einstein Toolkit (2019), to find out more, <http://einstein toolkit.org>.
- [52] F. Löffler, J. Faber, E. Bentivegna, T. Bode, P. Diener, R. Haas, I. Hinder, B. C. Mundim, C. D. Ott, E. Schnetter, G. Allen, M. Campanelli, and P. Laguna, *Classical Quantum Gravity* **29**, 115001 (2012).
- [53] M. Zilhão and F. Löffler, *Int. J. Mod. Phys. A* **28**, 1340014 (2013).
- [54] E. Schnetter, S. H. Hawley, and I. Hawke, *Classical Quantum Gravity* **21**, 1465 (2004).
- [55] Carpet, <http://www.carpetcode.org/>, Carpet: Adaptive mesh refinement for the cactus framework.
- [56] C. Reisswig, C. D. Ott, U. Sperhake, and E. Schnetter, *Phys. Rev. D* **83**, 064008 (2011).
- [57] D. Brown, P. Diener, O. Sarbach, E. Schnetter, and M. Tiglio, *Phys. Rev. D* **79**, 044023 (2009).
- [58] M. Zilhão, H. Witek, and V. Cardoso, *Classical Quantum Gravity* **32**, 234003 (2015).
- [59] H. Witek, M. Zilhao, G. Ficarra, and M. Elley, Canada: A public numerical relativity library to probe fundamental physics (2020), to find out more, <https://bitbucket.org/canuda/>.
- [60] L. Baiotti, R. de Pietri, G. M. Manca, and L. Rezzolla, *Phys. Rev. D* **75**, 044023 (2007).
- [61] K. D. Camarda, P. Anninos, P. C. Fragile, and J. A. Font, *Astrophys. J.* **707**, 1610 (2009).
- [62] K. Kiuchi, M. Shibata, P. J. Montero, and J. A. Font, *Phys. Rev. Lett.* **106**, 251102 (2011).
- [63] P. L. Espino, V. Paschalidis, T. W. Baumgarte, and S. L. Shapiro, *Phys. Rev. D* **100**, 043014 (2019).
- [64] K. Glampedakis and L. Gualtieri, Gravitational waves from single neutron stars: An advanced detector era survey, in *Astrophysics and Space Science Library*, Astrophysics and Space Science Library Vol. 457, edited by L. Rezzolla, P. Pizzochero, D. I. Jones, N. Rea, and I. Vidaña (Springer, Cham, 2018), p. 673, <https://doi.org/10.1007/978-3-319-97616-7>.
- [65] É. É. Flanagan and S. A. Hughes, *Phys. Rev. D* **57**, 4535 (1998).
- [66] E. L. Wright, *Publ. Astron. Soc. Pac.* **118**, 1711 (2006).
- [67] J. Aasi *et al.* (LIGO Scientific Collaboration), *Classical Quantum Gravity* **32**, 074001 (2015).
- [68] F. Acernese *et al.*, *Classical Quantum Gravity* **32**, 024001 (2015).
- [69] K. Somiya, *Classical Quantum Gravity* **29**, 124007 (2012).
- [70] M. Punturo *et al.*, *Classical Quantum Gravity* **27**, 194002 (2010).
- [71] P. Amaro-Seoane *et al.*, *GW Notes* **6**, 4 (2013), <https://astro-gr.org/wp-content/uploads/2017/06/1201.3621.pdf>.

-
- [72] C. J. Moore, S. R. Taylor, and J. R. Gair, *Classical Quantum Gravity* **32**, 055004 (2015).
- [73] R. N. Manchester, *Classical Quantum Gravity* **30**, 224010 (2013).
- [74] P. E. Dewdney, P. J. Hall, R. T. Schilizzi, and T. J. L. W. Lazio, *IEEE Proc.* **97**, 1482 (2009).
- [75] C. J. Moore, R. H. Cole, and C. P. L. Berry, *Classical Quantum Gravity* **32**, 015014 (2015).
- [76] V. Diemer, K. Eilers, B. Hartmann, I. Schaffer, and C. Toma, *Phys. Rev. D* **88**, 044025 (2013).
- [77] P. Amaro-Seoane, J. Barranco, A. Bernal, and L. Rezzolla, *J. Cosmol. Astropart. Phys.* **11** (2010) 002.

Multifield, Multifrequency Bosonic Stars and a Stabilization Mechanism

Nicolas Sanchis-Gual^{1,2}, Fabrizio Di Giovanni³, Carlos Herdeiro¹, Eugen Radu¹ and José A. Font^{3,4}

¹*Departamento de Matemática da Universidade de Aveiro and
Centre for Research and Development in Mathematics and Applications (CIDMA),
Campus de Santiago, 3810-183 Aveiro, Portugal*

²*Centro de Astrofísica e Gravitação—CENTRA, Departamento de Física, Instituto Superior Técnico—IST,
Universidade de Lisboa—UL, Avenida Rovisco Pais 1, 1049-001 Lisboa, Portugal*

³*Departamento de Astronomía y Astrofísica, Universitat de València, Dr. Moliner 50, 46100 Burjassot (València), Spain*

⁴*Observatori Astronòmic, Universitat de València, C/ Catedrático José Beltrán 2, 46980 Paterna (València), Spain*



(Received 29 March 2021; accepted 25 May 2021; published 17 June 2021)

Scalar bosonic stars (BSs) stand out as a multipurpose model of exotic compact objects. We enlarge the landscape of such (asymptotically flat, stationary, everywhere regular) objects by considering multiple fields (possibly) with different frequencies. This allows for new morphologies and a stabilization mechanism for different sorts of unstable BSs. First, any odd number of complex fields, yields a continuous family of BSs departing from the spherical, equal frequency, ℓ -BSs. As the simplest illustration, we construct the $\ell = 1$ BSs family, that includes several single-frequency solutions, including even parity (such as spinning BSs and a toroidal, static BS) and odd parity (a dipole BS) limits. Second, these limiting solutions are dynamically unstable, but can be stabilized by a hybrid- ℓ construction: adding a sufficiently large fundamental $\ell = 0$ BS of another field, with a different frequency. Evidence for this dynamical robustness is obtained by nonlinear numerical simulations of the corresponding Einstein-(complex, massive) Klein-Gordon system, both in formation and evolution scenarios, and a suggestive correlation between stability and energy distribution is observed. Similarities and differences with vector BSs are anticipated.

DOI: 10.1103/PhysRevLett.126.241105

Introduction.—Recent observations of dark compact objects, via gravitational waves [1–3], very large baseline interferometry imaging of M87* [4] or orbital motions near Sagittarius A* [5] support the black hole hypothesis. Yet, the issue of degeneracy remains a central question. This has been sharpened by recent illustrations, in both the gravitational and electromagnetic channels [6,7], using dynamically robust bosonic stars (BSs) to imitate the observed data.

In spite of many proposed black hole mimicker models [8], imposing an established formation mechanism and dynamical stability, within a sound effective field theory, restricts considerably the choices. The fundamental spherical (scalar [9,10] or vector [11]) BSs, occurring in Einstein’s gravity minimally coupled to a single complex, free bosonic field, fulfill these criteria [12], having become prolific testing grounds for strong-gravity phenomenology. The purpose of this Letter is to enlarge the landscape of dynamically robust BSs, by considering multifield, multi-frequency solutions, which will open new avenues of research, both theoretical and phenomenological, for these remarkable gravitational solitons.

Single and multifield BSs.—Single field BSs appear in different varieties [13] besides the aforementioned fundamental spherical (*monopole*) solutions [14], including

spinning BSs [11,15–17] and multipolar (static) BSs [18]. Concerning the former, only the vector case is dynamically robust [19]; concerning the latter, the simplest illustration is the *dipole* BS, shown to be unstable below.

Single-field BSs provide building blocks for multifield BSs, despite the nonlinearity of the model. Appropriate superpositions, moreover, change dynamical properties. An *excited* monopole scalar BS, which is unstable against decaying to a fundamental BS [20], is stabilized by adding a sufficiently large fundamental monopole BS of a second field [21] (see also [22–24]). In the same spirit, for the nonrelativistic BSs of the Schrödinger-Poisson system, a dipole configuration is stabilized by adding a sufficiently large fundamental monopole [25] (see also [26]). These examples turn out to be illustrations of a stabilization *mechanism*, as we shall discuss.

A particular type of multifield BSs, composed of an odd number ($2\ell + 1$, $\ell \in \mathbb{N}_0$) of (equal frequency) complex scalar fields was unveiled in [27] and dubbed ℓ -BSs. These are spherical and can be seen as a superposition of all m multipoles, with the same amplitude, for a given ℓ . ℓ -BSs were shown to be stable in spherical symmetry [28]; but nonspherical perturbations suggest new equilibrium configurations exist with different frequencies for different fields [29]. This will be confirmed herein: ℓ -BS are just the

symmetry-enhanced points of larger continuous families of multifield, multifrequency BSs [30].

The model.—Einstein’s gravity minimally coupled to a set of N free, complex, massive scalar fields $\Phi^{(j)}$ is $S = (16\pi G)^{-1} \int d^4x \sqrt{-g} [R - \mathcal{L}]$, where G is Newton’s constant, R the Ricci scalar and the matter Lagrangian is

$$\mathcal{L} = \sum_{j=1}^N (g^{\alpha\beta} \Phi_{,\alpha}^{(j)*} \Phi_{,\beta}^{(j)} + \mu^2 \Phi^{(j)*} \Phi^{(j)}); \quad (1)$$

μ is the (common) mass of all fields $\Phi^{(j)}$ and the asterisk (*) denotes complex conjugation.

All BSs studied herein are described by the metric ansatz $ds^2 = -e^{2F_0(r,\theta)} dt^2 + e^{2F_1(r,\theta)} (dr^2 + r^2 d\theta^2) + e^{2F_2(r,\theta)} r^2 \sin^2\theta (d\varphi - W(r,\theta) dt)^2$, in terms of four unknown metric functions of the coordinates (r, θ) ; the two Killing coordinates (t, φ) represent the time and azimuthal directions. The N scalar fields $\Phi^{(j)}$ are

$$\Phi^{(j)} = \phi_j(r, \theta) e^{-i(w_j t - m_j \varphi)}, \quad (2)$$

where $w_j \in \mathbb{R}^+$ are the fields’ frequencies and $m_j \in \mathbb{Z}$ the azimuthal harmonic indices. The fields’ amplitudes ϕ_j are real functions. This ansatz illustrates symmetry non-inheritance [34]: each $\Phi^{(j)}$ depends on the Killing coordinates but its energy-momentum tensor (EMT) does not [35].

Constructing the enlarged ℓ -BSs family.—Taking an odd number of fields, $N = 2\ell + 1$, for a fixed $\ell \in \mathbb{N}_0$, a spherical ansatz ($W = 0$, $F_1 = F_2$, with no angular dependence), equal frequencies ($w_j = w$), and equal radial amplitudes such that $\phi_j(r, \theta) e^{im_j \varphi} = f(r) Y_\ell^{-\ell-1+j}(\theta, \varphi)$, where Y_ℓ^m are the standard spherical harmonics, one obtains ℓ -BSs [27].

Taking still $N = 2\ell + 1$ but keeping the most general ansatz discussed above new possibilities emerge. We take $m_j = -\ell - 1 + j$, as for ℓ -BSs. For concreteness we focus on the simplest nontrivial $\ell = 1$ case. Then, the problem reduces to solving a set of seven partial differential equations (PDEs), for $F_{0,1,2}$, W , and $\phi_{1,2,3}$. This number reduces for particular cases [36]. These PDEs are solved with boundary conditions: (i) at $r = 0$, $\partial_r F_{0,1,2} = 0$, $\partial_r W = 0$, $\partial_r \phi_2 = \phi_{1,3} = 0$; (ii) at infinity all functions vanish, $F_{0,1,2} = W = \phi_i = 0$; (iii) at $\theta = 0, \pi$, $\partial_\theta F_{0,1,2} = 0$, $\partial_\theta \phi_2 = \phi_{1,3} = 0$; (iv) the geometry is invariant under a reflection along the equatorial plane $\theta = \pi/2$, and, as for ℓ -BSs, ϕ_2 and $\phi_{1,3}$ are parity odd and even functions, respectively. Thus, at $\theta = \pi/2$, $\partial_\theta F_{0,1,2} = \partial_\theta W = \phi_2 = \partial_\theta \phi_{1,3} = 0$. All configurations reported here are *fundamental*, with $n = 0$, where n is the number of nodes along the equatorial plane of $\phi_{1,3}(r, \pi/2)$ [37]. The solutions are constructed

numerically by employing the same approach as for the case of single-field BSs—see, e.g., the description in [38].

The single-frequency, multifield limits.—There are special limits where all fields have the same frequency ($w_j = w$). First, there are two types of single-field configurations: (i) dipole BSs (DBS₀), which are odd parity, obtained by taking only the $m = 0$ mode, $\phi_2 \neq 0$ [39] (see also [40]). Their angular momentum density vanishes ($W = 0$) and so does their total angular momentum, $J = 0$; (ii) spinning BSs (SBS_{±1}) [11,15–17], which are even parity and have $J \neq 0$, obtained by taking only either $\phi_1 \neq 0$ (SBS₋₁) or $\phi_3 \neq 0$ (SBS₊₁).

Second, combinations of single-field configurations lead to two types of two-field configurations: (iii) spinning dipolar BSs (DBS₀ + SBS_{±1}), in which case only either $\phi_1 \neq \phi_2 \neq 0$ (SBS₋₁ + DBS₀) or $\phi_2 \neq \phi_3 \neq 0$ (DBS₀ + SBS₊₁). These are novel solutions with $J \neq 0$, carried by the even-parity scalar field; (iv) toroidal static BSs (SBS₋₁ + SBS₊₁), for which $\phi_1 = \phi_3 \equiv \phi \neq 0$. Each field $\Phi^{(1)}, \Phi^{(3)}$ carries a *local* angular momentum density, with the corresponding EMT component $T_\varphi^{t(1)} = -T_\varphi^{t(3)} = 2e^{-2F_0} w \phi^2$, such that their sum is zero, $T_\varphi^t = 0$, and the spacetime is locally and globally static, with $J = 0$.

Finally, (v) ℓ -BSs (SBS₋₁ + DBS₀ + SBS₊₁), which are static, spherical, and have $\phi_i = \phi(r) (\sin\theta/\sqrt{2}, \cos\theta, \sin\theta/\sqrt{2})$. Figure 1 illustrates the single-frequency limits of the enlarged $\ell = 1$ BSs family as 3D plots.

For each of the five types of solutions described above, there is a one-dimensional family of BSs with $w_{\min} < w < \mu$, where w_{\min} is family dependent. In an ADM mass, M vs frequency w diagram, they describe a spiral-type curve (costumary for BSs)—Fig. 2 [41]. As the frequency is decreased from the maximal value, μ , the ADM mass increases up to a maximum value $M^{(\max)}$ which

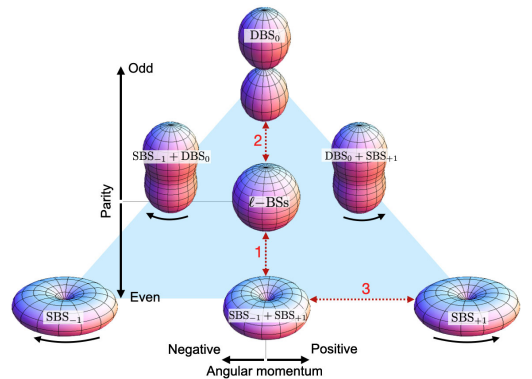


FIG. 1. $\ell = 1$ BSs family.

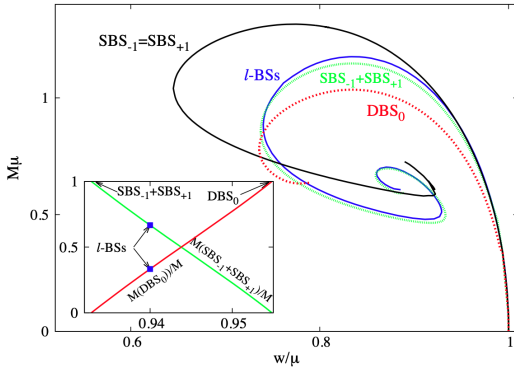


FIG. 2. ADM mass vs frequency for some of the single-frequency limits of the $\ell = 1$ BSs family. (Inset) Fraction of the total mass in $SBS_{-1} + SBS_{+1}$ and in DBS_0 along the static sequence 1 + 2 in Fig. 1 for $w_2 = 0.94\mu$ (and $w_1/\mu = w_3/\mu$ in the x axis).

is family dependent. The energy density distribution of the solutions is illustrated by the morphologies in Fig. 1.

The multifrequency, multifield interpolations.—Relaxing the equal frequency requirement a larger solution space emerges (blue triangle in Fig. 1). There are multifrequency BSs interpolating between the single-frequency ones, which are particular points in a manifold of solutions [42]. As an illustration consider the interpolation $SBS_{-1} + SBS_{+1} \leftrightarrow DBS_0$, which goes through an ℓ -BS. Fix, e.g., $w_2 = 0.94\mu$ for the ℓ -BS along the sequence—Fig. 2 (inset). On the one hand, decreasing $w_1 = w_3$ (w_2 fixed), the toroidal static BS ($SBS_{-1} + SBS_{+1}$) is approached for $w_1 = w_3 \simeq 0.933\mu$ —sequence 1 in Fig. 1. On the other hand, increasing $w_1 = w_3$ (w_2 fixed), the dipole DBS_0 is obtained for $w_1 = w_3 \simeq 0.955\mu$ —sequence 2. These are static BSs sequences; thus $W = 0$.

Similar interpolations occur between configurations with and without angular momentum, as in the transition $SBS_{-1} + SBS_{+1} \leftrightarrow SBS_{+1}$ —sequence 3 in Fig. 1. Starting from a static, toroidal BS with $w_1 = w_3 = 0.8\mu$, varying w_3 (w_1 fixed), the amplitude of $\Phi^{(1)}$ vanishes for a critical value of $w_3 \simeq 0.829\mu$, yielding the single-field SBS_{+1} . All intermediate solutions with $w_1 \neq w_3$ possess a nonvanishing angular momentum. In all sequences, a similar picture holds considering other frequencies.

The manifold of solutions of the $\ell = 1$ BSs family is as follows. Starting from an ℓ -BS with a fixed frequency $w_1 = w_2 = w_3$, the line of static ($J = 0$) BSs is obtained keeping $w_1 = w_3$ and varying the ratio $y \equiv w_1/w_2$ ($= w_3/w_2$). Then $y \in [y_{\min}, y_{\max}]$, y varies the parity of the BSs; the boundary values are the parity even and odd solutions, respectively. Then, for each fixed y one can vary $x \equiv w_3/w_1$, with $x \in [x_{\min}, x_{\max}]$, where the limits are y dependent. x varies J ; for $x > 1$ ($x < 1$), J is positive

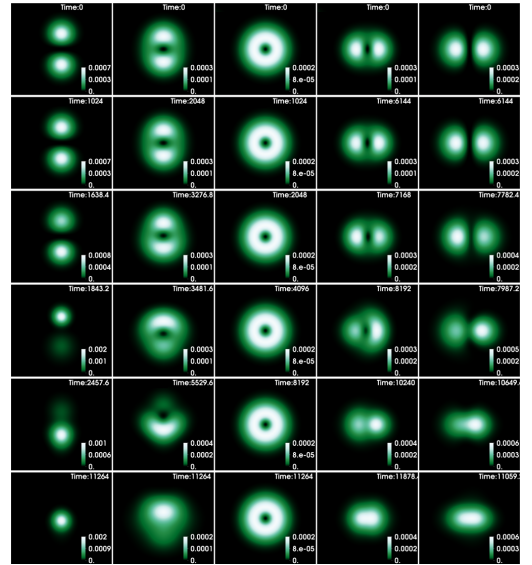


FIG. 3. Time evolutions of the energy density for five static BSs in the $\ell = 1$ family. Each column shows six sequential snapshots of the xz ($y = 0$) plane (time running from top to bottom). From left to right the values of $w_1 = w_3$ of the five models are: 0.955 (DBS_0), 0.945, 0.940 (ℓ -BS), 0.935, 0.933 ($SBS_{-1} + SBS_{+1}$).

(negative) [43]. Finally, varying the frequency of the starting ℓ -BS yields a 3D manifold of solutions. Thus, we expect a $(2\ell + 1)D$ manifold of multifrequency, multifield BSs for a model with $(2\ell + 1)$ complex scalar fields, including ℓ -BSs as symmetry-enhanced solutions.

Dynamical (in)stability.—We assess the dynamical stability of representative solutions in the $\ell = 1$ BS family by resorting to fully nonlinear dynamical evolutions of the corresponding Einstein–(multi-)Klein-Gordon system. The infrastructure used in the numerical evolutions is the same as in [19].

Figure 3 exhibits the results for a sequence of static solutions (i.e., along sequences 1 and 2 in Fig. 1, including the dipole, the ℓ -BS and the toroidal static BS). We find that all solutions (except the ℓ -BS) are dynamically unstable, decaying to a multifield BS in which all fields have $\ell = m = 0$. Including J does not improve dynamical stability. The $SBS_{\pm 1}$ are unstable against a nonaxisymmetric instability [19] and all hybrid cases we have studied (such as $SBS_{\pm 1} + DBS_0$) also decay to the fundamental $\ell = 0$ BSs.

Hybrid ℓ -BSs and a stabilization mechanism.—Instead of focusing on a single ℓ -BSs family we now allow superpositions of such families with different ℓ 's. The most elementary example is to add $\ell = 0$ BSs to the $\ell = 1$ family. Thus we add a fourth complex scalar field $\Phi^{(0)}$,

obeying (1) and (2) with $j = 0$ (hence, now $j = 0, 1, 2, 3$) and $m_j = 0$. Its boundary conditions are $\partial_r \phi_0|_{r=0} = \phi_0|_{r=\infty} = \partial_\theta \phi_0|_{\theta=0,\pi} = 0$, besides being parity even. Keeping only $\Phi^{(0)}$, the basic solution is the single-field, fundamental, monopole BS (MBS₀). We now show that adding MBS₀ can quench the instabilities observed in the $\ell = 1$ family.

To be concrete we consider the following superpositions: (A) MBS₀ + SBS₊₁ and (B) MBS₀ + DBS₀. As an illustration of (A), fixing $w_3/\mu = 0.98$, there is a continuous sequence of solutions reducing to the MBS₀ (SBS₊₁) for $w_0/\mu = 0.964$ (0.975). We refer to the intermediate configurations as “saturns.” Their dynamical evolutions—Fig. 4—exhibit a simple pattern: sufficiently close to the MBS₀ (SBS₊₁) limit, saturns are stable (unstable). Here, stability means no sign of instabilities for long evolutions ($t \simeq 24\,000$) [44]. Attempting to interpret the transition between the two regimes, we observe a correlation between instability and the r coordinate of the maximum of the

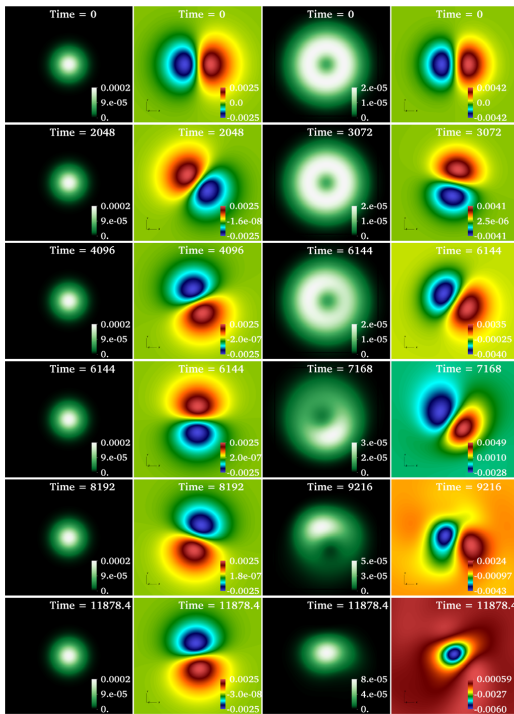


FIG. 4. Time evolution (top to bottom) of two saturns: (left and middle left) $w_1/\mu = 0.967$; (middle right and right) $w_1/\mu = 0.974$. For each case the energy density and the real part of $\Phi^{(3)}$ on the xy plane are shown. The first (second) saturn is close to MBS₀ (SBS₊₁) and is stable (unstable).

energy density—Fig. 5: when the latter is at the origin ($r = 0$) no instability is observed.

As an example of (B), fixing $w_0/\mu = 0.97$, there is a continuous sequence of solutions reducing to the MBS₀ (DBS₀) for $w_2/\mu = 0.983$ (0.973). We refer to the intermediate configurations as “pods.” Evolving this sequence of pods reveals analogous patterns: (a) sufficiently close to the MBS₀ (DBS₀) limit, pods are stable (unstable)—see Sec. I of Supplemental Material [45] for snapshots of the evolutions; (b) when the energy density maximum, which, in general, has two symmetric points located on the z axis (i.e., $\theta = 0, \pi$) is at the origin, no instability is observed—Fig. 5 (inset).

Generality and remarks.—An analogous family of vector $\ell = 1$ BSs should exist. Preliminary results show an important difference: the whole sequence 3 (see Fig. 1) is stable in the vector case, including the SBS₋₁ + SBS₊₁ static configuration, which is now spheroidal rather than toroidal (see Sec. II of Supplemental Material [45] for details). This is a consequence of the stability of vector SBS_{±1} [19]. On the other hand, we have evidence that the vector DBS₀ is unstable, as in the scalar case (see Sec. III of Supplemental Material [45]).

A byproduct of our construction is the realization that all single-frequency BSs arising in (combinations of) models of type (1) are continuously connected within a multidimensional solution manifold, interpolated by multifrequency solutions. For instance, spherical (MBS₀) and spinning (SBS_{±1}) BSs, typically described as disconnected, are connected (via saturns).

Adding the fundamental MBS₀, which is the ground state of the whole family, stabilizes different types of

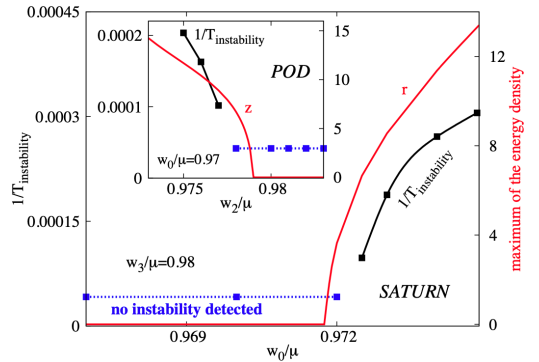


FIG. 5. Instability timescale (black dots and lines) and maximum of the total energy density (red lines) for the sequence of saturns (main panel) and pods (inset) described in the text. The blue points and line are thresholds when no instability is seen. The z coordinate in the inset is r for $\theta = 0, \pi$. $T_{\text{instability}}$ refers to the time when we observe that the solution begins to clearly deviate from axisymmetry for saturns and from equatorial symmetry for pods.

unstable BSs, such as excited monopole BSs [21], spinning BSs, and dipole BSs. Such stable configurations can actually form from the (incomplete) gravitational collapse of dilute distributions of the corresponding fields and multipoles—see Sec. III of Supplemental Material [45]. It would be interesting to probe the generality of this cooperative stabilization mechanism, and if other (higher ℓ , say) multipolar BSs can be stabilized similarly [50].

Another mechanism for mitigating instabilities is adding self-interactions [52], which was suggested to quench the instability of spinning BSs, without requiring the energy density to be maximized at the origin [53]. It would be interesting to construct the corresponding $\ell = 1$ BS family in models with self-interactions and investigate whether other members of the family can be stabilized by self-interactions.

Finally, among the possible generalizations, one could consider different masses for the fields in (1). At least for slightly different masses multifield, multifrequency solutions still exist, albeit with a modified solution space, for instance without an exactly spherically symmetric composite state. Different generalizations could be obtained by introducing a target space metric (see, e.g., [54,55]) in the multifield model.

We thank Darío Núñez, Víctor Jaramillo, Argelia Bernal, Juan Carlos Degollado, Juan Barranco, Francisco Guzmán and Luis Ureña-López, for useful discussions and valuable comments. This work was supported by the Spanish Agencia Estatal de Investigación (Grant No. PGC2018-095984-B-I00), by the Generalitat Valenciana (PROMETEO/2019/071 and GRISOLIAP/2019/029), by the Center for Research and Development in Mathematics and Applications (CIDMA) through the Portuguese Foundation for Science and Technology (FCT—Fundação para a Ciência e a Tecnologia), references UIDB/04106/2020 and UIDP/04106/2020, by national funds (OE), through FCT, I.P., in the scope of the framework contract foreseen in the numbers 4, 5, and 6 of article 23, of the Decree-Law 57/2016, changed by Law 57/2017 and by the projects PTDC/FIS-OUT/28407/2017, CERN/FIS-PAR/0027/2019 and PTDC/FIS-AST/3041/2020. This work has further been supported by the European Union's Horizon 2020 research and innovation (RISE) programme H2020-MSCA-RISE-2017 Grant No. FunFiCO-777740 and by FCT through Project No. UIDB/00099/2020. We would like to acknowledge networking support by the COST Action GWverse CA16104. Computations have been performed at the Servei d'Informàtica de la Universitat de València, the Argus and Blafis cluster at the U. Aveiro and on the "Baltasar Sete-Sois" cluster at IST.

[1] B. P. Abbott, R. Abbott, T. D. Abbott, M. R. Abernathy, F. Acernese, K. Ackley, C. Adams, T. Adams, P. Addesso,

- R. X. Adhikari *et al.* (LIGO Scientific and Virgo Collaborations), *Phys. Rev. Lett.* **116**, 061102 (2016).
 [2] B. P. Abbott *et al.* (LIGO Scientific and Virgo Collaborations), *Phys. Rev. X* **9**, 031040 (2019).
 [3] R. Abbott *et al.* (LIGO Scientific and Virgo Collaborations), arXiv:2010.14527 [Phys. Rev. X (to be published)].
 [4] K. Akiyama *et al.* (Event Horizon Telescope Collaboration), *Astrophys. J.* **875**, L1 (2019).
 [5] R. Abuter, A. Amorim, M. Bauböck, J. P. Berger, H. Bonnet, W. Brandner, Y. Clénet, V. Coudé Du Foresto, and P. T. de Zeeuw (Gravity Collaboration), *Astron. Astrophys.* **618**, L10 (2018).
 [6] J. Calderón Bustillo, N. Sanchis-Gual, A. Torres-Forné, J. A. Font, A. Vajpeyi, R. Smith, C. Herdeiro, E. Radu, and S. H. W. Leong, *Phys. Rev. Lett.* **126**, 081101 (2021).
 [7] C. A. R. Herdeiro, A. M. Pombo, E. Radu, P. V. P. Cunha, and N. Sanchis-Gual, *J. Cosmol. Astropart. Phys.* **04** (2021) 051.
 [8] V. Cardoso and P. Pani, *Living Rev. Relativity* **22**, 4 (2019).
 [9] D. J. Kaup, *Phys. Rev.* **172**, 1331 (1968).
 [10] R. Ruffini and S. Bonazzola, *Phys. Rev.* **187**, 1767 (1969).
 [11] R. Brito, V. Cardoso, C. A. R. Herdeiro, and E. Radu, *Phys. Lett. B* **752**, 291 (2016).
 [12] S. L. Liebling and C. Palenzuela, *Living Rev. Relativity* **15**, 6 (2012).
 [13] In this Letter we focus on non-self-interacting fields.
 [14] C. A. R. Herdeiro, A. M. Pombo, and E. Radu, *Phys. Lett. B* **773**, 654 (2017).
 [15] F. E. Schunck and E. W. Mielke, *Phys. Lett. A* **249**, 389 (1998).
 [16] S. Yoshida and Y. Eriguchi, *Phys. Rev. D* **56**, 762 (1997).
 [17] C. Herdeiro, I. Perapechka, E. Radu, and Y. Shnir, *Phys. Lett. B* **797**, 134845 (2019).
 [18] C. A. R. Herdeiro, J. Kunz, I. Perapechka, E. Radu, and Y. Shnir, *Phys. Lett. B* **812**, 136027 (2021).
 [19] N. Sanchis-Gual, F. Di Giovanni, M. Zilhão, C. Herdeiro, P. Cerdá-Durán, J. A. Font, and E. Radu, *Phys. Rev. Lett.* **123**, 221101 (2019).
 [20] J. Balakrishna, E. Seidel, and W.-M. Suen, *Phys. Rev. D* **58**, 104004 (1998).
 [21] A. Bernal, J. Barranco, D. Alic, and C. Palenzuela, *Phys. Rev. D* **81**, 044031 (2010).
 [22] T. Matos and L. A. Ureña-Lopez, *Gen. Relativ. Gravit.* **39**, 1279 (2007).
 [23] L. A. Ureña-Lopez and A. Bernal, *Phys. Rev. D* **82**, 123535 (2010).
 [24] F. Di Giovanni, S. Fakhry, N. Sanchis-Gual, J. C. Degollado, and J. A. Font, *Phys. Rev. D* **102**, 084063 (2020).
 [25] F. S. Guzmán and L. A. Ureña López, *Phys. Rev. D* **101**, 081302(R) (2020).
 [26] F. S. Guzmán, *Astron. Nachr.* **342**, 398 (2021).
 [27] M. Alcubierre, J. Barranco, A. Bernal, J. C. Degollado, A. Diez-Tejedor, M. Megevand, D. Nunez, and O. Sarbach, *Classical Quantum Gravity* **35**, 19LT01 (2018).
 [28] M. Alcubierre, J. Barranco, A. Bernal, J. C. Degollado, A. Diez-Tejedor, M. Megevand, D. Núñez, and O. Sarbach, *Classical Quantum Gravity* **36**, 215013 (2019).
 [29] V. Jaramillo, N. Sanchis-Gual, J. Barranco, A. Bernal, J. C. Degollado, C. Herdeiro, and D. Núñez, *Phys. Rev. D* **101**, 124020 (2020).

- [30] In spherical symmetry, multifrequency BSs were discussed in [31]; and BSs in multiscalar theories were recently constructed in [32,33].
- [31] M. Choptuik, R. Masachs, and B. Way, *Phys. Rev. Lett.* **123**, 131101 (2019).
- [32] S. S. Yazadjiev and D. D. Doneva, *Phys. Rev. D* **99**, 084011 (2019).
- [33] L. G. Collodel, D. D. Doneva, and S. S. Yazadjiev, *Phys. Rev. D* **101**, 044021 (2020).
- [34] I. Smolić, *Classical Quantum Gravity* **32**, 145010 (2015).
- [35] For the ℓ -BS, moreover, the fields depend on both the Killing and θ coordinates but the total EMT does not, albeit the individual EMT of each scalar field may still depend on the θ coordinate.
- [36] The nonvanishing Einstein equations are $E'_t, E'_r, E^\theta_\theta, E^\phi_\phi, E'_\phi$, and E^θ_r . Four of them are solved together with the three Klein-Gordon equations, yielding a coupled system of seven PDEs on the unknown functions $F_{0,1,2}, W, \phi_{1,2,3}$. The remaining two Einstein equations are treated as constraints and used to check the numerical accuracy.
- [37] Excited solutions with $n > 0$ exist as well.
- [38] C. Herdeiro and E. Radu, *Classical Quantum Gravity* **32**, 144001 (2015).
- [39] It is $\Phi_{(2,1,0)}$ in the notation of [18].
- [40] C. A. R. Herdeiro, J. Kunz, I. Perapechka, E. Radu, and Y. Shnir, *Phys. Rev. D* **103**, 065009 (2021).
- [41] The same holds for the Noether charge of the fields.
- [42] Bear in mind each of these points is in fact a continuous family, spanning a range of frequencies.
- [43] Since J is carried by even parity fields, the x range is maximal (minimal) for y_{\min} (y_{\max}). This explains the triangular shape in Fig. 1.
- [44] The typical size of the BSs here is around $r \sim 15\text{--}30$; then $t \simeq 24\,000$ means 400–800 light-crossing times.
- [45] See Supplemental Material at <http://link.aps.org/supplemental/10.1103/PhysRevLett.126.241105> further details on the numerical evolution code and the construction of constraint-satisfying initial data for the formation scenario. We also show numerical results of the stability of pod configurations and the dynamical formation of multi-field bosonic stars, including a couple of examples of vector boson stars, which includes [19,46–49].
- [46] H. Witek, M. Zilhao, G. Ficarra, and M. Elley, *Canuda: A public numerical relativity library to probe fundamental physics* (2020), <https://dx.doi.org/10.5281/zenodo.3565475>.
- [47] M. Zilhão, H. Witek, and V. Cardoso, *Classical Quantum Gravity* **32**, 234003 (2015).
- [48] E. Seidel and W.-M. Suen, *Phys. Rev. Lett.* **72**, 2516 (1994).
- [49] F. Di Giovanni, N. Sanchis-Gual, C. A. R. Herdeiro, and J. A. Font, *Phys. Rev. D* **98**, 064044 (2018).
- [50] See also [51] for another multistate construction.
- [51] Y.-B. Zeng, H.-B. Li, S.-X. Sun, S.-Y. Cui, and Y.-Q. Wang, [arXiv:2103.10717](https://arxiv.org/abs/2103.10717).
- [52] F. Di Giovanni, N. Sanchis-Gual, P. Cerdá-Durán, M. Zilhão, C. Herdeiro, J. A. Font, and E. Radu, *Phys. Rev. D* **102**, 124009 (2020).
- [53] N. Siemonsen and W. E. East, *Phys. Rev. D* **103**, 044022 (2021).
- [54] D. D. Doneva and S. S. Yazadjiev, *Phys. Rev. D* **101**, 064072 (2020).
- [55] V. I. Danchev, D. D. Doneva, and S. S. Yazadjiev, *Eur. Phys. J. C* **80**, 878 (2020).

A stabilization mechanism for excited fermion-boson stars

Fabrizio Di Giovanni,¹ Saeed Fakhry,^{2,1} Nicolas Sanchis-Gual,³ Juan Carlos Degollado,⁴ and José A. Font^{1,5}

¹*Departamento de Astronomía y Astrofísica, Universitat de València,
Dr. Moliner 50, 46100, Burjassot (València), Spain*

²*Department of Physics, Shahid Beheshti University, G. C., Evin, Tehran 19839, Iran*

³*Centro de Astrofísica e Gravitação - CENTRA, Departamento de Física,
Instituto Superior Técnico - IST, Universidade de Lisboa - UL,
Avenida Rovisco Pais 1, 1049-001, Lisbon, Portugal*

⁴*Instituto de Ciencias Físicas, Universidad Nacional Autónoma de México,
Apdo. Postal 48-3, 62251, Cuernavaca, Morelos, México*

⁵*Observatori Astronòmic, Universitat de València,
C/ Catedrático José Beltrán 2, 46980, Paterna (València), Spain*

We study numerically the nonlinear stability of *excited* fermion-boson stars in spherical symmetry. Such compound hypothetical stars, composed by fermions and bosons, are gravitationally bound, regular, and static configurations described within the coupled Einstein-Klein-Gordon-Euler theoretical framework. The excited configurations are characterized by the presence in the radial profile of the (complex, massive) scalar field – the bosonic piece – of at least one node across the star. The dynamical emergence of one such configuration from the accretion of a cloud of scalar field onto an already-formed neutron star, was numerically revealed in our previous investigation. Prompted by that finding we construct here equilibrium configurations of excited fermion-boson stars and study their stability properties using numerical-relativity simulations. In addition, we also analyze their dynamical formation from generic, constraint-satisfying initial data. Contrary to purely boson stars in the excited state, which are known to be generically unstable, our study reveals the appearance of a cooperative stabilization mechanism between the fermionic and bosonic constituents of those excited-state mixed stars. While similar examples of stabilization mechanisms have been recently discussed in the context of ℓ -boson stars and multi-field, multi-frequency boson stars, our results seem to indicate that the stabilization mechanism is a purely gravitational effect and does not depend on the type of matter of the companion star.

I. INTRODUCTION

The nature of Dark Matter (DM) is an outstanding open issue in modern cosmology. Abundant evidence in support of its existence has been collected, starting with observations of galaxy rotation curves, gravitational lensing, and the cosmic microwave background [1–8]. Since those indications arise only through gravitational effects, gravitational interactions are a promising channel to unveil the nature of DM. Although several possibilities have been proposed, it has been recognized that ultralight boson fields with masses of the order of 10^{-22} eV are a compelling candidate as the main component of DM [9–17]. Bosons can clump together to form self-gravitating equilibrium states, known as boson stars, which provides a natural alternative to standard structure formation through DM seeds (see [18–20]).

Kaup [21] and Ruffini and Bonazzola [22] pioneered the investigation of boson stars. Their studies showed that the mass of a boson star is $\sim M_{\text{Pl}}^2/\mu$ and that its characteristic size is of the order of the Compton wavelength of the boson particle, $\sim 1/\mu$, where μ is the mass of the particle and M_{Pl} is the Planck mass. Later, Colpi, Shapiro and Wasserman [23] incorporated self-interacting scalar particles and found that the corresponding boson stars have (larger) masses of $\sim \Lambda^{1/2} M_{\text{Pl}}^2/\mu$, where Λ is a parameter characterizing the strength of the self interaction. For $\Lambda^{1/2} \gg 1$, this scaling is no longer valid and the maximum mass of the star turns out to be of the

order of the Chandrasekhar mass $\sim M_{\text{Pl}}^3/\mu^2$ for fermion stars [18].

The stability of equilibrium models of ground-state, spherical boson stars subject to perturbations has been studied using both linear perturbation analysis [24, 25] and nonlinear numerical simulations [26, 27]. This body of work has showed that ground-state models – the so-called fundamental family – are stable as long as the central value of the scalar field, ϕ_c , is smaller than that of the configuration with the maximum Arnowitt-Dessner-Misner (ADM) mass. These findings support the hypothesis that boson stars may form dynamically under general initial conditions, as shown by [28]. The stability of *excited* boson stars, i.e. stars for which the scalar-field amplitude exhibits at least one radial node across the star, was investigated in [25, 26]. Equilibrium configurations were also found for excited-state models. However, those are intrinsically unstable under generic perturbations: the excited-state configurations decay to the ground-state, collapse to a black hole, or disperse away.

As already noticed in [22] there exists the possibility that bosons within a boson star are not all in the ground state, but rather populating different coexisting states forming multi-state boson stars. In Ref. [29] Bernal *et al* studied the dynamical evolution of perturbed multi-state boson stars demonstrating that stable states can form when the number of particles in the first excited state is smaller than the number of particles in the ground state. As we shall see, this type of stabilization mechanism has

in part motivated the study we present here.

In a recent work [30] we investigated the properties of macroscopic astrophysical objects that contain both bosons and fermions, known as fermion-boson stars [31, 32]. The study of the dynamics of these compound objects is important for a number of reasons, ranging from the way they interact with surrounding matter [33, 34] to their stability [35, 36]. In [30] we built spherically-symmetric equilibrium configurations of fermion-boson stars and studied their nonlinear dynamical stability, through numerical-relativity simulations, under generic radial perturbations. Moreover, we presented a dynamical scenario in which fermion-boson stars might form following the gravitational collapse of a cloud of scalar field surrounding an already-formed neutron star. The equilibrium models considered in [30] were all ground-state solutions, where the scalar field has no radial nodes across the star. However, the simulations of [30] that dealt with the dynamical formation scenario revealed the emergence of a final configuration with a node in the scalar field, similar to a static solution with an excited state. This suggests that there might be *stable* fermion-boson stars with nodes.

To investigate this issue we shall consider here spherically-symmetric equilibrium solutions of excited-state fermion-boson stars, i.e. configurations in which the radial profile of the boson part has at least one radial node across the star, analyzing their nonlinear dynamics. Both, models with and without self-interaction in the bosonic part will be considered. In addition, the formation scenario will receive extra attention here, by discussing new evolutions of neutron stars surrounded by scalar field clouds. Our investigation reveals the existence of a cooperative stabilization mechanism at work: the presence of a stable fermionic core that only interacts gravitationally with the scalar field stabilizes the excited state of the bosonic part of the compound star. We note that for purely boson stars in the excited state such mechanism is not active and those models are generically unstable [25, 26]. Similar examples of stabilization mechanisms have been recently discussed in the context of ℓ -boson stars [37] and multi-field, multi-frequency boson stars [38] (see also [39, 40]). While those studies have uncovered a cooperative stabilization mechanism by accounting for a second boson star (or a third one for ℓ -boson stars) the results reported in this paper seem to indicate that the mechanism is a purely gravitational effect and does not depend on the type of matter of the companion star but rather on its dynamical properties. This effect could be similar to the *stabilization* of flat galactic rotation curves by dark matter halos in galaxies [41].

This paper is organized as follows: In Section II we introduce the theoretical framework for mixed fermion-boson stars we will use to build the equilibrium configurations and we also introduce the corresponding evolution equations that will be used for the simulations. The actual equilibrium models are discussed in Section III which

also describes the scenario for the dynamical formation of compound stars. In Section IV a brief description of the numerical framework is given. We do not go into much detail on purpose, since the framework is identical to that employed in our previous investigation [30]. Section V presents our main results. Finally, the main conclusions of this work are reported in Section VI. Throughout the manuscript Greek indices are spacetime while Latin indices are purely spatial. For our simulations we set $G = c = \hbar = 1$, where G is Newton's gravitational constant, c is the speed of light and \hbar is the reduced Planck's constant.

II. SETUP

Our setup is the same one as in our recent work [30]. Therefore, here we avoid unnecessary repetition and we focus on the basic equations that are needed in the definitions of physical quantities that will be used throughout the paper. The interested reader is addressed to [30] for further details.

A. Matter models

We study models of fermion-boson stars in which the bosonic matter and the fermionic matter only interact through gravity. Therefore, the total stress-energy tensor describing the physical system is the sum of two contributions, one from a complex scalar field and one from a perfect fluid:

$$T_{\mu\nu} = T_{\mu\nu}^{\text{fluid}} + T_{\mu\nu}^{\phi}, \quad (1)$$

where

$$T_{\mu\nu}^{\text{fluid}} = [\rho(1 + \epsilon) + P]u_{\mu}u_{\nu} + Pg_{\mu\nu}, \quad (2)$$

$$T_{\mu\nu}^{\phi} = -\frac{1}{2}g_{\mu\nu}\partial_{\alpha}\bar{\phi}\partial^{\alpha}\phi - V(\phi) + \frac{1}{2}(\partial_{\mu}\bar{\phi}\partial_{\nu}\phi + \partial_{\mu}\phi\partial_{\nu}\bar{\phi}). \quad (3)$$

The fermionic matter is described by the fluid pressure P , its rest-mass density ρ , its internal energy ϵ and its 4-velocity u^{μ} . The scalar-field potential is defined as

$$V(\phi) = \frac{1}{2}\mu^2\bar{\phi}\phi + \frac{1}{4}\lambda(\bar{\phi}\phi)^2, \quad (4)$$

where μ and λ are the mass and the self-interaction parameter of the bosonic particle, respectively. The bar symbol denotes complex conjugation. The equations of motion are given by the conservation laws of the stress-energy tensor and of the baryonic particles for the perfect fluid, and by the Klein-Gordon equation for the complex scalar field, together with the Einstein equations for the spacetime dynamics. The system is then closed by an equation of state (EoS) for the fluid. For simplicity we

choose both a (zero-temperature) polytropic EoS and an ideal-gas EoS,

$$P = K\rho^\Gamma = (\Gamma - 1)\rho\epsilon, \quad (5)$$

where K is the polytropic constant and Γ the adiabatic index. We employ the polytropic EoS to construct the equilibrium configurations while the evolution code implements the Γ -law equation as it allows to take into account potential shock-heating effects during the simulations. All equilibrium models are built using $K = 100$ and $\Gamma = 2$.

B. Equilibrium configuration equations

In order to construct the equilibrium configurations we assume a static and spherically-symmetric metric in Schwarzschild coordinates

$$ds^2 = -\alpha(r)^2 dt^2 + \tilde{a}(r)^2 dr^2 + r^2(d\theta^2 + \sin^2\theta d\varphi^2), \quad (6)$$

written in terms of two geometrical functions $\tilde{a}(r)$ and $\alpha(r)$.

The boson star is described by a harmonic time dependence for the complex scalar field, $\phi(t, r) = \phi(r)e^{-i\omega t}$, where ω is its eigenfrequency. We employ a quartic self-interaction potential as defined in Eq. (4), where we replace the self-interaction parameter λ by the dimensionless variable

$$\Lambda = \frac{M_{\text{Pl}}^2 \lambda}{4\pi\mu^2}, \quad (7)$$

where $M_{\text{Pl}} = \sqrt{\hbar c/G}$ is the Planck mass (which is one in our units). As in [30] we use the mass of the boson particle to rescale the radial coordinate, the mass of the star, the time, and the frequency according to $r \rightarrow r\mu$, $M \rightarrow M\mu$, $t \rightarrow t\mu$, and $\omega \rightarrow \omega/\mu$. Details on this scaling and on how to recover the physical units from those used in the numerical code are provided in [30]. In the same reference the interested reader can find the set of ordinary differential equations (ODEs) that we solve to obtain the equilibrium configurations.

C. Evolution equations

The formalism of the numerical evolutions relies on a spherically-symmetric metric in isotropic coordinates

$$ds^2 = -\alpha(\hat{r})^2 dt^2 + \psi(\hat{r})^4 \gamma_{ij}(dx^i + \beta^i dt)(dx^j + \beta^j dt), \quad (8)$$

where α is the lapse function, β^i is the shift vector, and $\psi(\hat{r})$ is a conformal factor. The spatial 3-metric components are

$$\gamma_{ij} dx^i dx^j = a(\hat{r}) d\hat{r}^2 + b(\hat{r}) \hat{r}^2 (d\theta^2 + \sin^2\theta d\varphi^2). \quad (9)$$

Note that a and \tilde{a} should not be confused, as they refer to two different metrics; the hat symbol is used

to distinguish the isotropic radial coordinate from the Schwarzschild one. From now on, to simplify the notation, we will neglect the hat in the radial coordinate, keeping in mind that r will refer to the isotropic radial coordinate.

We follow Brown's covariant form [42, 43] of the Baumgarte-Shapiro-Shibata-Nakamura (BSSN) formulation of Einstein's equations [44–46] to perform our numerical evolutions. The evolved quantities are the spatial metric γ_{ij} , the BSSN conformal factor χ , the trace of the extrinsic curvature K , its traceless part $A_a = A_r^r$, $A_b = A_\theta^\theta = A_\varphi^\varphi$, and the radial component of the BSSN conformal connection functions Δ^r . The reader is addressed to Ref. [45, 46] for definitions of those quantities and to Ref. [47] for details of the full system of evolution equations we solve and on the gauge conditions..

The matter source terms appearing in the evolution equations arise from projections of the total stress-energy tensor $T_{\mu\nu}$. Those are the energy density \mathcal{E} , the momentum density j_i measured by a normal observer n^μ , and the spatial projection of the energy-momentum tensor S_{ij} , and read:

$$\mathcal{E} = n^\mu n^\nu T_{\mu\nu}, \quad (10)$$

$$j_i = -\gamma_i^\mu n^\nu T_{\mu\nu}, \quad (11)$$

$$S_{ij} = \gamma_i^\mu \gamma_j^\nu T_{\mu\nu}. \quad (12)$$

These quantities are obtained for both the fluid and the scalar field, considering $T_{\mu\nu}^{\text{fluid}}$ or $T_{\mu\nu}^\phi$, respectively. Again, explicit expressions of the matter source terms and of our first-order system of evolution and constraint equations are reported in [30].

III. INITIAL DATA

A. Equilibrium configurations

We solve the set of ODEs alluded to in Section IIB (see [30] for details) to construct suitable initial data representing equilibrium configurations of fermion-boson stars. The system of ODEs is written as an eigenvalue problem for the frequency of the scalar field ω , which depends on two parameters, the central values of the scalar field ϕ_c and of the fermionic rest-mass density ρ_c . We adopt the two-parameter shooting method to find the eigenfrequency ω_{shoot} corresponding to an excited state of the scalar field. Once ω_{shoot} is found, we use a 4th-order Runge-Kutta method to integrate the ODEs and reconstruct the entire solution. Finally we rescale both the lapse function α and ω_{shoot} to impose Schwarzschild outer boundary conditions. We require regularity at the origin to be satisfied by the metric functions, together with a vanishing scalar field at the outer boundary. Hence, the

boundary conditions read as follows:

$$\begin{aligned} \tilde{a}(0) &= 1, & \phi(0) &= \phi_c, \\ \alpha(0) &= 1, & \lim_{r \rightarrow \infty} \alpha(r) &= \lim_{r \rightarrow \infty} \frac{1}{\tilde{a}(r)}, \\ \Psi(0) &= 0, & \lim_{r \rightarrow \infty} \phi(r) &= 0, \\ \rho(0) &= \rho_c, & P(0) &= K\rho_c^\Gamma, \quad \lim_{r \rightarrow \infty} P(r) = 0. \end{aligned} \quad (13)$$

Purely boson-star models can be built solving the set of ODEs assuming $\rho_c = 0$. For such stars it is known [21, 22] that there is a countably infinite set of solutions, labelled by the number of nodes in the radial profile of the scalar field, n . Nodeless solutions, $n = 0$, are considered to be the ground-state solutions, while all other $n \neq 0$ solutions are excited states.

We next define some useful physical quantities that describe the properties of the equilibrium configurations. The total gravitational mass can be computed from the value of the metric coefficients at infinity, and reads

$$M_T = \lim_{r \rightarrow \infty} \frac{r}{2} \left(1 - \frac{1}{\tilde{a}^2} \right), \quad (14)$$

which coincides with the ADM mass at infinity. Noether's theorem predicts the existence of a conserved charge related to the invariance of the Klein-Gordon Lagrangian under global U(1) transformations of the scalar field, $\phi \rightarrow \phi e^{i\delta}$. This charge is associated with the number of bosonic particles N_B . Moreover, a definition of the number of fermionic particles N_F follows by the conservation of the baryonic number. These conserved charges can be evaluated by integrating their volume densities as follows:

$$N_B = 4\pi \int \frac{\tilde{a}\omega\phi^2 r^2}{\alpha} dr, \quad N_F = 4\pi \int \tilde{a}\rho r^2 dr. \quad (15)$$

Finally, we define the radius of the bosonic (fermionic) contribution to the fermion-boson star, R_B (R_F), as the radius of the sphere containing 99% of the corresponding particles.

In Fig. 1 we depict the mass of the $n = 1$ mixed star models, Eq. (14), as a function of the two parameters, ρ_c and ϕ_c , for three different values of Λ . As fermion stars do not depend on Λ their threshold (or critical) mass, $M_c\mu$, which is highlighted with red dots on the x -axis of all plots in Fig. 1, is constant for all values of Λ and equal to $M_c\mu = 1.637$. The black solid lines in the different panels of Fig. 1 indicate the boundary separating stable and unstable regions in the parameter space. A comparison with the corresponding existence plot of ($n = 0$) ground-state mixed-star solutions (see Fig. 1 of [30]) shows that the stability region shrinks significantly for the $n = 1$ excited-state models.

To assess the stability of excited fermion-boson stars (and to be able to draw the black lines in the figure) we rely on nonlinear numerical evolutions. While it might be interesting to carry out a linear stability analysis of

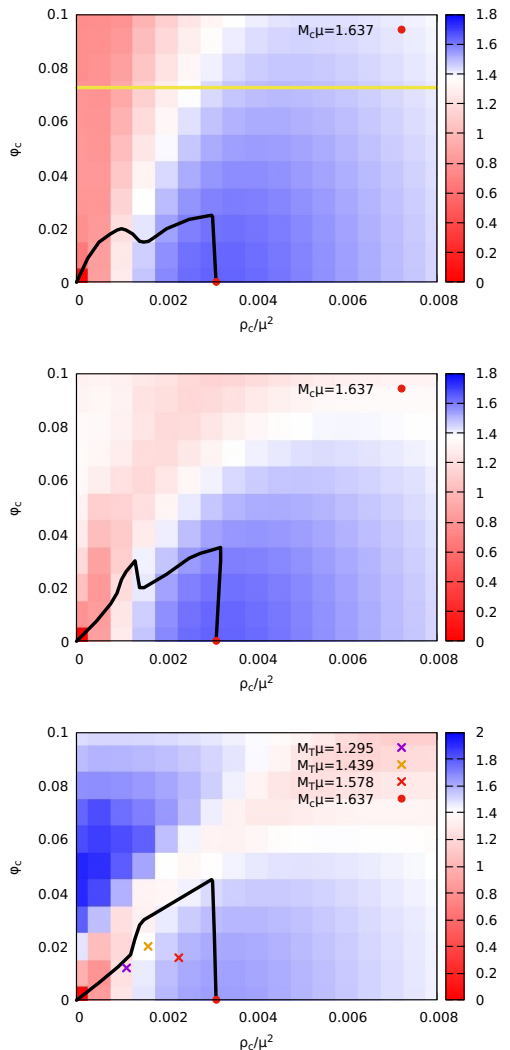


FIG. 1: Equilibrium configurations of $n = 1$ excited-state, fermion-boson stars for $\Lambda = -30$ (top), $\Lambda = 0$ (middle), and $\Lambda = 30$ (bottom). The black solid lines depict the boundary between stable models (bottom-left-corner regions of the plots) and unstable models. The yellow solid line for the case $\Lambda = -30$ indicates the maximum value of ϕ_c that ensures the non-negativity of the scalar field potential $V(\phi)$ in the entire spatial domain.

the models, it is unclear if such an analysis would provide meaningful information, telling from earlier results with excited boson stars [25, 26]. To construct the black lines in Fig. 1 we explore the region of the parameter

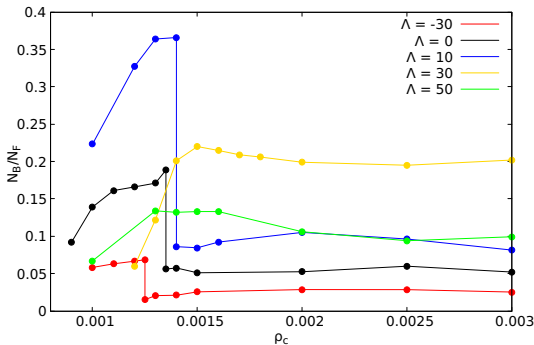


FIG. 2: Ratio between bosonic and fermionic particles, N_B/N_F , as a function of the central density of fermionic matter, ρ_c , for $\Lambda = -30, 0, 10, 30, 50$. The ratio is computed for mixed-star models at the boundary between stable and unstable regions (indicated by the filled circles).

space close to the stable branch of the neutron star models (which is the x -axis in the plots) because we expect to see stability only if the contribution of the fermionic part is large enough to stabilise an otherwise unstable excited scalar field. By performing numerical evolutions of models in this region, keeping fixed the value of ρ_c and increasing ϕ_c , it is possible to find the first unstable model. As expected, we find a region in the parameter space where excited fermion-boson stars are stable, for the three values of the self-interaction parameter Λ considered. The red crosses in the $\Lambda = 30$ plot (bottom panel in Fig. 1) are models that we could also form dynamically and which we discuss in detail below. As we pointed out in our previous work [30] considering negative values of Λ raises the issue that the scalar potential may break the weak-energy condition (see e.g. the discussion in [48]). The horizontal yellow line in the plot for $\Lambda = -30$ (top panel) indicates the maximum central value of ϕ that ensures the non-negativity of the scalar-field potential, which is $\phi_c = 0.0728$. We do not consider models above this line as their evolution might give rise to naked singularities.

In their work on multi-state boson stars [29] Bernal *et al* found that models for which the number of bosonic particles in the ground state is higher than in the first excited state are stable, and unstable otherwise. A similar relation might occur between the number of fermionic and bosonic particles in the case of compound stars. Fig. 2 depicts the ratio between the number of bosonic and fermionic particles, N_B/N_F , as a function of ρ_c for $\Lambda = -30, 0, 10, 30$, and 50 . We only consider models at the boundary between stable and unstable regions (the black solid lines in Fig. 1). We observe two different regimes. Up to a certain threshold value of the fluid central density, the value of N_B/N_F increases monotonically. When a critical value ρ_c^{crit} is reached N_B/N_F

saturates and becomes roughly constant with ρ_c . The value of ρ_c^{crit} increases with Λ . Specifically we obtain $\rho_c^{\text{crit}} = 0.00125, 0.00135, 0.0014, 0.0015, 0.0016$ for values of $\Lambda = -30, 0, 10, 30, 50$, respectively. We also observe that when the threshold value ρ_c^{crit} is reached, the ratio N_B/N_F at the boundary between stable and unstable regions sharply drops, as shown in Fig. 2. This drop disappears when the self-interaction parameter Λ is high enough, somewhere between 10 and 30, as above $\Lambda = 30$ the drop is not visible. While the analogy with the findings of [29] for multi-state boson stars is not fully apparent for our models of excited-state mixed stars, we can nevertheless point out that having $N_B/N_F < 1$ appears as a necessary condition for the stability of the models.

B. Dynamical formation

As in our previous work [30] in this paper we also study the dynamical formation of fermion-boson stars, starting from a generic Gaussian cloud of a bosonic field surrounding an already formed fermionic star. We will focus on the formation of excited stars. As mentioned before, in [30] we already found the dynamical formation of one excited ($n = 1$) fermion-boson star which, in turn, prompted the more detailed investigation we present in the current paper. Here, we will study the dependence of the dynamical formation of excited fermion-boson stars on the initial parameters of the bosonic cloud and of the initial neutron star, populating the stable region of the parameter space. We will limit our study to the $\Lambda = 30$ case as a representative choice.

Our initial data is built by solving the Hamiltonian and momentum constraints. It describes a fermionic star of central density ρ_c surrounded by a bosonic cloud with a Gaussian radial distribution of the form

$$\phi(r, t) = A_0 e^{-\frac{r^2}{2\sigma^2}} e^{-i\omega t}. \quad (16)$$

The freely specifiable parameters A_0 and σ are the amplitude and width of the Gaussian cloud, and ω is the initial frequency of the scalar field, that we set to one for all models considered. The central density ρ_c is the corresponding free parameter for the fermionic piece. We address the reader to [30] for further details on the initial-data construction.

IV. NUMERICAL FRAMEWORK

Both, to study the stability of the equilibrium models as well as their dynamical formation, we resort to numerical-relativity simulations of the Einstein-Klein-Gordon-Euler system, as in [30]. The numerical evolutions are performed with the numerical-relativity code originally developed by [47] and subsequently upgraded to take into account the complex scalar-field equations

TABLE I: Representative equilibrium (static) models of excited (one-node) fermion-boson stars. From left to right the columns report the model name, its stability properties, the value of the self-interaction parameter Λ , the central value of the fluid density ρ_c and of the scalar field ϕ_c , the field frequency obtained with the shooting method ω_{shoot} , the rescaled frequency ω , the total mass M_T , the ratio of bosons to fermions $N_B\mu/N_F$, the number of bosons N_B , the radius containing 99% of bosonic and fermionic particles, R_B and R_F , and the radius containing 95% of the total mass of the star R_T . All radii are evaluated using Schwarzschild coordinates.

Model	Branch	Λ	ρ_c/μ^2	ϕ_c	$\omega_{\text{shoot}}/\mu$	ω/μ	$M_T\mu$	$N_B\mu/N_F$	$N_B\mu^2$	$R_B\mu$	$R_F\mu$	$R_T\mu$
MS1	stable	-30	0.0011	0.017	1.2284	0.8653	1.2743	0.0541	0.0697	13.67	9.28	8.78
MS2	stable	-30	0.0014	0.020	1.2717	0.8323	1.3864	0.0490	0.0696	12.06	8.85	8.31
MS3	unstable	-30	0.0035	0.020	1.5427	0.6821	1.6151	0.0138	0.0241	7.65	7.04	6.47
MS4	stable	0	0.0015	0.019	1.2938	0.8267	1.4206	0.0466	0.0681	11.90	8.72	8.18
MS5	unstable	0	0.0010	0.024	1.2253	0.8885	1.1776	0.1772	0.1873	15.28	9.28	8.78
MS6	unstable	0	0.0035	0.035	1.2284	0.8653	1.2743	0.0541	0.0697	13.67	9.19	9.31
MS7	stable	30	0.0020	0.032	1.4068	0.8142	1.4403	0.1443	0.1959	11.18	7.97	7.62
MS8	unstable	30	0.0017	0.033	1.3731	0.8456	1.3651	0.2433	0.2859	12.61	8.11	8.19
MS9	unstable	30	0.0025	0.045	1.5365	0.8164	1.3958	0.3338	0.3745	10.90	7.24	7.33

in [49]. The code employs a second-order Partially Implicit Runge-Kutta method developed by [50, 51] to evaluate the time update of the evolved quantities. This scheme can handle potential numerical instabilities arising from singular terms appearing in the equations due to our choice of curvilinear coordinates. This computational infrastructure has been extensively tested and used by our group in previous studies of fundamental bosonic fields in strong-gravity spacetimes (see e.g. [30, 52–56]).

To build the initial data we use Schwarzschild coordinates and an equally spaced linear grid, while we use isotropic coordinates and a logarithmic grid in the evolution code. The logarithmic grid allows us to place the outer boundary sufficiently far from the origin and perform long-term stable evolutions. For the simulations reported in this work we employ a minimum radial resolution of $\Delta_r = 0.0125$ with a Courant factor $\Delta_t = 0.3\Delta_r$. The inner boundary is set at $r_{\text{min}} = \Delta_r/2$ and the outer boundary is at $r_{\text{max}} = 6000$. We employ 4th-order Kreiss-Oliger numerical dissipation terms to damp spurious high-frequency numerical noise. All advection terms (such as $\beta^r \partial_r f$) are treated with an upwind scheme. At the outer boundary we impose radiative boundary conditions. The interested reader is addressed to [30, 53] for further details. We plan to release soon a public version of the code we developed to construct the equilibrium configurations of fermion-boson stars.

V. RESULTS

To determine the stability lines in Fig. 1 we evolved numerically about $\mathcal{O}(400)$ models. We turn now to discuss the results for a few representative solutions of the sample to illustrate all possible fates that are expected in evolutions of excited fermion-boson stars. Table I reports the most relevant physical properties for nine specific models. For each value of Λ , namely -30, 0, and 30, we consider one stable model, one model that migrates to a nodeless (ground state) configuration, and one model

that collapses to form a black hole, since those are the three possible outcomes. In Fig. 3 the time evolution of different physical quantities for the three models with $\Lambda = 30$ are displayed. For the solutions that do not collapse (i.e. either stable models – left column – or models that migrate to the ground state – central column) we plot the number of bosonic and fermionic particles, N_B and N_F , and the central values of the scalar field, ϕ_c , and of the rest-mass fluid density, ρ_c . For the model that collapses to form a black hole (right column) we display the apparent-horizon mass, M_{AH} , the ADM mass of the system, and ρ_c , and ϕ_c . The expected time evolution of any of these representative models can be immediately recognized in the figure.

To better show the results of an excited star that migrates to the nodeless configuration (model MS8 in Table I, also shown in the central panels of Fig. 3) we display in Fig. 4 three radial profiles of the scalar field, $\phi(r)$, for late time snapshots, comparing them to the profile of the initial configuration (black dashed line). The evolution clearly exhibits that this model is indeed unstable and migrates to a stable ground-state fermion-boson star where no nodes are visible across the star. The final profiles neatly oscillate around a new stable configuration.

Once the stability of equilibrium configurations of excited mixed stars has been established, we turn our attention to the dynamical formation scenario. We performed simulations varying the shape of the bosonic cloud, considering different initial fermionic star models. A subset of those models, namely those for $\sigma = 70$, are reported in Table II. Our simulations show that excited mixed stars with one or even more nodes in the radial profile of ϕ can indeed form dynamically from the collapse/accretion of an initial bosonic cloud through the gravitational-cooling mechanism. By keeping fixed the cloud width σ we observe that the lower the amplitude A_0 of the initial cloud, the lower the final value of ϕ_c and the more radial nodes appear in the scalar-field profile. This means that excited states with nodes are *preferred* final configurations to ground-state mixed stars for some region of the pa-

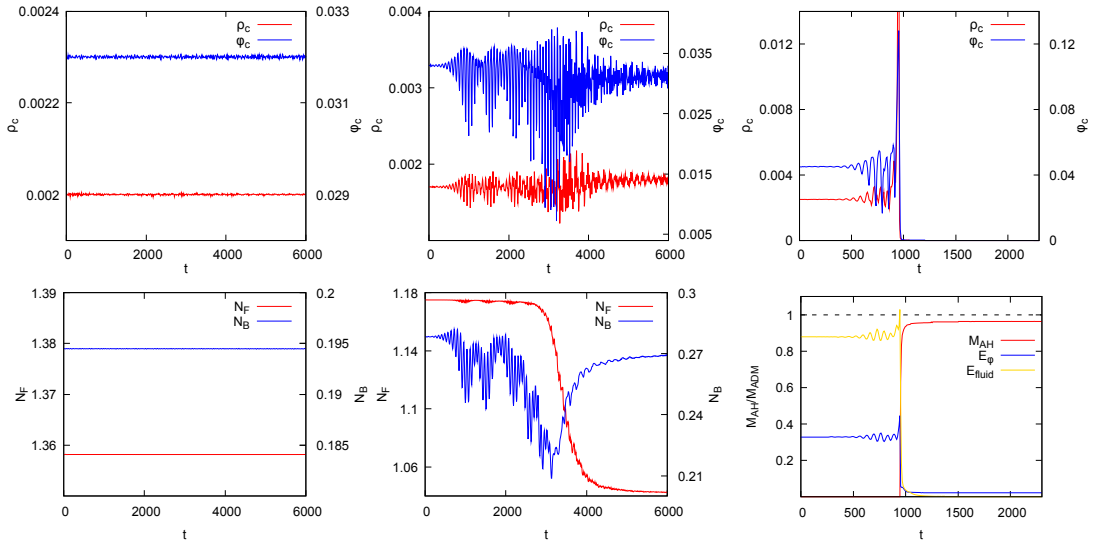


FIG. 3: Time evolution of representative equilibrium (static) $n = 1$ models with self-interaction parameter $\Lambda = 30$. *Left column*: stable model MS7. The top row (in all three columns) depicts the central value of the fluid density ρ_c and of the scalar field ϕ_c while the bottom row shows the number of bosons N_B and fermions N_F . *Middle column*: migrating (unstable) model MS8. Both rows show the same physical quantities as in the left column. *Right column*: collapsing (unstable) model MS9. The bottom row displays the AH mass in units of the ADM mass (red solid line), the volume integrated energy of the scalar field and the fluid, and the time evolution of the ADM mass normalized by its initial value (black dashed line).

TABLE II: Dynamical formation of stable excited fermion-boson stars. The two vertical lines separate the information about the initial model parameters (left), about physical quantities evaluated at the end of the formation process (center), and about physical quantities of the corresponding equilibrium configuration (right). All models correspond to $\Lambda = 30$ and $\sigma = 70$. Columns on the left box report the central rest-mass density ρ_c and the amplitude of the scalar field Gaussian profile A_0 at the initial time. Columns on the middle box indicate the number of nodes in the radial profile, n , the scalar-field frequencies, ω_n (only the one corresponding to the dominant peak in the Fourier transform is reported), the fermionic energy, E_{30}^{fluid} within a sphere of radius $r = 30$, the bosonic energy, E_{30}^ϕ , the ratio between number of bosons and fermions, N_{30}^B/N_{30}^F , and the ADM mass M_{ADM} . Columns on the right box indicate the central values of the rest-mass density and scalar field amplitude, the frequency ω , the fermionic energy E^{fluid} , the bosonic energy E^ϕ , the ratio between number of bosons and fermions, N^B/N^F , and the ADM mass M_{ADM} of the corresponding equilibrium configuration (with the same number of nodes n in the central box).

Model	ρ_c/μ^2	A_0	n	ω_n/μ	$E_{30}^{\text{fluid}}/\mu$	E_{30}^ϕ/μ	N_{30}^B/N_{30}^F	M_{ADM}	ρ_c	ϕ_c	ω/μ	E^{fluid}/μ	E^ϕ/μ	N^B/N^F	M_{ADM}
MS10	0.0008	45×10^{-5}	1	0.899	1.250	0.058	0.035	1.17	0.00090	0.012	0.894	1.244	0.062	0.048	1.182
MS11	0.0010	37×10^{-5}	1	0.870	1.415	0.050	0.035	1.28	0.00110	0.012	0.868	1.407	0.048	0.033	1.295
MS12	0.0010	25×10^{-5}	2	0.923	1.419	0.015	0.014	1.28	0.00103	0.006	0.922	1.421	0.018	0.012	1.287
MS13	0.0010	15×10^{-5}	3	0.950	1.418	0.005	0.004	1.27	0.00102	0.003	0.957	1.421	0.004	0.003	1.275
MS14	0.0020	30×10^{-5}	1	0.760	1.880	0.037	0.019	1.57	0.00227	0.016	0.760	1.863	0.036	0.018	1.576
MS15	0.0020	25×10^{-5}	3	0.897	1.883	0.020	0.007	1.57	0.00208	0.008	0.897	1.879	0.016	0.008	1.586
MS16	0.0020	20×10^{-5}	4	0.927	1.880	0.015	0.009	1.57	0.00210	0.007	0.929	1.887	0.016	0.008	1.593

parameter space.

The final object resulting from the (incomplete) gravitational collapse of a bosonic cloud is always radially perturbed. We notice that some of the objects oscillate between different states with zero, one or more nodes. The region of stability of the excited stars becomes smaller as the number of nodes in the scalar field increases, shrink-

ing towards the neutron star stability lines in Fig. 1. From these findings we hypothesize that if the final configuration resides in a region of the parameter space where several stable excited states exist, the perturbation that the object undergoes due to the gravitational cooling process can cause the migration to a different state of the scalar field.

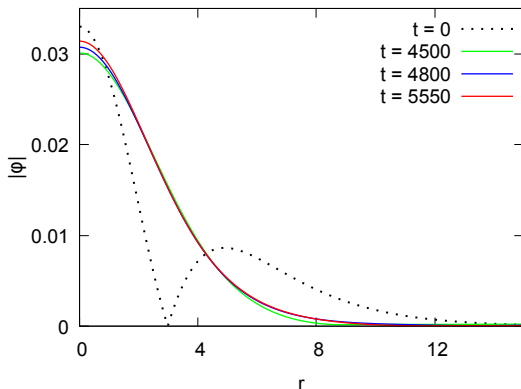


FIG. 4: Late-time snapshots of the radial profile of the module of the scalar field ϕ for model MS8, compared to the initial state (dashed black line). The model is unstable and migrates to a nodeless configuration.

Table II reports a summary of the parameters of the initial data that we have evolved and the relevant physical quantities of the final object. Those are compared to the same quantities of a static configuration with similar properties. In particular the table reports the number of nodes, n , and the oscillation frequency of the models. The latter is evaluated by means of a Fast-Fourier transform of the scalar field amplitude in the time window $t \in [4000, 6000]$. The frequency reported is the one corresponding to the dominant peak in the Fourier transform. As an illustrative example we show in Fig 5 the Fourier transform of models MS14 and MS12. In the first case we see a larger peak corresponding to the dominant frequency of the first excited state, while for the latter the peaks corresponding to the first, second and third excited states are comparable. This means that the final object resulting from the evolution of model MS12 is oscillating between these three configurations.

Fig. 6 depicts a few late-time snapshots of the radial profiles of the module of the scalar field, $|\phi(r)|$, after the formation process has been completed. We show two different initial data setups, namely MS10 and MS15. We compare the objects formed dynamically with the corresponding static solutions with similar physical properties (in terms of mass and oscillation frequency) to identify the stars. The dashed black lines in Fig 6 display the radial profiles corresponding to those static solutions. As we can see, model MS15 shows three distinctive nodes in the scalar-field radial profile as a result of its dynamical formation.

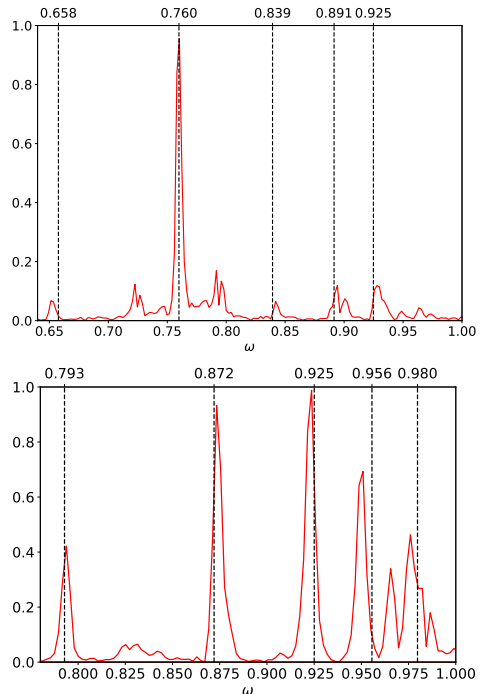


FIG. 5: Fourier transform of the time evolution of the scalar field ϕ for models MS14 (top) and MS12 (bottom). From left to right, the vertical dashed lines correspond to the values of the frequencies of the ground state and of the first four excited states of static models similar to the end result of models MS14 and MS15 (the specific values are reported at the top of each panel). An apparent peak corresponding to the $n = 1$ excited state can be seen for model MS14 while the coexistence of more than one excited state is visible for MS12. The units of the vertical axes are arbitrary.

VI. DISCUSSION

In this paper we have studied the nonlinear stability of *excited* fermion-boson stars in spherical symmetry, i.e. models for which the radial profile of the scalar field shows at least one node across the star. This investigation has extended previous results concerning the dynamical properties of fermion-boson stars (see e.g. [30, 35, 36]) by considering for the first time a complex scalar field in an excited state. We have constructed (hundreds of) equilibrium (static) configurations of excited fermion-boson stars with and without a quartic self-interaction term in the potential, studying their evolution in order to identify possible regions of stability in the parameter space. For purely spherically symmetric boson stars, excited configurations are known to be generically unstable [25, 26]. Through numerical-relativity simulations of

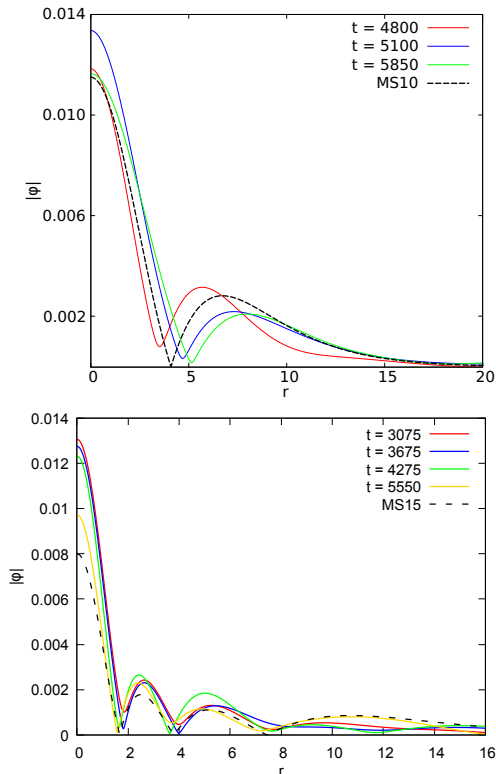


FIG. 6: Late-time snapshots of the radial profile of the module of the scalar field ϕ for models MS10 (top) and MS15 (bottom). The dashed black lines indicate the profiles of the corresponding static models with similar ρ_c and ϕ_c .

the Einstein-Klein-Gordon-Euler system we have shown that the presence of enough fermionic matter, in the form of a neutron star, can stabilise the (otherwise unstable) excited scalar field. Such a cooperative mechanism between the fermionic and bosonic constituents of a compound star allows for the existence of a stable region in the parameter space of solutions. Our results have thus confirmed that excited mixed stars with one node can indeed be stable, first reported in [30], and their existence plots have been studied in detail here. Moreover, we have also observed that fermion-boson stars with even more than one node in the radial profile of the scalar field can also be stable.

In addition to building static models of excited fermion-boson stars we have also analyzed their dynamical formation. To do so we have constructed constraint-satisfying initial data describing a neutron star, modelled by a zero-temperature polytropic EoS, surrounded by an accreting Gaussian cloud of a massive, complex scalar field. These initial data have been evolved to study the

potential formation of excited compound stars through the gravitational cooling mechanism. Our results have shown that, depending on the initial parameters of the cloud, different final states can be reached, corresponding to fermion-boson star models either in the ground-state or in an excited state. In some cases, the perturbed final object resulting from the formation oscillates between different scalar-field states with zero, one or more nodes. This outcome is possible because there exist regions in the parameter space of (ϕ_c, ρ_c) that can be populated by more than one stable configuration corresponding to states of the scalar field with different number of nodes. The final object that resides in such a region can therefore migrate from one configuration to another due to the perturbation given by the gravitational cooling mechanism, which can yield a positive or negative contribution to the energy stored in the scalar field. Such an outcome is not possible in the case of boson stars since all the excited-state solutions are unstable. Tentatively, this process might be compared to the excitation of the Hydrogen atom, occurring when the electron gains (or loses) the sufficient amount of energy to move from one shell to another.

Our findings confirm that the instability of excited boson stars can be quenched by considering the superposition of two stars, one being stable, that only interact through gravity, irrespective of the type of matter of the stable star. This cooperative stabilization mechanism has already been shown to operate against different instabilities in boson stars [29, 37–40, 57]. The presence of a second (or a third) star strengthens the stability properties of unstable compact objects that lay in their linearly stable branch. Therefore, those unstable configurations, when combined with other stars, give rise to new mixed objects that can modify the stability properties of both constituents.

Acknowledgments

We thank Eugen Radu, Carlos Herdeiro and Alexandre Pombo for useful suggestions. This work was supported by the Spanish Agencia Estatal de Investigación (grant PGC2018-095984-B-I00), by the Generalitat Valenciana (PROMETEO/2019/071 and GRISOLIAP/2019/029), by the European Unions Horizon 2020 RISE programme H2020-MSCA-RISE-2017 Grant No. FunFiCO-777740, by DGAPA-UNAM through grant No. IN105920, by CONACyT Ciencia de Frontera Projects No. 376127 “Sombras, lentes y ondas gravitatorias generadas por objetos compactos astrofísicos”, and No. 304001 “Estudio de campos escalares con aplicaciones en cosmología y astrofísica”, by the Fundação para a Ciência e a Tecnologia (FCT) projects PTDC/FIS-OUT/28407/2017 and UID/FIS/00099/2020 (CENTRA), and CERN/FIS-PAR/0027/2019. SF gratefully acknowledges support by the Erasmus+ International Credit Mobility Program KA-107 for an academic stay at the University of Valen-

cia.

-
- [1] G. Hinshaw et al. (WMAP), *Astrophys. J. Suppl.* **208**, 19 (2013), 1212.5226.
- [2] B. A. Reid et al., *Mon. Not. Roy. Astron. Soc.* **426**, 2719 (2012), 1203.6641.
- [3] W. Hu, R. Barkana, and A. Gruzinov, *Phys. Rev. Lett.* **85**, 1158 (2000), astro-ph/0003365.
- [4] R. R. Caldwell and M. Kamionkowski, *Ann. Rev. Nucl. Part. Sci.* **59**, 397 (2009), 0903.0866.
- [5] C. Blake et al., *Mon. Not. Roy. Astron. Soc.* **418**, 1707 (2011), 1108.2635.
- [6] R. Hlozek, D. Grin, D. J. E. Marsh, and P. G. Ferreira, *Phys. Rev. D* **91**, 103512 (2015), 1410.2896.
- [7] J. Chluba et al. (2019), 1909.01593.
- [8] K. Abazajian et al. (2019), 1907.04473.
- [9] A. R. Liddle and M. S. Madsen, *Int. J. Mod. Phys. D* **11**, 101 (1992).
- [10] W. Hu, *Astrophys. J.* **506**, 485 (1998), astro-ph/9801234.
- [11] T. Matos, F. S. Guzman, and L. A. Urena-Lopez, *Class. Quant. Grav.* **17**, 1707 (2000), astro-ph/9908152.
- [12] T. Matos and L. A. Urena-Lopez, *Class. Quant. Grav.* **17**, L75 (2000), astro-ph/0004332.
- [13] L. Amendola and R. Barbieri, *Phys. Lett. B* **642**, 192 (2006), hep-ph/0509257.
- [14] A. Arvanitaki, S. Dimopoulos, S. Dubovsky, N. Kaloper, and J. March-Russell, *Phys. Rev. D* **81**, 123530 (2010), 0905.4720.
- [15] A. P. Lundgren, M. Bondarescu, R. Bondarescu, and J. Balakrishna, *Astrophys. J.* **715**, L35 (2010), 1001.0051.
- [16] D. J. E. Marsh and P. G. Ferreira, *Phys. Rev. D* **82**, 103528 (2010), 1009.3501.
- [17] L. Hui, J. P. Ostriker, S. Tremaine, and E. Witten, *Phys. Rev. D* **95**, 043541 (2017), 1610.08297.
- [18] P. Jetzer, *Phys. Rept.* **220**, 163 (1992).
- [19] F. E. Schunck and E. W. Mielke, *Class. Quant. Grav.* **20**, R301 (2003), 0801.0307.
- [20] S. L. Liebling and C. Palenzuela, *Living Rev. Rel.* **15**, 6 (2012), 1202.5809.
- [21] D. J. Kaup, *Phys. Rev.* **172**, 1331 (1968).
- [22] R. Ruffini and S. Bonazzola, *Phys. Rev.* **187**, 1767 (1969).
- [23] M. Colpi, S. L. Shapiro, and I. Wasserman, *Phys. Rev. Lett.* **57**, 2485 (1986).
- [24] M. Gleiser, *Phys. Rev. D* **38**, 2376 (1988), [Erratum: *Phys. Rev. D* **39**, no.4, 1257 (1989)].
- [25] T. D. Lee and Y. Pang, *Nucl. Phys.* **B315**, 477 (1989), [129(1988)].
- [26] J. Balakrishna, E. Seidel, and W.-M. Suen, *Phys. Rev. D* **58**, 104004 (1998), gr-qc/9712064.
- [27] E. Seidel and W.-M. Suen, *Phys. Rev. D* **42**, 384 (1990).
- [28] E. Seidel and W.-M. Suen, *Physical review letters* **72**, 2516 (1994).
- [29] A. Bernal, J. Barranco, D. Alic, and C. Palenzuela, *Phys. Rev. D* **81**, 044031 (2010), 0908.2435.
- [30] F. Di Giovanni, S. Fakhry, N. Sanchis-Gual, J. C. Degollado, and J. A. Font, *Phys. Rev. D* **102**, 084063 (2020), URL <https://link.aps.org/doi/10.1103/PhysRevD.102.084063>.
- [31] A. Henriques, A. R. Liddle, and R. Moorhouse, *Physics Letters B* **251**, 511 (1990), ISSN 0370-2693, URL <http://www.sciencedirect.com/science/article/pii/0370269390907899>.
- [32] L. M. Lopes and A. B. Henriques, *Physics Letters B* **285**, 80 (1992), ISSN 0370-2693, URL <https://www.sciencedirect.com/science/article/pii/037026939291303Q>.
- [33] R. Brito, V. Cardoso, and H. Okawa, *Physical review letters* **115**, 111301 (2015).
- [34] R. Brito, V. Cardoso, C. F. B. Macedo, H. Okawa, and C. Palenzuela, *Phys. Rev. D* **93**, 044045 (2016), URL <https://link.aps.org/doi/10.1103/PhysRevD.93.044045>.
- [35] S. Valdez-Alvarado, C. Palenzuela, D. Alic, and L. A. Ureña-López, *Phys. Rev. D* **87**, 084040 (2013), URL <https://link.aps.org/doi/10.1103/PhysRevD.87.084040>.
- [36] S. Valdez-Alvarado, R. Becerril, and L. A. Ureña López, *Phys. Rev. D* **102**, 064038 (2020), URL <https://link.aps.org/doi/10.1103/PhysRevD.102.064038>.
- [37] M. Alcubierre, J. Barranco, A. Bernal, J. C. Degollado, A. Diez-Tejedor, M. Megevand, D. Nunez, and O. Sarbach, *Class. Quant. Grav.* **35**, 19LT01 (2018), 1805.11488.
- [38] N. Sanchis-Gual, F. Di Giovanni, C. Herdeiro, E. Radu, and J. A. Font, arXiv preprint arXiv:2103.12136 (2021).
- [39] F. S. Guzmán and L. A. Ureña López, *Phys. Rev. D* **101**, 081302 (2020), 1912.10585.
- [40] F. S. Guzmán, *Astronomische Nachrichten* (2021).
- [41] V. C. Rubin, W. K. Ford Jr, and N. Thonnard, *The Astrophysical Journal* **225**, L107 (1978).
- [42] J. D. Brown, *Phys. Rev. D* **79**, 104029 (2009), URL <http://link.aps.org/doi/10.1103/PhysRevD.79.104029>.
- [43] M. Alcubierre and M. D. Mendez, *Gen.Rel.Grav.* **43**, 2769 (2011), 1010.4013.
- [44] T. Nakamura, K. Oohara, and Y. Kojima, *Progress of Theoretical Physics Supplement* **90**, 1 (1987).
- [45] M. Shibata and T. Nakamura, *Phys. Rev. D* **52**, 5428 (1995).
- [46] T. W. Baumgarte and S. L. Shapiro, *Phys. Rev. D* **59**, 024007 (1998).
- [47] P. J. Montero and I. Cordero-Carrion, *Phys. Rev. D* **85**, 124037 (2012), 1204.5377.
- [48] C. Barceló and M. Visser, *Classical and Quantum Gravity* **17**, 3843 (2000), URL <https://doi.org/10.1088/2F0264-9381%2F17%2F18%2F318>.
- [49] A. Escorihuela-Tomás, N. Sanchis-Gual, J. C. Degollado, and J. A. Font, *Phys. Rev. D* **96**, 024015 (2017), URL <https://link.aps.org/doi/10.1103/PhysRevD.96.024015>.
- [50] I. Cordero-Carrión and P. Cerdá-Durán, ArXiv e-prints (2012), 1211.5930.
- [51] I. Cordero-Carrión and P. Cerdá-Durán, *Advances in Differential Equations and Applications*, SEMA SIMAI Springer Series Vol. 4 (Springer Interna-

- tional Publishing Switzerland, Switzerland, 2014).
- [52] N. Sanchis-Gual, J. C. Degollado, P. J. Montero, and J. A. Font, *Phys. Rev. D* **91**, 043005 (2015), 1412.8304.
 - [53] N. Sanchis-Gual, J. C. Degollado, P. J. Montero, J. A. Font, and V. Mewes, *Phys. Rev. D* **92**, 083001 (2015), 1507.08437.
 - [54] N. Sanchis-Gual, J. C. Degollado, P. J. Montero, J. A. Font, and C. Herdeiro, *Phys. Rev. Lett.* **116**, 141101 (2016), 1512.05358.
 - [55] N. Sanchis-Gual, C. Herdeiro, E. Radu, J. C. Degollado, and J. A. Font, *Phys. Rev. D* **95**, 104028 (2017).
 - [56] F. Di Giovanni, N. Sanchis-Gual, C. A. R. Herdeiro, and J. A. Font, *Phys. Rev.* **D98**, 064044 (2018), 1803.04802.
 - [57] V. Jaramillo, N. Sanchis-Gual, J. Barranco, A. Bernal, J. C. Degollado, C. Herdeiro, and D. Nez (2020), 2004.08459.

Can fermion-boson stars reconcile multimessenger observations of compact stars?

Fabrizio Di Giovanni[⊗],¹ Nicolas Sanchis-Gual[⊗],^{1,2} Pablo Cerdá-Durán[⊗],¹ and José A. Font[⊗]^{1,3}

¹*Departamento de Astronomía y Astrofísica, Universitat de València, Carrer del Doctor Moliner 50, 46100 Burjassot (València), Spain*

²*Departamento de Matemática da Universidade de Aveiro and Centre for Research and Development in Mathematics and Applications (CIDMA),*

Campus de Santiago, 3810-183 Aveiro, Portugal

³*Observatori Astronòmic, Universitat de València,*

Catedrático José Beltrán 2, 46980 Paterna (València), Spain



(Received 27 October 2021; accepted 10 February 2022; published 7 March 2022)

Mixed fermion-boson stars are stable, horizonless, everywhere-regular solutions of the coupled Einstein-(complex, massive) Klein-Gordon-Euler system. While isolated neutron stars and boson stars are uniquely determined by their central energy density, mixed configurations conform to an extended parameter space that depends on the combination of the number of fermions and (ultralight) bosons. The wider possibilities offered by fermion-boson stars could help to explain the tension in the measurements of neutron star masses and radii reported in recent multimessenger observations and nuclear physics experiments. In this work, we construct equilibrium configurations of mixed fermion-boson stars with realistic equations of state for the fermionic component and different percentages of bosonic matter. We show that our solutions are in excellent agreement with multimessenger data, including gravitational-wave events GW170817 and GW190814 and x-ray pulsars PSR J0030 + 0451 and PSR J0740 + 6620, as well as with nuclear physics constraints from the PREX-2 experiment.

DOI: [10.1103/PhysRevD.105.063005](https://doi.org/10.1103/PhysRevD.105.063005)

I. INTRODUCTION

The determination of the equation of state (EOS) of matter at the supernuclear densities attained in neutron star interiors is a long-standing issue in nuclear astrophysics (see Refs. [1,2] and references therein). High-precision measurements of the masses and radii of neutron stars are necessary to confidently constrain the EOS. Recent observations in both the electromagnetic channel and the gravitational-wave channel, together with constraints from nuclear physics, are helping to shed light on this issue, yet uncertainties remain [3–13].

During the last decade, it has been possible to accurately measure the mass of two millisecond pulsars with masses close to $2 M_{\odot}$, PSR J1614 – 2230 [14,15] and PSR J0348 + 0432 [16]. These results impose a strong lower limit to the maximum mass of neutron stars and have constrained considerably the properties of dense matter [2]. However, only recently has it been possible to make an accurate joint determination of the mass *and* the radius of a neutron star. Bayesian inference on the pulse-profile modeling of observations from the Neutron Star Interior Composition Explorer (NICER) of the rotation-powered, x-ray millisecond pulsar PSR J0030 + 0451 has yielded values for its mass and (circumferential) radius of $\sim 1.4 M_{\odot}$ and ~ 13 km, respectively [5,6]. Even more recently, the

same teams of researchers have reported the joint determination of the mass and radius of PSR J0740 + 6620 [10,11], the most massive known neutron star. Combining data from NICER and XMM-Newton [11], and also accounting for radio timing (Shapiro delay) in the case of Ref. [10] (see also Ref. [15]), these teams have inferred values for its mass and radius of $2.08 M_{\odot}$ and ~ 13 km, respectively. The fact that J0740 + 6620 is about 50% more massive than J0030 + 0451 while both objects are essentially the same size challenges theoretical models of neutron star interiors.

Gravitational waves have also been able to put joint constraints on the neutron star mass and radius. The first-ever detection of a binary neutron star merger by the LIGO-Virgo Collaboration (LVC), GW170817 [17], made it possible to place constraints not only on the individual masses of the components of the binary, but also on the tidal deformability of neutron stars, which has been used to constrain the neutron star radius [3] (see also Refs. [9,18] and references therein).

In addition, the interpretation of the recent LVC detection of the compact binary merger event GW190814 [19] poses some difficulties. While the mass of the primary component, $23.2 M_{\odot}$, allows us to conclusively identify it as a black hole, the mass of the secondary, $2.50\text{--}2.67 M_{\odot}$,

raises doubts on the nature of this component, which might be either a black hole or a neutron star. If the latter is the case, it would be the most massive neutron star ever observed. A number of recent investigations have tried to explain such a large mass [20–33]. Proposals include the possibility that the secondary is a rapidly rotating neutron star that collapsed to a spinning black hole before merger [20,21], a neutron star with a stiff high-density EOS or a sufficiently large spin [24] (see also Ref. [25]), or a neutron star with exotic degrees of freedom—i.e., a strange-quark star, within the scenario in which neutron stars and quark stars coexist [26] (see also Ref. [27]). Somewhat more exotic possibilities involving slowly rotating neutron stars in 4D Einstein-Gauss-Bonnet gravity [31], primordial black holes [29], Thorne-Zytkow objects [30], or dark-matter-admixed neutron stars [32,33], have also been suggested.

The neutron star radius can also be constrained by improving the measurement of nuclear interaction parameters [1,34]. Very recently, the PREX-2 experiment has measured with high accuracy the neutron skin thickness of ^{208}Pb [35] which constrains the neutron star radius for a $1.4 M_{\odot}$ neutron star to be larger than 13.25 km [36]. Although compatible with millisecond pulsar radius measurements, this result is in some tension with the gravitational-wave determinations [37]. The combined constraints of the multimessenger data and PREX-2 measurements have been shown by Refs. [38,39] to be compatible with models of hybrid stars with first-order phase transition from nucleonic to quark matter in the core, a result disfavored by the analysis of Ref. [40].

Additionally, the nuclear physics modeling of realistic EOSs at high densities has led to the so-called hyperon problem (see, e.g., Ref. [41] and references therein). In order to reach the high masses necessary to fulfill the observational constraints on the maximum mass of neutron stars, models have to reach high central densities, at which the appearance of hyperons is expected. However, the presence of hyperons may soften the EOS at those densities and limit the possible values for the maximum mass, making it difficult to reach the $\sim 2 M_{\odot}$ constraint.

Motivated by these observational and experimental results, we put forward in this paper a theoretically motivated new model based on mixed fermion-boson stars—i.e., neutron stars that incorporate some amount of bosonic matter. Using this model, we are able to construct existence plots (mass-radius equilibrium configurations) compatible with multimessenger observational data, including gravitational-wave events GW170817 and GW190814, and x-ray pulsars PSR J0030 + 0451 and PSR J0740 + 6620. We note that our model shares some similarities with those of Refs. [32,33], but also some differences. The study of Ref. [32] is only focused on GW190814 and explains the mass of the secondary by admixing neutron stars modeled by stiff EOSs with non-annihilating weakly interacting massive particles of dark

matter. On the other hand, the very recent study of Ref. [33] also focuses only on GW190814 and explains the mass of the secondary by resorting to a neutron star admixed with at least $2.0 M_{\odot}$ of dark matter made of axion-like particles. In our study (see below), we employ a complex scalar field, while in Ref. [33] the authors consider a real field to model QCD axions.

Ultralight bosons form localized, coherently oscillating configurations akin to Bose-Einstein condensates [42,43]. For light-enough bosonic particles—i.e., with a mass $\mu \sim 10^{-22}$ eV, these condensates have been proposed to explain large-scale structure formation through dark matter seeds [44,45]. Heavier bosons lead to much smaller configurations with the typical size and mass of neutron stars—hence the name boson stars [46,47] (see Refs. [48,49] and references therein). It is worth mentioning that recent examples have shown the intrinsic degeneracy between the prevailing Kerr black hole solutions of general relativity and boson-star solutions, using both gravitational-wave data [50] and electromagnetic data [51] (see also Ref. [52]). Moreover, macroscopic composites of fermions and bosons, dubbed fermion-boson stars, have also been proposed [53–59]. Such mixed configurations could form from the condensation of some primordial gas containing both types of particles, or through episodes of accretion. The dynamical formation of fermion-boson stars through accretion along with their nonlinear stability properties has recently been studied by Refs. [55,58,60,61]. In most studies, the neutron star is modeled with a polytropic EOS, the only exception being Ref. [62], which employed a realistic EOS. Mergers of fermion-boson stars have also been studied by Ref. [63]. In this work, we perform a systematic analysis of the physical properties of fermion-boson stars built using different state-of-the-art, tabulated EOSs for the fermionic part. Moreover, we evaluate the prospects for these models to fit the multimessenger constraints set by XMM-Newton, NICER, and the LVC detections. Similar studies using models of neutron stars with admixed fermionic dark matter are reported in Refs. [64–66].

This paper is organized as follows: Section II briefly describes the theoretical framework to build equilibrium models of fermion-boson stars. (Further details are reported in Ref. [60].) Section III contains our main results. Finally, in Sec. IV, we discuss our findings and outline possible extensions of this work.

II. FRAMEWORK

In our setup, the scalar field is assumed to be only minimally coupled to Einstein's gravity. Therefore, fermions and bosons only interact gravitationally, with the total stress-energy tensor being the sum of both contributions, $T_{\mu\nu} = T_{\mu\nu}^{\text{NS}} + T_{\mu\nu}^{\phi}$, where (using units with $c = G = \hbar = 1$)

$$T_{\mu\nu}^{\text{NS}} = [\rho(1 + \epsilon) + P]u_\mu u_\nu + P g_{\mu\nu}, \quad (1)$$

$$T_{\mu\nu}^\phi = -\frac{1}{2}g_{\mu\alpha}\partial_\alpha\bar{\phi}\partial^\alpha\phi - \left(\frac{1}{2}\mu^2\bar{\phi}\phi - \frac{1}{4}\lambda(\bar{\phi}\phi)^2\right)g_{\mu\nu} + \frac{1}{2}(\partial_\mu\bar{\phi}\partial_\nu\phi + \partial_\mu\phi\partial_\nu\bar{\phi}). \quad (2)$$

The fermionic part involves the fluid pressure P , rest-mass density ρ , internal energy ϵ , and four-velocity u^μ , with $g_{\mu\nu}$ denoting the space-time metric. The bosonic matter is described by the complex scalar field ϕ (with $\bar{\phi}$ being the complex conjugate) and by the particle mass μ and self-interaction parameter λ .

The equations of motion are obtained from the conservation laws of the stress-energy tensor and of the baryonic particles for the fermionic part,

$$\nabla_\mu T_{\text{NS}}^{\mu\nu} = 0, \quad (3)$$

$$\nabla_\mu(\rho u^\mu) = 0, \quad (4)$$

and from the Klein-Gordon equation for the complex scalar field,

$$\nabla_\mu\nabla^\mu\phi = \mu^2\phi + \lambda|\phi|^2\phi, \quad (5)$$

together with the Einstein equations, $G_{\mu\nu} = 8\pi T_{\mu\nu}$, for the spacetime dynamics. Mixed-star models are built using a static and spherically symmetric metric in Schwarzschild coordinates,

$$ds^2 = -\alpha(r)^2 dt^2 + a(r)^2 dr^2 + r^2(d\theta^2 + \sin^2\theta d\varphi^2), \quad (6)$$

written in terms of two geometrical functions, $a(r)$ and $\alpha(r)$. A harmonic time dependence ansatz for the scalar field is assumed, $\phi(r, t) = \phi(r)e^{i\omega t}$, where ω is its eigenfrequency. Furthermore, we consider a static perfect fluid $u^\mu = (-1/\alpha, 0, 0, 0)$. In order to construct equilibrium configurations, we solve the following set of ordinary differential equations (ODEs), which are obtained from Einstein's equations:

$$\frac{da}{dr} = \frac{\alpha}{2} \left(\frac{1 - a^2}{r} + 4\pi r \left[\left(\frac{\omega^2}{\alpha^2} + \mu^2 + \frac{\lambda}{2}\phi^2 \right) a^2 \phi^2 + \Psi^2 + 2a^2\rho(1 + \epsilon) \right] \right), \quad (7)$$

$$\frac{d\alpha}{dr} = \frac{\alpha}{2} \left(\frac{a^2 - 1}{r} + 4\pi r \left[\left(\frac{\omega^2}{\alpha^2} - \mu^2 - \frac{\lambda}{2}\phi^2 \right) a^2 \phi^2 + \Psi^2 + 2a^2 P \right] \right), \quad (8)$$

$$\frac{d\phi}{dr} = \Psi, \quad (9)$$

$$\frac{d\Psi}{dr} = - \left(1 + a^2 - 4\pi r^2 a^2 (\mu^2 \phi^2 + \frac{\lambda}{2} \phi^4 + \rho(1 + \epsilon) - P) \right) \frac{\Psi}{r} - \left(\frac{\omega^2}{\alpha^2} - \mu^2 - \lambda \phi^2 \right) a^2 \phi^2, \quad (10)$$

$$\frac{dP}{dr} = -[\rho(1 + \epsilon) + P] \frac{\alpha'}{\alpha}, \quad (11)$$

where the prime indicates the derivative with respect to r . The system of equations is closed by the EOS for the nucleonic matter. Previous works on fermion-boson stars [55–61] assumed a simple polytropic EOS to build equilibrium models and a Γ -law EOS for numerical evolutions to take into account possible shock-heating (thermal) effects. In this work, we improve the microphysical treatment of the fermionic part of the models and construct new equilibrium solutions described with realistic, tabulated EOSs (see Sec. III). Despite our models being spherically symmetric, we can nevertheless apply them to the x-ray millisecond pulsars J0030 + 0451 and J0740 + 6620, since the degree of deformation rotation might induce in these objects is negligible [5,6].

The set of ODEs [Eqs. (7)–(11)] is an eigenvalue problem for the frequency of the scalar field ω , which depends on two parameters: namely, the central value of the rest-mass density, ρ_c , and that of the scalar field, ϕ_c . As in Ref. [60], to obtain the value of the frequency for each solution, we employ a two-parameter shooting method to search for the physical solution that fulfills the requirement of vanishing ϕ at the outer boundary. Once ω is obtained, we use a fourth-order Runge-Kutta integrator to solve the ODEs and reconstruct the radial profiles of all variables.

In order to construct physical initial data, we must impose appropriate boundary conditions for the geometric quantities, and for both the scalar field and the perfect fluid. We require that the metric functions be regular at the origin. We employ Schwarzschild outer boundary conditions, together with a vanishing scalar field. Explicitly, the boundary conditions read

$$\begin{aligned} a(0) &= 1, & \phi(0) &= \phi_c, \\ \alpha(0) &= 1, & \lim_{r \rightarrow \infty} \alpha(r) &= \lim_{r \rightarrow \infty} \frac{1}{a(r)}, \\ \Psi(0) &= 0, & \lim_{r \rightarrow \infty} \phi(r) &= 0, \\ \rho(0) &= \rho_c, & P(0) &= K\rho_c^\Gamma. \end{aligned} \quad (12)$$

The total gravitational mass of the solutions can be defined as

$$M_{\text{T}} = \lim_{r \rightarrow \infty} \frac{r}{2} \left(1 - \frac{1}{a^2} \right), \quad (13)$$

which coincides with the Arnowitt-Dessner-Misner (ADM) mass at infinity. We define the radius of the fermionic part

as the radial coordinate at which the fluid pressure vanishes, $R_f = r(P=0)$, which for the Schwarzschild metric coincides with the circumferential radius. As the bosonic component of our mixed stars does not have a hard surface, the radius of this contribution, R_b , is evaluated, as is customary, as the radius of the sphere containing 99% of bosonic particles. The particle numbers for both bosons and fermions are computed as in Ref. [60].

III. RESULTS

Figure 1 displays the mass-radius relations for a large sample of realistic EOSs (gray curves) corresponding to all cold EOSs described in Refs. [67,68]. Those take into account generic nuclear effects, while some of them also include hyperons, pion and kaon condensates, and quarks. We compare those results with the observational constraints placed by NICER on PSRJ0030 + 0451 [5,6]; the NICER/XMM-Newton combined analysis of PSRJ0740 + 6620 [10,11]; the constraints set by the gravitational-wave event GW170817 [3] (EOS-insensitive relations); the mass measurement of two neutron stars with masses close to $2 M_\odot$, PSR J0348 + 0432 [16] and PSR J1614-2230 [69]; and the lower mass component in the binary merger GW190814 [19] as a possible neutron star with mass $\geq 2.5 M_\odot$. All constraints are given as 95% (2σ) confidence intervals. Those have been computed using the publicly available posteriors provided by the different groups. Additionally, Fig. 1 also shows the 1σ lower limit for the radius of a $1.4 M_\odot$ derived from the PREX-2 measurements of the neutron skin thickness [36] (see, however, the related discussion in Refs. [37,70]).

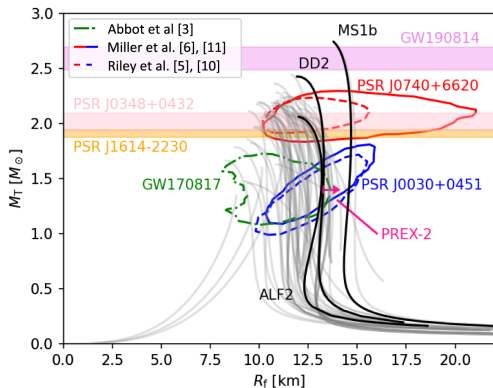


FIG. 1. Gravitational mass vs circumferential fermionic radius for different realistic EOSs including the observational constraints (95% confidence levels) from LIGO-Virgo, NICER/XMM-Newton, and mass measurements of two high-mass pulsars. We also indicate the PREX-2 1σ lower limit on the radius for a $1.4 M_\odot$ neutron star. Gray curves correspond to all cold EOSs compiled by Refs. [67,68]. We highlight in black the three EOSs used for the calculations in this work.

For our analysis, we select the three EOSs highlighted in black in Fig. 1: namely ALF2, which is a hybrid EOS with mixed APR nuclear matter and color-flavor-locked quark matter [71]; MS1b, which is a relativistic mean field theory EOS [71]; and DD2 [72], which is a finite-temperature hadronic EOS which we evaluate at zero temperature and beta equilibrium. The three EOSs fulfill the constraints from the recent NICER and XMM-Newton results, and the observations of the two high-mass pulsars, as well as the PREX-2 constraints. Of the three, only MS1b would be compatible with the low-mass component of GW190814 being a neutron star. On the other hand, only ALF2 and DD2 are compatible with the results of GW170817, albeit only marginally. This selection of EOSs illustrates the current tension that exists between different observational and experimental constraints of the mass and radius of neutron stars. Although it is still possible to find EOSs that fit all constraints within the 2σ confidence level (except for GW190814), if these constraints were to tighten in future observations maintaining similar median values, it would pose a serious problem to the modeling of matter at high densities. We explore next the possibility of alleviating some of this tension by considering stars with a bosonic component additional to the fermionic component.

With this aim, we build sequences of equilibrium configurations both of fermion stars described by those three EOSs, and of mixed stars with different values of the ratio of the number of bosons to fermions, N_b/N_f , and the particle mass, μ . Models are computed for $N_b/N_f = \{0.1, 0.2, 0.3\}$ and $\mu = \{0.1, 1.0\}$ in our units, which correspond to $\mu = \{1.34 \times 10^{-11}, 1.34 \times 10^{-10}\}$ eV. These choices of μ are motivated by the following considerations: On the one hand, lower values of μ yield more diluted boson stars for the same boson star mass range, leading to milder and more global effects on the neutron star; on the other hand, higher values of μ decrease the maximum mass of boson stars and the number of particles, hence making those models less relevant in the context of this work (e.g., for $\mu = 10.0$, the maximum mass of a boson star is $0.0633 M_\odot$). Constraints for real bosonic fields on the mass of ultralight bosonic particles have been set by spin measurements of astrophysical black holes and direct searches of continuous gravitational waves emitted by boson clouds around spinning black holes [73–75]. An exclusion range of boson masses has been established between $\sim 10^{-13}$ eV and 10^{-11} eV. However, we note that our model is not bounded by these constraints, as we are considering a complex scalar field, and it is not yet clear how the results for a real field would apply to the complex case. Nevertheless, the particle mass range we consider is outside the observational bounds. For all models, the self-interaction parameter λ is set to zero (miniboson stars), and the fermionic matter always dominates over the bosonic matter, the latter being a small fraction of the total mass. The results are depicted in Fig. 2.

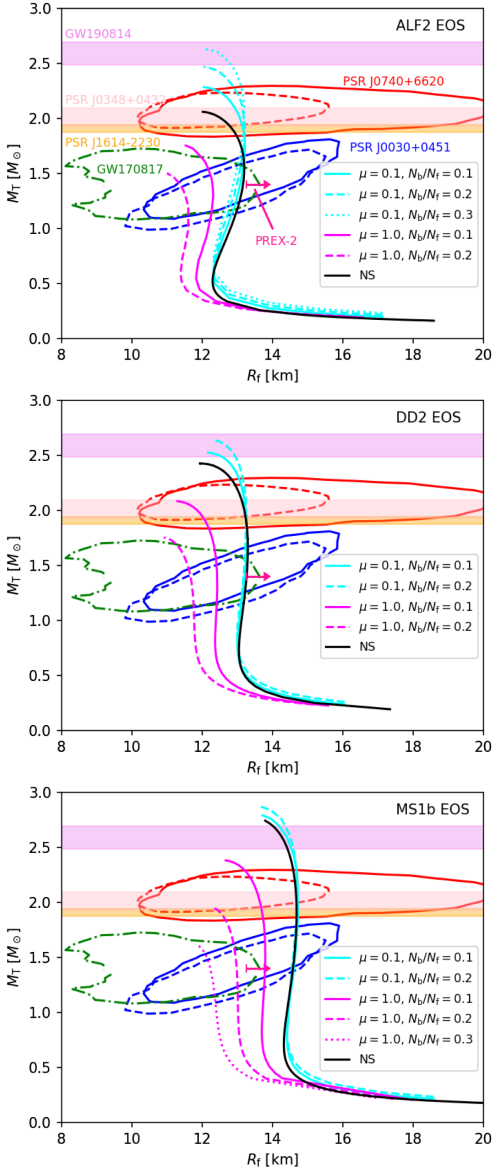


FIG. 2. Total gravitational mass vs circumferential fermionic radius for equilibrium models of neutron stars (black lines) and boson-fermion stars (magenta and cyan lines) for different parameters of the boson-to-fermion ratio N_b/N_f and particle mass μ . The observational constraints plotted are the same as in Fig. 1 and follow the same color code. Each panel corresponds to one of the three fermionic EOSs described in the text.

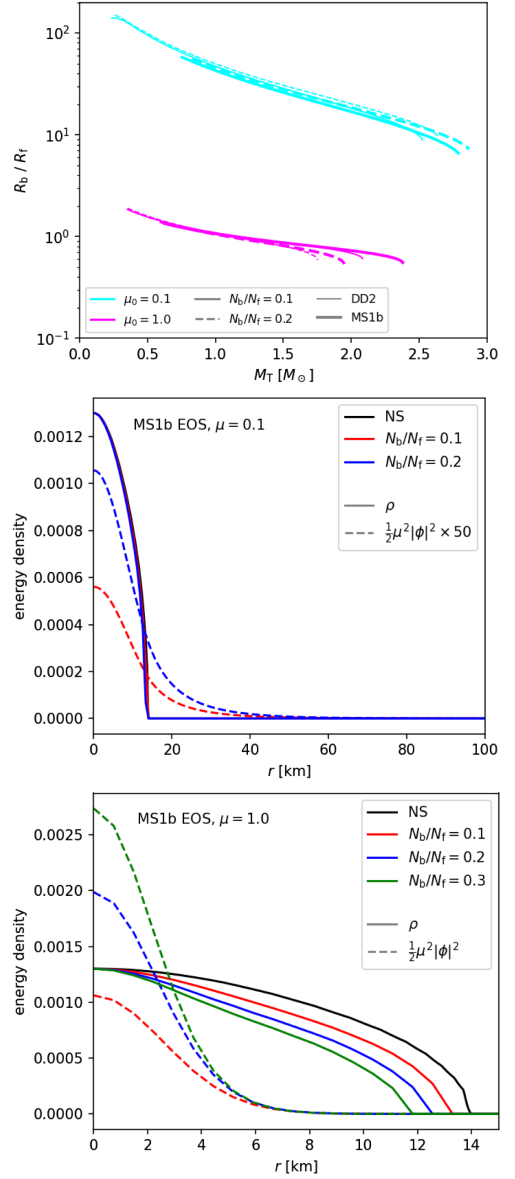


FIG. 3. Top panel: Ratio of the bosonic and fermionic radius as a function of the total mass, for a subset of the models considered in this work. Models not displayed follow a very similar trend. Middle panel: Radial profile of the rest-mass density ρ (solid lines) of an illustrative neutron star model described by the MS1b EOS, and of $\frac{1}{2}\mu^2|\phi|^2$ (dashed lines) for $\mu = 0.1$ and for different values of N_b/N_f . Bottom panel: Same as middle panel, but for $\mu = 1.0$.

For $\mu = 0.1$ (and similarly for smaller values of μ), the size of the bosonic component is larger than the fermionic radius ($R_b/R_f \sim 10\text{--}100$; see cyan curves in the top panel of Fig. 3). In this case, the contribution to the gravitational field of the bosonic component is relatively flat in the region where fermions are present, and therefore the impact in the equilibrium configuration of the fermionic component is small. This results in stars with similar fermionic radii. This is visible in the middle panel of Fig. 3, where we show the radial profiles of ρ and $\frac{1}{2}\mu^2|\phi|^2$ for a neutron star and for mixed stars described by the MS1b EOS with the same central value ρ_c . However, the additional energy provided by the bosonic component increases the total mass of the system. As a result, in these models (cyan lines in Fig. 2) the mass of the system increases as the ratio N_b/N_f increases while keeping the radius almost constant.

On the other hand, for $\mu = 1$ (and similarly for larger values of μ), the bosonic component is located in a region similar to or smaller than the region occupied by the fermionic component $R_b/R_f \sim 1$ (see magenta curves in the top panel of Fig. 3). In those cases, the bosonic component modifies the gravitational field in the neighborhood of the fermionic component to significantly modify the structure of the star by making it more compact. In those cases (magenta lines in Fig. 2), the fermionic radius decreases with increasing values of the ratio N_b/N_f (see bottom panel of Fig. 3). Additionally, due to this increase in compactness, the maximum mass supported by these models decreases.

IV. DISCUSSION

The additional degrees of freedom provided by the presence of a bosonic component may relieve some of the tension observed in the data in several ways. Leaving aside the question of the existence of ultralight bosonic fields in nature, the main uncertainty of our model is the astrophysical scenario in which fermion-boson stars could form. A number of theoretical works have tried to address this issue (see, e.g., Ref. [76] and references therein) in particular in the context of ultralight bosonic fields as a model for dark matter. In order to broadly assess the impact of bosonic fields, we explore here two situations that can be regarded as the two limiting cases in the range of possible models.

A. All stars have a constant bosonic-to-fermionic ratio

The first limiting scenario is the case in which the bosonic field is captured during the formation of the star, leading to an approximately universal N_b/N_f ratio for all fermion-boson stars. In this case, an EOS with relatively low maximum mass for the purely fermionic component, not fulfilling the GW190814 constraint, may produce more massive objects by adding a bosonic component with small values of μ and solve the issue. Examples are DD2 and

ALF2. In these two cases, supplementing a 10%–20% amount of bosonic component raises the maximum mass above $2.5 M_\odot$ while preserving the good agreement in radius at lower radii. Note that as a general feature of all EOSs (see gray lines in Fig. 1), the star radius decreases when the maximum mass decreases, meaning that it is difficult to have at the same time high maximum masses and small radii. The bosonic contribution is a way of precisely correcting this feature. Additionally, this procedure can also be used to increase the maximum mass even if in the purely fermionic case this mass is below $2 M_\odot$, which might be a solution to the so-called hyperon problem [41].

B. Bosonic-to-fermionic ratio changes over time

In the second limiting scenario, the bosonic matter is assumed to accrete onto the fermionic star after the latter has formed. In this case, the ratio N_b/N_f would increase over time, being higher for older objects. The set of neutron stars considered in this work can be classified into two categories according to their age. Electromagnetically observed pulsars have typical ages smaller than 10 Gyr: the characteristic age of PSR J0030 + 0451 is estimated to be 8 Gyr [77], PSR J0740 + 6620 is in the range 5–8.5 Gyr [78], PSR J0348 + 0432 is 2.6 Gyr [16], and PSR J1614 – 2230 is 5.2 Gyr [69]. On the other hand, typical ages of neutron stars found in mergers of compact binaries, such as those in GW170817 and GW190814, may be significantly larger. The merger time for a galactic binary neutron star is expected to be in the range $\sim 0.1\text{--}1000$ Gyr [79], which is consistent with the estimated merger time of the observed double neutron star systems in the Milky Way [80]. These estimates should be valid for the two gravitational-wave sources we consider, since the metallicity conditions of the host galaxies is likely to be similar to our Galaxy, given the low redshift of the sources. For the specific case of GW170817, it has been estimated that the age of the binary must be higher than 1 Gyr [81].

Therefore, it is plausible for the second class of objects to have accreted a significantly larger amount of bosonic field and thus have a larger ratio of N_b/N_f than the first class. In this scenario, neutron star radii could be relatively large for young objects with a very small amount of bosonic components, fulfilling the constraints set by PSR J0740 + 6620 and PSR J0348 + 0432. And at the same time, potentially older objects, such as those in GW170817, would have a significant bosonic component and thus smaller radii (see magenta lines in Fig. 2). In this situation, the bosonic field would need to have a particle mass of at least $\mu = 1$. On the other hand, the constraint set by GW190814 would be difficult to fulfill if the secondary were a neutron star, because in this scenario all stars should have much smaller maximum masses, but it could still be explained considering that the secondary is a low-mass black hole.

Finally, we have to address some of the caveats of our analysis. The observational constraints for the mass and radius considered here assume as a model that the observed object is a neutron star and obtain the posterior distributions according to this model. Therefore, if we change the model by adding a bosonic component, the observational constraints may in principle change as well. For electromagnetic observations of x-ray pulsars, the mass measurement (through Shapiro delay or orbital parameter measurements) relies almost exclusively on the effect of the total gravitational mass, regardless of its composition. The electromagnetic measurement of the radius, on the other hand, determines the size of the observable star—i.e., the fermionic component alone. The distribution of the bosonic field should affect weakly the analysis of NICER and XMM-Newton, because the main effect would be to modify the light bending close to the star (see, e.g., Ref. [5]). For $\mu = 1$ or larger, most of the bosonic field would be confined inside the fermionic radius. Therefore, the metric outside the observable surface would correspond to that of an object with the total mass of the star, and the analysis of NICER/XMM-Newton would be perfectly valid. On the other hand, for $\mu = 0.1$ or smaller, most of the bosonic field would be outside the observable surface, and the metric would differ with respect to the one corresponding to the total mass of the system (it would probably be closer to the space-time generated by the fermionic component alone). In that case, the analysis of NICER/XMM-Newton would require corrections.

We also recall that in all of our models, the self-interaction parameter of the bosonic field has been set to zero. It would be interesting to study the effect of self-interactions ($\lambda \neq 0$) on mixed fermion-boson stars with a realistic EOS, since a self-interaction potential allows us to increase the maximum mass without changing the particle mass μ . We leave this analysis as future work.

Regarding gravitational-wave observations, the measured component gravitational masses would probably be well estimated, since the structure of the compact objects appears only at 5PN order in the waveform models for binaries [82]. However, the estimation of the radius, as done in GW170817, may require modifications. This is actually an indirect estimation, as the actual parameter measured is the quadrupole tidal deformability. From this, assuming that the object is a neutron star, it is possible to put constraints on the radius [83]. Therefore, to do a proper analysis, one should have to either make the relevant corrections to estimate the fermion-boson star (fermionic) radius from the observational constraints on the tidal deformability, or compute the tidal deformability of our mixed stars (in particular, the quadrupole Love number) to compare directly with observations. Either of the two analyses is out of the scope of this paper. However, even if we do not perform this analysis, we expect that the trends found in our work should at least be qualitatively correct,

since there is a correlation between the tidal deformability and the radius.

It is also worth noticing that in scalar-tensor theories of gravity, in which the scalar field is not minimally coupled to gravity, neutron star models present significant deviations from general relativity through spontaneous scalarization, leading to neutron stars with significantly larger masses and radii [84–87]. In this regard, a suitable choice of the scalar field parameters and coupling constants of scalar-tensor theories could effectively reproduce the same mass-radius relations we have discussed in this paper for mixed fermion-boson stars in general relativity. Such potential degeneracy would make it difficult to distinguish between the two cases, and thus, between the underlying theories of gravity.

On a similar note, while our model resembles those of Refs. [32,33], we have applied it to explain a larger set of observational and experimental data than those authors, who exclusively focused on explaining the secondary component of GW190814 as a potential dark-matter-admixed neutron star. Our findings for GW190814 agree with those of Refs. [32,33], which provides an independent consistency check. Since in our model the bosonic component plays the role of dark matter, it is not surprising that any similar dark matter model would likely fit the data, irrespective of the type of matter considered.

To summarize, we conclude that the addition of a bosonic component to a neutron star leads to mixed configurations with mass-radius relations that are compatible with recent multimessenger observations of compact stars, both in the electromagnetic channel (PSR J0030 + 0451 and PSR J0740 + 6620) and in the gravitational-wave channel (GW170817 and GW190814), as well as with the latest PREX-2 experimental results. The possibility of enlarging the parameter space of neutron stars with different contributions from the bosonic component thus offers a theoretically motivated approach to reconcile the tension in the data collected by NICER/XMM-Newton and the LIGO-Virgo-KAGRA Collaboration.

ACKNOWLEDGMENTS

We thank Reed Essick, Nick Stergioulas, and Juan Carlos Degollado for useful comments. The work was supported by the Spanish Agencia Estatal de Investigación (Grant No. PGC2018-095984-B-I00), by the Generalitat Valenciana (PROMETEO/2019/071 and GRISOLIAP/2019/029), by the European Union's Horizon 2020 RISE program (H2020-MSCA-RISE-2017 Grant No. FunFICO-777740), and by the Fundação para a Ciência e a Tecnologia (FCT) (projects PTDC/FIS-OUT/28407/2017, CERN/FIS-PAR/0027/2019, and PTDC/FIS-AST/3041/2020). This work has further been supported by FCT through Project No. UIDB/00099/2020. P. C.-D. acknowledges support from the Spanish Ramon y Cajal program (RYC-2015-19074). N. S. G. was also supported by the

Spanish Ministerio de Universidades, reference UP2021-044, within the European Union-Next Generation EU. We acknowledge networking support by the COST Action GWverse CA16104. Computations have been performed at the Lluis Vives cluster of the Universitat de València and the Argus and Blafis clusters of the Universidade de Aveiro.

We also gratefully acknowledge the Italian Istituto Nazionale di Fisica Nucleare (INFN), the French Centre National de la Recherche Scientifique (CNRS) and the Netherlands Organization for Scientific Research, for the construction and operation of the Virgo detector and the creation and support of the EGO consortium.

-
- [1] J. M. Lattimer, *Annu. Rev. Nucl. Part. Sci.* **62**, 485 (2012).
 [2] J. M. Lattimer and M. Prakash, *Phys. Rep.* **621**, 127 (2016).
 [3] B. P. Abbott, R. Abbott (LIGO Scientific Collaboration, and Virgo Collaboration), *Phys. Rev. Lett.* **121**, 161101 (2018).
 [4] B. Margalit and B. D. Metzger, *Astrophys. J. Lett.* **850**, L19 (2017).
 [5] T. E. Riley, A. L. Watts, S. Bogdanov, P. S. Ray, R. M. Ludlam, S. Guillot, Z. Arzoumanian, C. L. Baker, A. V. Bilous, D. Chakrabarty, K. C. Gendreau, A. K. Harding, W. C. G. Ho, J. M. Lattimer, S. M. Morsink, and T. E. Strohmayer, *Astrophys. J. Lett.* **887**, L21 (2019).
 [6] M. C. Miller, F. K. Lamb, A. J. Dittmann, S. Bogdanov, Z. Arzoumanian, K. C. Gendreau, S. Guillot, A. K. Harding, W. C. G. Ho, J. M. Lattimer, R. M. Ludlam, S. Mahmoodifar, S. M. Morsink, P. S. Ray, T. E. Strohmayer, K. S. Wood, T. Enoto, R. Foster, T. Okajima, G. Prigozhin, and Y. Soong, *Astrophys. J. Lett.* **887**, L24 (2019).
 [7] T. Dietrich, M. W. Coughlin, P. T. H. Pang, M. Bulla, J. Heinzel, L. Issa, I. Tews, and S. Antier, *Science* **370**, 1450 (2020).
 [8] P. Landry, R. Essick, and K. Chatziioannou, *Phys. Rev. D* **101**, 123007 (2020).
 [9] K. Chatziioannou, *Gen. Relativ. Gravit.* **52**, 109 (2020).
 [10] T. E. Riley *et al.*, *Astrophys. J. Lett.* **918**, L27 (2021).
 [11] M. C. Miller *et al.*, *Astrophys. J. Lett.* **918**, L28 (2021).
 [12] G. Raaijmakers, S. K. Greif, K. Hebeler, T. Hinderer, S. Nisanke, A. Schwenk, T. E. Riley, A. L. Watts, J. M. Lattimer, and W. C. G. Ho, *Astrophys. J. Lett.* **918**, L29 (2021).
 [13] M. Breschi, A. Perego, S. Bernuzzi, W. Del Pozzo, V. Nedora, D. Radice, and D. Vescovi, *Mon. Not. R. Astron. Soc.* **505**, 1661 (2021).
 [14] P. B. Demorest, T. Pennucci, S. M. Ransom, M. S. E. Roberts, and J. W. T. Hessels, *Nature (London)* **467**, 1081 (2010).
 [15] E. Fonseca *et al.*, *Astrophys. J. Lett.* **915**, L12 (2021).
 [16] J. Antoniadis *et al.*, *Science* **340**, 448 (2013).
 [17] B. Abbott *et al.* (Virgo, LIGO Scientific Collaborations), *Phys. Rev. Lett.* **119**, 161101 (2017).
 [18] T. Dietrich, T. Hinderer, and A. Samajdar, *Gen. Relativ. Gravit.* **53**, 27 (2021).
 [19] R. Abbott (LIGO Scientific Collaboration, and Virgo Collaboration), *Astrophys. J. Lett.* **896**, L44 (2020).
 [20] E. R. Most, L. J. Papenfort, L. R. Weih, and L. Rezzolla, *Mon. Not. R. Astron. Soc.* **499**, L82 (2020).
 [21] A. Nathanael, E. R. Most, and L. Rezzolla, *Astrophys. J. Lett.* **908**, L28 (2021).
 [22] A. Sedrakian, F. Weber, and J. J. Li, *Phys. Rev. D* **102**, 041301 (2020).
 [23] A. Tsokaros, M. Ruiz, and S. L. Shapiro, *Astrophys. J.* **905**, 48 (2020).
 [24] B. Biswas, R. Nandi, P. Char, S. Bose, and N. Stergioulas, *Mon. Not. R. Astron. Soc.* **505**, 1600 (2021).
 [25] N.-B. Zhang and B.-A. Li, *Astrophys. J.* **902**, 38 (2020).
 [26] I. Bombaci, A. Drago, D. Logoteta, G. Pagliara, and I. Vidaña, *Phys. Rev. Lett.* **126**, 162702 (2021).
 [27] V. Dexheimer, R. O. Gomes, T. Klähn, S. Han, and M. Salinas, *Phys. Rev. C* **103**, 025808 (2021).
 [28] D. A. Godzieba, D. Radice, and S. Bernuzzi, *Astrophys. J.* **908**, 122 (2021).
 [29] K. Vattis, I. S. Goldstein, and S. M. Koushiappas, *Phys. Rev. D* **102**, 061301 (2020).
 [30] I. Cholis, K. Kritos, and D. Garfinkle, [arXiv:2106.07662](https://arxiv.org/abs/2106.07662).
 [31] C. Charmousis, A. Lehébel, E. Smymiotis, and N. Stergioulas, [arXiv:2109.01149](https://arxiv.org/abs/2109.01149).
 [32] H. C. Das, A. Kumar, and S. K. Patra, *Phys. Rev. D* **104**, 063028 (2021).
 [33] B. K. K. Lee, M.-c. Chu, and L.-M. Lin, *Astrophys. J.* **922**, 242 (2021).
 [34] C. Drischler, R. J. Furnstahl, J. A. Melendez, and D. R. Phillips, *Phys. Rev. Lett.* **125**, 202702 (2020).
 [35] D. Adhikari *et al.* (PREX Collaboration), *Phys. Rev. Lett.* **126**, 172502 (2021).
 [36] B. T. Reed, F. J. Fattoyev, C. J. Horowitz, and J. Piekarewicz, *Phys. Rev. Lett.* **126**, 172503 (2021).
 [37] R. Essick, P. Landry, A. Schwenk, and I. Tews, *Phys. Rev. C* **104**, 065804 (2021).
 [38] J. Jie Li, A. Sedrakian, and M. Alford, *Phys. Rev. D* **104**, L121302 (2021).
 [39] S.-P. Tang, J.-L. Jiang, M.-Z. Han, Y.-Z. Fan, and D.-M. Wei, *Phys. Rev. D* **104**, 063032 (2021).
 [40] P. T. H. Pang, I. Tews, M. W. Coughlin, M. Bulla, C. Van Den Broeck, and T. Dietrich, *Astrophys. J.* **922**, 14 (2021).
 [41] P. F. Bedaque and A. W. Steiner, *Phys. Rev. C* **92**, 025803 (2015).
 [42] S.-J. Sin, *Phys. Rev. D* **50**, 3650 (1994).
 [43] P.-H. Chavanis and T. Harko, *Phys. Rev. D* **86**, 064011 (2012).
 [44] T. Matos, F. S. Guzman, and L. A. Urena-Lopez, *Classical Quantum Gravity* **17**, 1707 (2000).
 [45] W. Hu, R. Barkana, and A. Gruzinov, *Phys. Rev. Lett.* **85**, 1158 (2000).
 [46] D. J. Kaup, *Phys. Rev.* **172**, 1331 (1968).
 [47] R. Ruffini and S. Bonazzola, *Phys. Rev.* **187**, 1767 (1969).

- [48] P. Jetzer, *Phys. Rep.* **220**, 163 (1992).
- [49] S. L. Liebling and C. Palenzuela, *Living Rev. Relativity* **20**, 5 (2017).
- [50] J. Calderón Bustillo, N. Sanchis-Gual, A. Torres-Forné, J. A. Font, A. Vajpeyi, R. Smith, C. Herdeiro, E. Radu, and S. H. W. Leong, *Phys. Rev. Lett.* **126**, 081101 (2021).
- [51] C. A. R. Herdeiro, A. M. Pombo, E. Radu, P. V. P. Cunha, and N. Sanchis-Gual, *J. Cosmol. Astropart. Phys.* **04** (2021) 051.
- [52] H. Olivares, Z. Younsi, C. M. Fromm, M. De Laurentis, O. Porth, Y. Mizuno, H. Falcke, M. Kramer, and L. Rezzolla, *Mon. Not. R. Astron. Soc.* **497**, 521 (2020).
- [53] A. Henriques, A. R. Liddle, and R. Moorhouse, *Phys. Lett. B* **251**, 511 (1990).
- [54] P. Jetzer, *Phys. Lett. B* **243**, 36 (1990).
- [55] S. Valdez-Alvarado, C. Palenzuela, D. Alic, and L. A. Urena-López, *Phys. Rev. D* **87**, 084040 (2013).
- [56] R. Brito, V. Cardoso, and H. Okawa, *Phys. Rev. Lett.* **115**, 111301 (2015).
- [57] R. Brito, V. Cardoso, C. F. Macedo, H. Okawa, and C. Palenzuela, *Phys. Rev. D* **93**, 044045 (2016).
- [58] S. Valdez-Alvarado, R. Becerril, and L. A. Ureña-López, *Phys. Rev. D* **102**, 064038 (2020).
- [59] A. A. Roque and L. A. Ureña-López, *Classical Quantum Gravity* **39**, 044001 (2022).
- [60] F. Di Giovanni, S. Fakhry, N. Sanchis-Gual, J. C. Degollado, and J. A. Font, *Phys. Rev. D* **102**, 084063 (2020).
- [61] F. Di Giovanni, S. Fakhry, N. Sanchis-Gual, J. C. Degollado, and J. A. Font, *Classical Quantum Gravity* **38**, 194001 (2021).
- [62] B. Kain, *Phys. Rev. D* **104**, 043001 (2021).
- [63] M. Bezares, D. Viganò, and C. Palenzuela, *Phys. Rev. D* **100**, 044049 (2019).
- [64] G. Panotopoulos and I. Lopes, *Phys. Rev. D* **96**, 083004 (2017).
- [65] B. Kain, *Phys. Rev. D* **103**, 043009 (2021).
- [66] T. Gleason, B. Brown, and B. Kain, *Phys. Rev. D* **105**, 023010 (2022).
- [67] Compose, <https://compose.obspm.fr/home> (2018).
- [68] F. Özel and P. Freire, *Annu. Rev. Astron. Astrophys.* **54**, 401 (2016).
- [69] Z. Arzoumanian *et al.* (NANOGrav Collaboration), *Astrophys. J. Suppl. Ser.* **235**, 37 (2018).
- [70] B. Biswas, *Astrophys. J.* **921**, 63 (2021).
- [71] M. Alford, M. Braby, M. Paris, and S. Reddy, *Astrophys. J.* **629**, 969 (2005).
- [72] M. Hempel and J. Schaffner-Bielich, *Nucl. Phys.* **A837**, 210 (2010).
- [73] A. Arvanitaki, M. Baryakhtar, and X. Huang, *Phys. Rev. D* **91**, 084011 (2015).
- [74] V. Cardoso, Ó. J. Dias, G. S. Hartnett, M. Middleton, P. Pani, and J. E. Santos, *J. Cosmol. Astropart. Phys.* **03** (2018) 043.
- [75] C. Palomba, S. D’Antonio, P. Astone, S. Frasca, G. Intini, I. La Rosa, P. Leaci, S. Mastrogiovanni, A. L. Miller, F. Muciaccia, O. J. Piccinni, L. Rei, and F. Simula, *Phys. Rev. Lett.* **123**, 171101 (2019).
- [76] R. Brito, V. Cardoso, C. F. B. Macedo, H. Okawa, and C. Palenzuela, *Phys. Rev. D* **93**, 044045 (2016).
- [77] A. N. Lommen, A. Zepka, D. C. Backer, M. McLaughlin, J. M. Cordes, Z. Arzoumanian, and K. Xilouris, *Astrophys. J.* **545**, 1007 (2000).
- [78] D. M. Beronya, A. V. Karpova, A. Y. Kirichenko, S. V. Zharikov, D. A. Zyuzin, Y. A. Shibanov, and A. Cabrera-Lavers, *Mon. Not. R. Astron. Soc.* **485**, 3715 (2019).
- [79] D. R. Lorimer, *Living Rev. Relativity* **11**, 8 (2008).
- [80] T. M. Tauris, M. Kramer, P. C. C. Freire, N. Wex, H. T. Janka, N. Langer, P. Podsiadlowski, E. Bozzo, S. Chaty, M. U. Kruckow, E. P. J. van den Heuvel, J. Antoniadis, R. P. Breton, and D. J. Champion, *Astrophys. J.* **846**, 170 (2017).
- [81] A. J. Levan *et al.*, *Astrophys. J.* **848**, L28 (2017).
- [82] L. Blanchet, *Living Rev. Relativity* **17**, 2 (2014).
- [83] J. S. Read, L. Baiotti, J. D. E. Creighton, J. L. Friedman, B. Giacomazzo, K. Kyutoku, C. Markakis, L. Rezzolla, M. Shibata, and K. Taniguchi, *Phys. Rev. D* **88**, 044042 (2013).
- [84] T. Damour and G. Esposito-Farese, *Classical Quantum Gravity* **9**, 2093 (1992).
- [85] T. Harada, *Phys. Rev. D* **57**, 4802 (1998).
- [86] H. Sotani and K. D. Kokkotas, *Phys. Rev. D* **70**, 084026 (2004).
- [87] J. C. Degollado, M. Salgado, and M. Alcubierre, *Phys. Lett. B* **808**, 135666 (2020).

Impact of ultralight bosonic dark matter on the dynamical bar-mode instability of rotating neutron stars

Fabrizio Di Giovanni¹,² Nicolas Sanchis-Gual,^{1,2} Davide Guerra,¹ Miquel Miravet-Tenés,¹ Pablo Cerdá-Durán,¹ and José A. Font^{1,3}

¹*Departamento de Astronomía y Astrofísica, Universitat de València, Dr. Moliner 50, 46100 Burjassot (València), Spain*

²*Departamento de Matemática da Universidade de Aveiro and Centre for Research and Development in Mathematics and Applications (CIDMA), Campus de Santiago, 3810-183 Aveiro, Portugal*

³*Observatori Astronòmic, Universitat de València, C/ Catedrático José Beltrán 2, 46980 Paterna (València), Spain*



(Received 8 June 2022; accepted 17 July 2022; published 2 August 2022)

We investigate the effects ultralight bosonic field dark matter may have on the dynamics of unstable differentially rotating neutron stars prone to the bar-mode instability. To this aim we perform numerical simulations in general relativity of rotating neutron stars accreting an initial spherically symmetric bosonic field cloud, solving the Einstein-(complex, massive) Klein-Gordon-Euler and the Einstein-(complex) Proca-Euler systems. We find that the presence of the bosonic field can critically modify the development of the bar-mode instability of neutron stars, depending on the total mass of the bosonic field and on the boson particle mass. In some cases, the accreting bosonic field can even quench the dominant $\ell = m = 2$ mode of the bar-deformation by dynamically forming a mixed (fermion-boson) star that retains part of the angular momentum of the original neutron star. However, the mixed star undergoes the development of a mixed bar that leads to significant gravitational-wave emission, substantially different to that of the isolated neutron star. Our results indicate that dark-matter accretion in neutron stars could change the frequency of the expected emission of the bar-mode instability, which would have an important impact on ongoing searches for continuous gravitational waves.

DOI: [10.1103/PhysRevD.106.044008](https://doi.org/10.1103/PhysRevD.106.044008)

I. INTRODUCTION

Differential rotation is expected to occur in neutron stars. It can be present in proto-neutron stars (PNS) formed in core-collapse supernova (CCSN) explosions, in the transient post-merger remnants that form after binary neutron star (BNS) mergers, and in x-ray binary systems where accretion can trigger high-amplitude oscillation (axial fluid) r-modes that might impact the neutron star rotation. In addition, rotating neutron stars are also expected to be subject to various types of nonaxisymmetric instabilities (for reviews see [1,2] and references therein). For sufficiently high values of the ratio of the rotational kinetic energy T and the gravitational potential energy W , namely $\beta \equiv T/|W| \gtrsim 0.27$, neutron stars are subject to the dynamical bar-mode instability. Through this instability the star is deformed into a bar by virtue of the nonlinear growth of the $\ell = 2$ oscillation mode (ℓ being the spherical harmonic index) which leads to the emission of high-frequency (kHz) gravitational waves [3–5]. As the degree of differential rotation increases, rotating stars are dynamically unstable against bar-mode deformation even for values of β of order 0.01 [6–10]. Moreover, highly differentially rotating

neutron stars can also become unstable to a dynamical one-arm ($m = 1$, spiral) instability [11,12]. At lower rotation rates secular nonaxisymmetric instabilities can also appear, driven by gravitational radiation (through the Chandrasekhar-Friedman-Schutz mechanism) or by viscosity (the latter, however, not being a generic instability in rotating neutron stars).

Interestingly, this phenomenology might not be exclusive of rotating compact bodies composed only of fermionic matter. Recently we have shown through numerical-relativity simulations of spinning bosonic stars [13,14] that those hypothetical objects can also be affected by the same type of dynamical bar-mode instabilities that operate in rapidly rotating neutron stars. Bosonic stars are self-gravitating compact objects that can be constructed by minimally coupling a complex, massive bosonic field, either scalar or vector, to Einstein's gravity [15–17]. They can form dynamically from incomplete gravitational collapse through the gravitational cooling mechanism [18,19] and are composed of ultralight bosonic fields that could account for (part of) dark matter. The fields' particles have masses that range from 10^{-10} to 10^{-22} eV and have been motivated by string

theory [20,21] and by simple extensions of the Standard Model of particles [22]. Such stars could be detected through their gravitational-wave emission in mergers [23] or through their effective shadow [24,25]. Both, linear analysis and numerical simulations have shown that spherical bosonic stars are dynamically robust [26–31] (see [32] for a review). However, spinning bosonic stars can undergo bar-mode deformation [13,14], during which the angular momentum of the star is emitted and the star decays into a nonspinning configuration. In particular, spinning scalar mini-boson stars without self-interaction terms in the potential and some spinning vector boson star models are bar-mode unstable. Mechanisms to stabilize unstable bosonic stars, either in spherical symmetry or in the rotating case, have been studied recently. Those include combinations of independent bosonic fields only interacting through gravity, such as ℓ —boson stars [33–35] and multistate, multifield boson stars [36–39] as well as the addition of self-interaction terms in the potential [40,41]. In the former two cases the combination of a stable bosonic star with an unstable one stabilizes the mixture, even in the spinning case.

These recent findings provide a theoretical motivation to study what could be the possible impact of adding a bosonic field to a rapidly rotating neutron star, particularly regarding the development of the bar-mode instability of the star. In addition to neutron stars and boson stars, macroscopic composites of fermions and bosons, dubbed fermion-boson stars, have also been proposed [42–51]. Such mixed configurations could form from the condensation of some primordial gas containing both types of particles or through episodes of accretion. These mixed configurations conform an extended parameter space that depends on the combination of the number of fermions and (ultralight) bosons. While hypothetical there have been proposals to endow these compact objects with potential astrophysical relevance. For example, in [52] spherically symmetric fermion-boson stars have been proposed to help explain the tension in the measurements of neutron star masses and radii reported in recent multimessenger observations and nuclear-physics experiments.

In this work we perform numerical-relativity simulations of three unstable differentially rotating neutron stars with an initial bosonic field distribution surrounding the star (the field can be both scalar and vector). We explore the effects of the field on the dynamics of the neutron stars by varying the initial energy of the cloud, from a small fraction to a mass comparable to that of the neutron star. In addition, we also consider three different values of the bosonic particle mass μ . Our simulations show that, in all cases, the bosonic field is quickly accreted by the neutron star and condenses into a nonspinning bosonic star within its rotating fermion counterpart—a dark matter core. The impact of this core on the development of the bar-mode instability is noticeable. We find that the larger the bosonic total mass and the lower μ , the instability takes longer to set in.

However, within the range of parameters of our study, the bar-mode deformation of the neutron star seems an unavoidable outcome. On the other hand, the modification in the dynamics of the composite star affects significantly the associated gravitational-wave emission as compared to the case of a bar-mode unstable neutron star without a bosonic core.

This paper is organized as follows: in Sec. II we introduce the matter model we employ and set up the basic equations of motion to solve. Section III addresses the issue of initial data. The numerical framework for our simulations is described in Sec. IV while the results and analysis of those simulations are presented in Sec. V. Finally, we outline our conclusions and final remarks in Sec. VI. Throughout this work we use units such that the relevant fundamental constants are equal to one ($G = c = M_\odot = 1$).

II. FORMALISM

A. Equations of motion

We assume that bosonic and fermionic matter are both minimally coupled to Einstein’s gravity,

$$R_{\alpha\beta} - \frac{1}{2}g_{\alpha\beta}R = 8\pi T_{\alpha\beta}. \quad (1)$$

Therefore, the total stress-energy tensor describing the matter content is given by the superposition of both contributions, one coming from a perfect fluid and the other from a scalar/vector complex field:

$$T_{\mu\nu} = T_{\mu\nu}^{\text{fluid}} + T_{\mu\nu}^{(s)}, \quad (2)$$

where superscript (s) stands for the spin of the bosonic particle, i.e., 0 for the case of a scalar field and 1 for a vector (Proca) field. The contribution for the perfect fluid reads

$$T_{\mu\nu}^{\text{fluid}} = [\rho(1 + \epsilon) + P]u_\mu u_\nu + P g_{\mu\nu}, \quad (3)$$

where P is the pressure of the perfect fluid, ρ its rest-mass density, ϵ its specific internal energy, and $u^\mu = (W/\alpha, W(v^i - \beta^i/\alpha))$ is the fluid’s 4-velocity, W being the Lorentz factor and v^i the fluid 3-velocity as seen by Eulerian observers. The contributions from the bosonic field are specified in the Secs. II B and II C.

The evolution equations are given by Einstein’s equations (1), by the conservation laws of the fluid stress-energy tensor and baryonic particles

$$\nabla_\mu T_{\text{fluid}}^{\mu\nu} = 0, \quad (4)$$

$$\nabla_\mu (\rho u^\mu) = 0, \quad (5)$$

together with a choice of an equation of state (EoS) for the fluid, and by the equations of motion for the bosonic field.

For the construction of the initial data we consider a polytropic EoS,

$$P = K\rho^\Gamma, \quad (6)$$

with $K = 100$ and $\Gamma = 2$. The equations of motion of the bosonic field are the Klein-Gordon equation for a complex scalar field ϕ ,

$$\nabla_\mu \nabla^\mu \phi = \mu_{(0)}^2 \phi, \quad (7)$$

and the Proca equations for a complex vector field \mathcal{A}^μ ,

$$\nabla_\mu \mathcal{F}^{\mu\nu} + \mu_{(1)}^2 \mathcal{A}^\nu = 0. \quad (8)$$

In the previous equations ∇_μ is the covariant derivative with respect to the metric $g_{\mu\nu}$ and $\mu_{(s)}$ is the mass of the particle for the scalar field ($s = 0$) or the vector field ($s = 1$). We consider the spacetime line element

$$\begin{aligned} ds^2 &= g_{\mu\nu} dx^\mu dx^\nu \\ &= -(\alpha^2 - \beta_i \beta^i) dt^2 + 2\gamma_{ij} \beta^i dt dx^j + \gamma_{ij} dx^i dx^j, \end{aligned} \quad (9)$$

where α is the lapse function, β^i is the shift vector, and γ_{ij} is the spatial metric. We employ the Baumgarte-Shapiro-Shibata-Nakamura (BSSN) formulation of Einstein's equations [53–55], references to which the reader is addressed for details. The BSSN equations involve energy-momentum source terms, namely the energy density \mathcal{E} , the momentum density j_i measured by a normal observer n^μ , and the spatial projection of the stress-energy tensor S_{ij} , which read

$$\mathcal{E} = n^\mu n^\nu T_{\mu\nu}, \quad (10)$$

$$j_i = -\gamma_i^\mu n^\nu T_{\mu\nu}, \quad (11)$$

$$S_{ij} = \gamma_i^\mu \gamma_j^\nu T_{\mu\nu}, \quad (12)$$

where the unit normal vector is $n^\mu = \frac{1}{\alpha}(1, -\beta^i)$ and γ_i^μ is the spatial projection operator. The source terms for the perfect fluid read

$$\mathcal{E}^{\text{fluid}} = (\rho(1 + \epsilon) + P)W^2 - P, \quad (13)$$

$$j_i^{\text{fluid}} = (\rho(1 + \epsilon) + P)W^2 v_i, \quad (14)$$

$$S_{ij}^{\text{fluid}} = (\rho(1 + \epsilon) + P)W^2 v_i v_j + \gamma_{ij} P. \quad (15)$$

B. Einstein-Klein-Gordon-Euler system

The stress-energy tensor associated with the scalar field ϕ is

$$T_{\mu\nu}^{(0)} = -\frac{1}{2}g_{\mu\nu}\partial_\alpha\bar{\phi}\partial^\alpha\phi - V(\phi) + \frac{1}{2}(\partial_\mu\bar{\phi}\partial_\nu\phi + \partial_\mu\phi\partial_\nu\bar{\phi}), \quad (16)$$

where for the potential of the scalar field we consider that of a miniboson star [32],

$$V(\phi) = \frac{1}{2}\mu_{(0)}^2\bar{\phi}\phi. \quad (17)$$

In the previous two equations the bar symbol denotes complex conjugation. As customary, in order to write the Klein-Gordon equation (7) as a first-order system we introduce the scalar-field conjugate momentum

$$\Pi = -\frac{1}{\alpha}(\partial_t - \mathcal{L}_\beta)\phi. \quad (18)$$

The source terms for this system read

$$\mathcal{E}^{(0)} = \frac{1}{2}\left(\bar{\Pi}\Pi + \mu_{(0)}^2\bar{\phi}\phi + \frac{1}{2}\lambda(\bar{\phi}\phi)^2 + D^i\bar{\phi}D_i\phi\right), \quad (19)$$

$$j_i^{(0)} = \frac{1}{2}(\bar{\Pi}\nabla_i\phi + \Pi\nabla_i\bar{\phi}), \quad (20)$$

$$\begin{aligned} S_{ij}^{(0)} &= \frac{1}{2}(\nabla_i\bar{\phi}\nabla_j\phi + \nabla_j\bar{\phi}\nabla_i\phi) \\ &+ \frac{1}{2}\gamma_{ij}\left(\bar{\Pi}\Pi - \mu_{(0)}^2\bar{\phi}\phi - \frac{1}{2}\lambda(\bar{\phi}\phi)^2 - D^k\bar{\phi}\nabla_k\phi\right). \end{aligned} \quad (21)$$

The set of evolution equations for the scalar field are described in [56].

C. Einstein-Proca-Euler system

The stress-energy tensor for a vector field \mathcal{A}_μ is

$$\begin{aligned} T_{\mu\nu}^{(1)} &= -\mathcal{F}_{\lambda(\mu}\bar{\mathcal{F}}_{\nu)}^\lambda - \frac{1}{4}g_{\mu\nu}\mathcal{F}_{\lambda\alpha}\bar{\mathcal{F}}^{\lambda\alpha} \\ &+ \mu_{(1)}^2\left[\mathcal{A}_{(\mu}\bar{\mathcal{A}}_{\nu)} - \frac{1}{2}g_{\mu\nu}\mathcal{A}_\lambda\bar{\mathcal{A}}^\lambda\right], \end{aligned} \quad (22)$$

where $\mathcal{F}_{\mu\nu} = \nabla_\mu\mathcal{A}_\nu - \nabla_\nu\mathcal{A}_\mu$ is the field strength, and the index notation (μ, ν) indicates, as usual, index symmetrization. We cast the splitting of the Proca 1-form \mathcal{A}^μ into its scalar potential \mathcal{X}_ϕ , its 3-vector potential \mathcal{X}_i , and the 3-dimensional electric E_i and magnetic B_i field, defined by

$$\mathcal{X}_\phi = -n^\mu\mathcal{A}_\mu, \quad (23)$$

$$\mathcal{X}_i = \gamma_i^\mu\mathcal{A}_\mu, \quad (24)$$

$$E^i = -i\frac{\gamma^{ij}}{\alpha}(D_j(\alpha\mathcal{X}_\phi) + \partial_t\mathcal{X}_j), \quad (25)$$

$$B^i = \epsilon^{ijk} D_j \mathcal{X}_k, \quad (26)$$

where ϵ^{ijk} is the Levi-Civita tensor. The energy-momentum source terms for this system read

$$\mathcal{E}^{(1)} = \frac{1}{2} \gamma_{ij} (\bar{E}^i E^j + \bar{B}^i B^j) + \frac{1}{2} \mu_{(1)}^2 (\bar{\mathcal{X}}_\phi \mathcal{X}_\phi + \gamma^{ij} \bar{\mathcal{X}}_i \mathcal{X}_j), \quad (27)$$

$$j_i^{(1)} = \frac{1}{2} \mu_{(1)}^2 (\bar{\mathcal{X}}_\phi \mathcal{X}_i + \mathcal{X}_\phi \bar{\mathcal{X}}_i), \quad (28)$$

$$\begin{aligned} \mathcal{S}_{ij}^{(1)} = & -\gamma_{ik} \gamma_{jl} (\bar{E}^k E^l + \bar{B}^k B^l) + \frac{1}{2} \gamma_{ij} (\bar{E}^k E_k + \bar{B}^k B_k \\ & + \mu_{(1)}^2 \bar{\mathcal{X}}_\phi \mathcal{X}_\phi - \mu_{(1)}^2 \bar{\mathcal{X}}^k \mathcal{X}_k) + \mu_{(1)}^2 \bar{\mathcal{X}}_i \mathcal{X}_j. \end{aligned} \quad (29)$$

The set of evolution equations for the Proca field are described in [57].

III. INITIAL DATA

We construct configurations describing a cloud of bosonic matter surrounding a rotating neutron star (RNS) model. As scalar spinning miniboson stars may develop nonaxisymmetric instabilities, as shown in [13, 14, 40], we consider purely spherically symmetric scalar field clouds with zero angular momentum. However, for the vector field clouds we construct also models with nonzero angular momentum. To obtain physical initial data it is mandatory to solve the Einstein Hamiltonian and momentum constraint equations. Moreover, for the case of a vector field, an additional constraint comes into play, the Gauss constraint $D_i E^i = \mu_{(1)}^2 \mathcal{X}_\phi$, where D_i stands for the covariant derivative with respect to the 3-metric γ_{ij} . In this section we schematically describe the procedure to construct constraint-satisfying initial data for the physical situation we are considering.

We begin by building highly differentially RNS models, which we choose among the bar-mode unstable models considered in [4]. We employ the RNS numerical code [58] to construct such configurations. We then add a bosonic cloud assuming a harmonic time dependence and a particular cloud “shape.” For spherically symmetric scalar clouds we consider a Gaussian radial profile for the scalar field, yielding

$$\phi(r, t) = A_0 e^{-\frac{r^2}{\sigma^2}} e^{i\omega t}, \quad (30)$$

where parameters A_0 and σ are the amplitude and the width of the Gaussian shell, respectively, and ω is the initial frequency of the field. The ansatz for the vector field is more involved as there are several field component involved and we must also solve the Gauss constraint. We address the interested reader to the appendix of [14] and

to [57] for specific details about the initial data for the vector field case.

Once we have constructed a RNS model and the surrounding bosonic cloud, we can evaluate the source terms entering in the Hamiltonian and momentum constraints. Those are going to be simply the sum of the terms from the fermionic matter (13) and the ones from either the scalar field (19) or the vector field (23). Finally as initial guess for the spacetime variables we consider those take the values of the isolated RNS and we solve the constraint equations with the updated matter source terms iteratively until convergence is reached. This procedure is described in more detail in the appendix of [14] and it relies on the so-called conformally flat approximation (CFC) of the full Einstein equations, as described in [59].

To characterize our initial models we compute several physical quantities: the angular velocity of the fluid Ω , the baryonic mass M_0 , the gravitational mass M_{grav} , the internal energy E_{int} , the angular momentum J_{NS} , the rotational kinetic energy T , and the gravitational binding energy W of the RNS, respectively defined as

$$\Omega = \frac{u^\phi}{u_t}, \quad (31)$$

$$M_0 = \int d^3x D\sqrt{\gamma}, \quad (32)$$

$$M_{\text{grav}} = \int d^3x (-2T_0^0 + T_\mu^\mu) \alpha \sqrt{\gamma}, \quad (33)$$

$$E_{\text{int}} = \int d^3x D\epsilon \sqrt{\gamma}, \quad (34)$$

$$J_{\text{NS}} = \int d^3x T_\phi^0 \alpha \sqrt{\gamma}, \quad (35)$$

$$T = \frac{1}{2} \int d^3x \Omega T_\phi^0 \alpha \sqrt{\gamma}, \quad (36)$$

$$W = M_0 + E_{\text{int}} + T - M_{\text{grav}}. \quad (37)$$

We note that in the previous equations we employ only the stress-energy contribution from the perfect fluid but we omit the subscript “fluid” to simplify the notation. We also recall the notation for the ratio between the rotational and binding energy $\beta \equiv T/|W|$.

The bosonic cloud is instead characterized by the total mass and angular momentum stored in it, which are evaluated as:

$$M_{\text{cloud}} = \int d^3x (-2T_0^0 + T_\mu^\mu) \alpha \sqrt{\gamma}, \quad (38)$$

$$J_{\text{cloud}} = \int d^3x T_\phi^0 \alpha \sqrt{\gamma}, \quad (39)$$

TABLE I. Models of RNS with an accreting scalar/Proca cloud. From left to right the columns report: the name of the RNS model [4], its central rest-mass density ρ_c , its baryon mass M_0 , its gravitational mass M_{grav} , its angular momentum J_{NS} , its kinetic energy T , its binding energy W , the ratio between rotational and binding energy β , the type of bosonic cloud, the mass parameter of the scalar/vector boson μ , the amplitude of the Gaussian profile A_0 , and the total mass stored in the cloud M_{cloud} . Most models have an $\ell = m = 0$ bosonic cloud and the amplitude of the Gaussian profile $\sigma = 60$. Only the last model in the Table corresponds to a spinning $\ell = 1$, $m = \pm 1$ Proca cloud with angular momentum $J_{\text{cloud}}^{(1)} = \pm 1.315$. The width of the Gaussian cloud σ is also indicated.

$l = m = 0, \sigma = 60$											
RNS model	$\rho_c(10^{-4})$	M_0	M_{grav}	J_{NS}	$T(10^{-2})$	$W(10^{-2})$	β	Cloud	μ	$A_0(10^{-3})$	M_{cloud}
U13	0.599	1.506	1.466	3.757	2.188	7.452	0.294	None
U13-a	0.599	1.600	1.521	3.980	2.319	11.53	0.201	Scalar	1.0	1.1	0.628
U13-b	0.599	1.600	1.521	3.980	2.319	11.53	0.201	Scalar	0.5	2.2	0.629
U13-c	0.599	1.592	1.516	3.961	2.308	11.17	0.206	Scalar	0.33	3.2	0.578
U13-d	0.599	1.556	1.496	3.874	2.256	9.595	0.235	Scalar	0.33	2.5	0.346
U13-e	0.599	1.531	1.481	3.811	2.220	8.499	0.261	Scalar	0.33	1.8	0.176
U7	1.406	1.512	1.462	3.406	2.337	8.366	0.279	None
U7-a	1.406	1.563	1.495	3.523	2.418	10.79	0.224	Scalar	0.5	1.7	0.368
D2	3.154	2.752	2.614	7.583	9.211	30.50	0.302	None
D2-a	3.154	2.862	2.678	7.870	9.560	35.75	0.267	Scalar	0.33	1.9	0.222
D2-b	3.154	2.956	2.733	8.119	9.867	40.24	0.245	Scalar	0.5	1.6	0.372
D2-c	3.154	2.850	2.671	7.838	9.520	35.18	0.270	Scalar	1.0	0.6	0.205
U13-f	0.599	1.591	1.507	3.960	2.306	12.00	0.192	Proca	0.5	23	1.182
U13-g	0.599	1.541	1.488	3.836	2.234	8.766	0.255	Proca	1.0	3.0	0.505
U13-h	0.599	1.590	1.520	3.958	2.306	10.65	0.216	Proca	1.0	4.5	1.172
$l = 1, m = \pm 1, \sigma = 40$											
U13-i	0.599	1.658	1.564	4.122	1.382	13.17	0.182	Proca	1.0	3.0×10^{-4}	1.302

where again we omit the subscript (s) which identifies the scalar/vector field.

In Table I we summarize the parameters and the main properties of the models we consider for this study. We choose three RNS models, labeled D2, U7, and U13 (see [4] and references therein for details), and different cloud parameters for the scalar and Proca fields that surround them. Since the models used in this work are constructed using the CFC formalism, which is an approximation of the full Einstein equations, the global quantities of our RNS models show a small discrepancy with respect to the original models generated by the RNS numerical code. For instance, comparing the physical quantities (M_0 , M_{grav} , T , E_{im}) in Table I for model U13 with respect to those shown in [4], a discrepancy of order 0.3% is observed, which is expected for the 2PN error resulting from the CFC approximation. The discrepancy becomes higher for more compact neutron stars like model D2 where it is of order 1%. We note that the relative error in the evaluation of the binding energy W is higher because it is a 1PN correction to the energy of the system. In practice this means that while the error is small for M_0 and M_{grav} (e.g., 4×10^{-3} for model U13, for values of $M_0 \sim M_{\text{grav}} \sim 1.5$), this same error, contributing to the error of W through Eq. (37), is larger for W itself (which has a value of $W = 7.452 \times 10^{-2}$ for U13) resulting in a 5% error, still consistent with its expected post-Newtonian order. A similar effect is observed for β , which is also a 1PN quantity.

IV. SUMMARY OF NUMERICAL ASPECTS

We employ the community-driven software platform EinsteinToolkit [60–62] for the numerical evolutions, based on the CACTUS framework and CARPET [63,64] for mesh-refinement capabilities. We use the MCLACHLAN infrastructure [65,66], which implements the BSSN formulation of Einstein’s equations for evolving the spacetime variables. The evolution of the scalar field and the Proca field, along with the computation of their contribution to the stress-energy tensor are managed by a private code that we tested and employed in previous works [13,14,35,39,67]. The code for the complex Proca field is an extension of the one originally developed in [57] and currently publicly available in the CANUDA repository [68] and distributed within each new release of the EinsteinToolkit. We employ GRHydro for the fluid dynamics and EOSomni for the EoS. The evolutions are carried out using a Γ -law EoS $P = (\Gamma - 1)\rho c$.

The Cartesian-coordinate-based numerical grid for our simulations is discretized with five refinement levels, each spanning a different spatial domain with a different resolution. From the outermost to the innermost grid, the spatial domains are $\{300, 240, 200, 100, 50\}$ in units of the total mass, and the corresponding $(\Delta x = \Delta y = \Delta z)$ resolutions of each level are $\{10, 5, 2.5, 1.25, 0.65\}$. We choose a Courant factor such that the time step is $\Delta t = 0.25\Delta x$, where Δx is the grid spacing of the innermost grid along the

x direction. We assume reflection symmetry with respect to the equatorial plane ($z = 0$). We employ radiative (Sommerfeld) outer boundary conditions, which are implemented in the `NEWRAD` code.

V. RESULTS

As stated before, the aim of this work is to investigate numerically the potential effects of ultralight bosonic dark matter accreting on to differentially RNS on the stability properties of these objects. Our simulations start with a transient phase during which the bosonic cloud accretes on to the neutron star, with a timescale shorter than that of the development of the dynamical bar-mode instability. After the cloud has been accreted its effect on the dynamics of the neutron star are significant, as we discuss next.

A. Dynamics

We perform long-term simulations ($\mathcal{O}(100)$ ms) of the full 16 models of Table I. However, for the sake of clarity in the analysis we present results only for an illustrative subset of models that best display the effects of the bosonic field on the bar-mode instability (and on the gravitational waveforms). We start discussing results for models U13, U13-a, U13-b, and U13-c. For the last three models the mass of the scalar cloud is roughly equal ($M_{\text{cloud}} \approx 0.6$) which allows us to isolate the effects of varying the particle mass μ . Moreover, throughout this section we only discuss the scalar-field case, since the conclusions we draw for this case remain unaltered for a Proca-field cloud.

The columns of Fig. 1 display snapshots of the rest-mass density ρ at the equatorial plane for those four models. Note that except for the first row (initial data) the snapshots selected in subsequent rows are different for each model. The isolated RNS model U13 is depicted in the left column while the next three columns show the evolution of models U13-a, U13-b, and U13-c for which the scalar-field cloud is built with correspondingly smaller values of the bosonic particle mass, $\mu = 1$, $\mu = 0.5$, and $\mu = 0.33$, respectively. The green contour visible in some of the snapshots of Fig. 1 indicates the level surface of constant bosonic energy density $\mathcal{E}^{(0)}$ which contains 95% of the total mass of the bosonic cloud. We note that during the accretion process the bosonic cloud loses mass through the mechanism known as gravitational cooling [18,19]. On the one hand, in models U13-b and U13-c the amount of scalar field expelled is about 5% of the total stored in the cloud, which means that most of the mass of the cloud accretes on to the RNS in a short timescale, less than 10 ms. On the other hand, model U13-a undergoes the highest mass loss, losing almost half of the initial bosonic mass by the end of the simulation (at which time the process still continues). The evaluation of the surface containing 95% of the total mass for model U13-a is affected by the mass released through gravitational cooling during the accretion process, and for

this reason we obtain surfaces which are far from being spheroidal. The differences observed in the dynamical evolution of the bosonic cloud in models U13a, U13b, and U13c, can be understood by recalling the stability properties of spherically-symmetric boson stars. Such stars have a maximum mass of $M_{\text{max}} = 0.633/\mu$ (see, e.g., [69]), separating the stable and unstable branches in the mass-frequency existence plot. We relate the different behavior of model U13-a with the fact that the mass stored in the cloud ($M_{\text{cloud}} = 0.628$) is very close to the maximum allowed mass for a boson star with $\mu = 1$. As a result, the dynamical process leads to the simultaneous ejection of a large amount of mass from the cloud and the gradual formation of a spherical boson star residing in a more stable region in the parameter space (away from the maximum). On the other hand, models U13-b and U13-c are already initially well inside the corresponding boson-star stable region and, thus, they do not radiate a lot of scalar field to reach stability.

All models are subject to nonaxisymmetric instabilities throughout the evolution. We note that we do not impose any ad-hoc perturbation on the initial data to trigger those but the only source of perturbation is the discretization error of the finite-difference approximations of the partial derivatives of the equations we solve. The presence of the accreting scalar field leads to different dynamics. For the purely RNS model U13, shown in the leftmost column of Fig. 1, the development of an $m = 2$ -dominated instability is apparent at around $t \approx 10$ ms (second row). This dynamical timescale is similar to that reported in [4] for the same model. This leads to the appearance of a bar-like deformation during which the star sheds mass and angular momentum and finally settles into a perturbed stable configuration. During this process the maximum value of the rest-mass density ρ moves from the end-points of the bar toward the center of the star, whose morphology changes from toroidal to spheroidal.

When a scalar field is included, the evolution of the RNS is modified but the star continues to undergo nonaxisymmetric instabilities with different timescales and features. The most salient characteristic of all models involving an accreting scalar field is that no bar is formed and the dominant mode of the deformation shifts from $m = 2$ to $m = 1$, i.e., those models mostly develop a one-arm instability. This morphological change can be identified by the appearance of a rotating over-density blob (see, e.g., the third snapshots from the top in the last two columns of Fig. 1). Eventually, when angular momentum is radiated away through gravitational waves, this over-density blob collapses into a spheroidal RNS. In addition, the timescale of the $m = 1$ instability increases with respect to the isolated RNS case: for U13-a ($\mu = 1.0$) it occurs at $t \approx 15$ ms, for U13-b ($\mu = 0.5$) at $t \approx 25$ ms, and finally for U13-c ($\mu = 0.33$) at $t \approx 40$ ms. We note that the timescale increases as we decrease the value of μ when keeping the same total initial mass in the cloud. We

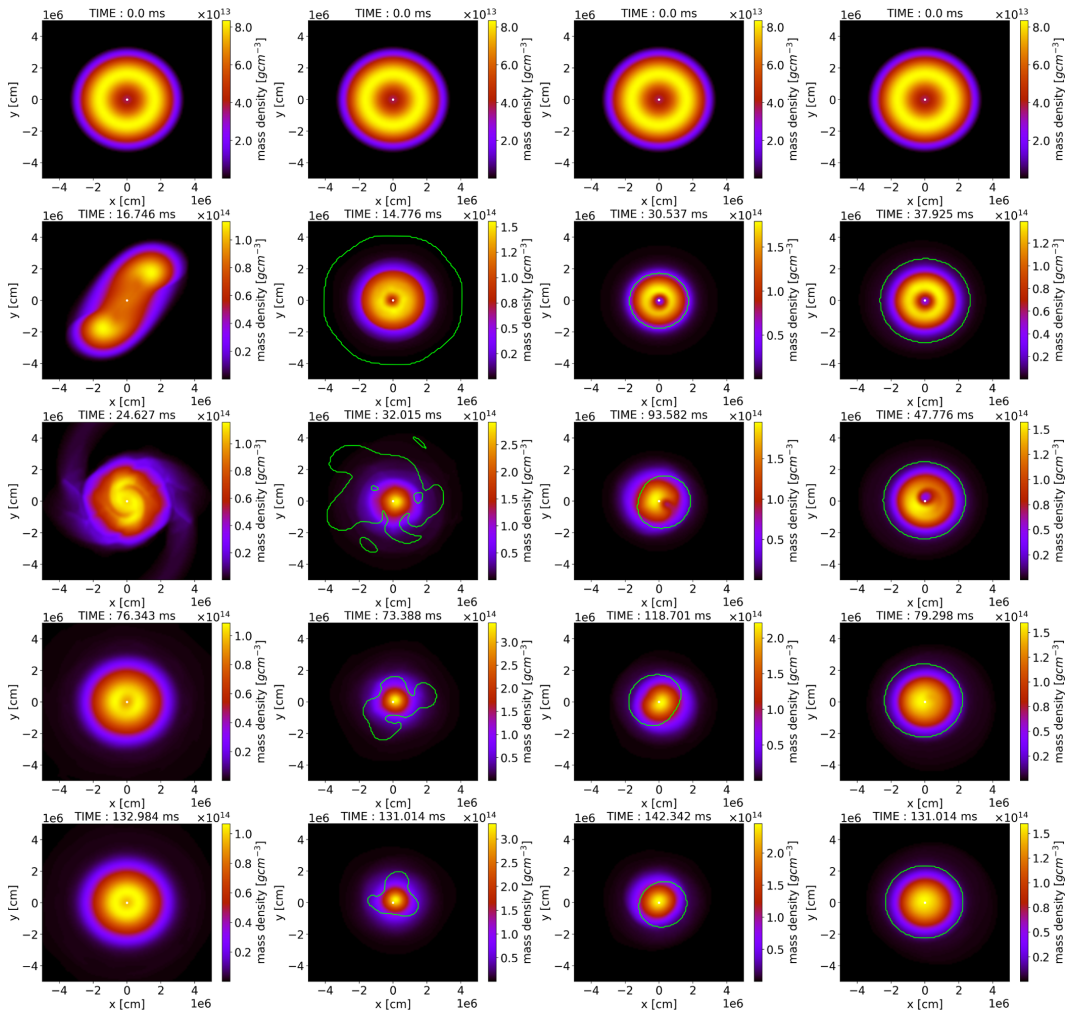


FIG. 1. Time evolution of the rest-mass density ρ (in cgs units) at the equatorial plane. The four columns correspond, respectively, to the isolated RNS model U13 (left), model U13-a with $\mu = 1.0$ (center-left), model U13-b with $\mu = 0.5$ (center-right), and model U13-c with $\mu = 0.33$ (right). The contour in green indicates the level surface of constant bosonic energy density $\mathcal{E}^{(0)}$ which contains 95% of the total mass of the bosonic cloud. The center of the computational grid is highlighted with a white dot.

tentatively identify the reason for this behavior with the fact that as the cloud becomes more diluted so does the entire configuration, hence the fermionic part gets increasingly less compact and the instability takes longer to set in.

A more quantitative representation of the fundamental properties of the instabilities that develop in our systems can be obtained by monitoring the evolution of the volume-integrated azimuthal Fourier mode decomposition of the fermion energy density, evaluated as

$$\mathcal{C}_m = \int d^3\mathbf{x} \mathcal{E}^{\text{fluid}}(\mathbf{x}) e^{im\varphi}. \quad (40)$$

We point out that when odd modes (such as $m = 1$) start to grow, the center-of-mass of the object is displaced from the origin of the Cartesian grid. As explained in [8] we take into account this displacement to properly evaluate \mathcal{C}_m and the computation of the angular momentum J_{NS} and J_{cloud} during the evolution. To this end we evaluate the coordinates of the center-of-mass of the entire object and we

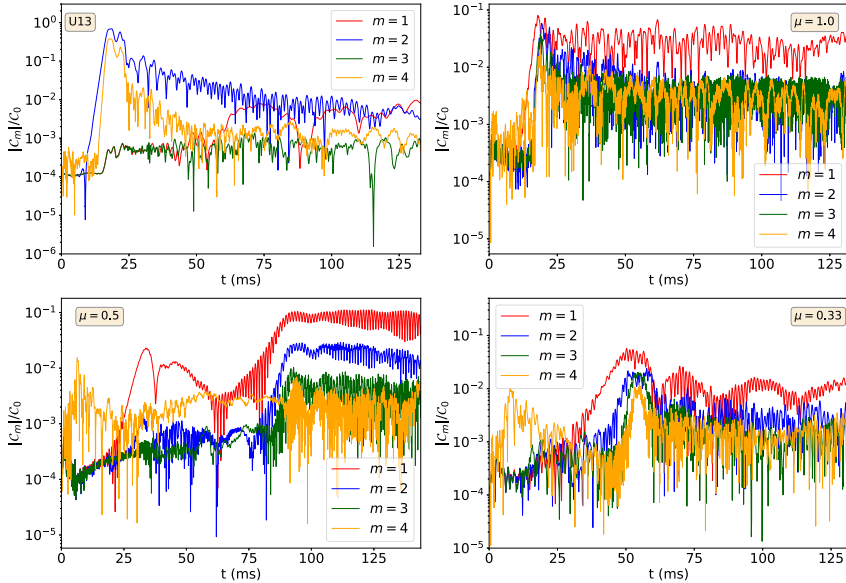


FIG. 2. Time evolution of the azimuthal mode decomposition of the fermion energy density, from $m = 1$ to $m = 4$, for the same models shown in Fig. 1. Top-left panel: model U13; top-right panel: model U13-a; bottom-left panel: model U13-b; bottom-right panel: model U13-c.

redefine the azimuthal coordinate φ with respect to this center instead of the center of the numerical grid, as we explain in [14].

Quantities C_m defined in Eq. (40) monitor the departure from axisymmetry in the fermion density. In Fig. 2 we show, for the same models discussed in Fig. 1, the time evolution of the absolute value of the mode decomposition for the first four Fourier modes, $m = \{1, 2, 3, 4\}$, normalized to the total energy C_0 . In all cases we observe an exponential growth of the different modes. As discussed above we can clearly see that in the case of an isolated RNS (model U13; top-left panel of Fig. 2) only the even modes $m = 2$ and $m = 4$ are significantly excited initially, the dominant one being the $m = 2$ bar-mode. At later times the amplitude of both modes decay, especially that of the $m = 4$ mode which shows a steeper rate, and by the end of the simulation the dominant modes are the $m = 2$ and $m = 1$. However, their late-time amplitudes are about two orders of magnitude smaller than that of the $m = 2$ mode at maximum amplitude (attained around $t = 20$ ms). We note that the response of the different modes observed in our simulation of model U13 is in perfect agreement with what was found in [4] (see, in particular, their Fig. 7).

The remaining panels of Fig. 2 show the time evolution of $|C_m|$ for models U13-a, U13-b, and U13-c. In the presence of a scalar field all modes are excited to significant levels, with the $m = 1$ becoming dominant in all cases. We

observe the same excitation also when we depict the Fourier mode decomposition of the bosonic energy density, evaluated in the same fashion as in Eq. (40). We note that in models U13-b and U13-c the odd modes are excited in both the boson and fermion sectors in such a way that, collectively, they give rise to an *even* distribution of the total energy density in the form of a “mixed bar” (one end of the bar made of bosonic matter, the other of fermionic matter). This morphology guarantees the conservation of the total linear momentum for the case of comparable masses of both sectors. This dynamics is illustrated in the left and center panels of Fig. 3. The panels exhibit two late-time snapshots of the bosonic energy density $\mathcal{E}^{(0)}$ and the fermionic rest-mass density ρ on the equatorial plane for model U13-b. The fermionic contribution is shown in orange isocontours. These two panels illustrate how the two different matter components rotate around the Cartesian origin with a π phase difference, in such a way that the center-of-mass of the total object remains close to the center of the computational grid. This means that the total linear momentum is approximately conserved as the mixed bar compensates the excitation of the dominant $m = 1$ modes in both matter constituents. This is further demonstrated in the right panel of Fig. 3 which displays the time evolution of the x -component of the center-of-mass of both the bosonic and fermionic energy density parts (depicted in red and blue, respectively) as well as the total

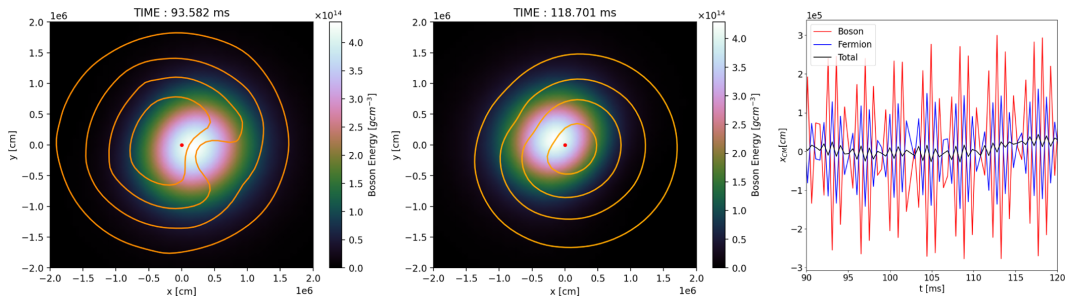


FIG. 3. The left and middle panels show two time snapshots of an equatorial cut of $\mathcal{E}^{(0)}$ for model U13-b and of the rest-mass density ρ . The latter is indicated by the orange contours. The maximum of the fermionic energy and its center-of-mass are located inside the smallest contours. These two snapshots reveal the transient formation of a mixed (fermionic-bosonic) bar. In the right panel we show the time evolution (spanning the time interval depicted in the left and center panels) of the x -component of the center-of-mass evaluated for the bosonic and fermionic contribution, to highlight the π phase difference, and for the total object.

energy density (i.e., the sum of the two, depicted in black). The evolution shown spans the time interval indicated in the left and center panels of the figure. A very similar result is observed for the y -component of the center-of-mass. The red and blue curves clearly reveal a constant π phase difference between the two matter components as long as the mixed bar persists, while the black curve shows that the total center-of-mass stays close to the origin.

A similar behavior occurs for model U13-c. For both models, U13-b and U13-c, the maximum displacement of the center-of-mass from the origin is about 3 times smaller than the resolution of our finest grid. On the other hand, for model U13-a we observe a small displacement of the center-of-mass which starts to be significant at $t \approx 30$ ms. We tentatively associate the different behavior of model U13-a with respect to models U13-b and U13-c with the larger ejection of scalar field during the accretion process, the formation of a more compact bosonic star core, and the transfer of angular momentum to the scalar component due the dragging of the neutron star. A larger amount of angular momentum is then expected to be emitted in the form of gravitational waves for model U13-a, as we discuss below.

We turn now to briefly discuss the dynamics of models with constant boson particle mass μ and varying initial cloud mass M_{cloud} . Those models are U13-c, U13-d, and U13-e in Table I, all with $\mu = 0.33$ and correspondingly decreasing M_{cloud} . Time snapshots on the equatorial plane of the rest-mass density ρ for these models, also including the purely RNS model U13, are plotted in Fig. 4. As in Fig. 1 the green contour visible in most snapshots corresponds to the surface containing 95% of the bosonic energy density which allows to better evaluate the effects of the scalar field on the dynamics of the neutron stars. Model U13-e, plotted in the second column from the left, is the one with less initial bosonic mass M_{cloud} . During its early evolution the neutron star develops the bar-mode instability, as in the no-scalar-field model U13 plotted in the first

column, and in a very similar timescale of $\mathcal{O}(10$ ms). However, at late times an $m = 1$ spiral mode develops in the energy profile (see the last two snapshots of the second column) which is not present in model U13. This transition from an initial $m = 2$ -dominated neutron star to a final $m = 1$ -dominated one is still in effect as the initial mass of the bosonic cloud increases, as shown in models U13-d and U13-c plotted in the third and fourth columns of Fig. 4, respectively. As M_{cloud} increases the transition accelerates—the $m = 2$ barlike deformation quickly disappears while the $m = 1$ bloblike deformation becomes dominant.

B. Gravitational-wave emission

We characterize the gravitational-wave emission by computing the mode decomposition of the Newman-Penrose scalar Ψ_4 in spin-weighted spherical harmonics with spin -2 . We extract the coefficients $\Psi_4^{\ell,m}$ for $\ell = 2$ and $m = 1, 2$ at three different radii, namely $r = \{100, 150, 200\}$. These extraction radii are both far enough from the source (to be in the wave zone) and not too close to the outer boundary of our numerical grid (to avoid unphysical effects from spurious numerical reflections). We interpolate with a third-order polynomial fit the values from the three different extraction radii to obtain $r\Psi_4^{2,m}$. The waveforms for models U13, U13-e, U13-d, and U13-c, the last three having the same bosonic particle mass ($\mu = 0.33$) and increasing initial boson cloud mass, are shown in Fig. 5. We display the (retarded) time evolution of the real part of $r\Psi_4^{2,m}$ for $m = 1, 2$. The waveforms shown in the top-left panel of Fig. 5 correspond to model U13, which has no accreting bosonic field. As expected, the dominant contribution to the waveform is the $\ell = m = 2$ mode, reflecting the distinct bar-mode deformation this model undergoes. The $m = 1$ mode is hardly excited for this model, its amplitude being a few orders of magnitude smaller than

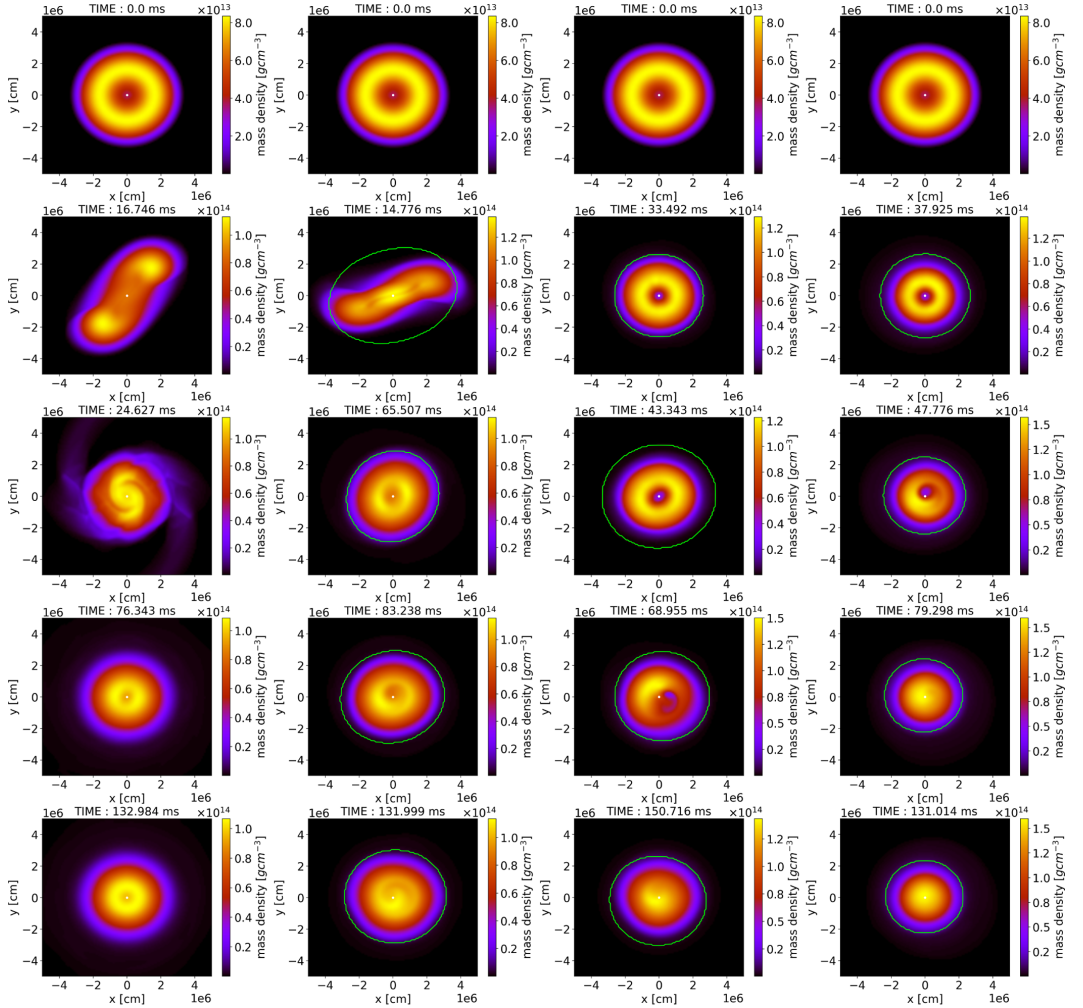


FIG. 4. Time evolution of the rest-mass density ρ (in cgs units) at the equatorial plane. The green isocontour indicates the level surface of constant bosonic energy density which contains 95% of the total mass of the bosonic cloud. From left to right the columns correspond to model U13, U13-e, U13-d, and U13-c. The last three models have the same value of the bosonic particle mass ($\mu = 0.33$) but the total mass stored in the cloud increases from left to right.

that of the $m = 2$ mode. By the end of the simulation the amplitude of the $m = 2$ waveform has not yet decreased substantially.

As we discussed in the previous section, the presence of an accreting bosonic cloud has a major impact on the dynamics of the stars. This is also imprinted on the waveforms. From Fig. 5 we observe that the more massive the scalar-field cloud, the larger (smaller) the amplitude of the $m = 1$ ($m = 2$) gravitational-wave mode. Indeed, by the end of our simulations the $m = 1$ amplitude of the most

massive case, U13-c, becomes comparable to the amplitude of the $m = 2$ mode (see bottom-right panel). For model U13-e (top-right) the $m = 1$ mode is still largely suppressed. Therefore, the fact that by increasing M_{cloud} the appearance of the bar-mode instability becomes less clear as the spiral-mode instability becomes more prominent, has a recognizable manifestation on the gravitational-wave signals as well.

By direct inspection of Fig. 5 we can also observe that the frequency of the $m = 2$ mode seems to significantly

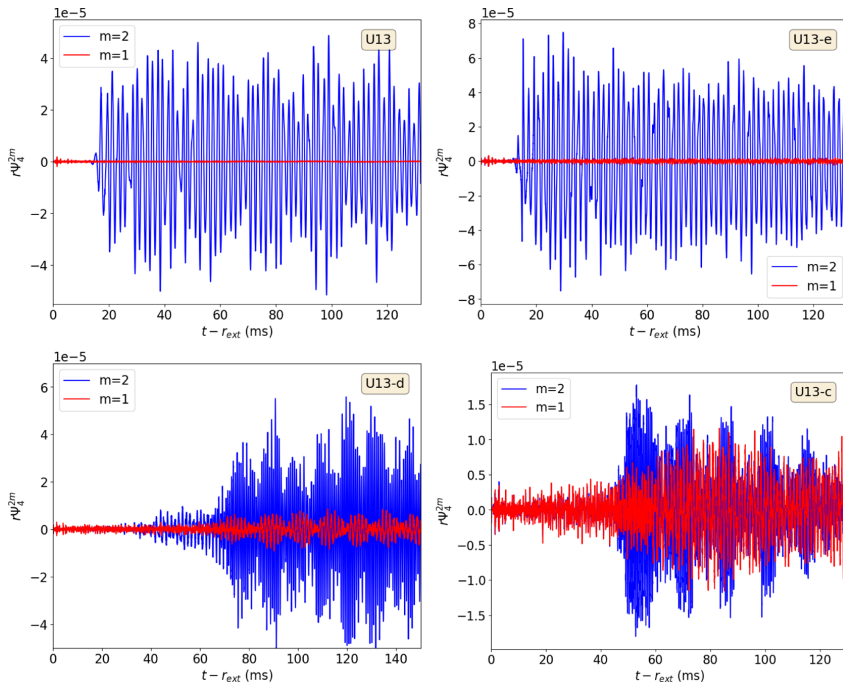


FIG. 5. Real part of $r\Psi_4^{2,m}$ with $m = 1, 2$ as a function of the retarded time for models U13 (top-left panel), U13-e (top-right panel), U13-d (bottom-left panel), and U13-c (bottom-right panel). The curves are obtained after a third-order polynomial fit interpolation of the corresponding waveforms from the three extraction radii we select.

increase as the mass stored in the cloud is larger. Moreover, a noticeable feature of the waveforms is the presence of beating patterns in the oscillations. This is a clear sign of the existence and superposition of more than one significant oscillation frequency of comparable values. We compute those frequencies by performing fast Fourier transforms of the gravitational-wave time series $r\Psi_4^{2,m}$. The associated magnitudes are depicted in Fig. 6 for the same four models of Fig. 5. We show two types of modes in this figure, namely the $\ell = m = 2$ and the $\ell = 2, m = 0$ modes, to emphasize the possible contribution of quasiradial oscillations ($\ell = 0$) to the frequency pattern. The top-left panel of Fig. 6 shows the main frequencies that are excited during the evolution of model U13. The first thing to notice is that the spectrum for this model, and those of the other models, present the same essential features, with a fundamental mode and a series of overtones. We note the presence of a double-peaked feature at $f_{\text{GW}} \approx 505$ Hz and $f_{\text{GW}} \approx 555$ Hz. We identify the former with the fundamental bar-mode frequency (see below). The proximity of the two frequencies could explain the beating pattern shown in the blue curve of Fig. 5. For the same model [4] did not observe such beating and only reported a single frequency

of 457 Hz, in broad agreement with our value, given the different resolutions employed in the two simulations and the length of the time series (much shorter in the case of [4]) which limits the accuracy of the computation of the frequency. As a consistency check we have verified that the same frequency pattern is obtained when evolving the same U13 model but constructing the initial data with the `Hydro_RNSID` numerical code. Details on this comparison are provided in Appendix.

While the value of the β parameter of the U13 model is high enough for the model to develop the nonaxisymmetric bar-mode instability, the star is also subjected to axisymmetric pulsating modes during its evolution. The frequency spectrum of nonlinear axisymmetric pulsations of rotating relativistic stars was studied in detail by [70]. Their sequence of differentially rotating models with a fixed rest mass of $M_0 = 1.506$ (same as that of U13) extends from the nonrotating model to a model with $\beta = 0.223$ (model A10 in [70]). Hence, those models are stable against the dynamical bar-mode deformation. Their frequency spectrum is dominated by the fundamental quasiradial ($\ell = 0$) F mode (and its first overtone), the fundamental quadrupole ($\ell = 2$) mode (and its first two overtones), and three

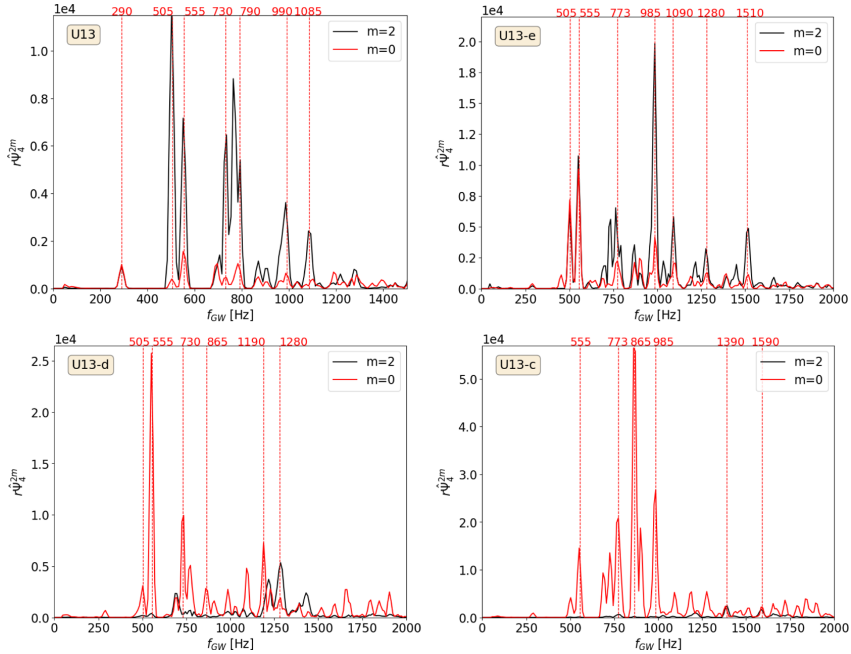


FIG. 6. Fourier transform of $r\Psi_4^{2,m}$ for $m = 0, 2$ for models U13 (top-left panel), U13-e (top-right panel), U13-d (bottom-left panel) and U13-c (bottom-right panel).

inertial modes (see Table 2 and Fig. 1 in [70]). Along their sequence, the frequency of the F mode decreases fairly linearly with β . Extrapolating that trend to our U13 model, with $\beta = 0.29$, would yield a value of the F mode frequency of ≈ 400 Hz (and of ≈ 450 Hz for $\beta = 0.28$ as used in [4]). To infer the actual frequency of the F mode we monitor the time evolution of the rest-mass density ρ at the center of the star for model U13. This particular choice is motivated by the fact that as ρ at the center is unaffected by even mode deformations (such as the bar) we can isolate the effects of the quasiradial oscillations. By evaluating the Fourier transform of ρ in the first 35 ms we observe a wide peak for the F mode at around 407 Hz. The limited time window does not allow us to better resolve the frequency but our result is in broad agreement with the value we extrapolated from [70]. In addition, we repeat the same procedure for a fixed point on the equatorial plane, namely at $r \approx 9$ km, in order to obtain the spectrum of frequencies of *both* the quasiradial oscillations and the bar-mode instability. By subtracting the magnitude of the Fourier transform at $r \approx 9$ km and at the center of the star, we eliminate from the former the contribution of the quasiradial oscillations and we isolate the frequency of the bar. This yields a frequency peak at ≈ 500 Hz which is in close agreement with what we infer from Fig. 6.

After the bar has mostly dissipated, we also observe the appearance of a well-defined frequency at ≈ 785 Hz. We interpret this frequency as associated with the actual $\ell = 0$ quasiradial F mode oscillation of the *new* equilibrium configuration reached by model U13 once the bar deformation has disappeared. In addition, we speculate that the secondary peak of ≈ 555 Hz depicted in the top-left panel of Fig. 6 may have been originated by the coupling with the frequency of the $\ell = 2, m = 0$ mode. However, the presence of the fundamental quasiradial F mode may have also helped triggering the double-peaked structure seen in the figure.

The discrete modes we observe in the PSD are nonlinear harmonics of linear pulsation modes, which is a general property of nonlinear systems [71]. To lowest order, these arise as linear sums and differences of different linear modes, including self-couplings. For a system with eigenfrequencies f_i , the nonlinearity of the equations of motion excites modes at frequencies $f_i \pm f_j$. Such nonlinear harmonics have been noted in other types of oscillating compact objects, as e.g., thick disks around black holes [72,73] and pulsating relativistic stars [70]. In our case one such harmonic appears at $f_{\text{GW}} \approx 1$ kHz, where we observe the same double-peaked structure at a frequency which corresponds, roughly, to twice the frequency of the fundamental mode (a self-coupling). In between those two modes

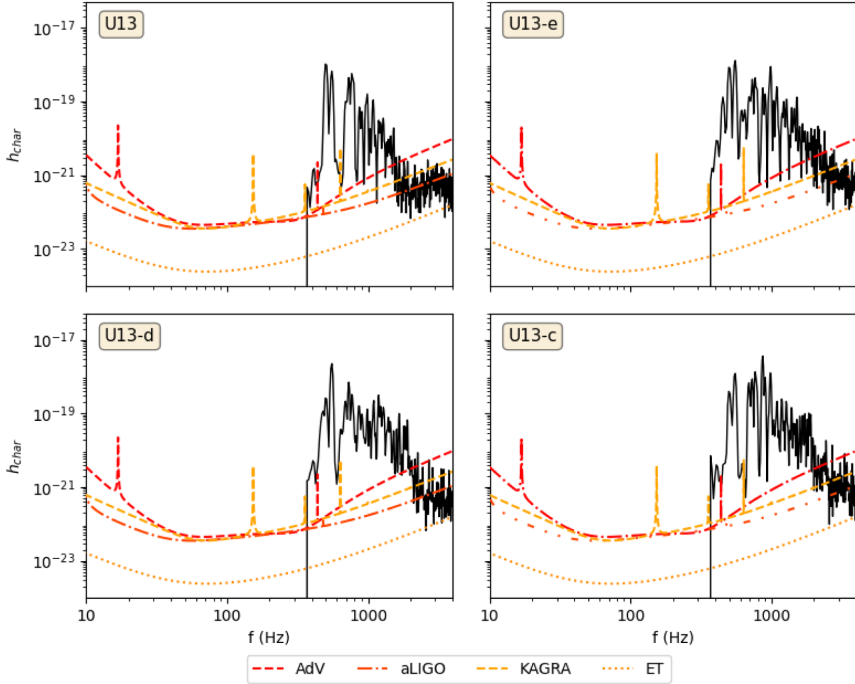


FIG. 7. Characteristic gravitational-wave strain against frequency for model U13 (top-left panel), U13-e (top-right panel), U13-d (bottom-left panel) and U13-c (bottom-right panel), compared with the sensitivity curves of current second-generation detectors and the planned Einstein Telescope. A source distance of $D = 10$ kpc is assumed.

the spectrum depicts two further combinations of intermediate frequencies which may correspond to other non-linear harmonics arising as linear sums or differences of the bar-mode frequency and other modes. In the top-left panel of Fig. 6 we highlight the peaks at $f_{\text{GW}} \approx 730$ Hz and $f_{\text{GW}} \approx 790$ Hz which can be identified with linear combinations of the peak at 505 Hz and the one at 290 Hz, namely $2 \times 505 - 290 = 720$ Hz and $505 + 290 = 795$ Hz.

The presence of the scalar field which interacts gravitationally with the baryonic matter and modifies the evolution of the whole system makes the gravitational-wave emission more complex, as we saw in Fig. 5. In general, as we increase the scalar field contribution, the $m = 2$ amplitude becomes smaller, due to the fact that the bar-mode instability tends to disappear. Moreover the $m = 0$ spectra in Fig. 6 become increasingly prominent, due to the higher perturbation the neutron star undergoes and the gravitational cooling process of the scalar cloud which leads to a radially perturbed stationary configuration (see also [18,19]). The model with the lightest scalar cloud (top-right panel of Fig. 6) still displays a similar frequency pattern than model U13, associated with the formation of the bar. The dominant peak is now, however, at ≈ 1 kHz,

and an additional overtone is present at ≈ 1510 Hz. For the last 2 models (U13-d and U13-c; bottom-left and bottom-right panels of Fig. 6) the dominant contributions come from the $m = 0$ mode, where we observe the double peak structure at around 500–550 Hz and at 730–790 Hz and the appearance of a new peak at ≈ 865 Hz, which could be roughly identified as the sum of the frequencies at 555 Hz and 290 Hz. In model U13-c, in particular, the dominant peak appears at this new overtone at ≈ 865 Hz.

In Fig. 7 we show the characteristic gravitational-wave strain h_{char} at a distance $D = 10$ kpc for models U13, U13-e, U13-d, and U13-c compared with the designed sensitivity curves of ground-base detectors Advanced LIGO (aLIGO) [74], Advanced Virgo (AdV) [75], KAGRA [76], and the future Einstein Telescope (ET) [77]. For burst-like sources the characteristic GW strain is (see, e.g., [78])

$$h_{\text{char}}(f) = \frac{1}{\pi D} \sqrt{2 \frac{dE}{df} [f]}, \quad (41)$$

where D is the distance of the source and dE/df is the energy spectrum of the gravitational waves. The interested

TABLE II. Horizon distances of the gravitational-wave signal studied in this work for models U13, U13-e, U13-d, and U13-c with increasing bosonic contribution, evaluated for the ground-based detectors Advanced Virgo (AdV), Advanced LIGO (aLIGO), KAGRA, and Einstein Telescope (ET).

Model	Horizon distance (Mpc)			
	AdV	aLIGO	KAGRA	ET
U13	0.747	1.460	0.872	14.791
U13-e	0.813	1.690	0.994	16.880
U13-d	1.037	2.245	1.318	22.371
U13-c	0.860	2.695	1.425	24.403

reader is addressed to [14] for further details on the definition of the energy spectrum. We note that for the reasons explained in Appendix we cut the contribution at high frequencies of the $m = 0$ mode in the evaluation of h_{char} .

The spectra shown in Fig. 7 closely parallel the Fourier transforms depicted in Fig. 6. For the U13 model (no scalar field cloud) the maximum of h_{char} is at $f_{\text{GW}} \approx 505$ Hz which is the main peak of the $m = 2$ mode shown in Fig. 6, linked to the bar-mode instability. For models U13-e and U13-d, the maxima in the spectra are at around 555 Hz which we associate with the $m = 0$ mode that is excited by quasiradial oscillations of the neutron star. Moreover the overtones at higher frequencies become more relevant. Finally for model U13-c, which is the one with the largest amount of scalar field, the $m = 0$ overtone at frequency $f_{\text{GW}} \approx 860$ Hz becomes the maximum of the characteristic strain.

We evaluate the matched-filtering signal-to-noise ratio (SNR) squared for an optimally oriented detector, averaged over all possible source directions as [78]

$$\rho_{\text{optimal}}^2 = \int_0^\infty d(\ln f) \frac{h_{\text{char}}(f)^2}{f S_n(f)}, \quad (42)$$

where $S_n(f)$ is the power spectral density (PSD) of the detector noise. We consider the SNR averaged over all possible detector orientations and sky localizations, which is simply $\langle \rho^2 \rangle = \rho_{\text{optimal}}^2 / 5$. We define the horizon distance as the distance at which $\text{SNR} = 8$. We report in Table II this quantity for the four models shown in Fig. 7 and for the four gravitational-wave detectors considered. For second-generation detectors, the signal studied in this paper could be detectable up to distances of about 1 Mpc while ET could observe it up to a distance of a few tens of Mpc. Interestingly, Table II shows that the horizon distance of the signal increases, in most cases, as the amount of scalar field in the models becomes larger, to almost reach a factor two in model U13-c with respect to model U13.

The LIGO-Virgo-KAGRA (LVK) Collaboration has conducted various searches of continuous signals generated

by nonaxisymmetric neutron stars, including r-modes and other types of instabilities (see, e.g., [79] for the most recent search employing O3 data). The results reported in our work might be relevant for those studies. Taking our findings at face value the potential detection of such continuous signals in an unexpected range of frequencies could hint at the possible presence of dark matter in neutron stars. On the other hand, a lack of detections could also convey information about the composition and dynamics of such composite stars, since the frequencies of the gravitational-wave emission could be outside the LVK sensitivity range.

VI. CONCLUSIONS

We have investigated the effects ultralight bosonic field dark matter may have on the dynamics of unstable differentially rotating neutron stars prone to the bar-mode instability. We have found that the presence of the bosonic field can critically modify the development of the bar-mode instability of neutron stars, depending on the total mass of the bosonic field and on the boson particle mass. This, in turn, implies that dark-matter accretion in neutron stars could change the frequency of the expected gravitational-wave emission from the bar-mode instability, which would have an impact on ongoing searches for continuous gravitational waves. In this paper we have focused on ultralight bosonic dark matter but our results could be extrapolated to other dark matter models.

The kind of composite (fermion-boson) stars we have studied in this work remain an intriguing possibility. Dark matter can pile up in neutron stars, either by accretion during the life of the supernova progenitor star, by capture during the evolution of the neutron star itself, or both. A number of theoretical works have explored such scenarios in the context of fermion-boson stars (see, e.g., [45,46,52]). In the case dark matter is accreted before the formation of the neutron star, a similar ratio between the bosonic and fermionic components in all composite stars should be expected. On the other hand, if dark matter is captured during the neutron star evolution, older stars might have a higher bosonic contribution than younger ones. In this situation, one could expect that in BNS mergers the contribution of the bosonic field could be large enough to have an impact in the dynamics. Concerning rotation, highly differentially rotating composite stars might form as a result of the merger of two such fermion-boson stars [80], or of one neutron star with a boson star. Current simulations are, however, still unable to prove this as the latter are restricted to head-on collisions [81,82]).

Our results have been obtained from a large set of numerical simulations in general relativity of rotating neutron stars accreting an initial spherically symmetric bosonic field cloud, solving the Einstein-(complex, massive) Klein-Gordon-Euler and the Einstein-(complex) Proca-Euler systems. For our purely neutron star models

(no bosonic field) a bar-like deformation appears and we observe, as expected, the exponential growth of the Fourier density modes of the star, with the $m = 2$ mode being the dominant one. Incorporating the bosonic field leads to different dynamics and mode excitation, with the $m = 1$ becoming now the dominant mode. In some of our models, the accreting bosonic field can effectively quench the dominant $\ell = m = 2$ mode of the bar-deformation by dynamically forming a mixed (fermion-boson) star that retains part of the angular momentum of the original neutron star. Interestingly, the mixed star undergoes the development of a mixed bar that leads to significant gravitational-wave emission, substantially different to that of the isolated neutron star. The timescale of the instability is also affected by the presence of dark matter, being significantly delayed as the amount of bosonic field increases. We note, however, that our setup is such that the unstable neutron star accretes a large amount of bosonic field in a short period of time. It might be possible that in another region of the parameter space of the problem the bar-mode instability could actually be quenched without triggering the $m = 1$ deformation, e.g., for different neutron star models or further exploring different bosonic masses. It would also be interesting to perform evolutions of equilibrium sequences of stationary, rotating fermion-boson star models to address their stability in a more controlled system. Given the absence of such models presently, this is a task we defer for the future.

We have also found that the differences in the evolution of the composite stars due to the presence of the bosonic field are imprinted in the gravitational-wave emission. This was studied by computing the Newman-Penrose scalar Ψ_4 to evaluate the gravitational-wave frequency for our models. Those quantities are affected by the presence of the bosonic field, yielding complex gravitational-wave signals in which different modes contribute and leading, in particular, to a remarkable increase of the dominant frequency. The signals studied in this work are within reach of current ground-base detectors up to distances of about 1 Mpc. This increases to a few tens of Mpc for third-generation detectors as the ET. Therefore, the results reported might be of some interest for searches of continuous signals from neutron stars, routinely carried out by the LVK Collaboration in every scientific run. The potential detection of such continuous signals in an unexpected range of frequencies could hint at the possible presence of dark matter in neutron stars.

ACKNOWLEDGMENTS

Work supported by the Spanish Agencia Estatal de Investigación (PGC2018-095984-B-I00), by the Generalitat Valenciana (PROMETEO/2019/071 and GRISOLIAP/2019/029), by the Center for Research and Development in Mathematics and Applications (CIDMA) through the Portuguese Foundation for Science and Technology

(FCT—Fundação para a Ciência e a Tecnologia), references UIDB/04106/2020 and UIDP/04106/2020, by national funds (OE), through FCT, I.P., in the scope of the framework contract foreseen in the numbers 4, 5 and 6 of the article 23, of the Decree-Law 57/2016, of August 29, changed by Law 57/2017, of July 19 and by the Projects No. PTDC/FIS-OUT/28407/2017, No. CERN/FIS-PAR/0027/2019 and No. PTDC/FIS-AST/3041/2020, and by the European Union’s Horizon 2020 research and innovation (RISE) programme H2020-MSCA-RISE-2017 Grant No. FunFiCO-777740. N. S. G. acknowledges support by the Spanish Ministerio de Universidades, Reference No. UP2021-044, within the European Union-Next Generation EU. M. M. T. acknowledges support by the Spanish Ministry of Science, Innovation and Universities (Ministerio de Ciencia, Innovación y Universidades del Gobierno de España) through the FPU Ph.D. Grant No. FPU19/01750. D. G. acknowledges support by the Spanish Ministry of Science and Innovation and the Nacional Agency of Research (Ministerio de Ciencia y Innovación, Agencia Estatal de Investigación) through the Grant No. PRE2019-087617. Computations have been performed at the Servei d’Informàtica de la Universitat de València. The authors gratefully acknowledge the Italian Istituto Nazionale di Fisica Nucleare (INFN), the French Centre National de la Recherche Scientifique (CNRS) and the Netherlands Organization for Scientific Research, for the construction and operation of the Virgo detector and the creation and support of the EGO consortium. This manuscript has ET Preprint No. ET-0105A-22.

APPENDIX: COMPARISON BETWEEN XCFC AND Hydro_RNSID INITIAL DATA

The initial data for the evolutions reported in this work have been constructed using the numerical code introduced in [59] in polar spherical coordinates and assuming the conformal flatness condition for the Einstein equations. We developed a private *thorn*, which is a component of the *EinsteinToolkit* software, to read and linearly interpolate the initial data into the Cartesian grid used for the evolutions.

In this Appendix we show a brief comparison of the results obtained evolving the neutron star model U13 up to $t \approx 80$ ms, making use of our initial data *thorn* and *Hydro_RNSID* which is part of the official release of the *EinsteinToolkit*. The main dynamical features of the two evolutions are essentially identical, with the appearance of the bar-mode instability at around $t \approx 10$ ms. The main difference we observe is in the gravitational-wave emission, specifically in the $\ell = 2, m = 0$ component of Ψ_4 .

In Fig. 8 we compare the frequency spectrum obtained for model U13 using our *thorn* (left panels) and *Hydro_RNSID* (right panels). In the top plots, where we show only the frequencies up to $f_{\text{GW}} = 1500$, we can appreciate that the main peaks connected to the bar-mode instability and to the quasiradial oscillations are essentially the same with the

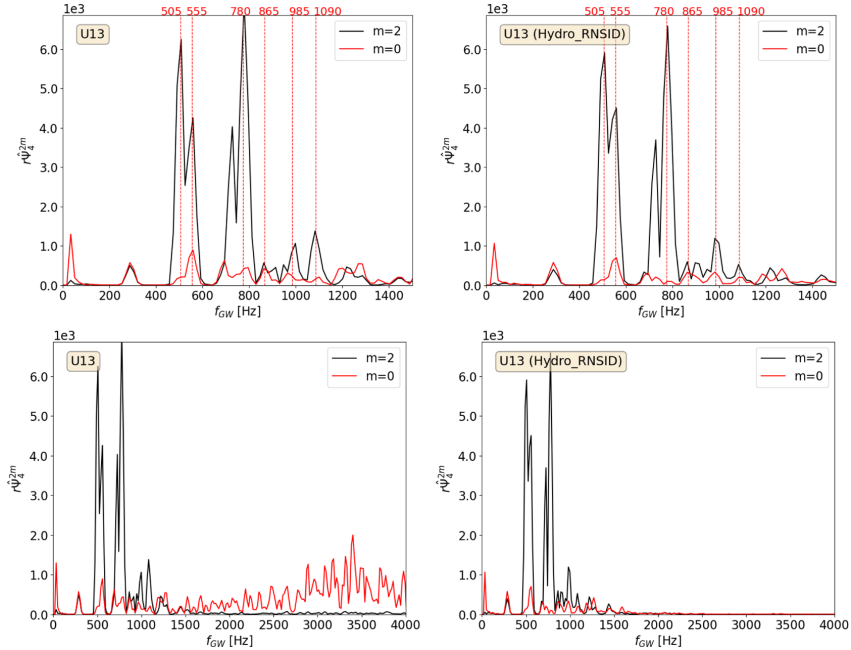


FIG. 8. Fourier transform of $r\Psi_4^{2,m}$ for $m = 0$ and $m = 2$ for model U13. The left panels correspond the evolutions performed using our CFC initial data code while the right panels are the ones using `Hydro_RNSID`. The frequency range in the top row extends up to 1500 Hz while in the bottom row it goes up to 4 kHz. The agreement between the two approaches, as seen in the top panels, is remarkable.

two approaches, validating the results obtained in this work. The frequency range of the bottom plots extends to 4 kHz. This is to highlight the presence of high-frequency noise in the $m = 0$ component of Ψ_4 when using the CFC initial data (left panel). This feature is not present if we use the `Hydro_RNSID` initial data (right panel). We suspect that the reasons behind this difference might be the poor interpolation into the Cartesian grid and the low resolution used in the angular coordinate of our initial data models, which is 5 times coarser than the one employed in

`Hydro_RNSID`. These two factors do not influence the evolutions in a significant way but they do induce a stronger initial perturbation on the CFC initial data which triggers stronger quasiradial oscillations in the star from the beginning of the simulation. This effect is visible in the gravitational-wave emission but was not evident from the time snapshots of the energy density on the equatorial plane. For this reason, as we write in the main text, we depict in Fig. 7 the evaluation of h_{char} without the contribution of the $m = 0$ mode at high frequencies.

-
- [1] K. Glampedakis and L. Gualtieri, *Astrophys. Space Sci. Libr.* **457**, 673 (2018).
 - [2] V. Paschalidis and N. Stergioulas, *Living Rev. Relativity* **20**, 7 (2017).
 - [3] M. Shibata, T. W. Baumgarte, and S. L. Shapiro, *Astrophys. J.* **542**, 453 (2000).
 - [4] L. Baiotti, R. de Pietri, G. M. Manca, and L. Rezzolla, *Phys. Rev. D* **75**, 044023 (2007).
 - [5] F. Löffler, R. De Pietri, A. Feo, F. Maione, and L. Franci, *Phys. Rev. D* **91**, 064057 (2015).
 - [6] M. Shibata, S. Karino, and Y. Eriguchi, *Mon. Not. R. Astron. Soc.* **334**, L27 (2002).
 - [7] A. L. Watts, N. Andersson, and D. I. Jones, *Astrophys. J.* **618**, L37 (2005).
 - [8] P. Cerdá-Durán, V. Quilis, and J. A. Font, *Comput. Phys. Commun.* **177**, 288 (2007).

- [9] G. Corvino, L. Rezzolla, S. Bernuzzi, R. De Pietri, and B. Giacomazzo, *Classical Quantum Gravity* **27**, 114104 (2010).
- [10] S. Yoshida and M. Saijo, *Mon. Not. R. Astron. Soc.* **466**, 600 (2017).
- [11] J. M. Centrella, K. C. B. New, L. L. Lowe, and J. D. Brown, *Astrophys. J. Lett.* **550**, L193 (2001).
- [12] M. Saijo and S. Yoshida, *Mon. Not. R. Astron. Soc.* **368**, 1429 (2006).
- [13] N. Sanchis-Gual, F. Di Giovanni, M. Zilhão, C. Herdeiro, P. Cerdá-Durán, J. Font, and E. Radu, *Phys. Rev. Lett.* **123**, 221101 (2019).
- [14] F. Di Giovanni, N. Sanchis-Gual, P. Cerdá-Durán, M. Zilhão, C. Herdeiro, J. A. Font, and E. Radu, *Phys. Rev. D* **102**, 124009 (2020).
- [15] D. J. Kaup, *Phys. Rev.* **172**, 1331 (1968).
- [16] R. Ruffini and S. Bonazzola, *Phys. Rev.* **187**, 1767 (1969).
- [17] R. Brito, V. Cardoso, C. A. Herdeiro, and E. Radu, *Phys. Lett. B* **752**, 291 (2016).
- [18] E. Seidel and W.-M. Suen, *Phys. Rev. Lett.* **72**, 2516 (1994).
- [19] F. Di Giovanni, N. Sanchis-Gual, C. A. R. Herdeiro, and J. A. Font, *Phys. Rev. D* **98**, 064044 (2018).
- [20] A. Arvanitaki, S. Dimopoulos, S. Dubovsky, N. Kaloper, and J. March-Russell, *Phys. Rev. D* **81**, 123530 (2010).
- [21] A. Arvanitaki and S. Dubovsky, *Phys. Rev. D* **83**, 044026 (2011).
- [22] F. F. Freitas, C. A. R. Herdeiro, A. P. Morais, A. Onofre, R. Pasechnik, E. Radu, N. Sanchis-Gual, and R. Santos, *J. Cosmol. Astropart. Phys.* **12** (2021) 047.
- [23] J. Calderón Bustillo, N. Sanchis-Gual, A. Torres-Forné, J. A. Font, A. Vajpeyi, R. Smith, C. Herdeiro, E. Radu, and S. H. W. Leong, *Phys. Rev. Lett.* **126**, 081101 (2021).
- [24] H. Olivares, Z. Younsi, C. M. Fromm, M. De Laurentis, O. Porth, Y. Mizuno, H. Falcke, M. Kramer, and L. Rezzolla, *Mon. Not. R. Astron. Soc.* **497**, 521 (2020).
- [25] C. A. Herdeiro, A. M. Pombo, E. Radu, P. V. Cunha, and N. Sanchis-Gual, *J. Cosmol. Astropart. Phys.* **04** (2021) 051.
- [26] M. Gleiser and R. Watkins, *Nucl. Phys.* **B319**, 733 (1989).
- [27] T. D. Lee and Y. Pang, *Nucl. Phys.* **B315**, 477 (1989).
- [28] E. Seidel and W.-M. Suen, *Phys. Rev. D* **42**, 384 (1990).
- [29] P. Jetzer, *Phys. Rep.* **220**, 163 (1992).
- [30] A. Escorihuela-Tomás, N. Sanchis-Gual, J. C. Degollado, and J. A. Font, *Phys. Rev. D* **96**, 024015 (2017).
- [31] N. Sanchis-Gual, C. Herdeiro, E. Radu, J. C. Degollado, and J. A. Font, *Phys. Rev. D* **95**, 104028 (2017).
- [32] S. L. Liebling and C. Palenzuela, *Living Rev. Relativity* **20**, 5 (2017).
- [33] M. Alcubierre, J. Barranco, A. Bernal, J. C. Degollado, A. Diez-Tejedor, M. Megevand, D. Nunez, and O. Sarbach, *Classical Quantum Gravity* **35**, 19LT01 (2018).
- [34] M. Alcubierre, J. Barranco, A. Bernal, J. C. Degollado, A. Diez-Tejedor, M. Megevand, D. Núñez, and O. Sarbach, *Classical Quantum Gravity* **36**, 215013 (2019).
- [35] V. Jaramillo, N. Sanchis-Gual, J. Barranco, A. Bernal, J. C. Degollado, C. Herdeiro, and D. Núñez, *Phys. Rev. D* **101**, 124020 (2020).
- [36] A. Bernal, J. Barranco, D. Alic, and C. Palenzuela, *Phys. Rev. D* **81**, 044031 (2010).
- [37] F. S. Guzmán and L. A. Ureña López, *Phys. Rev. D* **101**, 081302 (2020).
- [38] F. S. Guzmán, *Astron. Nachr.* **342**, 398 (2021).
- [39] N. Sanchis-Gual, F. Di Giovanni, C. Herdeiro, E. Radu, and J. A. Font, *Phys. Rev. Lett.* **126**, 241105 (2021).
- [40] N. Siemonsen and W. E. East, *Phys. Rev. D* **103**, 044022 (2021).
- [41] N. Sanchis-Gual, C. Herdeiro, and E. Radu, *Classical Quantum Gravity* **39**, 064001 (2022).
- [42] A. Henriques, A. R. Liddle, and R. Moorhouse, *Phys. Lett. B* **251**, 511 (1990).
- [43] P. Jetzer, *Phys. Lett. B* **243**, 36 (1990).
- [44] S. Valdez-Alvarado, C. Palenzuela, D. Alic, and L. A. Ureña-López, *Phys. Rev. D* **87**, 084040 (2013).
- [45] R. Brito, V. Cardoso, and H. Okawa, *Phys. Rev. Lett.* **115**, 111301 (2015).
- [46] R. Brito, V. Cardoso, C. F. Macedo, H. Okawa, and C. Palenzuela, *Phys. Rev. D* **93**, 044045 (2016).
- [47] S. Valdez-Alvarado, R. Becerril, and L. A. Ureña-López, *Phys. Rev. D* **102**, 064038 (2020).
- [48] F. Di Giovanni, N. Fakhry, N. Sanchis-Gual, J. C. Degollado, and J. A. Font, *Phys. Rev. D* **102**, 084063 (2020).
- [49] A. A. Roque and L. A. Ureña-López, *Classical Quantum Gravity* **39**, 044001 (2022).
- [50] B. Kain, *Phys. Rev. D* **104**, 043001 (2021).
- [51] N. Sanchis-Gual and P. Izquierdo, *Phys. Rev. D* **105**, 084023 (2022).
- [52] F. Di Giovanni, N. Sanchis-Gual, P. Cerdá-Durán, and J. A. Font, *Phys. Rev. D* **105**, 063005 (2022).
- [53] T. Nakamura, K. Oohara, and Y. Kojima, *Prog. Theor. Phys. Suppl.* **90**, 1 (1987).
- [54] M. Shibata and T. Nakamura, *Phys. Rev. D* **52**, 5428 (1995).
- [55] T. W. Baumgarte and S. L. Shapiro, *Phys. Rev. D* **59**, 024007 (1998).
- [56] H. Okawa, H. Witek, and V. Cardoso, *Phys. Rev. D* **89**, 104032 (2014).
- [57] M. Zilhão, H. Witek, and V. Cardoso, *Classical Quantum Gravity* **32**, 234003 (2015).
- [58] N. Stergioulas and J. L. Friedmann, *Astrophys. J.* **444**, 306 (1995).
- [59] I. Cordero-Carrion, P. Cerda-Duran, H. Dimmelmeier, J. L. Jaramillo, J. Novak, E. Bentevegna, T. Bode, P. Diener *et al.*, *Phys. Rev. D* **79**, 024017 (2009).
- [60] M. Babiuc-Hamilton *et al.*, The EinsteinToolkit (2019), to find out more, visit <http://einstein toolkit.org>.
- [61] F. Löffler, J. Faber, E. Bentevegna, T. Bode, P. Diener *et al.*, *Classical Quantum Gravity* **29**, 115001 (2012).
- [62] M. Zilhão and F. Löffler, *Int. J. Mod. Phys. A* **28**, 1340014 (2013).
- [63] E. Schnetter, S. H. Hawley, and I. Hawke, *Classical Quantum Gravity* **21**, 1465 (2004).
- [64] Carpet, <http://www.carpetcode.org/>, Carpet: Adaptive Mesh Refinement for the Cactus Framework.
- [65] C. Reisswig, C. D. Ott, U. Sperhake, and E. Schnetter, *Phys. Rev. D* **83**, 064008 (2011).
- [66] D. Brown, P. Diener, O. Sarbach, E. Schnetter, and M. Tiglio, *Phys. Rev. D* **79**, 044023 (2009).
- [67] N. Sanchis-Gual, C. Herdeiro, J. A. Font, E. Radu, and F. Di Giovanni, *Phys. Rev. D* **99**, 024017 (2019).

- [68] H. Witek, M. Zilhao, G. Ficarra, and M. Elley, Canuda: A public numerical relativity library to probe fundamental physics (Zenodo, 2020), [10.5281/zenodo.3565474](https://doi.org/10.5281/zenodo.3565474).
- [69] C. A. R. Herdeiro, A. M. Pombo, and E. Radu, *Phys. Lett. B* **773**, 654 (2017).
- [70] H. Dimmelmeier, N. Stergioulas, and J. A. Font, *Mon. Not. R. Astron. Soc.* **368**, 1609 (2006).
- [71] L. Landau and E. Lifshitz, *Mechanics* (Pergamon Press, Oxford, 1976).
- [72] O. Zanotti, J. A. Font, L. Rezzolla, and P. J. Montero, *Mon. Not. R. Astron. Soc.* **356**, 1371 (2005).
- [73] P. J. Montero, O. Zanotti, J. A. Font, and L. Rezzolla, *Mon. Not. R. Astron. Soc.* **378**, 1101 (2007).
- [74] The LIGO Scientific Collaboration *et al.*, *Classical Quantum Gravity* **32**, 074001 (2015).
- [75] F. Acernese *et al.*, *Classical Quantum Gravity* **32**, 024001 (2015).
- [76] K. Somiya, *Classical Quantum Gravity* **29**, 124007 (2012).
- [77] S. Hild *et al.*, *Classical Quantum Gravity* **28**, 094013 (2011).
- [78] É. É. Flanagan and S. A. Hughes, *Phys. Rev. D* **57**, 4535 (1998).
- [79] R. Abbott *et al.* (LIGO Scientific Collaboration, and Virgo Collaboration), *Phys. Rev. D* **104**, 082004 (2021).
- [80] M. Bezares, D. Viganò, and C. Palenzuela, *Phys. Rev. D* **100**, 044049 (2019).
- [81] K. Clough, T. Dietrich, and J. C. Niemeyer, *Phys. Rev. D* **98**, 083020 (2018).
- [82] T. Dietrich, F. Day, K. Clough, M. Coughlin, and J. Niemeyer, *Mon. Not. R. Astron. Soc.* **483**, 908 (2019).

Fermion-axion stars: static solutions and dynamical stability

Fabrizio Di Giovanni,¹ Davide Guerra,¹ Simone Albanesi,^{2,3} Miquel Miravet-Tenés,¹ and Dimitra Tseneklidou⁴

¹*Departamento de Astronomía y Astrofísica, Universitat de València,
Dr. Moliner 50, 46100, Burjassot (València), Spain*

²*Dipartimento di Fisica, Università di Torino, via P. Giuria 1, 10125 Torino, Italy*

³*INFN Sezione di Torino, Via P. Giuria 1, 10125 Torino, Italy*

⁴*Theoretical Astrophysics, IAT, Eberhard-Karls University of Tübingen, 72076 Tübingen, Germany*

We construct spherically-symmetric static solutions of the Einstein-Klein-Gordon-Euler system involving a complex scalar field governed by a periodic potential which emerges in models of axion-like particles, and fermionic matter modeled by a perfect fluid with a polytropic equation of state. Such solutions describe gravitationally bound composites of fermions and axions which we dub as fermion-axion stars. Sequences of pure axion-stars in the existence domain may show the presence of multiple stable branches depending on the value of the decay constant parameter in the potential; this reflects in the appearance of multiple islands of stability in the 2-dimensional parameter space of fermion-axion configurations. We investigate the domain of existence for three different values of the decay constant, identifying one or more regions of linear stability making use of a method we already employed in previous works. We confirm the results from the linear analysis performing fully non-linear numerical relativity evolutions. In this context we perform several numerical simulations to identify regions in the parameter space where unstable models face different fates: the collapse to a Schwarzschild black hole, the migration to a stable model and finally the dispersion of the scalar field together with the dilution of the fermionic matter, which approaches a static fermion star model with very low mass. This latter scenario was never observed in previous models without the periodic potential.

PACS numbers: 95.30.Sf, 04.70.Bw, 04.40.Nr, 04.25.dg

I. INTRODUCTION

Unveiling the nature of dark matter (DM) is one of the fundamental challenges in modern cosmology. Its existence finds support from a wide set of observational results, such as the measurements of galaxy rotation curves, gravitational lensing and the cosmic microwave background [1–8]. Several candidates have been proposed as constituents of DM, including macroscopic objects like primordial black holes [9–12] and a zoo of hypothetical particles which are considered to lack electromagnetic interactions with baryonic matter, thus being invisible through electromagnetic observations. Among the most compelling particle DM candidates there is the axion, a pseudo-scalar (boson) particle which was introduced in order to solve the strong CP problem by Peccei and Quinn [13], but that could play a role in cosmology [14–17]. Ultralight axion-like fields naturally arise also from string theory compactifications [18, 19], serving as another theoretical prediction of their existence. Motivated by these theoretical studies, various experiments have been proposed or are currently ongoing to search for this family of particles in a wide mass range [20–22].

Bosonic particles can clump together to form localized and coherently oscillating equilibrium configurations which resemble Bose-Einstein condensates [23, 24]. These compact objects are known in the literature as boson stars [25], and they may have astrophysically relevant masses when the mass of the bosons is lower than 10^{-11} eV. Since the pioneer works of Kaup [26] and Ruffini and Bonazzola [27], their characterization has

been broadened including different potentials such as the self-interaction [28], the solitonic [29], the KKLS [30, 31] and the axionic potentials [32], including charge [33], rotation [34, 35], oscillating solitonic stars [36], multi-field boson stars [37–39], or even vector field (Proca stars [40]). The interested reader is addressed to the reviews found in references [41, 42]. The dynamics of these configurations have been extensively studied with full non-linear numerical relativity simulations [43–47]; their stability properties have been investigated in [48–50], and a formation mechanism called gravitational cooling has been proposed in [51] by Seidel and Suen, and in [52, 53] in the Newtonian limit, and has been extended to the vector field case in [54]. All these studies confirmed the dynamical robustness of scalar-field stellar systems.

In this work we consider the novel class of boson stars firstly studied in the relativistic regime by [32]. The scalar field is governed by a periodic potential inspired by that of the QCD axion, which depends on two independent parameters, the axion mass μ and the decay constant f_a . If such axion-like particles exist and they could form such compact objects, it is natural to assume that objects made out of a mixture of axions and fermions might also exist in the Universe, either considering the formation from a primordial gas comprised of axions and fermions, or by the dynamical capture of axionic or fermionic particles by an already formed neutron or axion star. Macroscopic composites of fermion and bosons are known in the literature as fermion-boson stars [55–59]. The presence of bosonic matter in fermion stars can modify their physical properties and potentially be observed as discussed in [60, 61] for neutron stars (NSs)

and in [62] for white dwarfs. Gravitational-wave emission from orbital mergers of fermion-boson stars have also been analyzed in [63]. Here we will investigate the properties of macroscopic objects made of fermions and axions which we dub as fermion-axion stars. We point out that we consider a complex scalar field for our models, while in most of their applications, from fundamental physics to cosmology, axion-like particles are considered to be real fields. Real fields in astrophysics can play a role as quasi-stationary solutions dubbed oscillatons, which have similar physical properties, but differ from the complex case especially in the relativistic regime. Studying these configurations is out of the scope of this work, in which we focus on the stationary solutions made of complex axion-like particles.

We construct equilibrium configurations of fermion-axion stars and explore different possible values of the axion decay constant assessing their stability properties both in the linear regime and through fully non-linear numerical relativity simulations. Linear stability analysis can be carried out studying the radial perturbation of the equilibrium configurations and evaluating the modes in the linearized equations, as in [64] for fermion stars and in [33, 49, 50] for boson stars. The linear perturbation analysis has not yet been applied to fermion-boson stars, but the linear stability has been studied in previous works [56, 60, 65, 66] using a variation of the method developed by Henriques et al. [55, 67] which consists in evaluating the gravitational mass and the number of bosonic and fermionic particle as functions of the two free parameters searching for critical points for these three physical quantities in the 2-dimensional parameter space. In this work we employ this method for fermion-axion models, and confirm the results of the linear analysis through non-linear numerical evolutions, and we present a detailed study of the different fates of the unstable models, identifying the regions in the parameter space where models collapse to black holes (BHs) or migrate to a stable configuration or face the dispersion of the scalar field leaving a very low-mass fermion star remnant.

The paper is organized as follows. In section II we present the basic equations employed to obtain the evolution equations and the matter source terms. Section III addresses the construction of the static configurations and in section IV we briefly describe the linear analysis method and we present two sequences of equilibrium models and illustrate how the critical points are found. The numerical framework for the evolutions is described in section V, and the results are presented in section VI. Finally we report the conclusions and final remarks in section VII. We employ units such that the relevant fundamental constants are equal to one ($G = c = M_{\odot} = 1$). For details on how to recover the physical units for radius and time we address the reader to our previous work [66].

II. FORMALISM

Models of mixed stars, where fermionic and bosonic matter coexist and interact only through gravity, can be characterised by a total stress-energy tensor which is the sum of two independent contributions, one from a perfect fluid and one from a complex scalar field, in the form

$$T_{\mu\nu} = T_{\mu\nu}^{\text{fluid}} + T_{\mu\nu}^{\phi}, \quad (1)$$

$$T_{\mu\nu}^{\text{fluid}} = [\rho(1 + \epsilon) + P]u_{\mu}u_{\nu} + Pg_{\mu\nu}, \quad (2)$$

$$T_{\mu\nu}^{\phi} = -g_{\mu\nu}\partial_{\alpha}\bar{\phi}\partial^{\alpha}\phi - g_{\mu\nu}V(|\phi|) + (\partial_{\mu}\bar{\phi}\partial_{\nu}\phi + \partial_{\mu}\phi\partial_{\nu}\bar{\phi}). \quad (3)$$

The perfect fluid is defined by its rest-mass density ρ , its pressure P , its internal energy ϵ and its four-velocity u^{μ} . The complex scalar field is specified by its potential $V(|\phi|)$, which we choose in this work to be

$$V(|\phi|) = \frac{2\mu^2 f_a^2}{B} \left(1 - \sqrt{1 - 4B \sin^2 \left(\frac{|\phi|}{2f_a} \right)} \right), \quad (4)$$

where $B = \frac{z}{z+1} \approx 0.22$ is a constant and $z = m_u/m_d \approx 0.48$ is the mass ratio between up and down quarks (see [68]). The two independent parameters μ and f_a represent the particle mass and the decay constant respectively. The bar in the previous equations denotes complex conjugation. The system of equations governing the dynamics is given by the Einstein equations $G_{\mu\nu} = 8\pi T_{\mu\nu}$, by the conservation laws of the fermionic stress-energy tensor and of the baryonic mass

$$\nabla_{\mu} T_{\text{fluid}}^{\mu\nu} = 0, \quad (5)$$

$$\nabla_{\mu} (\rho u^{\mu}) = 0, \quad (6)$$

and by the Klein-Gordon equation

$$\nabla_{\mu}\nabla^{\mu}\phi = U(\phi)\phi \quad (7)$$

for the complex scalar field. In the previous equations the symbol ∇ represents the covariant derivative with respect to the 4-metric $g_{\mu\nu}$, and $U(\phi) = \frac{\partial V(\phi)}{\partial |\phi|^2}$. The system is closed by a suitable choice of an equation of state (EoS) for the fluid, which relates the pressure with the rest-mass density and the internal energy. In this work we consider a polytropic EoS for the equilibrium configurations, and an ideal fluid EoS for the evolutions to take into account possible shock-heating effects, yielding

$$P = K\rho^{\Gamma} = (\Gamma - 1)\rho\epsilon. \quad (8)$$

where we fix the parameters $K = 100$ and $\Gamma = 2$.

Our framework for the evolutions is based on a numerical code [69] which employs a spherically-symmetric metric in isotropic coordinates

$$ds^2 = -\alpha^2 dt^2 + \psi^4 \gamma_{ij} (dx^i + \beta^i dt)(dx^j + \beta^j dt), \quad (9)$$

where $x^i = \{r, \theta, \varphi\}$ are the spherical coordinates, α and β^i are the lapse function and the shift vector respectively, $\psi = e^{4\chi}$ is the conformal factor, and γ_{ij} is the spatial metric, which takes the form

$$\gamma_{ij} dx^i dx^j = a(r) dr^2 + b(r) r^2 (d\theta^2 + \sin^2 \theta d\varphi^2), \quad (10)$$

which depends on two generic functions $a(r)$ and $b(r)$.

We employ the Baumgarte-Shapiro-Shibata-Nakamura (BSSN) formulation of Einstein's equations [70–72], in its covariant formulation introduced by Brown [73, 74]. In this formalism, the evolved quantities are the spatial metric γ_{ij} , the conformal factor χ , the trace of the extrinsic curvature K , its traceless part $A_a = A_r^r$, $A_b = A_\theta^\theta = A_\varphi^\varphi$, and the radial component of the so-called conformal connection functions Δ^r (see [71, 72] for definitions). In our simulations we employ the “non-advective 1+log” gauge condition for the lapse function α and a variation of the Gamma-driver condition for the shift vector β^r . The interested reader is addressed to [69] for further details regarding the BSSN evolution equations, gauge conditions, and the formalism for the hydrodynamic equations of our numerical code.

Even if we do not report here the entire system of equations, we remind the reader that they involve matter source terms emerging from suitable projections of the stress-energy tensor onto the spatial metric, namely

$$\mathcal{E} = n^\mu n^\nu T_{\mu\nu}, \quad (11)$$

$$j_i = -\gamma_i^\mu n^\nu T_{\mu\nu}, \quad (12)$$

$$S_{ij} = \gamma_i^\mu \gamma_j^\nu T_{\mu\nu}, \quad (13)$$

where $\gamma_\nu^\mu = \delta_\nu^\mu + n^\mu n_\nu$ are the projection operators on the spatial hypersurfaces, n_μ is the unit normal vector, and δ_ν^μ is the Kronecker delta.

In the case of fermion-axion stars, we can evaluate the contribution to the matter source terms from the fluid and from the scalar field separately. The perfect fluid matter source terms read

$$\mathcal{E}^{\text{fluid}} = [\rho(1 + \epsilon) + P] W^2 - P, \quad (14)$$

$$j_r^{\text{fluid}} = e^{4\chi} a [\rho(1 + \epsilon) + P] W^2 v^r, \quad (15)$$

$$S_a^{\text{fluid}} = e^{4\chi} a [\rho(1 + \epsilon) + P] W^2 v^r + P, \quad (16)$$

$$S_b^{\text{fluid}} = P, \quad (17)$$

where $S_a = S_r^r$ and $S_b = S_\theta^\theta = S_\varphi^\varphi$, $W = \alpha u^t$ is the Lorentz factor and v^r is the radial component of the fluid 3-velocity. Following the work [75] we introduce two auxiliary variables

$$\Pi = \frac{1}{\alpha} (\partial_t - \beta^r \partial_r) \phi, \quad (18)$$

$$\Psi = \partial_r \phi. \quad (19)$$

In this formalism the bosonic contribution to the source

terms takes the form

$$\mathcal{E}^\phi = \left(\bar{\Pi} \Pi + \frac{\bar{\Psi} \Psi}{e^{4\chi} a} \right) + V(|\phi|) \quad (20)$$

$$j_r^\phi = -(\bar{\Pi} \Psi + \bar{\Psi} \Pi), \quad (21)$$

$$S_a^\phi = \left(\bar{\Pi} \Pi + \frac{\bar{\Psi} \Psi}{e^{4\chi} a} \right) - V(|\phi|) \quad (22)$$

$$S_b^\phi = \left(\bar{\Pi} \Pi - \frac{\bar{\Psi} \Psi}{e^{4\chi} a} \right) - V(|\phi|), \quad (23)$$

and the Klein-Gordon equation (7) is now recast as a first-order system of linear equations, which reads

$$\partial_t \phi = \beta^r \partial_r \phi + \alpha \Pi, \quad (24)$$

$$\partial_t \Pi = \beta^r \partial_r \Pi + \frac{\alpha}{ae^{4\chi}} \left[\partial_r \Psi + \Psi \left(\frac{2}{r} - \frac{\partial_r a}{2a} + \frac{\partial_r b}{b} + 2\partial_r \chi \right) \right] + \frac{\Psi}{ae^{4\chi}} + \alpha K \Pi - \alpha U(\phi), \quad (25)$$

$$\partial_t \Psi = \beta^r \partial_r \Psi + \Psi \partial_r \beta^r + \partial_r (\alpha \Pi). \quad (26)$$

Finally we report here the elliptic sector of Einstein equations, which provides a set of constraint equations, namely the Hamiltonian constraint and the momentum constraint, which read as

$$\mathcal{H} = R - (A_a^2 + 2A_b^2) + \frac{2}{3} K^2 - 16\pi \mathcal{E} = 0, \quad (27)$$

$$\mathcal{M}_r = \partial_r A_a - \frac{2}{3} \partial_r K + 6A_a \partial_r \chi + (A_a - A_b) \left(\frac{2}{r} + \frac{\partial_r b}{b} \right) - 8\pi j_r = 0, \quad (28)$$

where R is the Ricci scalar.

III. INITIAL DATA

To perform numerical evolutions, a mandatory step is to construct initial data that solve the constraint equations (27) and (28) to obtain the physical solutions of Einstein equations. In this context, we employ a spherically-symmetric metric in Schwarzschild coordinates

$$ds^2 = -\alpha(r)^2 dt^2 + \tilde{a}(r)^2 dr^2 + r^2 (d\theta^2 + \sin^2 \theta d\varphi^2), \quad (29)$$

where $\tilde{a}(r)$ and $\alpha(r)$ are two geometrical functions; for simplicity we use the same symbol r for the radial coordinate, even though this is now a different coordinate than the one appearing in (9). The bosonic field is assumed to have an harmonic time dependence $\phi(t, r) = \phi(r) e^{-i\omega t}$ where ω is its eigenfrequency. Assuming a static fluid, $u^\mu = (-1/\alpha, 0, 0, 0)$, Einstein's equations can be recast as ordinary differential equations (ODEs) which read

$$\frac{d\tilde{a}}{dr} = \frac{\tilde{a}}{2} \left(\frac{1 - \tilde{a}^2}{r} + 8\pi r \left[\frac{\omega^2 \tilde{a}^2 \phi^2}{\alpha^2} + \tilde{a}^2 V(|\phi|) + \Psi^2 + \tilde{a}^2 \rho(1 + \epsilon) \right] \right), \quad (30)$$

$$\frac{d\alpha}{dr} = \frac{\alpha}{2} \left(\frac{\tilde{a}^2 - 1}{r} + 8\pi r \left[\frac{\omega^2 \tilde{a}^2 \phi^2}{\alpha^2} - \tilde{a}^2 V(|\phi|) + \Psi^2 + \tilde{a}^2 P \right] \right), \quad (31)$$

$$\frac{d\phi}{dr} = \Psi, \quad (32)$$

$$\frac{d\Psi}{dr} = - \left[1 + \tilde{a}^2 - 8\pi r^2 \tilde{a}^2 \left(V(|\phi|) + \frac{1}{2}(\rho(1 + \epsilon) - P) \right) \right] \frac{\Psi}{r} - \frac{\omega^2 \tilde{a}^2 \phi^2}{\alpha^2} - \tilde{a}^2 U(|\phi|) \phi, \quad (33)$$

$$\frac{dP}{dr} = -[\rho(1 + \epsilon) + P] \frac{\alpha'}{\alpha}, \quad (34)$$

where the prime indicates the derivative with respect to r . This system is closed by the EoS as in equation 8.

To construct suitable equilibrium configurations we solve the ODE system with a 4th-order Runge-Kutta method, applying appropriate boundary conditions. Each numerical solution is characterised by the central values of the rest-mass density ρ_0 and of the scalar field ϕ_0 . We then require the metric functions to be regular at the origin, and we apply Schwarzschild outer boundary conditions. Finally we require that the scalar field vanishes at $r \rightarrow \infty$, and this condition can be fulfilled by evaluating the correct value of the eigenfrequency ω ; to achieve this, we make use of a two-parameter shooting method. To summarize, the set of boundary conditions that we apply are

$$\begin{aligned} \tilde{a}(0) &= 1, & \phi(0) &= \phi_c, \\ \alpha(0) &= 1, & \lim_{r \rightarrow \infty} \alpha(r) &= \lim_{r \rightarrow \infty} \frac{1}{\tilde{a}(r)}, \\ \Psi(0) &= 0, & \lim_{r \rightarrow \infty} \phi(r) &= 0, \\ \rho(0) &= \rho_c, & P(0) &= K \rho_c^\Gamma. \end{aligned} \quad (35)$$

We evaluate the total gravitational mass for each model as

$$M_T = \lim_{r \rightarrow \infty} \frac{r}{2} \left(1 - \frac{1}{\tilde{a}^2} \right), \quad (36)$$

which corresponds to the Arnowitt-Deser-Misner (ADM) mass at infinity.

IV. LINEAR STABILITY

In the previous section we have illustrated how to construct static solutions of fermion-axion stars. Once we have populated the parameter space with models, a natural question that arises is whether we can delineate the

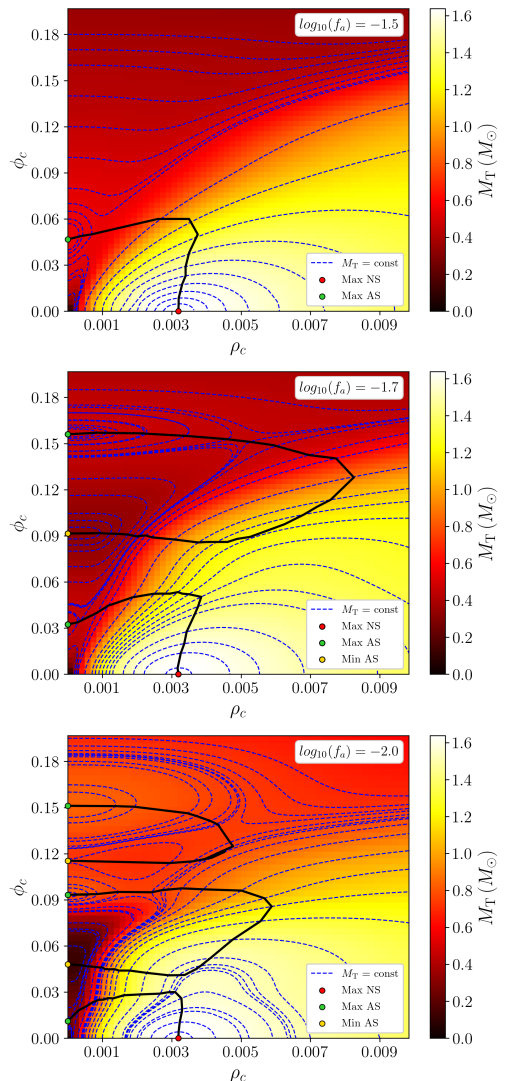


FIG. 1: Equilibrium configurations of fermion-axion stars for $\log_{10}(f_a) = -1.5$ (top), $\log_{10}(f_a) = -1.7$ (middle), and $\log_{10}(f_a) = -2.0$ (bottom). Dashed lines correspond to models with the same total mass M_T . The black solid line depicts the boundary between stable and unstable models.

boundary between the stable and unstable regions in phase space. In this section we explain how to determine the linear stability of these solutions.

Identifying the stable and unstable branches for single-fluid systems like fermion stars and boson stars is straightforward, as this transition occurs at the equilibrium configuration with the largest mass, which is called

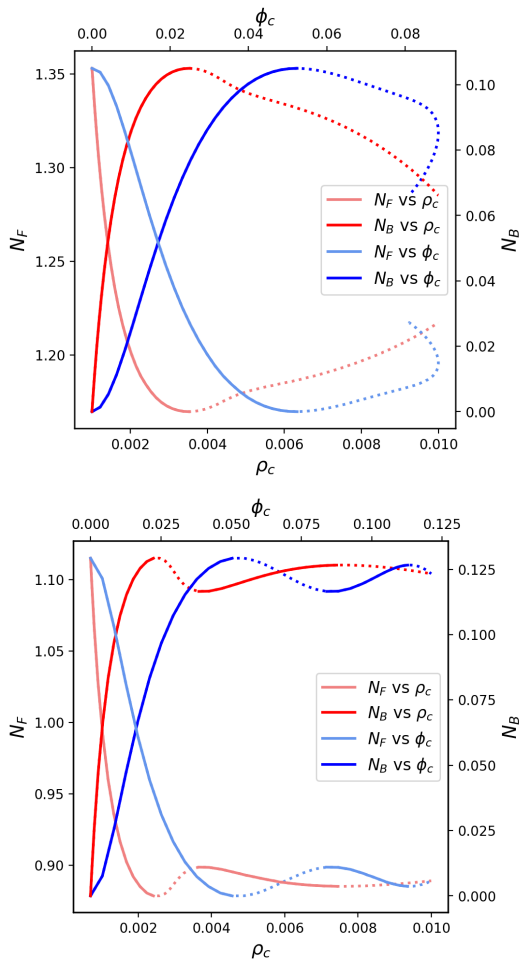


FIG. 2: Number of fermions N_F and bosons N_B for the equilibrium configurations of equal mass $M_T = 1.27$ (top plot) and $M_T = 1.06$ (bottom plot), varying the value of ϕ_c and ρ_c . The solid lines indicates the stable branches, while the dashed line the unstable ones.

the critical point. One method for computing the critical point is to consider an harmonic perturbation around each field static value and solve the linearized system of equations. This has been done for boson stars [48–50, 76], fermion stars [64] and dark matter admixed NSs with fermionic dark matter [77, 78]. We are not aware of such a study for fermion-boson or fermion-axion stars.

In the case of mixed systems, as we have a 2-dimensional space of parameters, the boundary between stable and unstable regions is not a point but it is a curve, called the critical curve. An alternative and sim-

pler method to identify the critical curve for fermion-boson stars has been proposed by [55]. Critical curves identify the transition from linearly stable and unstable with respect to perturbations which conserve mass and particle number, and hence fulfill the conditions

$$\begin{aligned} \left. \frac{\partial N_B}{\partial \rho_c} \right|_{M=\text{constant}} &= \left. \frac{\partial N_F}{\partial \rho_c} \right|_{M=\text{constant}} = 0, \\ \left. \frac{\partial N_B}{\partial \phi_c} \right|_{M=\text{constant}} &= \left. \frac{\partial N_F}{\partial \phi_c} \right|_{M=\text{constant}} = 0, \end{aligned} \quad (37)$$

where N_B and N_F are the number of bosonic particles and of fluid elements respectively. These quantities are associated with the conserved Noether charge related to the invariance under global $U(1)$ transformations $\phi \rightarrow \phi e^{i\delta}$ and with the conservation of the baryonic number respectively, and they can be evaluated by integrating their volume densities as follows

$$N_B = 4\pi \int \frac{\tilde{a}\omega\phi^2 r^2}{\alpha} dr, \quad N_F = 4\pi \int \tilde{a}pr^2 dr. \quad (38)$$

To solve (37) for the critical curve, we follow the same procedure already presented in previous works [56, 65, 66]. We construct many contour lines with equal mass M_T which populate the parameter space; we then move along each single line and we determine the point at which N_B and N_F present a critical value, meaning a change of the sign of their derivative with respect to the parameters ρ_c and ϕ_c . To automatize this procedure, we have developed a numerical code which can generate contour lines in the parameter space for fermion-boson stars, which details are briefly discussed in appendix A. This numerical code is publicly available¹.

In Fig 1 we depict with a colormap the total gravitational mass as a function of the two parameters characterizing the models $M_T(\rho_0, \phi_0)$ for 3 different values of the decay constant $\log_{10}(f_a) = \{-1.5, -1.7, -2.0\}$, which show one, two, and three stable branches for axion stars respectively. On top of that, we show many contour lines of equal mass in dashed blue, and we construct with the method described in the previous paragraph the black solid line which is the boundary between the stable and unstable regions. Depending on the value of f_a the existence line for axion stars present one or more critical points, outlining one or more stable branches [32]. We expected that the presence of more stable branches gives rise to different islands of stability for the fermion-axion configurations, and our results confirm this prediction. In the middle plot of figure 1 we observe a secondary region of linear stability that starts from the critical points of the axion star models, the minimum at $\phi_c = 0.092$ and second maximum at $\phi_c = 0.157$, and interestingly it extends up to around $\rho_c = 0.008$ which is fairly higher

¹ See the git repository at <https://github.com/SimoneA96/fermion-axion-pywrap>

than the value of the critical point for isolated NS which is around $\rho = 0.0031$. Therefore we could reach stable neutron stars with extremely dense interiors due to the presence of axion particles, with interesting implications for the properties of dense matter. In the bottom plot we observe the appearance of a third island of stability corresponding to the third stable branch in the pure axion star existence plot.

We now focus on two illustrative examples of sequences of equilibrium models with $\log_{10}(f_a) = -1.7$ with masses $M_T = 1.27$ and $M_T = 1.06$ which start from a purely fermionic star; in figure 2 we depict the number of bosons N_B and fermions N_F of these two sequences as functions of ϕ_c and ρ_c . In the first case (top plot) we can identify only one critical point in the curve, corresponding to a maximum of N_B and a minimum of N_F at the values of $\rho_c = 0.00352$ and $\phi_c = 0.052$; this contour curve in fact only crosses the boundary of the primary stability region. All the models on the left of the critical point lie in the stable region (solid line), and the ones on the right (dashed line) are unstable. The second case with $M_T = 1.06$ (bottom plot) instead presents two stable branches, which correspond to the intervals in which N_B (N_F) increases (decreases); this equal-mass curve crosses the primary stable region at the first maximum (minimum) of N_B (N_F), then crosses the secondary stable region in the minimum (maximum) and second maximum (minimum) of N_B (N_F). Sequences of equilibrium configurations which start from a purely fermion star have the feature that the number of fermions N_F firstly decreases up to the critical point and the number of bosons N_B increases; sequences starting with a pure axion star shows the opposite trend.

V. SETUP FOR EVOLUTIONS

To confirm the study of the linear stability in the non-linear regime we perform numerical evolutions of the Einstein-Klein-Gordon-Euler system described in section II, with the spherically symmetric numerical code developed by [69], upgraded with the evolution equations and the matter source terms of the complex scalar field by [79], where the authors showed a second order convergence. We have extensively tested and used this numerical framework in past works (see e.g. [75, 80–83]). We further test our numerical code, evolving the configurations in table I using three different resolutions and confirming that the results on the dynamical fate of the models shown in this work do not depend on the resolution (see Appendix B). The numerical code solves the Einstein equations in spherical isotropic coordinates, making use of a Partially Implicit Runge-Kutta (PIRK) method, developed in [84, 85], to treat and handle the numerical instabilities coming from the terms in the equations that carry the typical $\frac{1}{r}$ singularities. We employ a non-equally spaced numerical grid firstly introduced in [80], which covers the computational domain with two differ-

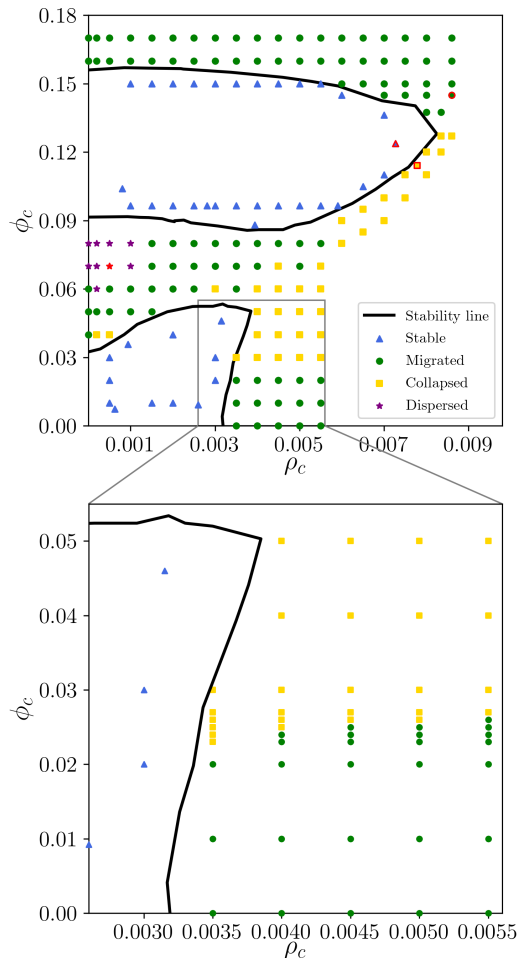


FIG. 3: The thick black curve is the same critical curve as in middle panel of figure 1 for $\log_{10}(f_a) = -1.7$. The blue triangles are linearly stable models that we evolved, the green dots are unstable models that migrates to the stable region, the yellow squares are unstable models which collapse to a BH, and the violet stars are models which show the dispersion of the scalar field. We highlight with a red outline the models whose physical properties are summarized in table I. Bottom plot is a zoom of the region close to the unstable branch of pure NSs.

ent patches, a geometrical progression up to a certain radius and an hyperbolic cosine outside from it. This allows us to move the outer boundaries far away from the origin, and hence prevent the effects of reflections for longer computational time.

In our simulations we consider a minimal resolution of $\Delta r = 0.0125$, and a Courant-Friedrichs-Lewy factor of

TABLE I: Static fermion-axion star models with decay constant $\log_{10}(f_a) = -1.7$. From left to right the columns indicate the model name, its fate, the central value of the scalar field ϕ_c and of the rest-mass density ρ_c , the field frequency obtained with the shooting method ω_{shoot} , the normalized frequency ω , the total Misner-Sharp mass M_T , the number of bosons to fermions ratio N_B/N_F , the number of bosons N_B , the radius containing 99% of bosons, fermions and total particles, R_B , R_F , R_T , respectively. We used the Schwarzschild coordinates to evaluate the radii.

Model	Fate	ϕ_c	ρ_c	ω_{shoot}	ω	M_T	N_B/N_F	N_B	R_B	R_F	R_T
MS1	Stable	1.24×10^{-1}	7.27×10^{-3}	1.521	0.617	0.861	0.246	0.152	3.19	5.95	5.86
MS2	Collapsing	1.11×10^{-1}	7.78×10^{-3}	1.485	0.885	1.060	0.143	0.127	3.26	6.24	6.18
MS3	Migrating	1.45×10^{-1}	8.62×10^{-3}	1.741	0.550	0.595	0.670	0.181	3.00	4.51	4.36
MS4	Dispersing	7.00×10^{-2}	5.00×10^{-4}	1.167	0.882	0.369	41.50	0.181	7.31	1.79	7.41

$\frac{\Delta t}{\Delta r} = 0.3$. The grid is shifted by $\Delta r/2$ to avoid the origin, meaning that our inner boundary is set at $r_{\text{min}} = \frac{\Delta r}{2}$, while we set the outer boundary at $r_{\text{max}} = 6000$. We adopt a 4-th order Kreiss-Oliger numerical dissipation to our evolution equations to damp out high-frequencies modes. We employ an upwind scheme to treat the advection terms, and we impose radiative boundary conditions.

VI. NUMERICAL EVOLUTIONS

In this section we intend to verify if the regions of linear stability that we outlined in section III are populated by models which are also stable in the non-linear regime. To achieve this goal we perform numerical evolutions of the full non-linear Einstein-Euler-Klein-Gordon system, and we consider the equilibrium configurations to be weakly perturbed by the numerical truncation errors introduced by the discretization of the otherwise continuous differential equations. We expect that for stable mixed stars the fermionic density ρ and the absolute value of the scalar field $|\phi|$ oscillate slightly around their initial values, while the scalar field itself oscillate at its eigenfrequency ω .

For unstable models, however, even the small perturbation induced by the numerical discretization is expected to grow, and eventually the fate of these models can be of three types: the migration to a stable configuration, the gravitational collapse to a Schwarzschild BH or the total dispersion of the bosonic particles.

We perform numerical evolutions of several stable and unstable models for the three values of the decay constant $\log_{10}(f_a) = \{-1.5, -1.7, -2.0\}$, but we show the results only for $\log_{10}(f_a) = -1.7$ as a representative example; the results from the other cases are similar.

Top plot of figure 3 shows the parameter space for $\log_{10}(f_a) = -1.7$ populated by models that we have numerically evolved to verify the linear stability analysis. The blue triangles represent linearly stable models which we confirm to be stable in the non-linear regime, the green dots represent unstable models which migrate to the stable region, the yellow squares are unstable models which collapse to a Schwarzschild BH only being perturbed by the numerical truncation errors, and the violet stars represent models where we observe the dispersion of the scalar field. The area above the first stable re-

gion is mostly populated by models which migrates to the first stable island; close to the first unstable branch of pure axion stars we find models which show the dispersion of the scalar field. The region above the second stable island is only populated by models that migrate to the second stable region. The unstable branch of NS is populated by configurations that migrate; as we add a small amount of bosons to the system this feature is preserved, up to a certain point where we discover a region where fermion-axion stars collapse to BHs. In the bottom plot of figure 3 we show a zoom of this area with more evolutions; we can appreciate how for higher values of ρ_c we need a higher contribution of scalar matter to trigger the collapse to BH. In Table I we report a list of the properties of one representative model for each of the possible fates, which we also depict in figures 4 and 5.

We show in the left panels of figure 4 the time evolution of ρ_c and ϕ_c (top plot) and the number of bosonic N_B and fermionic particles N_F (bottom plot) for the stable model MS1. We notice that the global quantities of the equilibrium solution are constant in time, revealing that the model is non-linearly stable. In the central panels of figure 4 we show the evolution of the same global quantities but for model MS3 which migrates to the stable region; the conserved quantities such as the number of fermionic and bosonic particles are constant during the evolution, but the system settles on a new static model, approaching the new central values $\rho_c = 0.0064$ and $\phi_c = 0.132$ which identify a point which lies on the secondary stable region. Finally in the right panels we show how in model MS2 the central values go to zero at the time when we also observe the appearance of an apparent horizon (bottom right plot), signaling the collapse to a BH.

Model MS4 is illustrated in figure 5 where we depict in the top panel the time evolution of the central value of the scalar field ϕ_c and of the rest-mass density ρ_c and in the middle panel the evolution of the minimum value of the lapse function α_{min} and the maximum value of the metric component g_{rr}^{max} ; it can be appreciated that both the central value of the scalar field and of the rest-mass density drops to zero, while the metric components approach approximately the value 1 of the flat metric. This only happens for models which are very close to the first unstable branch of pure axion stars; interestingly while the scalar field is radiated away, the fermionic matter starts

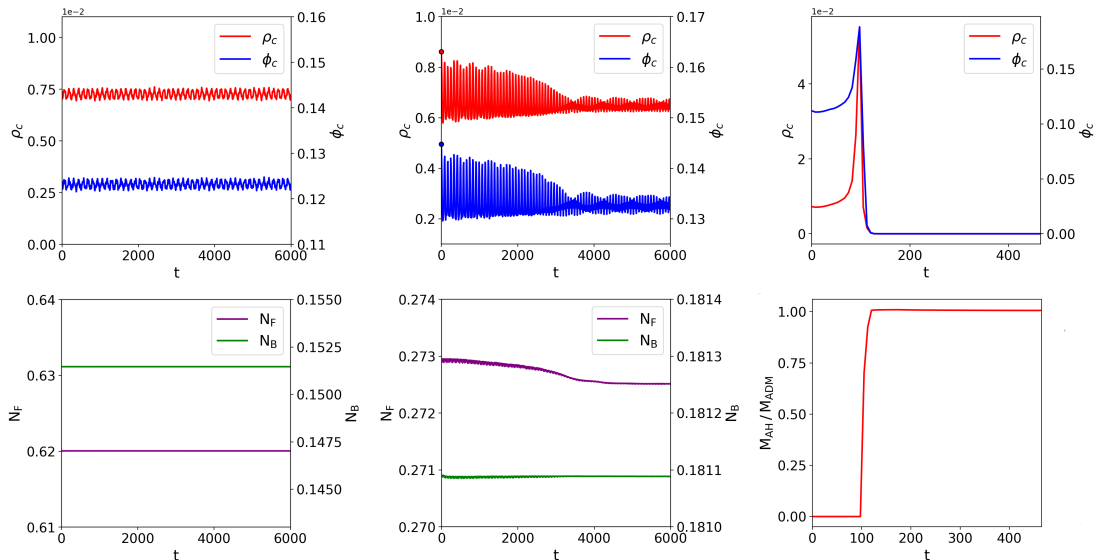


FIG. 4: Time evolution of three different static models with decay constant $\log_{10}(f_a) = -1.7$. Left panels show the central values of ρ_c and ϕ_c (top row) and number of bosons N_B and fermions N_F (bottom row) for the stable model MS1. Middle panels illustrate the same quantities for the unstable model MS3 with the dots in the top panel corresponding to the initial values of ρ_c and ϕ_c . Right panels show ρ_c and ϕ_c (top row) and the apparent horizon mass normalized with the ADM mass of the system (bottom row) for model MS2 which collapses to a Schwarzschild BH.

to get more dilute and there is a remnant object which seems to approach a static configuration of pure fermionic matter with a total ADM mass $M_T \approx 0.00435 M_\odot$. In the bottom plot of figure 5 we show a comparison between the latetime snapshots of the radial profile of ρ and the static model; we can appreciate that the final configuration is oscillating approximately around this new configuration. Due to the low contribution of the fermionic component we can consider these models as pure axion stars which either accreted some baryonic matter, for example from a NS companion in a mixed binary system, or which formed from a primordial mixture of axionic and a small percentage of fermionic particles. A possible scenario to observe this phenomenon could be that of an axion star in the second stable branch which accreted a low amount of fermionic matter and which loses part of the axionic matter due to accretion onto a second more compact object, moving to the first unstable branch and triggering the dispersion mechanism. We point out that we present this result as an academic proof of concept, as we do not consider this scenario very likely to occur. Moreover, we describe the perfect fluid with a polytropic EoS with $\Gamma = 2$ which is not a good description for such low rest-mass densities; a more precise study should involve more realistic EoS based on nuclear physics.

VII. CONCLUSIONS

We have studied models of fermion-axion stars, which are gravitationally bound objects composed by fermion and boson particles, where the latter are modeled by a complex scalar field whose equations of motion are governed by a periodic potential inspired by that of the QCD axion [32]. We have constructed equilibrium configurations for three different values of the decay constant f_a and we have depicted the existence diagram in the parameter space spanned by the central rest-mass density and central scalar field amplitude. We have analyzed the linear stability and delineated the boundary between stable and unstable regions, being able to identify more than one island of stability as expected for those values of f_a which show multiple stable branches in purely axion stars existence curves.

Finally we have presented a detailed study of the non-linear stability for a representative example. We have confirmed the results of the linear analysis; the evolutions of linearly stable models show how all physical quantities describing the star, such as the central values of the fields and the number of particles, remain constant in time. We have identified different areas in the unstable region where equilibrium models face different fates when they are weakly perturbed; some models migrate to the stable region, others collapse to a Schwarzschild BH, and finally

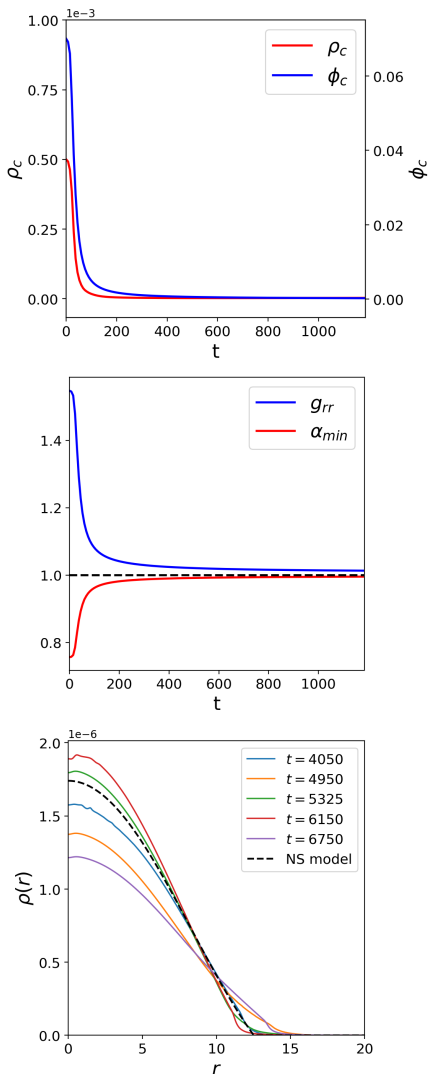


FIG. 5: Time evolution of the dispersed model MS4 with decay constant $\log_{10}(f_a) = -1.7$. Top plot illustrates the central value of the scalar field ϕ_c and the maximum value of the rest-mass density ρ_{max} as a function of time. We notice that both these quantities approach zero indicating dispersion mechanism. In the middle plot we show the minimum value of the lapse α_{min} and the maximum value of the metric component g_{rr}^{max} during the evolution. Both these quantities are converging to their Minkowski spacetime values, as expected. In the bottom plot we show the radial profile of latetime snapshots of ρ compared with a static NS solution with a similar number of fermionic particles N_F .

we have found a small region close to the first unstable branch of pure axion stars in which the scalar field is rapidly dispersed away, and we find evidence of a remnant fermion star. This latter scenario was never observed in previous works on fermion-boson stars.

Acknowledgments

We thank Nicolas Sanchis-Gual and José Antonio Font for useful comments and suggestions. This work was supported by the Spanish Agencia Estatal de Investigación (grant PGC2018-095984-B-I00), by the Generalitat Valenciana (PROMETEO/2019/071). FDG acknowledges support by the Generalitat Valenciana through the grant GRISOLIAP/2019/029. MMT acknowledges support by the Spanish Ministry of Universities (Ministerio de Universidades del Gobierno de España) through the FPU Ph.D. grant No. FPU19/01750. DG acknowledges support by the Spanish Ministry of Science and Innovation and the National Agency of Research (Ministerio de Ciencia e Innovación, Agencia Estatal de Investigación) through the grant PRE2019-087617. We thank the Institute of Pure and Applied Mathematics (IPAM) at the University of California Los Angeles for hospitality during the Long Program "Mathematical and Computational Challenges in the Era of Gravitational Wave Astronomy", during which we started working on this project.

Appendix A: Algorithm for equal-mass curves

In this appendix we discuss how we computed the equal-mass curves shown in blue in figure 1. We recall that the computation of the mass M_T associated to a pair (ρ_c, ϕ_c) involves the numerical solution of a set of ODEs. In particular, we have to solve Eqs. (30)-(34) using the boundary conditions of Eqs. (35), and then to take the limit of Eq. (36). In order to accurately identify the stability region in the parameter space, we need to compute many equal-mass curves, i.e. many level curves of $M_T(\rho_c, \phi_c)$. To accomplish this task in an efficient and accurate way, we proceed as follows. Given an initial point $\mathbf{p}_1 = (\rho_c^1, \phi_c^1)$ in the parameter space, we compute the corresponding mass $M_0 = M_T(\mathbf{p}_1)$. Then we find a second point $\mathbf{p}_2 = (\rho_c^2, \phi_c^2)$ of the level-curve identified by M_0 along a certain specified direction using a bisection algorithm requiring that $|M_0 - M_T(\mathbf{p}_2)| < \epsilon$, where ϵ is a specified tolerance which we choose to be $\epsilon = 10^{-6}$. The distance between \mathbf{p}_1 and the bisection interval used to find \mathbf{p}_2 is given in input by the user. Note that at this stage the algorithm can fail if the level-curve does not cross the bisection-interval. In our specific case, we always start from the ρ_c -axis or the ϕ_c -axis, i.e. from the NS or axion-star case respectively, so that choosing the direction in which searching the second point is trivial. Having two points, we can apply the following procedure:

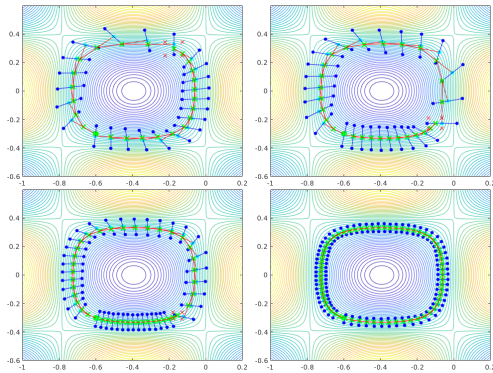


FIG. 6: Level curves of the function $f(x, y) = \sin(4x)\cos(4y)$. On the background we show the ones compute with the `Matlab` function `contour()`, while on top we show the points of the level curves found by our algorithm (green points). We consider as initial point $\mathbf{p}_1 = (-0.6, -0.30103)$, that corresponds to $f(\mathbf{p}_1) \simeq -0.242$, and we search the second point in the north direction using a tolerance of $\epsilon = 10^{-10}$. We show the results for 4 different initial steps. The red lines are segments of \bar{r}_1 , the blue lines are segment of \bar{r}_2 , the cyan point is \mathbf{q}_* , the blue dots are \mathbf{q}_L and \mathbf{q}_R , and the red crosses are the vertex of the square created in the cases where the tangent method fails.

1. we consider the line \bar{r}_1 passing through \mathbf{p}_{n-1} and \mathbf{p}_n , then we consider a third point \mathbf{q}_* on \bar{r}_1 such that $d(\mathbf{p}_{n-1}, \mathbf{p}_n) = d(\mathbf{p}_n, \mathbf{q}_*)$, where $d: \mathbb{R}^2 \times \mathbb{R}^2 \rightarrow \mathbb{R}$ is the Euclidean distance;
2. we consider \bar{r}_2 , a line perpendicular to \bar{r}_1 that passes through \mathbf{q}_* , and we find the two points \mathbf{q}_L and \mathbf{q}_R such that $d(\mathbf{q}_L, \mathbf{q}_*) = d(\mathbf{q}_*, \mathbf{q}_R) = d(\mathbf{p}_n, \mathbf{q}_*)$;
3. we evaluate $M_T^L = M_T(\mathbf{q}_L)$ and $M_T^R = M_T(\mathbf{q}_R)$;
4. depending on the sign of the product $(M_T^L - M_0)(M_T^R - M_0)$, we proceed as follows:
 - (a) if $(M_T^L - M_0)(M_T^R - M_0) \leq 0$, then we apply the bisection algorithm on the segment identified by \mathbf{q}_L and \mathbf{q}_R and we find the next point \mathbf{p}_{n+1} requiring $|M_0 - M_T(\mathbf{p}_{n+1})| < \epsilon$. We call this method of finding \mathbf{p}_{n+1} the *tangent* method;
 - (b) If $(M_T^L - M_0)(M_T^R - M_0) > 0$, i.e. if the level-curve is not passing through the segment identified by \mathbf{q}_L and \mathbf{q}_R , then we build a square whose center is in \mathbf{p}_n , then we evaluate M_T at the four vertices of the squares, and we search for the side crossed by the level-curve, and we apply the bisection algorithm to find \mathbf{p}_{n+1} requiring $|M_0 - M_T(\mathbf{p}_{n+1})| < \epsilon$. We denote this method as the *square* method;

5. we repeat this procedure until the curve closes or until we reach some specified boundary.

Note that the square method guarantees to find a point, but it is slower than the tangent method since requires two additional evaluations of M_T .

This method can be applied to any function $f(x, y)$, but if the function is known in closed form then there are faster algorithms to find the corresponding level curves. However, in order to test our algorithm, we consider an analytical function and compare the contour plot produced by the `Matlab` function `contour()` with the level-curve that we find with our algorithm. An illustrative example is shown in figure 6. As can be seen, the distance between the points tends to increase up to a point where the tangent method fails and thus we have to find the next point using the square method. After this step, a relatively small distance between the points is restored. Note that this is not imposed in the code, but it is just a consequence of the aforementioned procedure. Finally, consider that using a small initial step almost always guarantees the success of the tangent method.

Appendix B: Code assessment

As pointed out in the main text, a convergence test of the numerical code presented in [79] shows second-order convergence. We test the reliability of the results of the dynamical evolutions of the models presented in this work, analyzing the results for models MS1, MS2, and MS3 for two different resolutions, namely $\Delta r = 0.0125$ and $\Delta r = 0.00625$. In the top panels of figure 7, we show the time evolution of the central value of the rest-mass density ρ_0 and of the scalar field ϕ_0 for the two different grid spacing; we can appreciate how the results are consistent with each other, and the higher resolution run shows a better agreement with the values at initial time which are highlighted by the horizontal blue lines. In the central panels we show model MS3 which migrates to a stable configuration; the results using the two resolutions are in agreement. Finally, we confirm the case in which the model collapses to a black hole in the bottom panels.

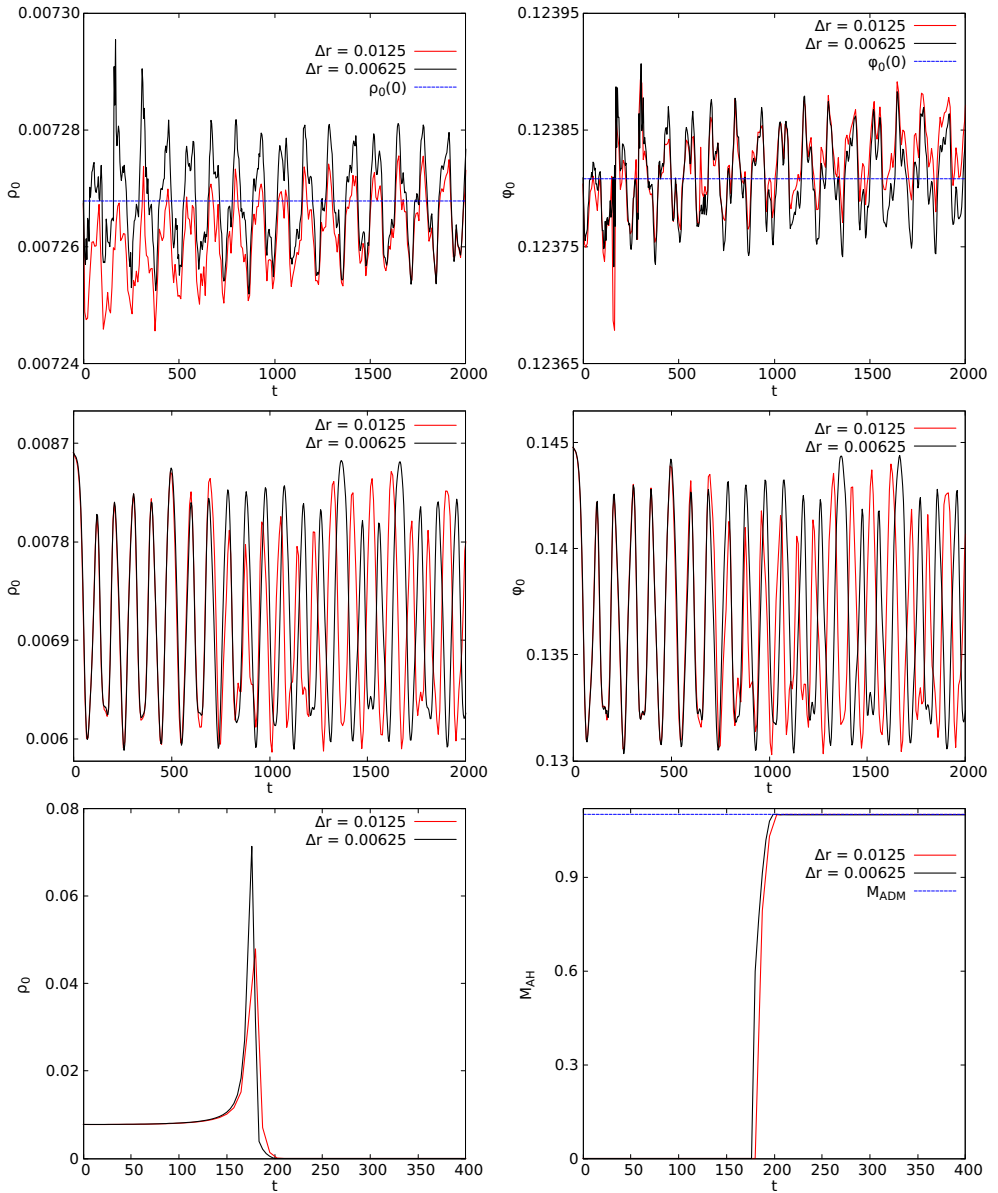


FIG. 7: Time evolution of models MS1 (top panels), MS3 (middle panels), and MS2 (bottom panels) for two different grid spacing $\Delta r = 0.0125$ and $\Delta r = 0.00625$. Left panels show the central value of the rest-mass density ρ_0 , while the right panels show the central value of the scalar field ϕ_0 for MS1 and MS3, and the apparent horizon mass A_{AH} for the collapsing model MS2. The blue horizontal lines represent the value of the corresponding quantity at initial time.

[1] G. Hinshaw et al. (WMAP), *Astrophys. J. Suppl.* **208**, 19 (2013), 1212.5226.

[2] B. A. Reid et al., *Mon. Not. Roy. Astron. Soc.* **426**, 2719

- (2012), 1203.6641.
- [3] W. Hu, R. Barkana, and A. Gruzinov, *Phys. Rev. Lett.* **85**, 1158 (2000), astro-ph/0003365.
 - [4] R. R. Caldwell and M. Kamionkowski, *Ann. Rev. Nucl. Part. Sci.* **59**, 397 (2009), 0903.0866.
 - [5] C. Blake et al., *Mon. Not. Roy. Astron. Soc.* **418**, 1707 (2011), 1108.2635.
 - [6] R. Hlozek, D. Grin, D. J. E. Marsh, and P. G. Ferreira, *Phys. Rev. D* **91**, 103512 (2015), 1410.2896.
 - [7] J. Chluba et al. (2019), 1909.01593.
 - [8] K. Abazajian et al. (2019), 1907.04473.
 - [9] Y. B. Zel'dovich and I. D. Novikov, *Soviet Astronomy* **10**, 602 (1967).
 - [10] S. Hawking, *Monthly Notices of the Royal Astronomical Society* **152**, 75 (1971).
 - [11] G. F. Chapline, *Nature* **253**, 251 (1975).
 - [12] B. J. Carr, *Astrophysical Journal* **201**, 1 (1975).
 - [13] R. D. Peccei and H. R. Quinn, *Phys. Rev. Lett.* **38**, 1440 (1977).
 - [14] L. Abbott and P. Sikivie, *Physics Letters B* **120**, 133 (1983), ISSN 0370-2693.
 - [15] S. Borsanyi, M. Dierigl, Z. Fodor, S. D. Katz, S. W. Mages, D. Nogradi, J. Redondo, A. Ringwald, and K. K. Szabo, *Physics Letters B* **752**, 175 (2016), 1508.06917.
 - [16] J. Preskill, M. B. Wise, and F. Wilczek, *Physics Letters B* **120**, 127 (1983), ISSN 0370-2693.
 - [17] D. J. E. Marsh, *Phys. Rep.* **643**, 1 (2016), 1510.07633.
 - [18] J. P. Conlon, *Journal of High Energy Physics* **2006**, 078 (2006), URL <https://doi.org/10.1088/1126-6708/2006/05/078>.
 - [19] P. Svrcek and E. Witten, *Journal of High Energy Physics* **2006**, 051 (2006), URL <https://doi.org/10.1088/1126-6708/2006/06/051>.
 - [20] A. Hook, in *TASI 2018 - Theory in an Era of Data* (2018), p. 4, 1812.02669.
 - [21] I. G. Irastorza and J. Redondo, *Prog. Part. Nucl. Phys.* **102**, 89 (2018), 1801.08127.
 - [22] P. W. Graham, I. G. Irastorza, S. K. Lamoreaux, A. Lindner, and K. A. van Bibber, *Annual Review of Nuclear and Particle Science* **65**, 485 (2015), <https://doi.org/10.1146/annurev-nucl-102014-022120>, URL <https://doi.org/10.1146/annurev-nucl-102014-022120>.
 - [23] S.-J. Sin, *Phys. Rev. D* **50**, 3650 (1994), hep-ph/9205208.
 - [24] P.-H. Chavanis and T. Harko, *Phys. Rev. D* **86**, 064011 (2012), 1108.3986.
 - [25] P. Jetzer, *Physics Reports* **220**, 163 (1992).
 - [26] D. J. Kaup, *Phys. Rev.* **172**, 1331 (1968).
 - [27] R. Ruffini and S. Bonazzola, *Phys. Rev.* **187**, 1767 (1969).
 - [28] M. Colpi, S. L. Shapiro, and I. Wasserman, *Phys. Rev. Lett.* **57**, 2485 (1986).
 - [29] R. Friedberg, T. D. Lee, and Y. Pang, *Phys. Rev. D* **35**, 3658 (1987), URL <https://link.aps.org/doi/10.1103/PhysRevD.35.3658>.
 - [30] B. Kleihaus, J. Kunz, and M. List, *Phys. Rev. D* **72**, 064002 (2005), URL <https://link.aps.org/doi/10.1103/PhysRevD.72.064002>.
 - [31] B. Kleihaus, J. Kunz, M. List, and I. Schaffer, *Phys. Rev. D* **77**, 064025 (2008), URL <https://link.aps.org/doi/10.1103/PhysRevD.77.064025>.
 - [32] D. Guerra, C. F. Macedo, and P. Pani, *Journal of Cosmology and Astroparticle Physics* **2019**, 061 (2019), URL <https://doi.org/10.1088/1475-7516/2019/09/061>.
 - [33] P. Jetzer and J. van der Bij, *Phys. Lett. B* **227**, 341 (1989).
 - [34] S. Yoshida and Y. Eriguchi, *Phys. Rev.* **D56**, 762 (1997).
 - [35] F. E. Schunck and E. W. Mielke, *Phys. Lett.* **A249**, 389 (1998).
 - [36] E. Seidel and W. M. Suen, *Phys. Rev. Lett.* **66**, 1659 (1991).
 - [37] M. Alcubierre, J. Barranco, A. Bernal, J. C. Degollado, A. Diez-Tejedor, M. Megevand, D. Nunez, and O. Sarbach, *Class. Quant. Grav.* **35**, 19LT01 (2018), 1805.11488.
 - [38] V. Jaramillo, N. Sanchis-Gual, J. Barranco, A. Bernal, J. C. Degollado, C. Herdeiro, and D. Núñez, *Phys. Rev. D* **101**, 124020 (2020), 2004.08459.
 - [39] N. Sanchis-Gual, F. Di Giovanni, C. Herdeiro, E. Radu, and J. A. Font, *Physical Review Letters* **126**, 241105 (2021).
 - [40] R. Brito, V. Cardoso, C. A. Herdeiro, and E. Radu, *Physics Letters B* **752**, 291 (2016).
 - [41] F. E. Schunck and E. W. Mielke, *Class. Quant. Grav.* **20**, R301 (2003), 0801.0307.
 - [42] S. L. Liebling and C. Palenzuela, *Living Reviews in Relativity* **20**, 5 (2017).
 - [43] E. Seidel and W.-M. Suen, *Phys. Rev.* **D42**, 384 (1990).
 - [44] J. Balakrishna, E. Seidel, and W.-M. Suen, *Phys. Rev.* **D58**, 104004 (1998), gr-qc/9712064.
 - [45] N. Sanchis-Gual, F. Di Giovanni, M. Zilhão, C. Herdeiro, P. Cerdá-Durán, J. Font, and E. Radu, *Physical Review Letters* **123**, 221101 (2019).
 - [46] F. Di Giovanni, N. Sanchis-Gual, P. Cerdá-Durán, M. Zilhão, C. Herdeiro, J. A. Font, and E. Radu, *Phys. Rev. D* **102**, 124009 (2020), 2010.05845.
 - [47] N. Siemonsen and W. E. East, *Phys. Rev. D* **103**, 044022 (2021), 2011.08247.
 - [48] P. Jetzer, *Nuclear Physics B* **316**, 411 (1989), ISSN 0550-3213, URL <https://www.sciencedirect.com/science/article/pii/0550321389900382>.
 - [49] M. Gleiser and R. Watkins, *Nucl. Phys.* **B319**, 733 (1989).
 - [50] T. D. Lee and Y. Pang, *Nucl. Phys.* **B315**, 477 (1989), [129(1988)].
 - [51] E. Seidel and W.-M. Suen, *Phys. Rev. Lett.* **72**, 2516 (1994), gr-qc/9309015.
 - [52] F. S. Guzman and L. A. Urena-Lopez, *Phys. Rev. D* **69**, 124033 (2004), gr-qc/0404014.
 - [53] F. Guzman and L. Urena-Lopez, *Astrophys. J.* **645**, 814 (2006), astro-ph/0603613.
 - [54] F. Di Giovanni, N. Sanchis-Gual, C. A. R. Herdeiro, and J. A. Font, *Phys. Rev.* **D98**, 064044 (2018), 1803.04802.
 - [55] A. Henriques, A. R. Liddle, and R. Moorhouse, *Physics Letters B* **251**, 511 (1990), ISSN 0370-2693, URL <http://www.sciencedirect.com/science/article/pii/0370269390907899>.
 - [56] S. Valdez-Alvarado, C. Palenzuela, D. Alic, and L. A. Urena-López, *Physical Review D* **87**, 084040 (2013).
 - [57] R. Brito, V. Cardoso, and H. Okawa, *Physical Review Letters* **115**, 111301 (2015).
 - [58] R. Brito, V. Cardoso, C. F. B. Macedo, H. Okawa, and C. Palenzuela, *Phys. Rev. D* **93**, 044045 (2016), 1512.00466.
 - [59] F. Di Giovanni, S. Fakhry, N. Sanchis-Gual, J. C. Degollado, and J. A. Font, *Class. Quant. Grav.* **38**, 194001 (2021), 2105.00530.
 - [60] F. Di Giovanni, N. Sanchis-Gual, P. Cerdá-Durán, and

- J. A. Font, Phys. Rev. D **105**, 063005 (2022), 2110.11997.
- [61] F. Di Giovanni, N. Sanchis-Gual, D. Guerra, M. Miravet-Tenét, P. Cerdá-Durán, and J. A. Font, arXiv e-prints arXiv:2206.00977 (2022), 2206.00977.
- [62] N. Sanchis-Gual and P. Izquierdo, Phys. Rev. D **105**, 084023 (2022), URL <https://link.aps.org/doi/10.1103/PhysRevD.105.084023>.
- [63] M. Bezares, D. Viganò, and C. Palenzuela, Phys. Rev. D **100**, 044049 (2019), URL <https://link.aps.org/doi/10.1103/PhysRevD.100.044049>.
- [64] S. Chandrasekhar, Astrophys. J. **140**, 417 (1964).
- [65] S. Valdez-Alvarado, R. Becerril, and L. A. Ureña-López, Physical Review D **102**, 064038 (2020).
- [66] F. Di Giovanni, S. Fakhry, N. Sanchis-Gual, J. C. Degollado, and J. A. Font, Phys. Rev. D **102**, 084063 (2020), 2006.08583.
- [67] A. Henriques, A. R. Liddle, and R. Moorhouse, Nuclear Physics B **337**, 737 (1990), ISSN 0550-3213, URL <https://www.sciencedirect.com/science/article/pii/055032139090514E>.
- [68] G. G. di Cortona, E. Hardy, J. P. Vega, and G. Villadoro, Journal of High Energy Physics **2016**, 34 (2016), 1511.02867.
- [69] P. J. Montero and I. Cordero-Carrion, Phys.Rev. **D85**, 124037 (2012), 1204.5377.
- [70] T. Nakamura, K. Oohara, and Y. Kojima, Progress of Theoretical Physics Supplement **90**, 1 (1987).
- [71] M. Shibata and T. Nakamura, Phys. Rev. D **52**, 5428 (1995).
- [72] T. W. Baumgarte and S. L. Shapiro, Phys. Rev. D **59**, 024007 (1998).
- [73] J. D. Brown, Phys. Rev. D **79**, 104029 (2009), URL <http://link.aps.org/doi/10.1103/PhysRevD.79.104029>.
- [74] M. Alcubierre and M. D. Mendez, Gen.Rel.Grav. **43**, 2769 (2011), 1010.4013.
- [75] N. Sanchis-Gual, J. C. Degollado, P. J. Montero, and J. A. Font, Phys. Rev. D **91**, 043005 (2015), 1412.8304.
- [76] B. Kain, Phys. Rev. D **103**, 123003 (2021), URL <https://link.aps.org/doi/10.1103/PhysRevD.103.123003>.
- [77] G. L. Comer, D. Langlois, and L. M. Lin, Phys. Rev. D **60**, 104025 (1999), URL <https://link.aps.org/doi/10.1103/PhysRevD.60.104025>.
- [78] B. Kain, Phys. Rev. D **102**, 023001 (2020), URL <https://link.aps.org/doi/10.1103/PhysRevD.102.023001>.
- [79] N. Sanchis-Gual, J. C. Degollado, P. J. Montero, J. A. Font, and C. Herdeiro, Phys. Rev. Lett. **116**, 141101 (2016), 1512.05358.
- [80] N. Sanchis-Gual, J. C. Degollado, P. J. Montero, J. A. Font, and V. Mewes, Phys. Rev. D **92**, 083001 (2015), 1507.08437.
- [81] N. Sanchis-Gual, J. C. Degollado, C. Herdeiro, J. A. Font, and P. J. Montero, Phys. Rev. **D94**, 044061 (2016), 1607.06304.
- [82] A. Escorihuela-Tomás, N. Sanchis-Gual, J. C. Degollado, and J. A. Font, Physical Review D **96**, 024015 (2017).
- [83] N. Sanchis-Gual, C. Herdeiro, and E. Radu, Class. Quant. Grav. **39**, 064001 (2022), 2110.03000.
- [84] I. Cordero-Carrión and P. Cerdá-Durán, ArXiv e-prints (2012), 1211.5930.
- [85] I. Cordero-Carrión and P. Cerdá-Durán, *Advances in Differential Equations and Applications*, SEMA SIMAI Springer Series Vol. 4 (Springer International Publishing Switzerland, Switzerland, 2014).

Bibliography

- [1] B. P. Abbott et al. “Observation of Gravitational Waves from a Binary Black Hole Merger.” In: *Physical Review Letters* 116.6, 061102 (Feb. 2016), p. 061102. arXiv: 1602.03837 [gr-qc].
- [2] R. Abbott et al. “Search for Subsolar-Mass Binaries in the First Half of Advanced LIGO’s and Advanced Virgo’s Third Observing Run.” In: *Phys. Rev. Lett.* 129 (6 2022), p. 061104. DOI: 10.1103/PhysRevLett.129.061104. URL: <https://link.aps.org/doi/10.1103/PhysRevLett.129.061104>.
- [3] M. Alcubierre. *Introduction to 3+1 Numerical Relativity*. Oxford University Press, 2008.
- [4] M. Alcubierre et al. “ ℓ -boson stars.” In: *Classical and Quantum Gravity* 35.19 (2018), 19LT01. DOI: 10.1088/1361-6382/aadcb6. URL: <https://doi.org/10.1088/1361-6382/aadcb6>.
- [5] C. Armendariz-Picon, V. Mukhanov, and P. J. Steinhardt. “Dynamical Solution to the Problem of a Small Cosmological Constant and Late-Time Cosmic Acceleration.” In: *Phys. Rev. Lett.* 85 (21 Oct. 2000), pp. 4438–4441. DOI: 10.1103/PhysRevLett.85.4438. URL: <https://link.aps.org/doi/10.1103/PhysRevLett.85.4438>.
- [6] R. Arnowitt, S. Deser, and C. W. Misner. “Republication of: The dynamics of general relativity.” In: *General Relativity and Gravitation* 40.9 (Sept. 2008), pp. 1997–2027. DOI: 10.1007/s10714-008-0661-1. arXiv: gr-qc/0405109 [gr-qc].
- [7] M. Babiuc-Hamilton et al. *The Einstein Toolkit*. Version The "Mayer" release, ET₂019₁0. To find out more, visit <http://einsteintoolkit.org>. Oct. 2019. DOI: 10.5281/zenodo.3522086. URL: <https://doi.org/10.5281/zenodo.3522086>.
- [8] L. Baiotti et al. “Accurate simulations of the dynamical bar-mode instability in full general relativity.” In: *Phys. Rev. D* 75.4, 044023 (Feb. 2007), p. 044023. DOI: 10.1103/PhysRevD.75.044023. arXiv: astro-ph/0609473 [astro-ph].
- [9] J. G. Baker et al. “Gravitational-wave extraction from an inspiraling configuration of merging black holes.” In: *Physical Review Letters* 96.11 (2006), p. 111102.
- [10] J. Balakrishna, E. Seidel, and W.-M. Suen. “Dynamical evolution of boson stars. 2. Excited states and selfinteracting fields.” In: *Phys. Rev. D* 58 (1998), p. 104004. DOI: 10.1103/PhysRevD.58.104004. arXiv: gr-qc/9712064 [gr-qc].

- [11] H. Barré, H. Nye, and G. Janin. “An overview of the XMM observatory system.” In: *ESA Bulletin* 100 (Dec. 1999), pp. 15–20.
- [12] T. W. Baumgarte and S. L. Shapiro. “Numerical integration of Einstein’s field equations.” In: *Phys. Rev. D* 59.2, 024007 (Jan. 1999), p. 024007. eprint: gr-qc/9810065.
- [13] T. W. Baumgarte and S. L. Shapiro. “Numerical relativity and compact binaries.” In: *Phys. Rep.* 376 (Mar. 2003), pp. 41–131. eprint: gr-qc/0211028.
- [14] A. Bernal et al. “Multistate boson stars.” In: *Phys. Rev. D* 81 (4 2010), p. 044031. DOI: 10.1103/PhysRevD.81.044031. URL: <https://link.aps.org/doi/10.1103/PhysRevD.81.044031>.
- [15] M. Bezares and C. Palenzuela. “Gravitational waves from dark boson star binary mergers.” In: *Classical and Quantum Gravity* 35.23 (2018), p. 234002. DOI: 10.1088/1361-6382/aae87c. URL: <https://doi.org/10.1088/1361-6382/aae87c>.
- [16] M. Bezares, C. Palenzuela, and C. Bona. “Final fate of compact boson star mergers.” In: *Physical Review D* 95.12 (2017), p. 124005.
- [17] C. Bona and J. Massó. “Einstein’s evolution equations as a system of balance laws.” In: *Phys. Rev. D* 40 (4 1989), pp. 1022–1026. DOI: 10.1103/PhysRevD.40.1022. URL: <https://link.aps.org/doi/10.1103/PhysRevD.40.1022>.
- [18] C. Bona and J. Massó. “Hyperbolic evolution system for numerical relativity.” In: *Phys. Rev. Lett.* 68 (8 1992), pp. 1097–1099. DOI: 10.1103/PhysRevLett.68.1097. URL: <https://link.aps.org/doi/10.1103/PhysRevLett.68.1097>.
- [19] C. Bona et al. “General-covariant evolution formalism for numerical relativity.” In: *Phys. Rev. D* 67 (10 2003), p. 104005. DOI: 10.1103/PhysRevD.67.104005. URL: <https://link.aps.org/doi/10.1103/PhysRevD.67.104005>.
- [20] C. Bona et al. “Symmetry-breaking mechanism for the Z4 general-covariant evolution system.” In: *Phys. Rev. D* 69 (6 2004), p. 064036. DOI: 10.1103/PhysRevD.69.064036. URL: <https://link.aps.org/doi/10.1103/PhysRevD.69.064036>.
- [21] C. Bona et al. “New Formalism for Numerical Relativity.” In: *Phys. Rev. Lett.* 75 (4 1995), pp. 600–603. DOI: 10.1103/PhysRevLett.75.600. URL: <https://link.aps.org/doi/10.1103/PhysRevLett.75.600>.
- [22] R. Brito, V. Cardoso, and H. Okawa. “Accretion of dark matter by stars.” In: *Physical review letters* 115.11 (2015), p. 111301.
- [23] R. Brito, V. Cardoso, and P. Pani. “Superradiance.” In: *Lect. Notes Phys.* 906 (2015), pp.1–237. DOI: 10.1007/978-3-319-19000-6. arXiv: 1501.06570 [gr-qc].
- [24] R. Brito et al. “Interaction between bosonic dark matter and stars.” In: *Phys. Rev. D* 93 (4 Feb. 2016), p. 044045. DOI: 10.1103/PhysRevD.93.044045. URL: <https://link.aps.org/doi/10.1103/PhysRevD.93.044045>.

- [25] R. Brito et al. “Proca stars: Gravitating Bose–Einstein condensates of massive spin 1 particles.” In: *Phys. Lett. B* 752 (2016), pp. 291–295. DOI: 10.1016/j.physletb.2015.11.051. arXiv: 1508.05395 [gr-qc].
- [26] D. Brown et al. “Turduckening black holes: an analytical and computational study.” In: *Physical Review D* 79.4 (2009), p. 044023.
- [27] J. D. Brown. “Covariant formulations of BSSN and the standard gauge.” In: *Phys. Rev. D* 79 (2009), p. 104029.
- [28] J. C. Bustillo et al. “GW190521 as a merger of Proca stars: a potential new vector boson of 8.7×10^{-13} eV.” In: *Phys. Rev. Lett.* 126 (8 2021), p. 081101. DOI: 10.1103/PhysRevLett.126.081101. URL: <https://link.aps.org/doi/10.1103/PhysRevLett.126.081101>.
- [29] J. Calderon Bustillo et al. “Gravitational-wave parameter inference with the Newman–Penrose scalar.” In: *arXiv e-prints*, arXiv:2205.15029 (May 2022), arXiv:2205.15029. arXiv: 2205.15029 [gr-qc].
- [30] J. Calderon Bustillo et al. “Searching for vector boson-star mergers within LIGO–Virgo intermediate-mass black-hole merger candidates.” In: *arXiv e-prints*, arXiv:2206.02551 (June 2022), arXiv:2206.02551. arXiv: 2206.02551 [gr-qc].
- [31] M. Campanelli et al. “Accurate evolutions of orbiting black-hole binaries without excision.” In: *Physical Review Letters* 96.11 (2006), p. 111101.
- [32] S. Capozziello and M. de Laurentis. “Extended Theories of Gravity.” In: *Phys. Rep.* 509.4 (Dec. 2011), pp. 167–321. DOI: 10.1016/j.physrep.2011.09.003. arXiv: 1108.6266 [gr-qc].
- [33] P. Cerdá-Durán, V. Quilis, and J. A. Font. “AMR simulations of the low T/|W| bar-mode instability of neutron stars.” In: *Computer Physics Communications* 177.3 (2007), pp. 288–297. ISSN: 0010-4655. DOI: <https://doi.org/10.1016/j.cpc.2007.04.001>.
- [34] S. Chandrasekhar. “The highly collapsed configurations of a stellar mass (Second paper).” In: *Monthly Notices of the Royal Astronomical Society* 95 (1935), pp. 207–225.
- [35] S. Chandrasekhar. “The highly collapsed configurations of a stellar mass.” In: *Monthly Notices of the Royal Astronomical Society* 91 (1931), pp. 456–466.
- [36] P. Ciarcelluti and F. Sandin. “Have neutron stars a dark matter core?” In: *Physics Letters B* 695.1-4 (Jan. 2011), pp. 19–21. DOI: 10.1016/j.physletb.2010.11.021. URL: <https://doi.org/10.1016%2Fj.physletb.2010.11.021>.
- [37] M. Colpi, S. L. Shapiro, and I. Wasserman. “Boson Stars: Gravitational Equilibria of Self-Interacting Scalar Fields.” In: *Phys. Rev. Lett.* 57 (20 1986), pp. 2485–2488. DOI: 10.1103/PhysRevLett.57.2485. URL: <https://link.aps.org/doi/10.1103/PhysRevLett.57.2485>.
- [38] I. Cordero-Carrión et al. “Improved constrained scheme for the Einstein equations: An approach to the uniqueness issue.” In: *Phys. Rev. D* 79.2, 024017 (Jan. 2009), p. 024017. arXiv: 0809.2325 [gr-qc].
- [39] I. Cordero-Carrión, P. Cerdá-Durán, and J. M. Ibáñez. “Gravitational waves in dynamical spacetimes with matter content in the fully constrained formulation.” In: *Physical Review D* 85.4 (2012), p. 044023.

- [40] P. V. P. Cunha et al. “The fate of the light-ring instability.” In: *arXiv e-prints*, arXiv:2207.13713 (July 2022), arXiv:2207.13713. arXiv: 2207.13713 [gr-qc].
- [41] F. Di Giovanni et al. “A stabilization mechanism for excited fermion–boson stars.” In: *Class. Quant. Grav.* 38.19 (2021), p. 194001. DOI: 10.1088/1361-6382/ac1b45. arXiv: 2105.00530 [gr-qc].
- [42] F. Di Giovanni et al. “Can fermion-boson stars reconcile multimessenger observations of compact stars?” In: *Phys. Rev. D* 105.6 (2022), p. 063005. DOI: 10.1103/PhysRevD.105.063005. arXiv: 2110.11997 [gr-qc].
- [43] F. Di Giovanni et al. “Dynamical bar-mode instability in spinning bosonic stars.” In: *Phys. Rev. D* 102 (12 2020), p. 124009. DOI: 10.1103/PhysRevD.102.124009. URL: <https://link.aps.org/doi/10.1103/PhysRevD.102.124009>.
- [44] F. Di Giovanni et al. “Dynamical formation and stability of fermion-boson stars.” In: *Phys. Rev. D* 102 (8 2020), p. 084063. DOI: 10.1103/PhysRevD.102.084063. URL: <https://link.aps.org/doi/10.1103/PhysRevD.102.084063>.
- [45] F. Di Giovanni et al. “Dynamical formation of Proca stars and quasistationary solitonic objects.” In: *Phys. Rev. D* 98 (6 2018), p. 064044. DOI: 10.1103/PhysRevD.98.064044. URL: <https://link.aps.org/doi/10.1103/PhysRevD.98.064044>.
- [46] F. Di Giovanni et al. “Fermion-axion stars: static solutions and dynamical stability.” In: *arXiv e-prints*, arXiv:2207.06174 (July 2022), arXiv:2207.06174. arXiv: 2207.06174 [gr-qc].
- [47] F. Di Giovanni et al. “Impact of ultralight bosonic dark matter on the dynamical bar-mode instability of rotating neutron stars.” In: *Phys. Rev. D* 106 (4 2022), p. 044008. DOI: 10.1103/PhysRevD.106.044008. URL: <https://link.aps.org/doi/10.1103/PhysRevD.106.044008>.
- [48] W. E. East. “Superradiant instability of massive vector fields around spinning black holes in the relativistic regime.” In: *Physical Review D* 96.2 (2017), p. 024004.
- [49] W. E. East and F. Pretorius. “Superradiant instability and backreaction of massive vector fields around Kerr black holes.” In: *Physical review letters* 119.4 (2017), p. 041101.
- [50] A. Einstein. “Die Feldgleichungen der Gravitation.” In: *Sitzungsberichte der Königlich Preußischen Akademie der Wissenschaften (Berlin)*, Seite 844-847. (1915).
- [51] A. Einstein. “Die Grundlage der allgemeinen Relativitätstheorie.” In: *Annalen der Physik* 354 (1916), pp. 769–822.
- [52] A. Einstein. “Über gravitationswellen.” In: *Sitzungsberichte der Königlich Preußischen Akademie der Wissenschaften (Berlin)*, Seite 154-167. (1918).
- [53] K. Eppley. “Evolution of time-symmetric gravitational waves: Initial data and apparent horizons.” In: *Phys. Rev. D* 16.6 (Sept. 1977), pp. 1609–1614. DOI: 10.1103/PhysRevD.16.1609.
- [54] K. R. Eppley. “The numerical evolution of the collision of two black holes.” PhD thesis. Princeton Univ., NJ., Jan. 1975.

- [55] Event Horizon Telescope Collaboration et al. “First M87 Event Horizon Telescope Results. IV. Imaging the Central Supermassive Black Hole.” In: *Astrophys. J. Lett.* 875.1, L4 (Apr. 2019), p. L4. DOI: 10.3847/2041-8213/ab0e85. arXiv: 1906.11241 [astro-ph.GA].
- [56] Y. Fourès-Bruhat. “Théorème d’existence pour certains systèmes d’équations aux dérivées partielles non linéaires.” In: *Acta Mathematica* 88.none (1952), pp. 141–225. DOI: 10.1007/BF02392131. URL: <https://doi.org/10.1007/BF02392131>.
- [57] K. Freese, J. A. Frieman, and A. V. Olinto. “Natural inflation with pseudo Nambu-Goldstone bosons.” In: *Phys. Rev. Lett.* 65 (26 Dec. 1990), pp. 3233–3236. DOI: 10.1103/PhysRevLett.65.3233. URL: <https://link.aps.org/doi/10.1103/PhysRevLett.65.3233>.
- [58] R. Friedberg, T. D. Lee, and Y. Pang. “Scalar soliton stars and black holes.” In: *Phys. Rev. D* 35 (12 1987), pp. 3658–3677. DOI: 10.1103/PhysRevD.35.3658. URL: <https://link.aps.org/doi/10.1103/PhysRevD.35.3658>.
- [59] K. C. Gendreau et al. “The Neutron star Interior Composition Explorer (NICER): design and development.” In: *Space Telescopes and Instrumentation 2016: Ultraviolet to Gamma Ray*. Ed. by J.-W. A. den Herder, T. Takahashi, and M. Bautz. Vol. 9905. International Society for Optics and Photonics. SPIE, 2016, 99051H. DOI: 10.1117/12.2231304. URL: <https://doi.org/10.1117/12.2231304>.
- [60] K. Glampedakis and L. Gualtieri. “Gravitational Waves from Single Neutron Stars: An Advanced Detector Era Survey.” In: *Astrophysics and Space Science Library*. Ed. by L. Rezzolla et al. Vol. 457. Astrophysics and Space Science Library. Jan. 2018, p. 673. DOI: 10.1007/978-3-319-97616-7_12. arXiv: 1709.07049 [astro-ph.HE].
- [61] M. Gleiser and R. Watkins. “Gravitational Stability of Scalar Matter.” In: *Nucl. Phys.* B319 (1989), pp. 733–746. DOI: 10.1016/0550-3213(89)90627-5.
- [62] I. Goldman et al. “Possible implications of asymmetric fermionic dark matter for neutron stars.” In: *Physics Letters B* 725.4-5 (Oct. 2013), pp. 200–207. DOI: 10.1016/j.physletb.2013.07.017. URL: <https://doi.org/10.1016%2Fj.physletb.2013.07.017>.
- [63] I. Goldman and S. Nussinov. “Weakly interacting massive particles and neutron stars.” In: *Phys. Rev. D* 40 (10 Oct. 1989), pp. 3221–3230. DOI: 10.1103/PhysRevD.40.3221. URL: <https://link.aps.org/doi/10.1103/PhysRevD.40.3221>.
- [64] M. I. Gresham and K. M. Zurek. “Asymmetric dark stars and neutron star stability.” In: *Physical Review D* 99.8 (Apr. 2019). DOI: 10.1103/physrevd.99.083008. URL: <https://doi.org/10.1103%2Fphysrevd.99.083008>.
- [65] D. Guerra, C. F. Macedo, and P. Pani. “Axion boson stars.” In: *Journal of Cosmology and Astroparticle Physics* 2019.09 (2019), pp. 061–061. DOI: 10.1088/1475-7516/2019/09/061. URL: <https://doi.org/10.1088/1475-7516/2019/09/061>.

- [66] F. S. Guzman. “Evolving spherical boson stars on a 3-D Cartesian grid.” In: *Phys. Rev. D* 70 (2004), p. 044033. DOI: 10.1103/PhysRevD.70.044033. arXiv: gr-qc/0407054 [gr-qc].
- [67] F. Guzmán. “The three dynamical fates of Boson Stars.” In: *Revista mexicana de física* 55.4 (2009), pp. 321–326.
- [68] S. G. Hahn and R. W. Lindquist. “The two-body problem in geometrodynamics.” In: *Annals of Physics* 29.2 (Sept. 1964), pp. 304–331. DOI: 10.1016/0003-4916(64)90223-4.
- [69] A. B. Henriques, A. R. Liddle, and R. G. Moorhouse. “Combined boson-fermion stars.” In: *Physics Letters B* 233.1-2 (Dec. 1989), pp. 99–106. DOI: 10.1016/0370-2693(89)90623-0.
- [70] A. B. Henriques, A. R. Liddle, and R. G. Moorhouse. “Combined boson-fermion stars: Configurations and stability.” In: *Nuclear Physics B* 337.3 (June 1990), pp. 737–761. DOI: 10.1016/0550-3213(90)90514-E.
- [71] A. Henriques, A. R. Liddle, and R. Moorhouse. “Stability of boson-fermion stars.” In: *Physics Letters B* 251.4 (1990), pp. 511–516. ISSN: 0370-2693. DOI: [https://doi.org/10.1016/0370-2693\(90\)90789-9](https://doi.org/10.1016/0370-2693(90)90789-9). URL: <http://www.sciencedirect.com/science/article/pii/0370269390907899>.
- [72] C. Herdeiro and E. Radu. “Construction and physical properties of Kerr black holes with scalar hair.” In: *Class. Quant. Grav.* 32.14 (2015), p. 144001. DOI: 10.1088/0264-9381/32/14/144001. arXiv: 1501.04319 [gr-qc].
- [73] C. Herdeiro, E. Radu, and H. Rúnarsson. “Kerr black holes with Proca hair.” In: *Classical and Quantum Gravity* 33.15 (2016), p. 154001. DOI: 10.1088/0264-9381/33/15/154001. URL: <https://doi.org/10.1088/0264-9381/33/15/154001>.
- [74] C. A. R. Herdeiro. “Black holes: on the universality of the Kerr hypothesis.” In: *arXiv e-prints*, arXiv:2204.05640 (Apr. 2022), arXiv:2204.05640. arXiv: 2204.05640 [gr-qc].
- [75] C. A. R. Herdeiro and E. Radu. “Kerr Black Holes with Scalar Hair.” In: *Phys. Rev. Lett.* 112 (22 2014), p. 221101. DOI: 10.1103/PhysRevLett.112.221101. URL: <https://link.aps.org/doi/10.1103/PhysRevLett.112.221101>.
- [76] C. A. Herdeiro, E. Radu, and N. M. Santos. “A bound on energy extraction (and hairiness) from superradiance.” In: *Physics Letters B* 824 (2022), p. 136835. ISSN: 0370-2693. DOI: <https://doi.org/10.1016/j.physletb.2021.136835>. URL: <https://www.sciencedirect.com/science/article/pii/S0370269321007759>.
- [77] W. Hu, R. Barkana, and A. Gruzinov. “Fuzzy Cold Dark Matter: The wave properties of ultralight particles.” In: *Phys. Rev. Lett.* 85 (2000), pp. 1158–1161. DOI: 10.1103/PhysRevLett.85.1158. arXiv: astro-ph/0003365.
- [78] J.-c. Hwang. “Roles of a coherent scalar field on the evolution of cosmic structures.” In: *Phys. Lett.* B401 (1997), pp. 241–246. DOI: 10.1016/S0370-2693(97)00400-0. arXiv: astro-ph/9610042.
- [79] P. Jetzer. “Stability of combined boson-fermion stars.” In: *Physics Letters B* 243.1-2 (June 1990), pp. 36–40. DOI: 10.1016/0370-2693(90)90952-3.

- [80] D. E. Kaplan, M. A. Luty, and K. M. Zurek. “Asymmetric dark matter.” In: *Physical Review D* 79.11 (June 2009). DOI: 10.1103/physrevd.79.115016. URL: <https://doi.org/10.1103%2Fphysrevd.79.115016>.
- [81] D. J. Kaup. “Klein-Gordon Geon.” In: *Phys. Rev.* 172 (5 Aug. 1968), pp. 1331–1342. DOI: 10.1103/PhysRev.172.1331. URL: <https://link.aps.org/doi/10.1103/PhysRev.172.1331>.
- [82] B. Kleihaus, J. Kunz, and M. List. “Rotating boson stars and Q -balls.” In: *Phys. Rev. D* 72 (6 2005), p. 064002. DOI: 10.1103/PhysRevD.72.064002. URL: <https://link.aps.org/doi/10.1103/PhysRevD.72.064002>.
- [83] B. Kleihaus et al. “Rotating boson stars and Q -balls. II. Negative parity and ergoregions.” In: *Phys. Rev. D* 77 (6 2008), p. 064025. DOI: 10.1103/PhysRevD.77.064025. URL: <https://link.aps.org/doi/10.1103/PhysRevD.77.064025>.
- [84] T. D. Lee and Y. Pang. “Stability of Mini - Boson Stars.” In: *Nucl. Phys.* B315 (1989). [129(1988)], p. 477. DOI: 10.1016/0550-3213(89)90365-9.
- [85] A. Lichnerowicz. “L’intégration des équations de la gravitation relativiste et le probleme des n corps.” In: *J. Math. Pures Appl* 23.37 (1944), p. 4.
- [86] S. L. Liebling and C. Palenzuela. “Dynamical boson stars.” In: *Living Reviews in Relativity* 15.1 (2012), p. 6.
- [87] F. Löffler et al. “The Einstein Toolkit: A Community Computational Infrastructure for Relativistic Astrophysics.” In: *Class. Quant. Grav.* 29 (2012), p. 115001. DOI: 10.1088/0264-9381/29/11/115001. arXiv: 1111.3344 [gr-qc].
- [88] D. J. E. Marsh. “Axion cosmology.” In: *Phys. Rep.* 643 (July 2016), pp. 1–79. DOI: 10.1016/j.physrep.2016.06.005. arXiv: 1510.07633 [astro-ph.CO].
- [89] D. J. E. Marsh and P. G. Ferreira. “Ultra-Light Scalar Fields and the Growth of Structure in the Universe.” In: *Phys. Rev.* D82 (2010), p. 103528. DOI: 10.1103/PhysRevD.82.103528. arXiv: 1009.3501 [hep-ph].
- [90] T. Matos, F. S. Guzman, and L. A. Urena-Lopez. “Scalar field as dark matter in the universe.” In: *Class. Quant. Grav.* 17 (2000), pp. 1707–1712. DOI: 10.1088/0264-9381/17/7/309. arXiv: astro-ph/9908152.
- [91] T. Matos and L. A. Urena-Lopez. “A Further analysis of a cosmological model of quintessence and scalar dark matter.” In: *Phys. Rev.* D63 (2001), p. 063506. DOI: 10.1103/PhysRevD.63.063506. arXiv: astro-ph/0006024 [astro-ph].
- [92] T. Matos and L. A. Urena-Lopez. “Quintessence and scalar dark matter in the universe.” In: *Class. Quant. Grav.* 17 (2000), pp. L75–L81. DOI: 10.1088/0264-9381/17/13/101. arXiv: astro-ph/0004332.
- [93] M. C. Miller et al. “PSR J0030+0451 Mass and Radius from NICER Data and Implications for the Properties of Neutron Star Matter.” In: *Astrophys. J. Lett.* 887.1, L24 (Dec. 2019), p. L24. DOI: 10.3847/2041-8213/ab50c5. arXiv: 1912.05705 [astro-ph.HE].
- [94] M. C. Miller et al. “The Radius of PSR J0740+6620 from NICER and XMM-Newton Data.” In: *Astrophys. J. Lett.* 918.2, L28 (Sept. 2021), p. L28. DOI: 10.3847/2041-8213/ac089b. arXiv: 2105.06979 [astro-ph.HE].

- [95] P. J. Montero, J. A. Font, and M. Shibata. “Nada: A new code for studying self-gravitating tori around black holes.” In: *Phys. Rev. D* 78.6, 064037 (Sept. 2008), p. 064037. arXiv: 0805.3099 [gr-qc].
- [96] P. J. Montero and I. Cordero-Carrión. “BSSN equations in spherical coordinates without regularization: Vacuum and nonvacuum spherically symmetric spacetimes.” In: *Physical Review D* 85.12 (2012), p. 124037.
- [97] T. Nakamura, K. Oohara, and Y. Kojima. “General Relativistic Collapse to Black Holes and Gravitational Waves from Black Holes.” In: *Progress of Theoretical Physics Supplement* 90 (1987), pp. 1–218.
- [98] C. Palenzuela, L. Lehner, and S. L. Liebling. “Orbital dynamics of binary boson star systems.” In: *Phys. Rev. D* 77 (4 2008), p. 044036. DOI: 10.1103/PhysRevD.77.044036. URL: <https://link.aps.org/doi/10.1103/PhysRevD.77.044036>.
- [99] C. Palenzuela et al. “Head-on collisions of boson stars.” In: *Phys. Rev. D* 75 (6 2007), p. 064005. DOI: 10.1103/PhysRevD.75.064005. URL: <https://link.aps.org/doi/10.1103/PhysRevD.75.064005>.
- [100] C. Palenzuela et al. “Gravitational wave signatures of highly compact boson star binaries.” In: *Physical Review D* 96.10 (2017), p. 104058.
- [101] V. Paschalidis and N. Stergioulas. “Rotating stars in relativity.” In: *Living Reviews in Relativity* 20.1, 7 (Nov. 2017), p. 7. DOI: 10.1007/s41114-017-0008-x. arXiv: 1612.03050 [astro-ph.HE].
- [102] R. D. Peccei and H. R. Quinn. “CP conservation in the presence of pseudoparticles.” In: *Phys. Rev. Lett.* 38.25 (June 1977), pp. 1440–1443. DOI: 10.1103/PhysRevLett.38.1440.
- [103] F. Pretorius. “Evolution of Binary Black-Hole Spacetimes.” In: *Physical Review Letters* 95.12, 121101 (Sept. 2005), p. 121101. eprint: gr-qc/0507014.
- [104] C. Reisswig et al. “Gravitational wave extraction in simulations of rotating stellar core collapse.” In: *Physical Review D* 83.6 (2011), p. 064008.
- [105] T. E. Riley et al. “A NICER View of PSR J0030+0451: Millisecond Pulsar Parameter Estimation.” In: *Astrophys. J. Lett.* 887.1, L21 (Dec. 2019), p. L21. DOI: 10.3847/2041-8213/ab481c. arXiv: 1912.05702 [astro-ph.HE].
- [106] T. E. Riley et al. “A NICER View of the Massive Pulsar PSR J0740+6620 Informed by Radio Timing and XMM-Newton Spectroscopy.” In: *Astrophys. J. Lett.* 918.2, L27 (Sept. 2021), p. L27. DOI: 10.3847/2041-8213/ac0a81. arXiv: 2105.06980 [astro-ph.HE].
- [107] R. Ruffini and S. Bonazzola. “Systems of Self-Gravitating Particles in General Relativity and the Concept of an Equation of State.” In: *Phys. Rev.* 187 (5 Oct. 1969), pp. 1767–1783. DOI: 10.1103/PhysRev.187.1767. URL: <https://link.aps.org/doi/10.1103/PhysRev.187.1767>.
- [108] N. Sanchis-Gual et al. “Nonlinear Dynamics of Spinning Bosonic Stars: Formation and Stability.” In: *Phys. Rev. Lett.* 123 (22 2019), p. 221101. DOI: 10.1103/PhysRevLett.123.221101. URL: <https://link.aps.org/doi/10.1103/PhysRevLett.123.221101>.

- [109] N. Sanchis-Gual et al. “Quasistationary solutions of self-gravitating scalar fields around collapsing stars.” In: *Phys. Rev. D* 92.8, 083001 (Oct. 2015), p. 083001. arXiv: 1507.08437 [gr-qc].
- [110] N. Sanchis-Gual et al. “Head-on collisions and orbital mergers of Proca stars.” In: *Phys. Rev. D* 99 (2 2019), p. 024017. DOI: 10.1103/PhysRevD.99.024017. URL: <https://link.aps.org/doi/10.1103/PhysRevD.99.024017>.
- [111] N. Sanchis-Gual et al. “Impact of the wave-like nature of Proca stars on their gravitational-wave emission.” In: *arXiv e-prints*, arXiv:2208.11717 (Aug. 2022), arXiv:2208.11717. arXiv: 2208.11717 [gr-qc].
- [112] N. Sanchis-Gual et al. “Multifield, Multifrequency Bosonic Stars and a Stabilization Mechanism.” In: *Phys. Rev. Lett.* 126 (24 2021), p. 241105. DOI: 10.1103/PhysRevLett.126.241105. URL: <https://link.aps.org/doi/10.1103/PhysRevLett.126.241105>.
- [113] N. Sanchis-Gual et al. “Numerical evolutions of spherical Proca stars.” In: *Physical Review D* 95.10 (2017), p. 104028.
- [114] N. Sanchis-Gual et al. “Synchronized gravitational atoms from mergers of bosonic stars.” In: *Phys. Rev. D* 102 (10 2020), p. 101504. DOI: 10.1103/PhysRevD.102.101504. URL: <https://link.aps.org/doi/10.1103/PhysRevD.102.101504>.
- [115] F. Sandin and P. Ciarcelluti. “Effects of mirror dark matter on neutron stars.” In: *Astroparticle Physics* 32.5 (Dec. 2009), pp. 278–284. DOI: 10.1016/j.astropartphys.2009.09.005. URL: <https://doi.org/10.1016%2Fj.astropartphys.2009.09.005>.
- [116] E. Schnetter, S. H. Hawley, and I. Hawke. “Evolutions in 3D numerical relativity using fixed mesh refinement.” In: *Classical and Quantum Gravity* 21 (Mar. 2004), pp. 1465–1488. eprint: gr-qc/0310042.
- [117] E. Seidel and W.-M. Suen. “Dynamical Evolution of Boson Stars. 1. Perturbing the Ground State.” In: *Phys. Rev. D* 42 (1990), pp. 384–403. DOI: 10.1103/PhysRevD.42.384.
- [118] E. Seidel and W.-M. Suen. “Formation of solitonic stars through gravitational cooling.” In: *Phys. Rev. Lett.* 72 (1994), pp. 2516–2519. DOI: 10.1103/PhysRevLett.72.2516. arXiv: gr-qc/9309015 [gr-qc].
- [119] M. Shibata and T. Nakamura. “Evolution of three-dimensional gravitational waves: Harmonic slicing case.” In: *Phys. Rev. D* 52 (Nov. 1995), pp. 5428–5444.
- [120] M. Shibata and K. ō. Uryū. “Simulation of merging binary neutron stars in full general relativity: $\Gamma=2$ case.” In: *Phys. Rev. D* 61.6, 064001 (Mar. 2000), p. 064001. eprint: gr-qc/9911058.
- [121] N. Siemonsen and W. E. East. “Gravitational wave signatures of ultralight vector bosons from black hole superradiance.” In: *Phys. Rev. D* 101 (2 2020), p. 024019. DOI: 10.1103/PhysRevD.101.024019. URL: <https://link.aps.org/doi/10.1103/PhysRevD.101.024019>.
- [122] N. Siemonsen and W. E. East. “Stability of rotating scalar boson stars with nonlinear interactions.” In: *Phys. Rev. D* 103 (4 2021), p. 044022. DOI: 10.1103/PhysRevD.103.044022. URL: <https://link.aps.org/doi/10.1103/PhysRevD.103.044022>.

- [123] L. Smarr et al. “Collision of two black holes: Theoretical framework.” In: *Phys. Rev. D* 14.10 (Nov. 1976), pp. 2443–2452. DOI: 10.1103/PhysRevD.14.2443.
- [124] N. Stergioulas and J. L. Friedman. “Comparing Models of Rapidly Rotating Relativistic Stars Constructed by Two Numerical Methods.” In: *Astrophys. J.* 444 (May 1995), p. 306. DOI: 10.1086/175605. arXiv: astro-ph/9411032 [astro-ph].
- [125] The LIGO Scientific Collaboration and the Virgo Collaboration. “GW170817: Observation of Gravitational Waves from a Binary Neutron Star Inspiral.” In: *Phys. Rev. Lett.* 119 (16 Oct. 2017), p. 161101. DOI: 10.1103/PhysRevLett.119.161101. URL: <https://link.aps.org/doi/10.1103/PhysRevLett.119.161101>.
- [126] The LIGO Scientific Collaboration and the Virgo Collaboration. “GW190425: Observation of a Compact Binary Coalescence with Total Mass $\sim 3.4 M_{\text{sub}\odot}$ /sub.” In: *The Astrophysical Journal Letters* 892.1 (Mar. 2020), p. L3. DOI: 10.3847/2041-8213/ab75f5. URL: <https://doi.org/10.3847/2041-8213/ab75f5>.
- [127] The LIGO Scientific Collaboration, the Virgo Collaboration, and the KAGRA Collaboration. “GWTC-3: Compact Binary Coalescences Observed by LIGO and Virgo During the Second Part of the Third Observing Run.” In: *arXiv e-prints*, arXiv:2111.03606 (Nov. 2021), arXiv:2111.03606. arXiv: 2111.03606 [gr-qc].
- [128] Carpet. <http://carpetcode.org>.
- [129] S. Valdez-Alvarado, R. Becerril, and L. A. Ureña López. “Fermion-boson stars with a quartic self-interaction in the boson sector.” In: *Phys. Rev. D* 102 (6 Oct. 2020), p. 064038. DOI: 10.1103/PhysRevD.102.064038. URL: <https://link.aps.org/doi/10.1103/PhysRevD.102.064038>.
- [130] S. Valdez-Alvarado et al. “Dynamical evolution of fermion-boson stars.” In: *Phys. Rev. D* 87 (8 Apr. 2013), p. 084040. DOI: 10.1103/PhysRevD.87.084040. URL: <https://link.aps.org/doi/10.1103/PhysRevD.87.084040>.
- [131] A. L. Watts, N. Andersson, and D. I. Jones. “The Nature of Low $T/|W|$ Dynamical Instabilities in Differentially Rotating Stars.” In: *Astrophys. J.* 618.1 (2005), pp. L37–L40. DOI: 10.1086/427653. arXiv: astro-ph/0309554 [astro-ph].
- [132] M. Wielgus et al. “Millimeter Light Curves of Sagittarius A* Observed during the 2017 Event Horizon Telescope Campaign.” In: *Astrophys. J. Lett.* 930.2, L19 (May 2022), p. L19. DOI: 10.3847/2041-8213/ac6428. arXiv: 2207.06829 [astro-ph.HE].
- [133] H. Witek et al. *Canuda: a public numerical relativity library to probe fundamental physics*. Oct. 2021. DOI: 10.5281/zenodo.5520862. URL: <https://doi.org/10.5281/zenodo.5520862>.
- [134] L. Witten. *Gravitation: An Introduction to Current Research*. Wiley, 1962. URL: <https://books.google.es/books?id=3lIAAAAIAAJ>.
- [135] J. York J. W. “Kinematics and dynamics of general relativity.” In: *Sources of Gravitational Radiation*. Ed. by L. L. Smarr. Jan. 1979, pp. 83–126.

-
- [136] S. Yoshida and Y. Eriguchi. “Rotating boson stars in general relativity.” In: *Phys. Rev. D* 56 (2 1997), pp. 762–771. DOI: 10.1103/PhysRevD.56.762. URL: <https://link.aps.org/doi/10.1103/PhysRevD.56.762>.
- [137] M. Zilhão and F. Löffler. “An Introduction to the Einstein Toolkit.” In: *Int. J. Mod. Phys. A* 28 (2013), p. 1340014. DOI: 10.1142/S0217751X13400149. arXiv: 1305.5299 [gr-qc].

